Reconstructing the timing and location of North-West Saharan rainfall with spatially distributed secondary carbonates

Thesis submitted to the University of Oxford

for the degree of Doctor of Philosophy

Department of Earth Sciences

St. Cross College, University of Oxford

April 2022

Supervised by Dr. Christopher Day

and Professor Gideon Henderson

Declaration

I declare that this work has not been submitted, either partially or in full, to any other university for any degree, diploma or other qualifications. The contents of this thesis are entirely my own work, unless otherwise stated. An appropriate author list is presented at the start of chapters which have co-author affiliations.

Dedicated to Norma and Alastair Couper

Scholars and humanitarians who improved the world

Abstract

There is significant evidence that the presently hyper-arid Sahara belt stretching across North Africa has experienced periods of increased rainfall and surface moisture coverage at numerous times during the middle to late Pleistocene. During these times, there was increased vegetation coverage, greater mega-fauna distributions and more extensive human occupation. However, our understanding of precisely where and when rainfall increased is currently limited due to a paucity of high-resolution paleoclimate data. Furthermore, present records are over-extrapolated in their interpretations of moisture source and the spatial distribution of rainfall. In this thesis, periods of past increased rainfall are assessed in the central and northern Sahara using the formation age, stable isotope compositions and trace element concentrations of radiometrically dated secondary carbonate deposits. Stalagmites from the High- and Anti-Atlas Mountains provide evidence that sub-tropical rainfall occurs in response to increasing North-South inter-hemispheric temperature anomalies during the mid-Holocene African Humid Period, rather than as the direct result of a northwards extension of the West African Monsoon. Subsequently, older periods of Saharan-, High- and Anti-Atlas speleothem formation throughout the middle to late Pleistocene identifies periods of increased northern Sahara rainfall during a number of major northern hemisphere interglacial and interstadials. In the central Sahara, chronology from flowstone-like secondary calcite samples provides the first evidence of carbonate deposition from this region formed from direct, local rainfall rather than as a result of increased surface moisture availability. Calcite formation during Marine Isotope Stage 11 suggests a consistent tropical source of rainfall in the central and northern Sahara. This thesis presents the north-west Sahara as a unique and climatically significant Saharan region, from which the activation of perennial southward flowing river systems was critical for human migration and development. Furthermore, this work better characterises the minimum geographic extent of increased north-west Saharan rainfall and identifies the need to move away from overly-generalised "Green Sahara" interpretations of Saharan climate.

Extended Abstract

Reconstructing the timing and location of North-West Saharan rainfall with spatially distributed secondary carbonates

The presently hyper-arid Sahara belt stretching across North Africa is a vitally important part of the global climate system, influencing distal atmospheric conditions and supplying oceans with nutrients via significant dust export. Human populations, as well as fauna and flora living on the extremities of the desert, rely heavily on seasonal rainfall to survive, placing them at high risk of future climate change. Despite the modern hyper-arid state of the region, North Africa once had much higher rates of annual precipitation, with increased vegetation coverage, greater mega-fauna distributions and extensive human occupation. However, understanding the climate dynamics and potential future rainfall change in this region is difficult due to a paucity in both modern instrumental, and high-resolution paleoclimate data. Secondary carbonates such as stalagmites are calcium carbonate deposits which can be radiometrically-dated, and provide an array of geochemical proxies from which we can infer information about past climate conditions. A limiting factor for the formation of stalagmites is the input of water to a karst system, and so just the presence of such features in presently hyper-arid environments is indicative of a wetter past. By using stalagmites and secondary carbonate deposits collected from presently arid regions of North Africa as terrestrial paleoclimate archives, periods of past increased effective precipitation in the region may be assessed at discrete locations, constraining the timing of such events, and improving our understanding of the controls on climate dynamics there.

This thesis presents research from the northern sections of the Sahara. Numerous new field sites and caves are presented between 28-32°N and 2°W-2°E. U-Th, stable isotope, calcium isotope, trace element and clumped isotope data are interpreted in a paleoclimate context, characterising periods of time through the middle to late Pleistocene in which these regions received much higher rates of annual precipitation than

during the modern day. In particular, U-Th chronology is used to define increased local rainfall at discrete locations across north-west Africa in a more accurate way than other paleoclimate proxies. This thesis first details the concept and importance behind this research (Chapter 1) before introducing three new field locations in two distinct regions of the Algerian Sahara, describing the geology, caves and samples collected from each site (Chapter 2). In Chapter 3, an extended methodology is presented which may be referred back to when data collection is discussed in subsequent chapters. In particular, U-Th data are critical for interpretations throughout this thesis, and so this short chapter introduces further information and theory behind U-Th dating methods. Subsequently, data are presented in Chapters 4, 5, 6 and 7, summarised here.

Chapter 4 presents the abstract and main text of the manuscript "North-West Saharan Holocene rainfall driven by inter-hemispheric temperature differences", as submitted to Science Advances. In this work, stalagmite records first presented in Barrott (2014) from the High- and Anti-Atlas Mountains of southern Morocco are used to demonstrate increased rainfall between 8.7-4.3 kyr BP. The location, timing and oxygen isotopes of this stalagmite-growth demonstrate that subtropical rainfall occurs in response to increasing North-South inter-hemispheric temperature anomalies, after the decline of the West African Monsoon, and that this increased rainfall supports a rapid increase in the region's Neolithic population. This improved habitability and increased recharge to rivers flowing south through the Sahara will have greatly facilitated connections across the Sahara, during a key period in the Holocene development of land use and animal production.

In Chapter 5, high-precision U-Th chronology of stalagmites from the Algerian Saharan Atlas Mountains reveals numerous periods of increased rainfall leading to speleothem growth, including robust evidence for formation at 386-378 kyr BP (Marine Isotope Stage (MIS) 11), 316-310 kyr BP (MIS 9), 155-145 kyr BP (MIS 6), 80-74 kyr BP (MIS 5a) and 8-5 kyr BP (MIS 1). This chronology correlates with periods of speleothem growth in the Moroccan High- and Anti-Atlas Mountains, implying that in-

creases in north-west Saharan rainfall are regional on the desert side of the Atlas range between 7°W-1°E and 30-33°N. These data provide important evidence for multiple periods of increased rainfall across north-west Africa during the past 450 kyrs, robustly increasing the temporal resolution of records of direct, local rainfall, and providing key information as to the minimum geographic extent of increased rainfall.

Chapter 6 introduces new U-Th, stable isotope, calcium isotope and clumped isotope data from central Saharan secondary calcite deposits, collected from the southern edge of the Tademaït Plateau, central Algeria. Well-laminated, flowstone-like block calcite samples provide the first evidence of secondary carbonate deposition in this region, and allow for high-resolution central Saharan paleoclimate reconstruction. U-Th chronology suggests calcite formation occurred during a major northern hemisphere interglacial, MIS 11, also coeval with stalagmite growth in samples located at the northernmost limits of the Sahara. These data provide the first evidence of secondary carbonate deposition from this region forming from direct, local rainfall rather than simply as a result of increased surface moisture availability. High-resolution stable isotope records exhibit similarities with northern hemisphere sea surface temperatures and other orbitally controlled paleoclimate proxies, suggesting a tropical source of rainfall at the northern extent of the Sahara, and interconnected environmental conditions between 28 and 32°N during MIS 11.

Finally, Chapter 7 presents three new high-resolution trace element records from a southern Morocco stalagmite, including two sub-monthly trace element and stable isotope records. These records are presented as further evidence for changes in the availability of moisture and seasonality of rainfall in the South of Atlas region during the mid-Holocene African Humid Period (AHP). These data provide robust initial evidence for the potential of using trace element variations in tracking changes in rainfall amount during the AHP in southern Morocco, for which information is currently limited, thus contributing further important theoretical interpretations of past climate.

This research thoroughly begins to address the ever-increasing need for improving

the spatial coverage of well-dated paleoclimate proxy data, for which chronology is unequivocal evidence of increased rainfall at that site. Strong evidence is provided for recurring mechanisms of tropical plumes being the source of rainfall in these regions, identifying the north-west Sahara as a unique zone during past periods of increased rainfall from which the activation of perennial southward flowing river systems was critical for human migration and development. This thesis also introduces suggestions for the need to better characterise periods of increased North African rainfall at discrete locations, rather than extrapolating the cause and coverage of periods of increased humidity across the continent using regional proxies.

Acknowledgments

Firstly, I would like to thank my supervisors Chris Day and Gideon Henderson for their support, patience during meetings, scientific guidance and laboratory advice throughout my DPhil. Gideon's input was vital in forming a partnership with CRAAG, our collaborators in Algeria, without which this project would not have been the same. Subsequently, Chris was central to the success of two field excursions into the Algerian Sahara with his caving and field expertise, and our regular musings into North African climate have been of endless use, interest and enjoyment, so thank you for always being so generous with your time both in and out of the lab.

A huge thank you to Mohamed, Said, Professor Chaouche, Aboubakr, Hishem and all of those at CRAAG for their support, time and expertise in the Algerian Sahara. I couldn't think of a better group to do fieldwork with and this project would not have been possible without the collaboration and support of CRAAG. In addition, a huge thanks to all of the people I met in the field at In Salah, Ain Sefra, Brezina, Algiers and all in between. Bread cooked beneath the sand, tea sat on dunes and endless North African coffees made the search for caves all the more rewarding, and we were greeted with meals, support and interest wherever we went. At Ain Sefra in particular, support from the *Friends of the Atlas* group, including from Bachir, Hicham and Mustapha, made the access of cave sites incredibly smooth.

Scientifically within department, there are multiple people to acknowledge. A massive thank you to Andrew Mason for his support with all things U-Th and mass spectrometry related. No question feels too stupid with Andrew and he brings Plasma 2 to life, making the long days much easier. Thank you to Alan Hsieh, Stacy Carolin, Jane Barling, Phil Holdship, Franzi Lechleitner, Owen Jones, Katherine Clayton, Matthew Beverley-Smith, Jon Wells, as well as all within Oxford's geochemistry Lab groups, for help with analyses and useful scientific discussion.

I have also met many people in Oxford who will be lifelong friends and who helped me through the DPhil massively. Anti-social coffees with Nick and Louis, mushroom

walks with Richard, picking room chats with Frankie, hot and dry noodles with Sean and egg deliveries from James made life in department worthwhile. To Ella, Oscar and Louis, I will always miss our three years at Oatlands and it was always a relief to come home to you and share the load of doing a PhD. Thank you Oli for my hello freshes and divot derby wins, Becca for nature walks and 0°C mental health swims, and to Will, Matt, Basil and Eoin for everything football related. Thank you Kate VF for your dog therapy and care packages whilst I've been in Oxford. Finally, to Chris Theaker, the co-creater of the worlds best sport, thank you for your excellent humour and endless help with all things stalagmites.

To my family. Mum, thank you for being my biggest fan and for supporting me in endless way. Dad, for your advice throughout the past 5 years and support whenever I needed it. Caitlin and Teigan, thank you for your never-ending laughter, support and Tilly pictures. Grandma and Grandpa for your love of what I do and for being so generous. Thank you to all the Hollises, Hughses and Coupers who have supported me, particularly through the zoom calls and quizzes of lockdown. Finally, thank you to Norma and Alastair, for teaching me to question, learn and care about the smallest details in life.

Thank you to the NERC Environmental Research DTP for funding me throughout this project, and for the additional funding as support for Covid19 related extensions.

Contents

1 Introduction **1**

1.1 Introduction 4

1.2 Study Area 6

1.3 Modern Climate 7

1.4 North African Paleoclimate 12

1.4.1 Significance of past increased rainfall 17

1.5 Speleothems as Paleoclimate Archives 19

1.5.1 North Africa Speleothem Records 21

1.5.2 Speleothem $\delta^{18}O$ as a paleoclimate proxy 22

1.5.3 Modern regional $\delta^{18}O$ 24

1.6 Research Goals 25

2 Fieldwork **27**

2.1 Introduction 30

2.2 Fieldwork Methodology 31

2.3 Central Sahara 32

2.3.1 Calcite Deposition 36

2.4 Northern Sahara 40

2.4.1 Grar Cave 42

2.4.1.1 Grar Cave Samples 44

2.4.2 Maqlae Cave 45

2.4.2.1 Maqlae Cave Samples 45

3 Extended Methodology **47**

3.1 Sample handling 49

3.1.1 Sub-sample milling 50

3.1.1.1 U-Th Milling 50

3.1.1.2 High-resolution micro-milling 50

3.2 Sample Characterisation 51

3.3 Stable Isotope Analysis 52

3.4 U-Th Dating 53

3.4.1 U-Th Theory 53

3.4.2 Chemistry methods 57

3.4.3 MC-ICP-MS analysis 60

3.4.4 Corrections 60

3.4.5 Data processing 61

4 North-West Saharan Holocene rainfall driven by interhemispheric temperature differences **62**

4.1 Abstract 65

4.2 Main Text 66

4.3 Additional Information 74

5 Regionally extensive periods of increased rainfall during the last 450 kyrs defined by northern Saharan stalagmites **75**

5.1 Introduction 78

5.2 Climate and cave settings 80

5.2.1 Grar Cave 81

5.2.2 Maqlae Cave 84

5.2.3 Other caves 86

5.3 Methods 86

5.3.1 XRD 86

5.3.2 U-Th Dating 87
5.3.3 Stable isotope analysis 88
5.4 Results 89
5.4.1 XRD 89
5.4.2 U-Th Chronology 89
5.4.3 OxCal Age Model 95
5.4.4 High-resolution stable isotope records 96
5.5 Discussion 98
5.5.1 Timing of SOA rainfall throughout the past 450 kyrs 98
5.5.2 The African Humid Period 103
5.6 Conclusion 106

6 Secondary carbonates record increased local rainfall in the central Sahara during MIS 11 108

6.1 Introduction 111
6.2 Study Site 113
6.3 Methods 116
6.3.1 XRD Analysis 116
6.3.2 U-Th Dating 118
6.3.3 OxCal Age Model 120
6.3.4 Stable Isotope Analysis 120
6.3.5 Calcium Isotope Analysis 121
6.3.6 Clumped Isotope paleo-thermometry 122
6.4 Results 122
6.4.1 XRD 122
6.4.2 U-Th 122
6.4.3 Stable Isotopes 130
6.4.4 Calcium Isotopes 132
6.4.5 Clumped Isotope paleo-thermometry 134

6.5 Discussion . . . 135
6.5.1 Calcite Chronology . . . 135
6.5.2 Saharan rainfall during MIS 11 . . . 137
6.5.3 Moisture Sources . . . 140
6.5.4 Paleoclimate Significance . . . 144
6.6 Conclusion . . . 146

7 Sub-monthly African Humid Period trace element records 147
7.1 Introduction . . . 150
7.1.1 Trace elements as a stalagmite proxy . . . 152
7.2 Methods . . . 153
7.2.1 Sub-sampling . . . 153
7.2.2 Trace element analysis . . . 154
7.2.3 Stable isotope analysis . . . 154
7.3 Results and discussion . . . 155
7.4 Conclusion . . . 159

8 Conclusions 160
8.1 Summary . . . 162
8.1.1 Climate variability during the African Humid Period . . . 163
8.1.2 Improved temporal coverage of north-west Sahara rainfall . . . 163
8.1.3 Records of direct rainfall in the central Sahara . . . 164
8.1.4 Potential for sub-annual measurements of paleo-hydrology in the northern Sahara . . . 164
8.2 "Green Sahara" periods . . . 165
8.3 The South of Atlas . . . 166
8.4 Future work . . . 166

Bibliography 168

List of Figures

1.1 North Africa and Study Sites 5
1.2 Modern Climatology of North Africa 9
1.3 Map of North-west Africa 10
1.4 South of Atlas Monthly Rainfall 11
1.5 North African Paleoclimate Records 15
1.6 Speleothem Formation 21

2.1 Research Fieldwork Sites 30
2.2 The Tademaït Plateau 34
2.3 Calcite Samples in the Field 37
2.4 Calcite Blocks 38
2.5 Saharan Atlas Field Site 42
2.6 Grar Cave 44
2.7 Maqlae Cave 46

3.1 U-Th Decay Chain 54
3.2 U-Th Closed-system Decay 55

4.1 AHP Manuscript Figure 1 68
4.2 AHP Manuscript Figure 2 71
4.3 AHP Manuscript Figure 3 72

5.1 Saharan Atlas Location and Climatology 79

5.2 North-west Africa Field Sites 81
5.3 Grar Cave Speleothem Scans and U-Th Ages 82
5.4 Maqlae Cave Speleothem Scans and U-Th Ages 84
5.5 South of Atlas Speleothems U-Th Ages 90
5.6 BZ-1A OxCal Age Model 95
5.7 Ksour Stalagmite Stable Isotope Records 97
5.8 Paleoclimate Stack Plot 101
5.9 MM vs BZ-1A δ^{18}O records 104
5.10 BZ-1A δ^{13}C, Anti-Atlas δ^{18}O and N-S Temperature Anomaly 105

6.1 Tademaït Plateau and Modern Climate 112
6.2 The Tademaït Plateau 115
6.3 Calcite Samples from the Tademaït Plateau 117
6.4 U-Th Activity Ratio Data 123
6.5 U-Th Isotopic Data 127
6.6 TPB1 Stable Isotopes Records 131
6.7 Levels Calcite $\delta^{44/42}$Ca and δ^{13}C Data 133
6.8 Cartoon Representation of Levels Calcite Formation 135
6.9 MIS 11 Paleoclimate Proxies 140
6.10 North Africa (Paleo)Rainfall Mechanisms 141
6.11 TPB1 and MM δ^{13}C Records 144
6.12 Calculated δ^{18}O Variations 145

7.1 Summary of ASD-1 Proxies 151
7.2 Full section ASD-1 Trace Element Record 156
7.3 Ultra-high-resolution ASD-1 Trace Element Records 158

List of Tables

5.1 Grar Cave U-Th Results 93
5.2 Maqlae Cave U-Th Results 94

6.1 Blocks U-Th Results 124
6.2 Geodes U-Th Results 126
6.3 Aquifer Isotopic Values 132

List of Abbreviations and Definitions

Paleoclimate Terms

AHP African Humid Period

MIS Marine Isotope Stage

LGM Last Glacial Maximum

yr Year

kyrs Thousands of years

BP Before Present (i.e. before the year 1950)

CE Common Era

Climate Terms

SOA South of Atlas

ATL Atlantic

MED Mediterranean

ITCZ Intertropical Convergence Zone

TEI Tropical-Extratropical Interaction

TP Tropical Plume

WAM West African Monsoon

TEJ Tropical Easterly Jet

SHL Saharan Heat Low

AMOC Atlantic Meridional Overturning Circulation

NAO North Atlantic Oscillation

NWSAS North-West Saharan Aquifer System

CT Complex Terminal Aquifer

CI Continental Intercalaire Aquifer

GMWL Global Meteoric Water Line

Measurements

VPDB Vienna Pee Dee Belemnite

VSMOW Vienna Standard Mean Ocean Water

CRM-145 Uranium standard

U-Th Uranium-Thorium

MC-ICP-MS Multicollector Inductively Coupled Plasma Mass Spectrometer

α Fractionation Factor

Δ Distilled

masl metres above sea level

km kilometre

mL millilitre

g gram

ppm parts per million

ppb parts per billion

m milli (10^{-3})

μ micro (10^{-6})

n nano (10^{-9})

Datasets

GNIP Global Network of Isotopes in Precipitation

IAEA International Atomic Energy Agency

GHCN-M Global Historical Climatology Network-Monthly

ERA-5 Reanalysis Data

Chapter 1

Introduction

Contents

1.1 Introduction 4

1.2 Study Area 6

1.3 Modern Climate 7

1.4 North African Paleoclimate 12

1.4.1 Significance of past increased rainfall 17

1.5 Speleothems as Paleoclimate Archives 19

1.5.1 North Africa Speleothem Records 21

1.5.2 Speleothem δ^{18}O as a paleoclimate proxy 22

1.5.3 Modern regional δ^{18}O 24

1.6 Research Goals 25

Summary

There are numerous components to North Africa's climate system. The region experiences a range of Mediterranean, mountainous, sub-tropical, tropical and hyper-arid conditions, with vastly varying temperatures and rainfall amounts. The study of past climates in North Africa have largely attempted to explain periods of increased rainfall and surface moisture availability by homogenous mechanisms, searching for single moisture sources which can explain proxy evidence for increased rainfall across the region. However, there are contradictions between proxy records and climate models, and the range of contemporary climate conditions means that it is unlikely that a single explanation can be used for past increased rainfall. This thesis aims to increase the spatial and temporal resolution of high-resolution and well-dated paleoclimate proxies from discrete, strategic locations in north-west Africa to strengthen interpretations of where, when and why rainfall increased in the past.

1.1 Introduction

At the northernmost reaches of North Africa, the Mediterranean climate belt stretches along the breadth of the region's coastline, with annual rainfall supplied via winter cyclones, supporting life and agriculture in abundance. In the east, the river Nile dominates, sourced by monsoonal rains in the tropics and flowing perennially through populated regions. At the southern limits of the northern hemisphere, summer insolation heats up the North African continent faster than it does the sea, forcing rains inland via the West African Monsoon (WAM) and giving way to rainforests and river valleys. Whilst in the west, rainfall peaks annually in the winter as a result of subtropical North Atlantic westerlies, with some regions of high topography in the Atlas Mountains capped perennially with snow. Despite these ranging climate conditions and biomes, the Sahara is the dominant feature of North Africa (Figure 1.1), extending over $> 15^{o}$ latitude and $> 50^{o}$ longitude and consisting of sand dunes, weathered rock and paleo-river channels visible from space. Barring regions of high-topography where orographic rainfall occurs, and oases where groundwater intersects the land surface, the Sahara is characterised by very low rates of annual precipitation, high winds, extremely limited surface moisture availability and intense summer heat, all of which limits human occupation of the desert.

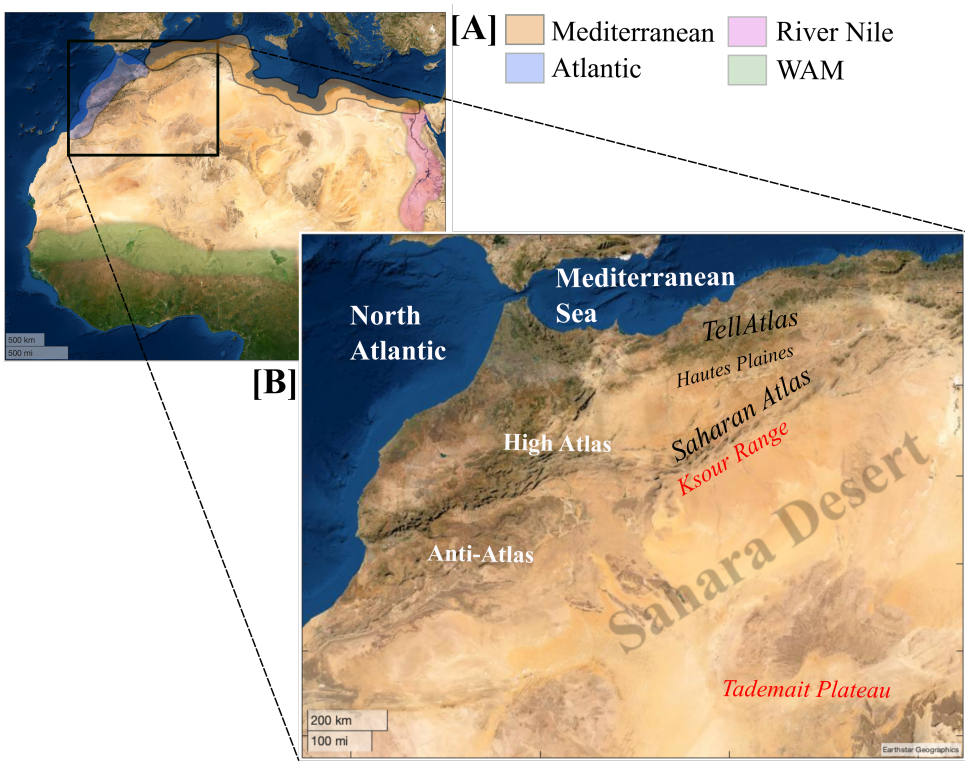


Figure 1.1: **North Africa and Study Sites** [A] Satellite image of North Africa with major climate and geographic features labelled, as per the text. [B] Zoomed-in satellite image of the study area, with major orographic and geographic features labelled. Regions from which study sites first presented in this thesis are found are annotated in red, whilst regions from which study sites first presented in Barrott (2014) are found are annotated in bold white.

However, this has not always been the case. Sustained periods of increased rainfall have taken place numerous times throughout the middle to late Pleistocene, leading to enhanced surface water coverage, megafaunal occupation and widespread vegetation cover, and are likely to have played a pivotal role in both the societal development and migration of early humans in North Africa. Despite this, there remains a lack of definitive knowledge as to precisely where, when and why Saharan climate altered in the past and how it may change in the future. Resultantly, there is a critical need for increased temporal and geospatial coverage of high-resolution and well-dated paleoclimate records, to improve understanding into where local rainfall increased or decreased, the controls on these changes, and what impact that had on human populations living in and around the desert.

Understanding these periods of increased moisture availability is of significant im-

portance due to the difficulties climate models have in representing where and when precipitation has changed over North Africa, and to what extent, hence limiting our understanding of future rainfall variations (McGee, 2020). Furthermore, the Sahara is the world's largest dust source (Middleton and Goudie, 2001), impacting cloud formation (Ansmann et al., 2008), ocean nutrients supply (Baker et al., 2003) and influencing the atmospheric radiation balance (Slingo et al., 2006). There are suggested links between Saharan climate, particularly through dust export, and the state of other global climate systems such as South American and Asian monsoons (Tabor et al., 2020; Griffiths et al., 2020), El Nino climate oscillations (Pausata et al., 2017) and regions as distal as the Arctic (Muschitiello et al., 2015). Therefore deciphering the nuances of Saharan climate throughout the middle to late Pleistocene is necessary for better understanding other changes in the global climate system.

1.2 Study Area

The study area for this research is situated across the northern limits of the Saharan Desert, in north-west Africa across southern Morocco and central Algeria. Within the remit of this project, fieldwork was strategically undertaken at two under-researched regions of central and northern Algeria (Figure 1.1); (1) the Ksour Mountains, which is the western-most range of the Saharan Atlas in the northern Sahara and (2) the Tademaït Plateau, a carbonate platform in the central Algerian Sahara, located over 900 km from Atlantic and Mediterranean coastlines. Further research is also reported on previously studied sites in southern Morocco (Barrott, 2014), in the Anti-Atlas and southern foothills of the High Atlas mountains (Figure 1.1), to complement regional interpretations of north-west Saharan climate. Combined, the Anti-Atlas and Ksour Mountain study sites are located in a region known as the "South of Atlas" (SOA), at the northern limits of the Sahara, whilst the Tademaït Plateau is located in the very centre of the desert.

1.3 Modern Climate

Understanding modern-day climate in North Africa, and being able to predict future changes, is key. Significant human populations live on the present-day boundaries between regions with reliable annual rainfall and extremely dry conditions. Livelihoods are intrinsically linked to annual variations in rainfall, moving livestock and planning crop yields around the rains (Zhang and Cook, 2014). Changes in the position of modern climate boundaries associated with anthoprogenic climate change are already impacting agriculture, migration and quality of life (Schilling et al., 2012). At the northern extremes of the desert, in the Saharan Atlas mountains, increased frequency of extreme rainfall events cause flooding in towns which have no infrastructure to deal with the amount of rainfall falling in such small periods of time (Derdour et al., 2018).

North African precipitation is predominantly supplied by three sources in the modern day; mid-latitude westerlies in the extreme north-west, Mediterranean cyclones along the extent of the northern coastline and annual monsoon rainfall between 0-15°N (Figure 1.2). Rainfall associated with North Atlantic mid-latitude westerlies are related to North Atlantic Oscillation (NAO) phases (Glueck and Stockton, 2001; Wassenburg et al., 2013), with negative (NAO-) conditions resulting in increased precipitation. Mediterranean precipitation has a low correlation with NAO phase (Knippertz et al., 2003a), instead associated with western Mediterranean cyclones bringing moisture directly off the Mediterranean Sea during boreal winter (Lionello et al., 2006).

The West African Monsoon (WAM) is fundamentally caused by differential heating between the North African land and neighbouring ocean during the summer months (maximum insolation), with the land heating up more quickly, reversing trade wind directions and drawing in moisture from the ocean (Thorncroft et al., 2011). The WAM is thus influenced significantly by the amount of boreal summer insolation the North African continent receives, although the amount of rainfall occurring each year also depends on the interaction between a number of elements of the WAM system, including the Tropical Easterly Jet (TEJ), the Saharan Heat Low (SHL) and the Intertropical

Convergence Zone (ITCZ) (Raj et al., 2019). The ITCZ itself migrates north and south towards the warmer hemisphere (i.e. shifting northwards during boreal summer and vice versa). The contemporary *mean* position of the ITCZ is slightly north of the equator due to greater energy inputs into the northern hemisphere atmosphere than the southern hemisphere, largely as a result of ocean heat transport from south to north (Marshall et al., 2014), although this mean position is postulated to shift (Broccoli et al., 2006; Schneider et al., 2014).

In the central Sahara, the subject of Chapter 6, annual rainfall is very low (averaging 12mm/yr) and temperatures are high (reaching over 45°C). At approximately 25°N, a boundary exists between annual rainfall amounts falling dominantly in either boreal winter or summer, identifying the geographic extent to which climate regimes operate across North Africa (Figure 1.2).

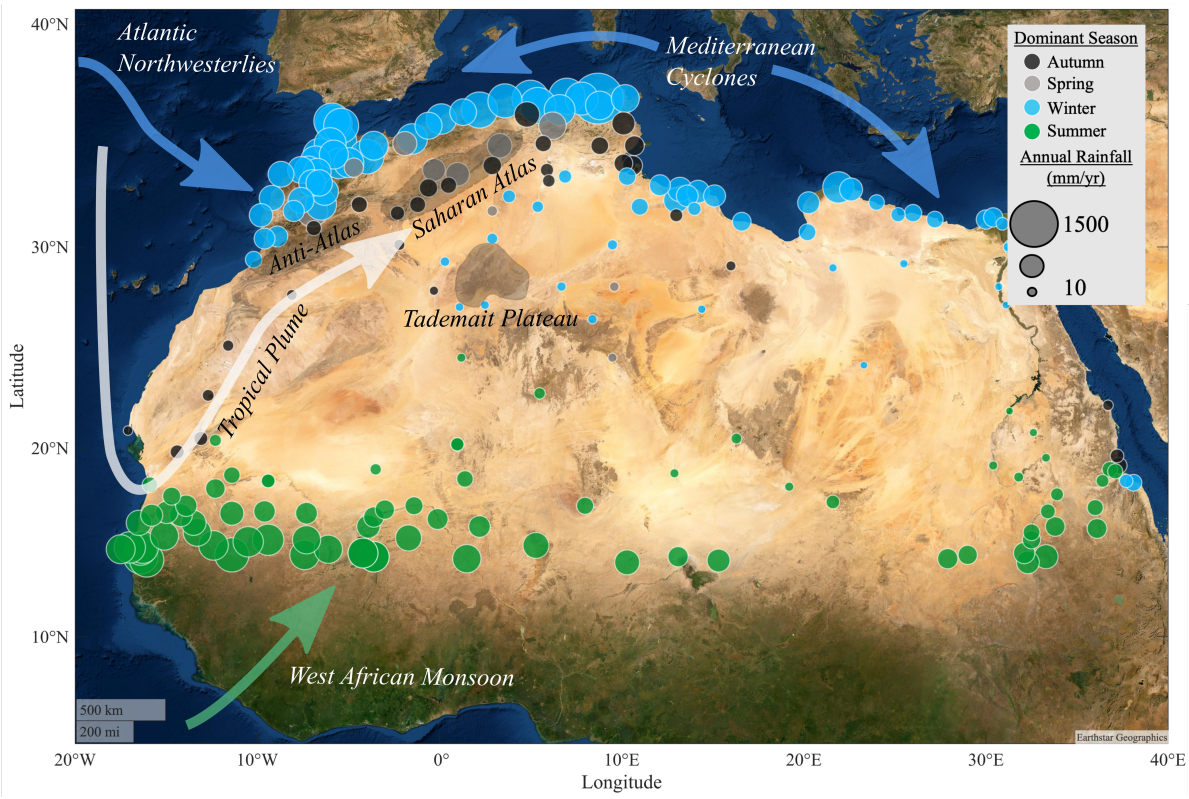


Figure 1.2: **Modern Climatology of North Africa**. North African GHCN-M meteorological station rainfall amounts and the dominant season in which rainfall occurs plotted on a high-resolution satellite image. Data sourced from http://climexp.knmi.nl (Trouet and Oldenborgh, 2013). Bubble size represents annual rainfall amount, ranging between 10 and 1542 mm/yr. Bubble colour represents the dominant season (highest percentage of annual rainfall) in which rainfall occurs; blue = winter, green = summer, black = autumn, grey = spring. The northern coast is dominated by large amounts of winter (blue) rainfall associated with North Atlantic and Mediterranean rainfall. The southern regions of North Africa are dominated by similarly large annual rainfall amounts but in summer (green), associated with West African Monsoon rainfall. A lower limit of 14°N was used during data collection. The South of Atlas region (Figure 1.3) has smaller amounts of rainfall falling dominantly during spring and autumn seasons, associated with tropical plumes (Knippertz, 2003). The central Sahara has rainfall occurring mainly during summer up to ∼25°N, and during other seasons in more northerly latitudes, dominantly winter. The general locations of the Anti-Atlas (Chapter 4), Saharan Atlas (Chapter 5) and Tademaït Plateau (Chapter 6) are plotted as grey shaded areas. A typical upper-level trough trajectory associated with tropical plumes is drawn as a white arrow, proximal to meteorological stations in which rainfall dominantly occurs in spring or autumn, agreeing with Knippertz and Martin (2005).

The north-western region of North Africa (Figure 1.3), the subject of Chapters 4 and 5, can be split into three distinct climate zones; Mediterranean (MED), Atlantic (ATL) and South of Atlas (SOA), as defined independently (Knippertz et al., 2003a).

The SOA region is shown to have a unique hydroclimate in the context of the Saharan region (Figure 1.2). Annual rainfall is typically < 150 mm/yr, falling in a bimodal distribution with rainfall dominantly occurring during the 'transition seasons' (spring and autumn; Knippertz et al. (2003a)).

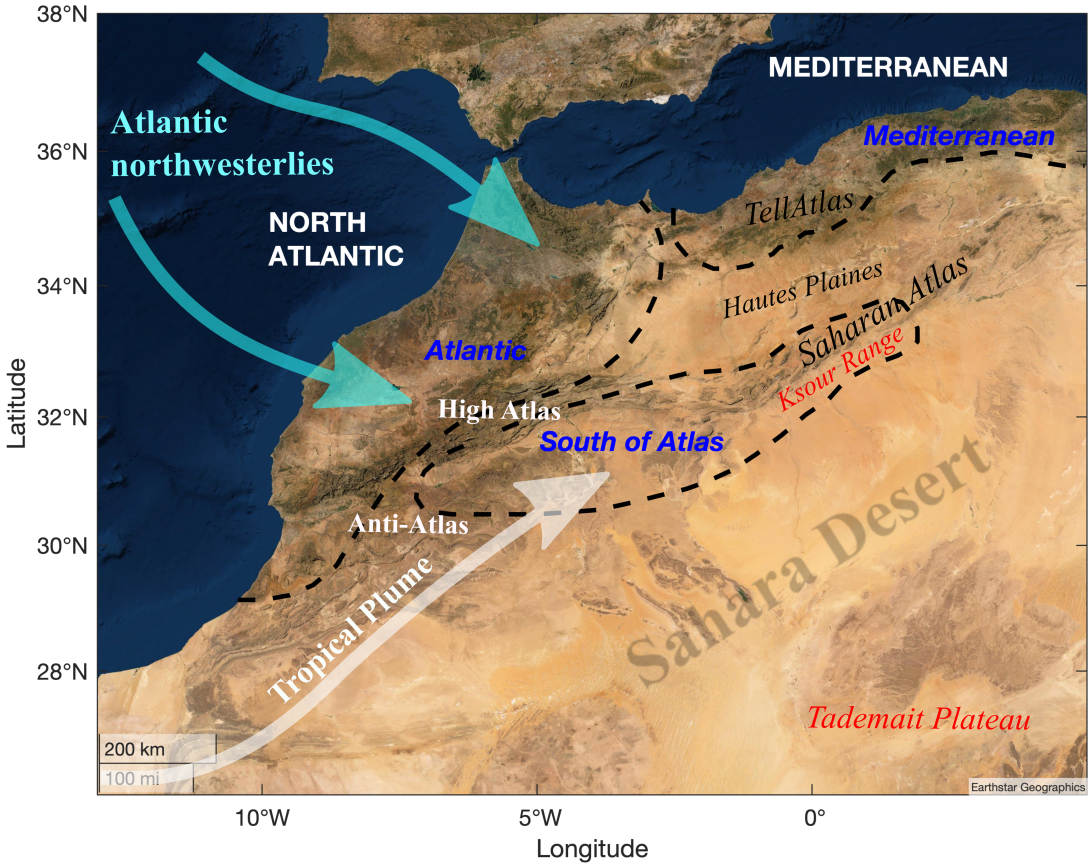


Figure 1.3: **Map of north-west Africa**. Map of north-west Africa with the field sites of this thesis (red) and Barrott (2014) (white) annotated. The three climate zones of Morocco are annotated with black dashed lines and extended into Algeria using knowledge of the meteorology of regions further east. Typical tropical plume (white) and Atlantic north-westerly (light blue) trajectories are annotated.

This small amount of modern day rainfall in the SOA zone is predominantly supplied by two main sources. Firstly, in large winter precipitation months (DJF), southward shifts of the North Atlantic storm track lead to enhanced moisture transport from the Atlantic, bringing rainfall inland along the Anti-Atlas and lee side of the High Atlas Mountains. Secondly, the characteristic peaks in rainfall during transition seasons (Figure 1.4) are suggested to be linked to tropical-extratropical interactions (TEIs),

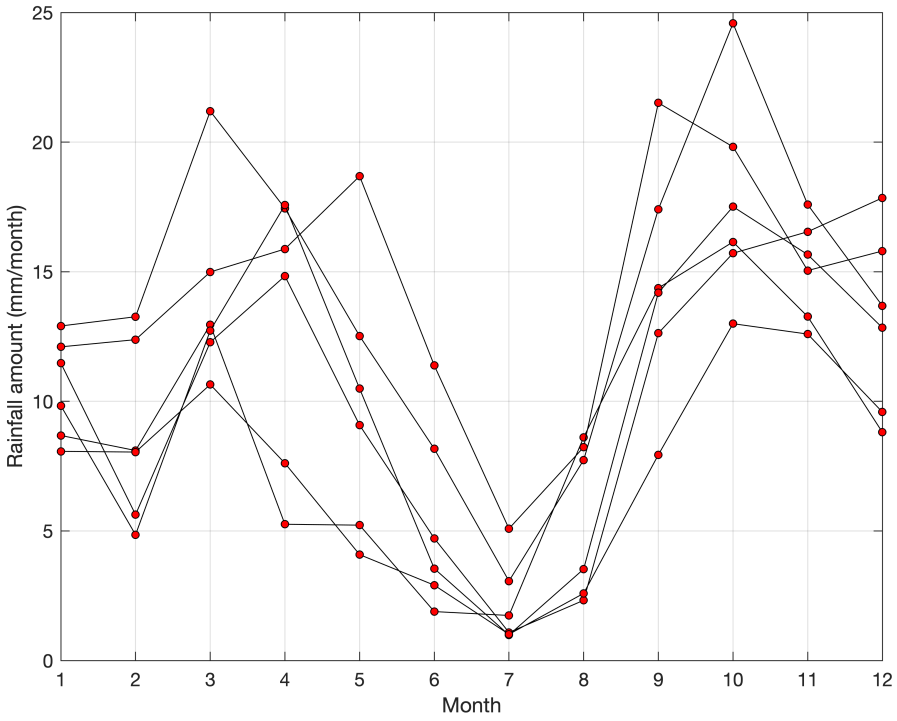


Figure 1.4: **South of Atlas Monthly Rainfall**. Annual rainfall from a number of GHCN-M climate stations situated within the South of Atlas climate zone (Knippertz et al., 2003a). Data sourced from http://climexp.knmi.nl (Trouet and Oldenborgh, 2013). January = month 1, December = month 12. The bimodal distribution of rainfall with peaks during transition seasons (spring and autumn) can be observed, associated with tropical plumes.

during which tropical moisture is carried northwards from lower latitudes in so called 'tropical plumes' (TPs) (Knippertz, 2003; Knippertz et al., 2003a,b; Knippertz and Martin, 2005; Knippertz, 2007)).

The role of TPs in transporting tropical rainfall to sub-tropical latitudes of NW Africa has been highlighted by a number of modern meteorological studies (Knippertz, 2003; Knippertz et al., 2003a,b; Fink and Knippertz, 2003; Knippertz and Martin, 2005; Knippertz, 2007; Frölich et al., 2013), and is observed in modern observations of SOA climate (Knippertz et al. (2003a); Cappy (2007); Figure 1.2). Strong tropical-extratropical interactions occur via the equator-ward penetration of subtropical upper-level troughs (white arrow in Figure 1.2), with moisture sourced from mesoscale convective clusters over tropical West Africa, or over the adjacent Atlantic Ocean, leading to elongated

cloud bands extending from the tropics into the sub-tropics. Rainfall occurs typically as heavy showers and is largely convection driven associated with orographic uplift across the Atlas Mountains. TPs generate most rainfall during transition seasons rather than peak summer months due to a stronger inflow of tropical air (Knippertz and Martin, 2005) and reduced influence of evaporation.

1.4 North African Paleoclimate

Throughout the middle to late Pleistocene, there are known to have been periods of time in which regional rainfall increased in North Africa, to the extent that perennial rivers flowed (Skonieczny et al., 2015) and mega-lakes existed in presently hyper-arid environments (Drake et al., 2022), conditions vastly different to the modern (Gasse, 2000). Terrestrial proxy evidence exists across the desert for widespread vegetation cover (Hély et al., 2014), extensive megafauna distribution (Drake et al., 2011) and increased human occupation of presently inhabitable environments (Manning and Timpson, 2014). These periods led to the recharge of major aquifers (Edmunds et al., 2003) and are suggested to have acted as 'windows of opportunity' for hominins (Gibert et al., 2022), forcing cultural interactions and potentially triggering 'Out of Africa' migrations (Scerri et al., 2014; Tierney et al., 2017a).

The most commonly cited cause of increased regional rainfall is associated with maximum boreal summer insolation during precession minima, leading to a strengthening and expansion of the West African Monsoon (WAM) system (Sha et al., 2019; Nicholson et al., 2020; Renssen et al., 2006; Lüning and Vahrenholt, 2019). However, discrepancies exist between model and proxy data (Dallmeyer et al., 2020; Hopcroft and Valdes, 2019), with models often unable to recreate the levels of increased moisture availability and vegetation observed in proxy records (Boos and Korty, 2016). Recently, modelling studies have applied the effect of dust, vegetation and moisture recycling feedbacks (Pausata et al., 2016; Hopcroft et al., 2017; Lu et al., 2018; Messori et al., 2019; Chandan and Peltier, 2020) in an attempt to recreate a large enough WAM

response to explain increased rainfall at higher latitudes, as is observed in proxy data (Krinner et al., 2012; Bosmans et al., 2015; Gaetani et al., 2017). Reduced atmospheric dust concentrations allow a northernmost WAM fringe to extend to 30°N, leading to increased rainfall up to the Mediterranean coastline (Pausata et al., 2016). This is challenged by others (Hopcroft and Valdes, 2019), with some models not realistically recreating increased rainfall amounts observed in the subtropics. In some cases, the potential for dual-moisture source increases, with both increased summer and winter rainfall, has been suggested to be the mechanism allowing for increased rainfall at the northern limits of the Sahara (Bosmans et al., 2015; Pausata et al., 2016; Cheddadi et al., 2021). Tropical plume processes have also been identified in models of past climate (Skinner and Poulsen, 2016; Dallmeyer et al., 2020), suggested to transport increased tropical moisture to north-west Africa, via processes apparent in the modern day (Knippertz, 2003). There is also some evidence for increased Saharan rainfall during northern hemisphere glacial periods (Sultan et al., 1997; Abouelmagd et al., 2012) as a result of strengthened and southward shifted North Atlantic paleo-westerlies, although this is less well constrained than increased rainfall during northern hemisphere interglacials and interstadials.

In terms of proxy evidence, wetter Saharan conditions can be extrapolated back 8 million years using records of organic-rich layers in Mediterranean marine sediments from increased continental river discharge (sapropels; Larrasoaña et al., 2013). Furthermore, weak northeasterly winds during strong monsoon intervals, combined with increased continental rainfall, reduce dust export from the continent and are recorded as low dust horizons (reduced export of terrigenous material) in marine records from Atlantic deep-sea deposits (McGee et al., 2013; Skonieczny et al., 2015, 2019). In each case, the most recent period of sustained increased North African humidity is exhibited between approximately 10 and 5 kyr BP, during a Holocene period dubbed the African Humid Period (AHP), associated with open grass savannah and increased tree species coverage across the desert (Tierney et al., 2011) and a northward extension of

tropical vegetation by up to 9° exhibited in pollen data (Hély et al., 2014). Quantitative assessments of changes in rainfall from leaf wax isotopes (Tierney et al., 2017b) suggest the potential for $>$ 500 mm/yr increases in annual precipitation up to 31°N during the AHP, whilst ^{14}C-dating of major groundwater reserves and shoreline dating of mega-lake deposits also identify a maximum of surface moisture availability during the mid-Holocene (Edmunds et al., 2003; Guendouz et al., 2003; Lézine et al., 2011; Drake et al., 2022). Further back through time, U-Th and OSL dates of secondary carbonates (lacustrine, tufa, travertine, calcretes, paleosols) across the past 350 kyrs exhibit considerable humidity during marine isotope stage (MIS) 5 (Drake et al., 2013), also coinciding with sapropel evidence for numerous periods of increased terrestrial runoff between 128 and 77 kyr BP (Larrasoaña et al., 2013; Ehrmann et al., 2013). Similarly, U-Th analysis of lacustrine deposits from the Murzuq Basin in the central Sahara (Figure 1.5) identified the existence of large lakes during northern hemisphere interglacials, in particular during MIS 5e, 7, 9 and 11 (Geyh and Thiedig, 2008), whilst travertines from the Western Desert (Figure 1.5; Jimenez, 2010; Sultan et al., 1997) exhibit numerous periods of increased moisture availability between 450 and 45 kyrs BP. Finally, a limited number of speleothem records from caves extend past the last 2 kyrs (Figure 1.5), suggesting an increase in north-west African rainfall during the AHP (Sha et al., 2019) and identifying periods of interglacial rainfall in the Western Desert (El-Shenawy et al., 2018). These records are discussed more thoroughly in Section 1.5.

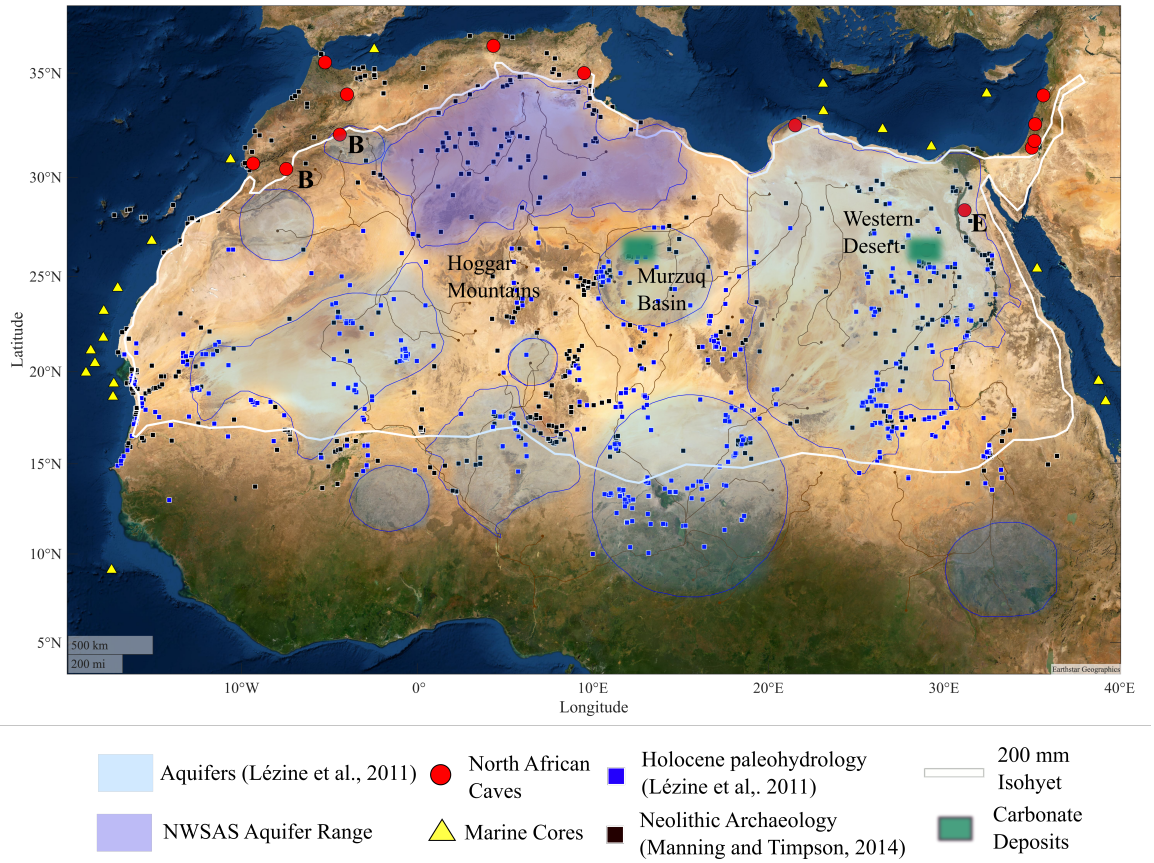


Figure 1.5: **North African Paleoclimate Records**. A selection of North African paleoclimate records. Blue and black squares identify Holocene lacustrine (Lézine et al.,2011) and archaeological (Manning and Timpson, 2014) records respectively, exhibiting the vast spatial extent of increased surface water coverage and human occupation of the desert during the most recent period of increased rainfall, the AHP. Major aquifer systems are plotted as blue shaded areas, annotated based on Lézine et al. (2011), with the NWSAS shaded a darker blue. Yellow triangles plot a selection of Atlantic marine core and Mediterranean sapropel records. The two green boxes identify the approximate locations of lacustrine and tufa deposits analysed in the Murzuq Basin (Geyh and Thiedig, 2008) and Western desert (Sultan et al., 1997; Jimenez, 2010) respectively. The location of the Hoggar Mountains (a region of high topography in the central Sahara) is annotated. Known cave sites are largely not within the 200mm/yr isohyet (white line) (Genty et al., 2006; Wassenburg et al., 2016; Ruan et al., 2016; Sha et al., 2019; Rogerson et al., 2019 Ait Brahim et al., 2017) and are largely close to coastlines and within Mediterranean climate regimes. Cave labelled "B" refer to those presented in Barrott (2014), and the cave labelled "E" is in the Western Desert, presented in El-Shenawy et al. (2018).

However, whilst these extensive proxy data act as robust evidence for increased moisture availability in the Sahara, records are limited in their interpretations as direct evidence for increased rainfall at discrete sites. Lacustrine records cannot be confirmed

to be representing permanent water bodies (Quade et al., 2018), whilst older shorelines are prone to erosion and burial via aeolian processes (Drake et al., 2022). Travertine, tufa and other groundwater-sourced deposits also do not necessarily directly record increases in local rainfall at a site, instead supplied by distal moisture sources and rising groundwater tables (Jimenez, 2010; Krinner et al., 2012). In particular, there is no direct evidence of increased rainfall in the low-altitude central Sahara, with mega-lakes and groundwater deposits potentially re-filled from rainfall in the Atlas Mountains and regions of high topography, such as the Hoggar Mountains (Figure 1.5). Saharan dust export recorded in marine cores may be representing integrating environmental change over large regions (Adkins et al., 2006), rather than identifying increases in rainfall at specific latitudes, whilst sapropels in the Mediterranean Sea are predominantly recording distal increases in tropical rainfall at the source of the River Nile. There also exist chronological constraints of ^{14}C dating when considering older periods of time through the middle to late Pleistocene, with the technique limited to the past $\sim$50 kyrs, whilst even the application of ^{14}C and U-Th in recent lake deposits can be unreliable due to reservoir effects, diagenesis and dead carbon (Drake et al., 2022).

As a result, numerous questions still remain as to the spatial and temporal extent and characteristics of periods of past increased rainfall, particularly with continually contradictory results from proxy and model data. To what latitude did increased monsoonal rainfall occur? Were changes in rainfall amount abrupt or time-transgressive? Did increased rainfall end first in the north or south and east or west of North Africa? Was there directly increased rainfall in the centre of the Sahara and what are the underlying mechanisms for this?

The only way to resolve these questions is by improving the spatial coverage of well-dated paleoclimate proxy data, for which chronology is unequivocal evidence of increased local rainfall at a site. This is particularly important for pre-Holocene periods and strategic areas geographically more central in the desert.

1.4.1 Significance of past increased rainfall

Aquifer Recharge

Two large fossil aquifers are situated in the north-west region of the Sahara (Moulla et al., 2012). The Complex Terminal (CT) and Continental Intercalaire (CI) aquifers are separated by an impermeable clay layer (Guendouz et al., 2003; Moulla et al., 2012), together forming the north-west Sahara Aquifer System (NWSAS; Figure 1.5), one of the largest groundwater reserves in the world (Guendouz et al., 2003; Tarki et al., 2011). NWSAS recharge is important for populations living in North Africa, with 2.2 billion m^3/yr withdrawn from the reserve (Darling et al., 2018). Subsequent drawdown of the NWSAS is already a critical policy issue in many North African countries, with groundwater consumption now apparent in aquifer monitoring via piezometric decline (Gonçalvès et al., 2013), and suggestions that the reserve is non-renewable (Elliot et al., 2014).

The youngest ^{14}C age for major groundwater recharge of the CT is reported as mid-Holocene (3-5 kyr BP) (Guendouz et al., 1998), whilst deeper CI groundwater ^{14}C data corresponds with late-Pleistocene recharge (Edmunds et al., 2003; Darling et al., 2018). There are however likely to have been numerous periods of NWSAS recharge which built up this reserve throughout the middle-late Pleistocene, with groundwater replenishment occurring in the Atlas Mountains (Al-Gamal, 2011) and regions of high topography in the centre of the desert (Edmunds et al., 2003). Whilst ^{14}C ($\sim$40 kyrs; Mao et al. (2018)) and ^{3}H ($\sim$60 yrs; Kipfer et al. (2002)) groundwater dating is limited in how far back through time it may extend (Darling et al., 2018), the application of other environmental indicators in precisely dating the recharge of the NWSAS would provide important constraints as to how often and over what timescales the reserve is replenished. The north and south extents of the NWSAS are at the study sites of Chapters 5 and 6 respectively, with both study areas suggested to be important recharge zones (Guendouz et al., 1998; Edmunds et al., 2003; Al-Gamal, 2011; Moulla et al., 2012), and so chronology of terrestrial paleoclimate proxies which are directly

recording past increased rainfall at these sites may be applied to understanding past groundwater recharge better.

Archaeology

North Africa is a region rich in archaeology, with a long and well-preserved record of hominin occupation and migration. From Early Stone Age sites at Ain Hanech, Algeria, dated to 1.78 Ma (Sahnouni et al., 2010), to evidence for human re-occupation across the breadth of the Sahara during the Neolithic middle-Holocene (Manning and Timpson, 2014), the region yields one of the richest hominin fossil records on Earth (Hublin et al., 2017), associated with the emergence of *Homo Sapiens* early cognitive complexity (Bouzouggar et al., 2018). Numerous technological advances are recorded in the Saharan archaeological record, particularly during the Arterian, a distinctive Middle Stone Age (MSA) stage, and it is thought that the wet-dry phases of the Sahara likely played an important role in the evolutionary processes modulated by human dispersal and population structure (Scerri, 2017). Drake et al. (2011) provided evidence for the development of ancient watercourses across the Sahara during periods of increased rainfall, with these strong hydrological connections suggested to allow human dispersal and societal interactions. Further rapid demographic shifts between $\sim$11 and 5 kyr BP are associated with increased rainfall in North Africa during the AHP (Manning and Timpson, 2014; Phelps et al., 2020), although temporal delays between increases in surface moisture availability and changes in demography shows that the relationship between climate and archaeology is still not well defined, largely due to the fact that the understanding of climate at this time is still fragmented (Drake et al., 2013). The establishment of well-dated climate records from the Sahara is therefore key to improving the robustness of archaeological interpretations across the Sahara, both in time and space.

It is these important questions which are tackled by this thesis. The El Bayadh and Naâma regions (Chapter 5) are significant areas of North African archaeological interest,

with abundant rock art and over 30 Neolithic sites along southwards flowing river channels extending from the regions into the Sahara (Manning and Timpson, 2014). Neolithic rock art depicts lions, antelopes, rhinoceros and elephants, amongst other animals not presently found in the region (Naimi and Cherif, 2021), a valuable example of the increased and diversified mega-fauna populations during the mid-Holocene AHP.

1.5 Speleothems as Paleoclimate Archives

Speleothems are secondary carbonate cave deposits which can be radiometrically dated to produce high-resolution, sometimes annually-resolved, records of climate change (Fairchild and Baker 2012; Atsawawaranunt et al., 2018; Cheng et al., 2019; Vaks et al., 2020; Wang et al., 2022). Stalagmites form as a process of water equilibrating with soil CO_2 from plant respiration and decomposition in the soil zone, which reacts with H_2O to form carbonic acid (H_2CO_3), leading to carbonate bedrock dissolution in the karst zone (Figure 1.6). Once water enters the cave environment, CO_2 degasses due to the difference in partial pressure of CO_2 (pCO_2) between drip-water and the cave atmosphere, leading to the precipitation of calcium carbonate ($CaCO_3$) and speleothem growth (Equation 1.1). Stalagmites grow upwards from the cave floor in laminae of calcite or aragonite (Baker et al., 2021) which can be accurately dated using U-Th methods (Wendt et al., 2021). Via temperature-controlled fractionation factors between solution and solid phases, stalagmites may record geochemical information withheld in drip-water such as trace element concentrations and stable isotope ratios, which indicate changes in numerous past climate proxies, namely hydrology (Baldini et al., 2021; Treble et al., 2022). Speleothems require both sufficient soil activity and a dominantly carbonate bedrock geology to form, but a fundamental limiting factor is high enough moisture input (precipitation $>$ evaporation + runoff) directly above the cave, without which they do not form (Vaks et al., 2010).

$$Ca^{2+} + 2HCO_3^- \longleftrightarrow CaCO_3 + CO_2 + H_2O \tag{1.1}$$

Speleothems therefore offer robust indicators of paleo-rainfall at cave sites in presently arid regions, by which just the presence of samples in an area for which currently evaporation >> precipitation, preventing contemporary speleothem growth, is indicative of increased rainfall in the past (Fleitmann et al., 2003; Vaks et al., 2010; El-Shenawy et al., 2018). Chronology of sample formation, normally via U-Th dating (Chapter 3), from samples collected from presently arid environments can therefore be used to constrain periods during which a region had enough annual rainfall for speleothem growth to occur. By interpreting these periods of growth alongside other North African and global paleoclimate recorders, the controls on regional climate and reasons for increases in rainfall may become apparent. Additionally, within periods of formation, stalagmites can be geochemically analysed to produce records of hydrological variability. Stable oxygen and carbon isotopes, calcium isotopes and trace element concentrations are all heavily researched speleothem proxies which can be measured and interpreted in a paleoclimate context.

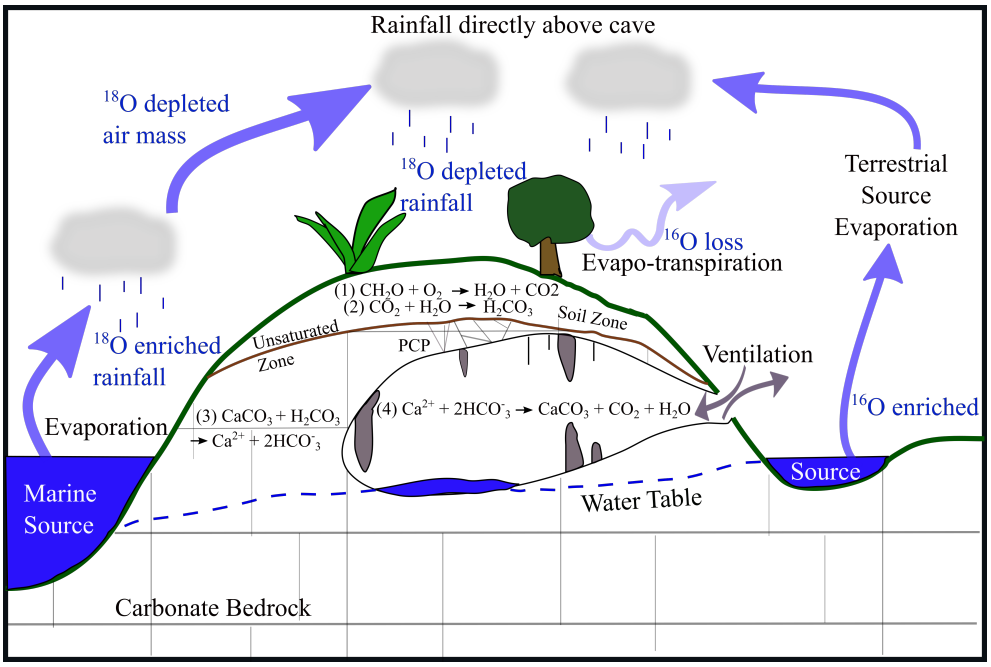


Figure 1.6: **Speleothem Formation**. Schematic cartoon summarising speleothem formation, adapted from Barrott (2014). Four important chemical equations in the soil, unsaturated and cave zones are annotated. Equation 4 in the figure is the same as Equation 1.1 in the text. Different moisture sources, such as marine and terrestrial water bodies, can have different $\delta^{18}O$ signatures, for example associated with the extent to which ^{18}O isotopes are depleted (Section 1.5.2).

1.5.1 North Africa Speleothem Records

Presently, stalagmite records from North Africa are largely limited to the extreme north, west or east of the continent (Figure 1.5), in regions close to coastlines or in environments which do have enough rainfall for contemporary speleothem growth (Genty et al., 2006; Ruan et al., 2016; Wassenburg et al., 2016; Sha et al., 2019; Ait Brahim et al., 2017). A single east African stalagmite record (El-Shenawy et al., 2018; cave labelled "E" in Figure 1.5) provides published evidence of past stalagmite growth in a cave presently under climate conditions which does not have sufficient moisture for speleothem formation, with U-Th chronology suggesting increased rainfall during MIS 5e (∼125 kyr BP), MIS 7 (∼215 kyr BP) and MIS 9 (∼330 kyr BP). Furthermore, speleothem records presented in Barrott (2014) from presently arid environments (caves labelled "B" in Figure 1.5) are discussed throughout this thesis, exhibiting evidence for

increased rainfall at numerous point during the middle to late Pleistocene. However, whilst valuable, these records cannot be used to extrapolate information about increased rainfall in central regions of the Sahara and only act as single data points which require regional corroboration from other distal records to support climate interpretations.

1.5.2 Speleothem δ^{18}O as a paleoclimate proxy

The stable oxygen isotope signature of a carbonate sample is calculated as the ratio of stable oxygen isotopes ^{18}O to ^{16}O expressed as a delta notation (δ^{18}O) in permil (‰), reported relative to the marine reference sample Vienna Pee Dee Belemnite (VPDB) (Equation 1.2). There are a number of controls which may influence the δ^{18}O signature of a stalagmite, of which the most relevant controls for this thesis are discussed here.

$$\delta^{18}O = ((\frac{\frac{^{18}O}{^{16}O}sample}{\frac{^{18}O}{^{16}O}standard}) - 1) * 1000‰) \tag{1.2}$$

Under equilibrium conditions, speleothem δ^{18}O ($\delta^{18}O_{CaCO_3}$) is expected to reflect the δ^{18}O of drip-water ($\delta^{18}O_{dripwater}$), via a temperature-controlled fractionation factor (Equation 1.5) which is slightly different between calcite and aragonite samples (Kim and O'Neil, 1997 (Equation 1.3); Kim et al., 2007 (Equation 1.4).

$$1000ln\alpha(Calite - H_2O) = 18.03(10^3T^{-1}) - 32.42 \tag{1.3}$$

$$1000ln\alpha(Aragonite - H_2O) = 17.88(10^3T^{-1}) - 31.14 \tag{1.4}$$

where

$$\alpha_{CaCO_3-dripwater} = (\frac{\delta^{18}O_{CaCO_3} + 1000}{\delta^{18}O_{dripwater} + 1000}) \tag{1.5}$$

In turn, $\delta^{18}O_{dripwater}$ is expected to approximate the δ^{18}O of rainwater falling above the cave ($\delta^{18}O_{rain}$), via a number of other karstic processes (Treble et al., 2022). $\delta^{18}O_{rain}$

may be also impacted upon by evaporative processes both in the vapour and liquid form (Lachniet, 2009; Cuthbert et al., 2014), which can preferentially cause a solution to lose the light isotope (^{16}O) and shift $\delta^{18}O$ values higher; a consideration particularly important in arid and semi-arid environments (Markowska et al., 2016). Altitude is also shown to impact on $\delta^{18}O_{rain}$, with lower values associated with increased altitude compared to the surrounding landscape (Cappy, 2007; Ait Brahim et al., 2016) as the heavy ^{18}O isotope preferentially 'rains out' first (Figure 1.6).

Different moisture sources may also have diagnostic $\delta^{18}O_{rain}$ values associated with them, including differentiating signals between terrestrial and marine sourced rainfall (Kathayat et al., 2021). Through time, stalagmite $\delta^{18}O$ may record changes in moisture source of rainfall at a site (Fleitmann et al., 2003, 2007; Baldini et al., 2010; Ait Brahim et al., 2016) based on the starting composition of different moisture sources (Ayalon et al., 1998; LeGrande and Schmidt, 2006). El-Shenawy et al. (2018) exhibited a significant effect on stalagmite $\delta^{18}O$ depending on if monsoonal Atlantic or winter Mediterranean moisture was sourcing drip water, with notably lower $\delta^{18}O$ values associated with monsoon rainfall.

Furthermore, the amount of rainfall which has fallen during a rain event, particularly in monsoonal environments, shifts $\delta^{18}O_{rain}$ to lower values as the progressive preferential rainout of the heavier isotope ^{18}O occurs, and hence can be used as a tracer for how intense a rainfall event is or how much rain has fallen prior to the moisture input to a speleothem. This phenomenon is also associated with contemporary tropical plume rain events in the SOA climate zone of north-west Africa (Cappy, 2007), with considerable shifts to lower isotope ratios as rainfall events progress (Section 1.5.3).

There are therefore numerous controls on a carbonate $\delta^{18}O$ signature, with interpretations made considerably more complex in samples which have not formed for thousands of years, and for which atmospheric circulation and karstic conditions may have been vastly different to present-day conditions. Furthermore, kinetic effects arising from temperature, pH and progressive degassing can limit the paleo-environmental

interpretations which can be drawn from speleothems (Fairchild and Baker 2012). Also, numerous effects on a sample's $\delta^{18}O$ signal such as rainfall amount or altitude may be changing signals in the same way (Kathayat et al., 2021), and mixing of $\delta^{18}O_{rain}$ signals can occur in the karst, making the deconvolution of dominant controls difficult.

Despite this, for samples which are only growing during periods of significantly increased rainfall, changes in $\delta^{18}O$ between growth periods have been shown to be powerful indicators for moisture source, particularly when significant changes in $\delta^{18}O$ are observed across hiatuses (long periods of no-growth) (Fleitmann et al., 2003; El-Shenawy et al., 2018). In general, the replication of speleothem $\delta^{18}O$ records within or between nearby caves is considered the 'gold standard' in using them as paleo-archives (Treble et al., 2022), reducing the likelihood of in-cave processes impacting on signals and increasing the robustness of using speleothem $\delta^{18}O$ as a moisture source tracer.

1.5.3 Modern regional $\delta^{18}O$

In the SOA and central Saharan regions, modern GNIP (Global Network of Isotopes in Precipitation) oxygen and deuterium isotope data of rainwater is limited to the past several decades and has poor spatial coverage, whilst paleo-measurements are severely lacking. It is therefore difficult to ascertain modern and past moisture trajectories and climate conditions based off these environmental isotopes.

Of the limited data from contemporary rainfall, there is generally a trend towards higher isotopic signatures during summer months and in arid inland regions, and lower isotopic signatures at higher altitudes and with distance from the coastlines in regions of higher rainfall (Cappy, 2007; Ait Brahim et al., 2016). In the Atlantic climate zone of Morocco (Figure 1.3; Knippertz et al. (2003a)), average rainfall $\delta^{18}O$ is -5.8‰ ± 2.4‰ (VSMOW; n = 29; 1 s.d.) based on modern measurements (Ait Brahim et al., 2016), with lower values occurring during winter months.

Cappy (2007) studied the isotopic signatures of TP rainfall events in the SOA, defining a 0.29 ‰/100m altitude gradient for $\delta^{18}O$ (lower values at higher altitudes)

and a strong shift to lower values as tropical plume rain events progressed, ranging between -4.9‰ at the start of an event to -21.4‰ by the third day.

Despite this limited information, GNIP data is sparse and often incomplete, particularly in regions in the Saharan Atlas and Sahara, restricting information which may be deduced.

1.6 Research Goals

Many of the contradictory interpretations which are currently drawn from proxy and model data regarding past periods of increased North African rainfall stem from the poor spatial and temporal coverage of well-dated records to date. Whilst current stalagmite records have begun to provide direct evidence of rainfall (Barrott, 2014; El-Shenawy et al., 2018; Sha et al., 2019), the records act as single data points and require corroboration from other, preferably distal, records to confirm regional rainfall patterns. By collecting and analysing further high-resolution, absolute-dated terrestrial paleoclimate archives from across the northern limits of the Sahara, the spatial coverage of data will improve and so the extent and timing of humid periods in north-west Africa will become more apparent. A better understanding of the underlying climate mechanisms will allow a mechanistic approach to be taken when considering future climate change, improving modelling studies in the region, critical to groundwater replenishment and water resource management for current and future populations.

This research begins to address the ever-increasing need for improving the spatial coverage of well-dated paleoclimate proxy data for which chronology is unequivocal evidence of increased effective precipitation at that site, particularly for areas geographically more central in the desert. Each of the sites presented in this thesis are in arid- or hyper-arid environments which (i) do not have enough contemporary rainfall for modern speleothem formation, (ii) are currently limited in the availability of paleoclimate proxy data identifying directly increased local rainfall, (iii) are regions of significant Neolithic and MSA archaeology, (iv) are regions for which direct rainfall acts as local recharge

for major North African groundwater systems and (v) have contemporary populations living in the region which rely on annual rainfall for food and water supply.

This research analyses speleothems and other secondary carbonates from the Sahara using U-Th chronology, alongside geochemical proxies which record environmental changes such as stable isotopes, trace elements, calcium isotopes and clumped isotopes, to better characterise periods of direct and local increased Saharan rainfall in the past.

Chapter 2

Fieldwork

Contents

2.1 Introduction 30

2.2 Fieldwork Methodology 31

2.3 Central Sahara 32

2.3.1 Calcite Deposition 36

2.4 Northern Sahara 40

2.4.1 Grar Cave 42

2.4.2 Maqlae Cave 45

Summary

Data reported in Chapter 4 of this thesis were measured from samples collected during fieldwork by Julia Barrott between 2009 and 2010, the details of which can be found in Barrott (2014). The data reported in Chapters 5 and 6 of this thesis are from samples collected during fieldwork in the Algerian Sahara, undertaken between 2019 and 2020, as part of this DPhil project.

Two field trips were undertaken to previously un-researched[1] regions of North Africa; to the Algerian Central Sahara in February 2019 and to the Algerian Saharan Atlas in March 2020, in both cases with the aim being to find speleothem-bearing caves in order to generate paleoclimate records from currently un-sampled regions. Numerous cave sites are reported from the Saharan Atlas sites and, despite the lack of speleothem-bearing caves in the central Sahara, the collection of secondary carbonates and other environmental proxies are presented. This chapter presents the motivation behind undertaking research at these field sites, describes the geology, environments and caves of each region, and details the samples collected for geochemical analysis. Whilst further scientific interpretations of field sites are described in Chapters 5 and 6, the aim of this chapter is to provide greater detail on the pre-fieldwork investigation of sites, cave plans and field photographs, as well as field methods.

[1] *The term 'un-researched' here is used in the context of published stalagmite records. The sites visited are known and visited by local populations and exhibit archaeological evidence of past human occupation.*

2.1 Introduction

In the modern day, the Sahara is an extreme environment. Temperatures as high as 49.8°C have been observed at In Salah, the site of fieldwork undertaken in February 2019, and annual rainfall amounts are generally < 25 mm in the centre of the desert. Fieldwork was therefore undertaken during winter and early spring months, before the hot season and to avoid dust storms and other natural risks. Significant geological, technical and logistical reconnaissance was undertaken before fieldwork, using both literature studies and satellite sources, to increase the prospects of finding speleothem-bearing caves.

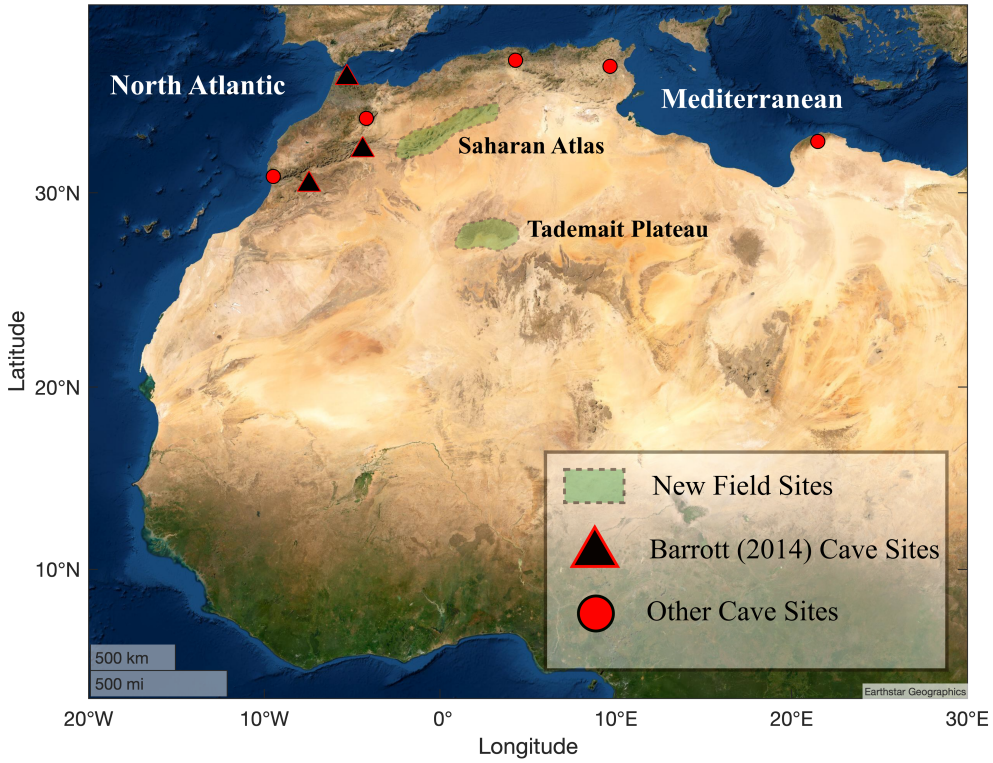


Figure 2.1: **Research Fieldwork Sites**. Satellite image of North Africa with field locations associated with this study plotted. Black triangles and red circles are published North African cave sites from Genty et al., 2006; Wassenburg et al., 2013; Barrott, 2014; Hoffmann et al., 2016b; Ruan et al., 2016; El-Shenawy et al., 2018; Ait Brahim et al., 2019; Sha et al., 2019 and Rogerson et al., 2019. Shaded green areas identify the general regions in which fieldwork was undertaken for this research; the Tademaït Plateau (central Algerian Sahara) and the Saharan Atlas (northern Algerian Sahara).

Field sites in the Algerian Sahara are further south and east than those reported in Barrott (2014) (Figure 2.1) increasing the spatial resolution of records. In February 2019, numerous non-cave secondary carbonate samples were collected from the Tademaït Plateau in the central Sahara (28°N) and in March 2020, several caves were accessed in the southern foothills of the Sahara Atlas range (30-33°N) (Figure 2.1). In both cases, sites are in presently arid conditions with not enough effective precipitation for speleothem growth and at the recharge zone for major Saharan aquifers. Saharan Atlas sites are also at the head of presently dry southwards-flowing rivers which extend several hundreds kilometers into the Sahara.

2.2 Fieldwork Methodology

A field description was taken at each site, including geological and geographic observations, GPS location and hydrological and vegetation conditions. When possible and relevant, detailed cave sketches and surveys were also undertaken, and a photographic record was kept of the sites. For as comprehensive an environmental study as possible, samples collected, where suitable, included speleothems (or other secondary carbonates), aquifer water (no caves were dripping) and bedrock.

Speleothem

Cave deposits can form over millions of years (Vaks et al., 2020) and, in the case of presently arid environments, have been fossilised in-situ for up to thousands of years without growing, making them precious and irreplaceable. Therefore, where possible only already broken stalagmite samples and less precious flowstone deposits were collected for analysis. In minimal cases, stalagmites were removed in-situ at their base with a hand-held drill or rock chisel.

Aquifer Water

Groundwater samples were collected in 15 mL vials, filled to the brim and stored in as cool an environment as possible to avoid secondary-evaporation or temperature effects on the isotopic compositions. Samples were measured within two weeks of return

to Oxford.

Other solid samples

Other samples collected for geochemical analysis included bedrock and ancient gypsum evaporites (Madi et al., 2016). These, being less precious than the speleothem deposits, were collected using a rock hammer and chisel and stored in separate labelled sample bags.

2.3 Central Sahara

Motivation and Investigation

The primary aim of fieldwork in the central Sahara was to source terrestrial records from more southern regions than current proxy records, towards the source of the WAM and away from sub-tropical climate regimes. Significant pre-fieldwork reviews of geological maps, satellite imagery, climate data and logistical information was undertaken to ensure as high a degree as certainty as possible that samples may be collected from speleothem-bearing caves. Analysis of Saharan geological maps and global karstic regions (Ford and Williams, 2013; Laumanns, 2008; Appendix I Figures 1 and 2) identified the Tademaït Plateau (Figure 2.1) as having karstic characteristics, with numerous sources identifying the top of the plateau as consisting of upper-Cretaceous limestone (Madi et al., 2016). Satellite imagery also revealed two significant geomorphological phenomena; (i) dolines (sinkholes) on the surface of the plateau, indicative of collapsed underground caverns and (ii) observations of resurgences (river channels) from the foothills of the plateau, indicating sub-surface water flow (Figure 2.2D). The plateau is also a recharge point for the Complex Terminal aquifer (Edmunds et al., 2003), providing further evidence for permeable geology allowing sufficient infiltration rates and karstic features.

Fieldwork

Fieldwork to the central Sahara was undertaken in February 2019. The Tademaït plateau is an elevated table of land, $\sim$ 900km from the Mediterranean Sea and over 1000km from any Atlantic coastline (Figure 2.2A). The southern Tademaït plateau region receives $<$ 30mm of annual rainfall, falling dominantly during winter months, and is within a BWh (hot, arid desert) Köppen climate classification (Chen and Chen, 2013). The plateau top consists of blackened, weathered limestone gravel and stone, closely packed on top of fine-grained sediment and occasional soil. Geologically, it is built from a number of sedimentary strata (Figure 2.2C), from lower Cretaceous Continental Intercalaire sandstone at the base (Draoui et al., 2022), through marine mudstones and Turonian gypsum deposits (Newell et al., 2015), before being capped by Upper Cretaceous limestone (Madi et al., 2016). This carbonate cap-rock, deposited during Late Cretaceous sea-level rise which swamped extensive areas of North Africa (Guendouz et al., 2003; Moulla et al., 2012; Newell et al., 2015), has an elevation of $\sim$750masl, sitting steeply above the surrounding desert landscape presiding at $\sim$ 250masl (Figure 2.2C). More extensive geological representations of the Tademaït Plateau may be found in Madi et al. (2016) and are presented in Appendix I Figure 2.

Flowing south- and westwards from the southern edge of the plateau are numerous paleo-river channels which are dry in the modern day, although are reported by local residents to flow during significant rainfall events. The width and prominence of some channels are indicative of much longer-duration riverine presence, likely remnants of previous humid periods. The plateau edge is impacted by severe weathering, with large blocks of bedrock undergoing apparently modern detachment at the scarps (Figure 2.2B). The erosion of the underlying clay bedrock during contemporary rainfall events may largely cause this, combined with the slower chemical erosion of the permeable carbonate cap-rock during wetter periods. This is similar to observations near Beni Abbes, western Algeria, where Smith (1978) attributed slope weathering to both past humid periods and the modern gullying of scarp faces from groundwater sapping.

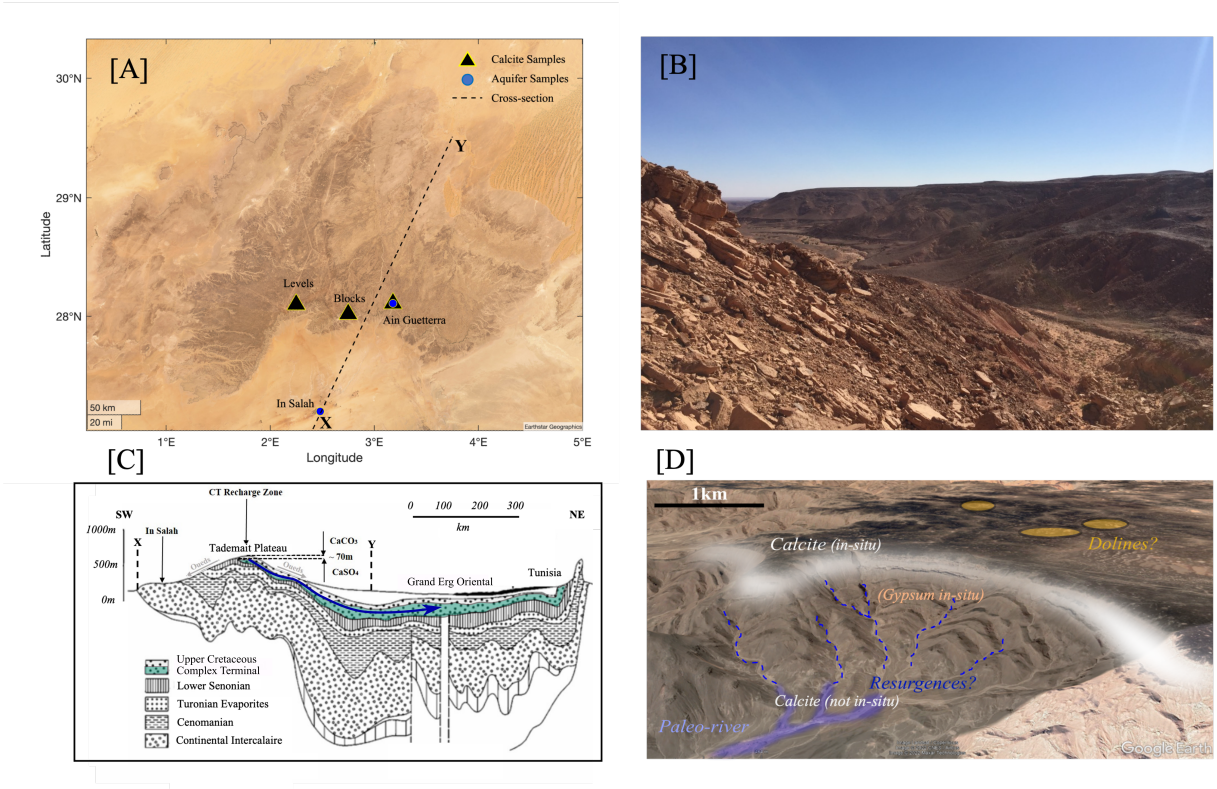


Figure 2.2: **The Tademaït Plateau**. [A] Satellite image of the Tademaït Plateau. Surrounding desert sand can be observed around the dark weathered carbonate top of the plateau. Locations of the collection points of calcite and aquifer samples are plotted as black triangles and blue circles respectively. The dashed line represents the cross section plotted in subplot C [B] Field image of the 'Levels' field site, from which numerous secondary calcite deposits were collected. The aridity of the field site is notable [C] Cross-section of the Tademaït Plateau adapted from Edmunds et al. (2003). Geological units are annotated. The CT aquifer can be observed at the top of the plateau and the CI aquifer at the bottom. The general sub-surface flow direction of the CT towards the Grand Erg Oriental is marked with a dark blue arrow. The locations of black dashed lines annotated as X and Y correlate with the black dashed line plotted in subplot A. Secondary calcite was found exclusively in the top 70m of the plateau, as annotated. [D] Google Earth image of the Tademaït Plateau edge. Suggestions of karstic processes such as dolines (sinkholes) on top of the plateau, and resurgences emerging from the side, are marked. The approximate region (top 70 metres) of the plateau from which secondary calcite was collected is marked with a transparent white band.

Two large aquifers are located in the region (Moulla et al., 2012); the Complex Terminal (CT) and Continental Intercalaire (CI) aquifers (Figure 2.2C), together forming the north-west Sahara Aquifer System (NWSAS). The CT is an unconfined, or semi-confined, aquifer (Guendouz et al., 2003) for which the Tademaït Plateau acts as a major recharge zone (Guendouz et al., 1998). CT ^{14}C ages are reported as mid-Holocene (3-5 kyr BP, Guendouz et al., 1998) and δ^{18}O averages -5.98 ‰ (Guendouz et al., 2003). Situated below the CT, separated by Cenomanian clays, is the CI aquifer, contained in Lower Cretaceous sediments (Moulla et al., 2012). The CI outcrops at the oasis city, In Salah, and has its dominant recharge source in the Atlas Mountains (Hamed et al., 2014), although based on the extensive evidence of southwards river flow (Figure 2.2D), runoff from rainfall occurring at the plateau borders also acts as partial recharge (Moulla et al., 2012). CI ^{14}C data corresponds with the late-Pleistocene (20-40 kyr BP) (Guendouz et al., 1998) and δ^{18}O averages -8.03 ‰ (Edmunds et al., 2003).

Despite significant pre-fieldwork study of the region, speleothem-bearing caves were not observed on the Tademaït Plateau. This may have been due to the logistical restrictions (the field excursion was short in duration) but may also be due to environmental factors such as the hostile environment of the plateau surface including high winds, perhaps restricting soil formation and vegetation growth during periods of increased rainfall, or limited thickness ($<$ 70m) of the carbonate cap-rock restricting the dissolution of large cave systems.

Despite this, large erosional caves were observed in clay successions which extended $>$ 50 metres into the plateau and had evidence of water flow and erosional features within them. In addition, numerous secondary carbonate deposits were collected both in and out of situ, along with other environmental samples, including gypsum and aquifer water samples.

2.3.1 Calcite Deposition

Despite the lack of speleothem-bearing caves, significant calcite deposition was observed, and samples collected, from the plateau in both geode and block/flowstone form (Figure 2.3). These samples consisted of very pure, clean calcite and, when correcting for the altitude of the top of the plateau, were found in-situ exclusively in the top ∼70m in carbonate bedrock (Figure 2.2), below which gypsum veins were observed in clay facies.

Calcite Geodes

Geodes were collected exclusively in-situ, predominantly from two locations; 'Levels' and Aïn Guetterra, but were observed across the plateau (Figure 2.2) . Geodes collected from the 'Levels' field site are labelled as such that, for example, sample "L1G1" was collected from 'level 1', at the highest altitude on the plateau, and sample "L4G1" was collected from 'level 4', at a lower altitude. Geodes are 2-10cm in diameter and are largely formed from non-layered, individual calcite crystals averaging ∼25mg in mass. Where possible, fresh geode surfaces were uncovered by removing surrounding bedrock, with the uncovered samples exhibiting very clean calcite.

Calcite Flowstone/Blocks

The most speleothem-like samples collected were laminated block/flowstone calcite samples (Figure 2.4) which are formed from dense, layered calcite crystals of various sizes, density and colouration. Block calcite is up to 4cm thick and 10cm wide, similar in morphology and size to samples presented in Jimenez (2010), who discussed the deposition of layered calcium carbonate in the Western Desert, Egypt as being deposited during pluvial episodes. Similarities with examples in the literature of 'groundwater speleothems' (Jimenez, 2010), as well as flowstone speleothems (Hellstrom et al., 2020; Johnston et al., 2021) suggests that they formed sub-aerially from flowing water in a karstic environment (Fairchild and Baker 2012). These samples were collected out of situ, found in the dry river beds extending from the top of the plateau, hypothesised to

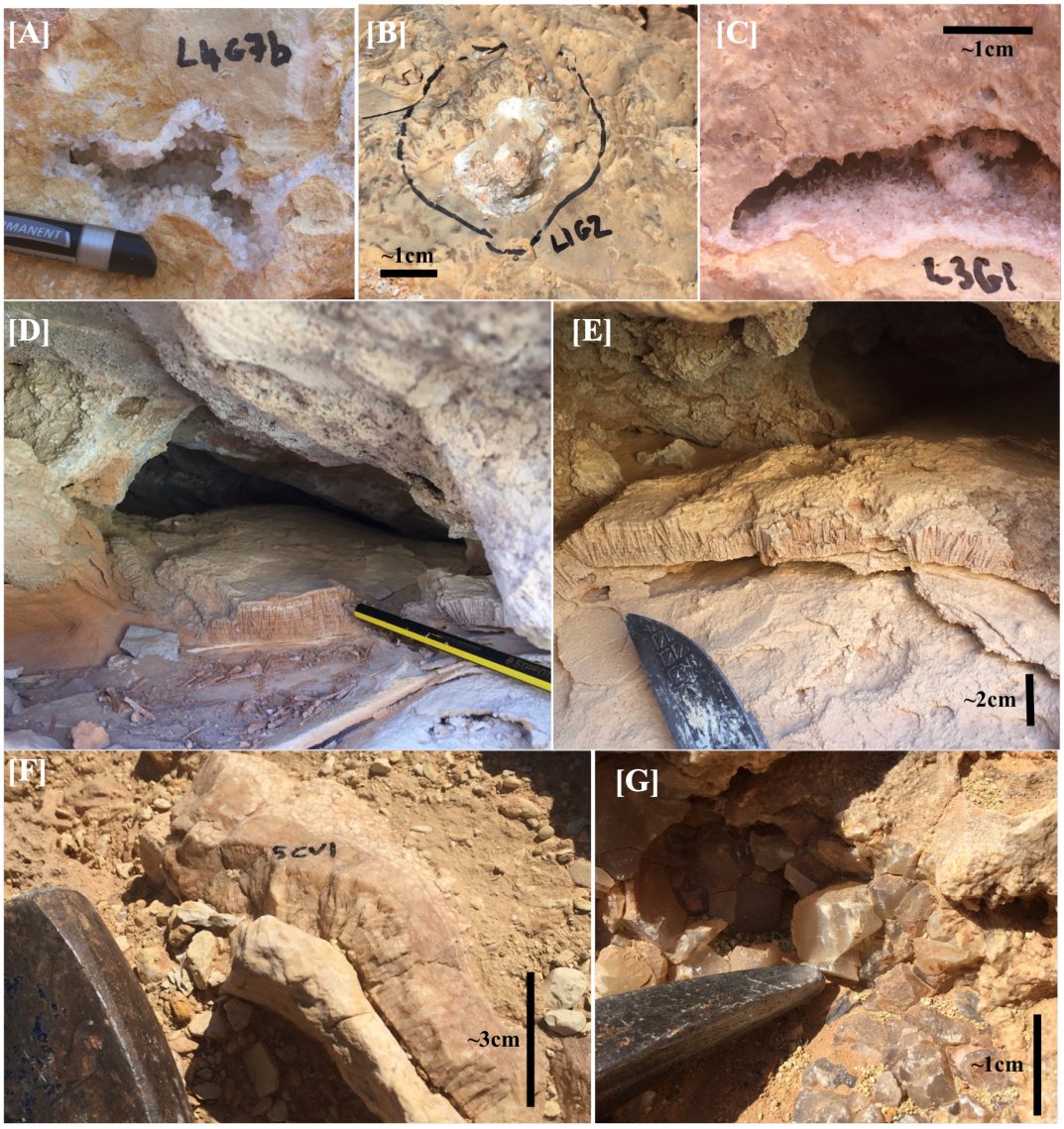


Figure 2.3: **Field Images of Calcite Samples.** Field images of a selection of secondary calcite samples collected from the Tademaït plateau. A wide range of morphologies were observed of calcite geodes and laminated blocks, many of which were formed in small cavities resembling caves. [A], [B] and [C] are in-situ calcite geodes from the Levels location (Figure 2.2). [D] and [E] are in-situ block/flowstone samples and [F] is a non-in-situ flowstone sample collected from a river channel extending from the top of the plateau. [G] is larger in-situ calcite crystals from the Ain Guetterra site.

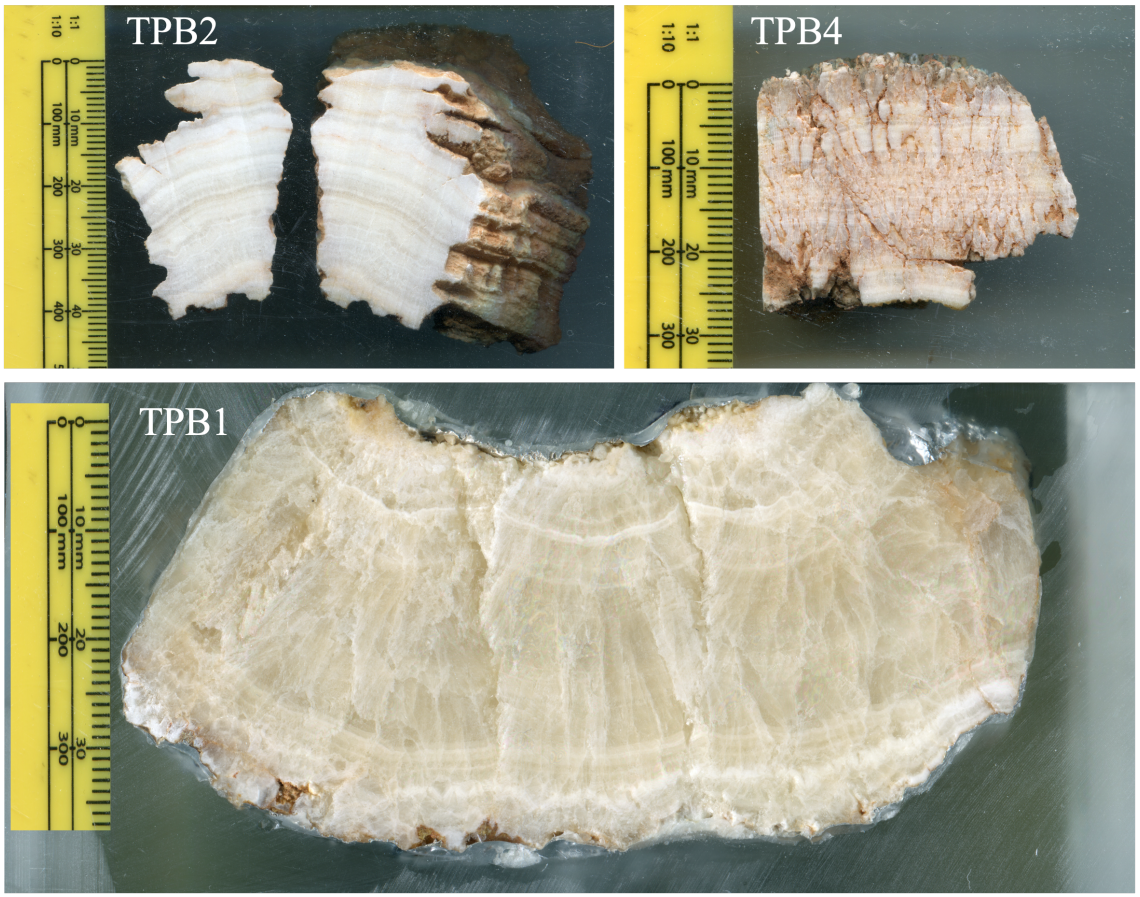


Figure 2.4: **Calcite Blocks**. Scanned images of calcite block samples collected from the Tademaït Plateau. There is a wide range in crystal size and colouration. Notable cracks run through each sample and clear laminations can be observed. Sample TPB1 is observed in the field in sub-plot F within Figure 2.3, there labelled "5CV1".

have been washed down from the top of the plateau during periods of erosion. Similar deposits were observed in-situ in the top carbonate units of the plateau, although not collected due to significant alteration, which corroborates with formation hypotheses due to their presence in small cavities resembling caves (Figure 2.3). Notable cracks run through several samples, and erosional features are evident on their outer layers, which may make the sample at risk to pore-water entering the calcite lattice (Chen et al., 2020).

Calcite Formation

Calcite was exclusively found in-situ at the highest elevation of the plateau, to which no surface water flows. Sub-surface flow generally converges towards a major depression in

the Grand erg Oriental, Tunisia (Figure 2.2C; Guendouz et al., 1998; Edmunds et al., 2003; Moulla et al., 2012; Gonçalvès et al., 2013; Nadhira and Omar, 2019), meaning that there is also likely no sub-surface water flowing to this point. This suggests that there is unlikely to be a sustained sub-aqueous environment at the field site, and that any secondary carbonate deposition found at the top of the plateau must have chemically precipitated from the percolation and flow of water through the karstic carbonate bedrock, leading to sub-aerial formation. This, combined with clumped and stable isotope data (presented in Chapter 6), suggest that these samples formed from meteoric rainfall, rather than sub-aqueously from increased aquifer levels or hydrothermal water sources, and that calcite can be used as a local indicator for periods of past rainfall and aquifer recharge.

Other plateau samples

Gypsum Samples

Gypsum ($CaSO_4$) was found in vertically and horizontally orientated veins in the lower Senonian clay facies. The majority of samples were hydrated gypsum ($CaSO_4 \cdot H_2O$) and were continuous throughout the lower Senonian units (compared to the semi-continuous and apparently random distribution of calcite), situated below the top carbonate caprock of the plateau. Veins ranged from a few mm in width to up to 10cm and largely appeared clean and homogenous.

Aquifer Samples

Five aquifer water samples were collected from two locations in the field; In Salah and Aïn Guetterra (Figure 2.2A). Three samples were collected from various locations at In Salah which is an oasis city lying at $\sim$ 250masl on top of the Continental Intercalaire sandstone sequence, $\sim$70km south of the plateau. Two samples were collected from Aïn Guetterra, a spring at $\sim$ 600masl, found approximately at the intersection between the upper and lower Senonian units.

Other observations

The top surface of the plateau has numerous regions of $>$ 1m deep soil coverage, found in the 'dolines' suppression features observed from satellite imagery, in which seasonal vegetation grows during the modern day (Appendix I Figure 3B), and the soil is damp past $\sim$ 10cm depth (as of February 2019). There was also significant evidence of water flow on and from the plateau, including erosional features such as waterfall plunge pools and well-rounded boulders indicating high-energy water transport, although these features were completely dry when observed during fieldwork. Finally, there was some archaeology on top of the plateau, with flint tools identified by archaeologist collaborators during fieldwork.

2.4 Northern Sahara

Motivation and Investigation

The motivation behind fieldwork in the Saharan Atlas was driven by the collection of samples from a region which was (i) eastwards from cave sites presented in Barrott (2014), which are a more significant distance from Atlantic and Mediterranean coastlines, (ii) north of central Sahara fieldwork, to complement isotopic and chronological interpretations latitudinally across the Sahara, and (iii) a site which is archaeologically significant, for which caves may have been occupied during Neolithic or earlier periods. There is local evidence and reporting of speleothem-bearing caves across the Saharan Atlas region, with caves discussed in the archaeological and chiropterological literature (Kowalski et al., 1986; Aberkane and Rabhi, 2022). Geological observations confirmed prospective sites near oasis cities of Ain Sefra and Brezina to be predominantly made up of upper-Cretaceous limestone bedrock, with numerous potential sites identified within the Ksour Mountain orographic belt.

Fieldwork

Fieldwork to the southern edge of the Saharan Atlas Mountains, where the mountain range meets the Sahara, was undertaken in March 2020 (Figure 2.5). The Saharan Atlas region is a central section of the Atlas Mountain System, which itself extends across much of North Africa from the western Atlantic coastline of Morocco to the north-east Mediterranean coastline of Tunisia, reaching $>$ 1800m in altitude and extending $>$150km in width at points, representing a significant stretch of topography at the northern limits of the Sahara. A principal range of the Saharan Atlas is the Ksour Mountains in the west, in which the study sites of this chapter lie (Figure 2.5). Rainfall at the Saharan Atlas acts as modern recharge for the Continental Intercalaire (CI) aquifer, the major constituent of the North-West Saharan Aquifer System (NWSAS), and so is an important region for groundwater replenishment for which modern human populations rely on as water supply. Major paleo-rivers can be observed from satellite imagery (Figure 2.5) and extend all the way from the Saharan Atlas to the northern edge of the Tademaït Plateau, visible for over 300 kms, implying significant amounts of rainfall occurring at times in the mountain range. The requirement of direct local rainfall for stalagmite growth means that periods of stalagmite formation may be used as evidence for periods of increased river flow.

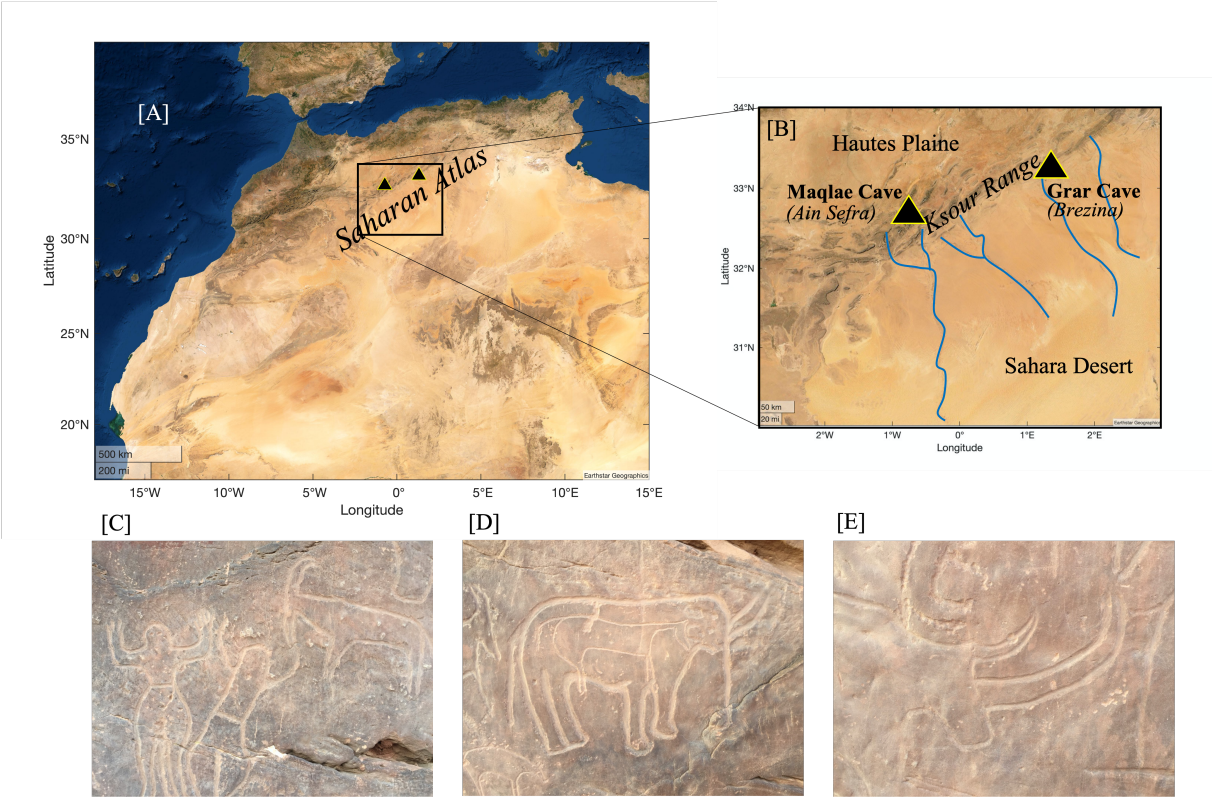


Figure 2.5: **Saharan Atlas Field Sites**. [A] Satellite image of North Africa with the extent of the Saharan Atlas Mountains annotated. [B] Expanded satellite image of the Ksour range, within the Saharan Atlas. The locations of Maqlae and Grar caves are annotated as black triangles. Ain Sefra and Brezina in parentheses indicate the nearest human settlement to cave sites. Blue lines are drawn over paleo-river channels observable from satellite imagery, of which several extend directly from cave sites. [C], [D] and [E] are rock art observed in Tiout, near Maqlae cave. Depictions of humans hunting antelope, and drawings of elephant and rhinoceros, at the very northern limit of the Sahara in which these mega-fauna do not currently preside, are evidence of different climate conditions. Ages of these drawings are reported as Neolithic (mid-Holocene) (Camps, 1990; Naimi and Cherif, 2021).

2.4.1 Grar Cave

Grar cave (33.2°N, 1.3°E) is situated on the apex of a NE-SW trending anticline, approximately 10km northeast of the village of Brezina, at the very eastern extent of the Ksour range (Figure 2.5). Annual rainfall at the GHCN-M climate station El Aliod (70km from Brezina) is 124mm/yr (data sourced from http://climexp.knmi.nl (Trouet and Oldenborgh, 2013)), falling dominantly during spring and autumn months, as is diagnostic of the South of Atlas region (Appendix I Figure 4). Bedrock consists of almost

vertically dipping limestone with the cave entrance situated underneath a shallow fold. The cave is accessed via a ∼5m by ∼2m entrance, is >150m long (this was the extent of our exploration, however more known caves lie > 5km SW from the site which could be connected to Grar cave via an extensive network), with significant speleothem deposition (Figure 2.6). The depth of overlying bedrock was 3-5 m above the entrance, at which there was little to no observable soil although some low-density shrub vegetation was growing. The modern cave is made up of numerous chambers of a fairly consistent (2-3m) height, connected via passages which can be comfortably walked through (no crawling was required past the entrance), extending almost horizontally below the ridge of the anticline. Observed speleothem features included stalactites, stalagmites, columns, fracture flow ceiling deposition and very large flowstone deposits. There was also desiccation of the cave floor suggesting pooled water, and concave tops to several stalagmites suggesting under-saturated dripping at times. Notably, the cave was heavily covered in dust and no dripping, water or evidence of modern speleothem growth was observed throughout.

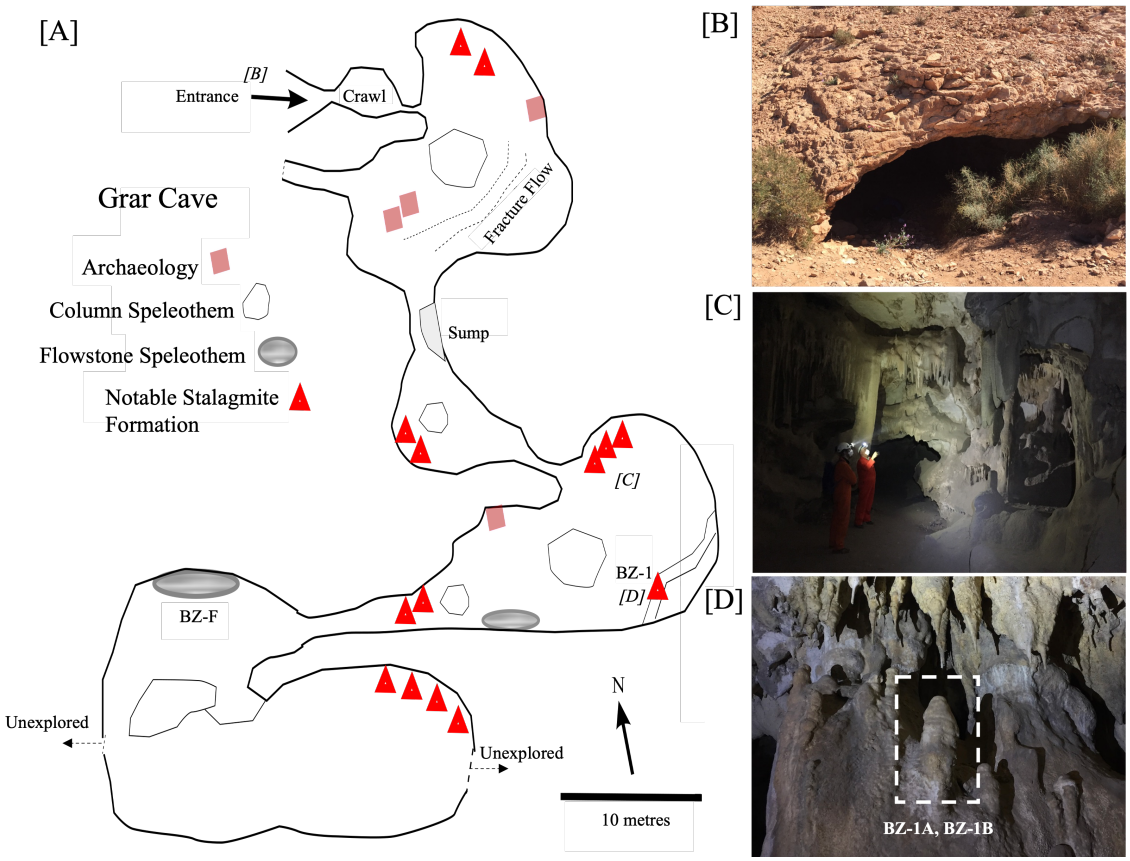


Figure 2.6: **Grar Cave.** [A] Cartoon plan of the explored sections Grar cave from field sketches. Notable observations are marked and italic annotations of B, C and D refer to the locations at which the images on the right were taken. [B] Grar cave entrance [C] Field image exhibiting the extent of speleothem deposition within the cave, collaborators for scale. [D] Stalagmite samples BZ-1A and BZ-1B (centre) photographed in-situ.

2.4.1.1 Grar Cave Samples

Samples collected from Grar cave include stalagmites BZ-1A and BZ-1B, which were collected 50 m into the cave as one conjoined sample from a shelf approximately 3m high. The sample is 20 cm long at its greatest extent and was notably chalky at its base when removed from its in-situ position. Samples were also collected from a 2 metre tall flowstone wall (BZ-F), ∼100 m into the cave. The flowstone was collected as 14 sub-parts where BZF_1 is collected from the top of the flowstone and BZF_14 the bottom. Scans of samples are exhibited in Chapter 5 of this thesis.

2.4.2 Maqlae Cave

Maqlae Cave is located in a quarry site with near vertical dipping bedrock, 13 km south-west of Ain Sefra, in the most western region of the Algerian Saharan Atlas (Figure 2.5). Ain Sefra is a semi-arid oasis city in the western limits of the Ksour range. Annual rainfall is 170mm/yr, also falling dominantly during spring and autumn months (Appendix I Figure 4). It is located in a watershed basin surrounded by mountains and has experienced significant and worsening flooding over the past 100 years (Derdour et al., 2018). The city lies ∼50 km due north from the southern limit of the Ksour range, with notable topography between itself and both the Sahara and Mediterranean (Figure 2.2B). Vegetation above the cave is limited.

The cave has no natural openings. Instead, it was discovered as a result of quarrying in 2016, and therefore will likely be destroyed due to further quarrying in the coming years, and so many speleothem samples were collected. The cave was accessed by the non-natural opening which is ∼5m x 3m in size, with a ∼3m descent to the cave floor. A large single chamber, ∼10m x ∼10m in dimension had both a smaller chamber and a separate long passageway extending from it. Speleothem deposition covered the majority of the cave and a large proportion of the cave walls (Figure 2.7). Some dampness was observed in the cave, although no active dripping was observed.

2.4.2.1 Maqlae Cave Samples

The extensive speleothem deposition inside Maqlae cave are formed predominantly of very large, dense calcite crystals of a wide variety of colourations. Nodules of calcite were observed on the outer edges of most speleothems within the cave. Speleothems collected included samples QC-1, QC-S and QC-L, of which QC-1 and L are stalagmites and QC-S is a small stalactite. QC-L is the largest sample, almost 1 metre tall and 20 cm diameter at the base. When stalagmites were sliced open, the nodular growth on the outer edges of the cave deposits can also be observed throughout the growth history of the sample, whilst numerous growth lines in the samples can be easily observed. Scans

of samples are exhibited in Chapter 5 of this thesis.

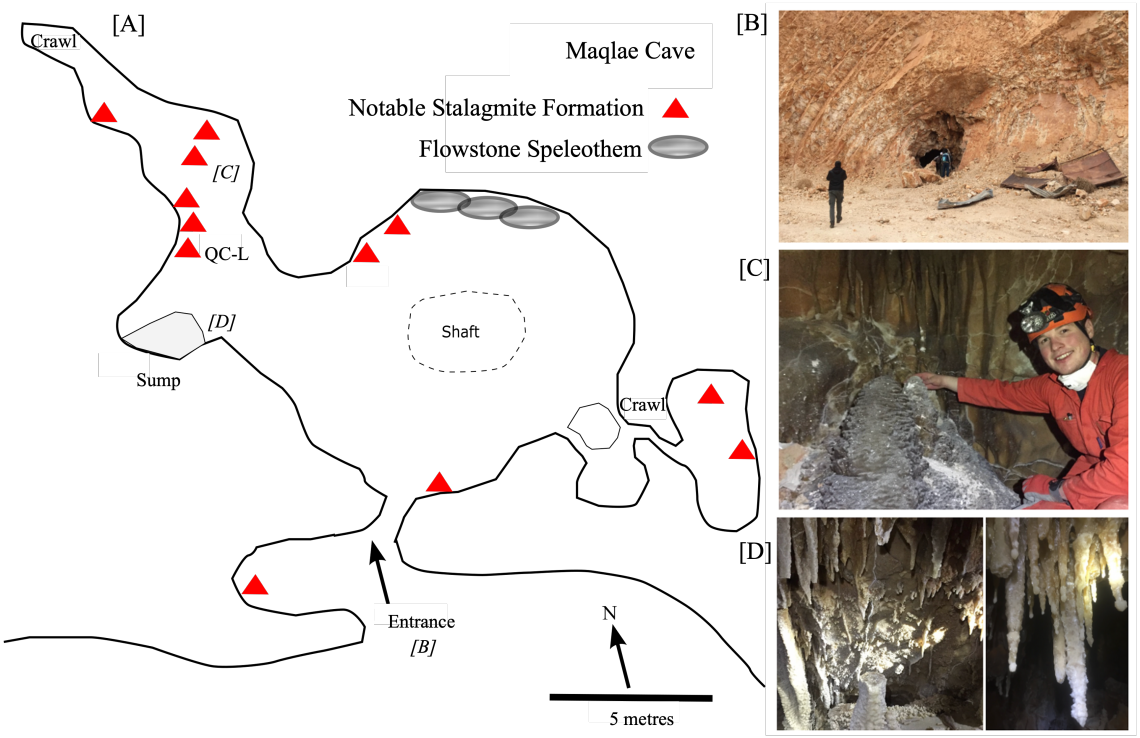


Figure 2.7: **Maqlae Cave.** [A] Cartoon plan of the explored sections Maqlae cave from field sketches. Notable observations are marked and italic annotations of B, C and D refer to the locations at which the images on the right were taken. [B] Maqlae cave entrance with people for scale [C] Author with a stalagmite from the north-west section of Maqlae cave. Nodules of calcite can be observed on the outer sides of the stalagmite. [D] Field images of speleothem deposition within Maqlae cave, which consists of slightly unusual growth formed from large clean calcite crystals.

Chapter 3

Extended Methodology

Contents

3.1 Sample handling 49

3.1.1 Sub-sample milling 50

3.2 Sample Characterisation 51

3.3 Stable Isotope Analysis 52

3.4 U-Th Dating 53

3.4.1 U-Th Theory 53

3.4.2 Chemistry methods 57

3.4.3 MC-ICP-MS analysis 60

3.4.4 Corrections 60

3.4.5 Data processing 61

Summary

Throughout this thesis, geochemical data is collected via repeatable methodologies. This chapter provides an extended methodology into XRD, stable isotope and U-Th data collection and may be referred back to when data collection is discussed in data chapters. In particular, U-Th data is critical for interpretations throughout this thesis, and so this short chapter introduces further information and theory behind U-Th dating methods. Geochemical methods only utilised once are introduced in the appropriate chapter.

3.1 Sample handling

Speleothem samples were sliced in half either in the rock cutting room at the CRAAG institute, Algiers or the rock preparation lab in the Department of Earth Sciences, Oxford. In all cases, cutting wheels were thoroughly cleaned with either isopropynol alcohol, ethanol or water to ensure that there was no contamination from the previous sample cut. Water (deionised water in the case of samples being cut in Oxford) was used as a lubricant and coolant. Stalagmite and stalactite samples were cut longitudinally, slightly offset from their predicted growth axis, leaving a flat surface to sub-sample from. The thicker side of the sample was used for sub-sampling to ensure that when drilling into the sample, the growth axis would be crossed at the flattest point on the sample, reducing the risk of mixing analyses across lamina.

Contamination reduction

Geochemical data retrieved from speleothem samples are often either trace measurements, thus impacted upon significantly by external contamination, or isotopic and therefore sensitive to changes in their signature through evaporative or temperature effects. All sampling was performed in a clean preparation laboratory in the Department of Earth Sciences, Oxford, which is exclusively used for carbonate sampling. Prior to

sampling (and between working on different samples), all surfaces were cleaned with isopropynol alcohol and deionised water, and wiped with a lint-free kimwipe, with samples then only placed on surfaces with a sheet of isopropynol-cleaned aluminium foil below them.

Sample vials were flushed with compressed air to remove any dust or other fine particles. Vials being used for U-Th analysis were first leached for 48 hours with 10% HNO_3 to prevent contamination from trace elements leached from the vials after sample dissolution. Any vials washed with ultra-pure (18 MΩ) Millipore water (hereafter referred to as MQ H_2O) prior to sampling were placed in an oven at 40°C until completely dry (> 24 hours), so as not to impact the oxygen isotope signature of measurements.

Tungsten carbide drill bits were wiped with isopropynol alcohol and MQ H_2O before use. In addition, before sampling for trace element data or U-Th ages, the uppermost (between 50-100 μm) surface of a sample was removed from the sampling region to remove any contaminants which may have been engrained into the sample surface during cutting or cleaning.

3.1.1 Sub-sample milling

3.1.1.1 U-Th Milling

All hand-held milling of samples was undertaken in a laminar flow hood in the preparation laboratory. It is also important to ensure that as little mixing across different periods of speleothem growth is taking place as possible when drilling the sample, an issue particularly when sub-sampling speleothems for which the age of layers is unknown. Where possible, long and shallow U-Th trenches were milled insofar as to sample across individual lamina as best as possible.

3.1.1.2 High-resolution micro-milling

Sub-sampling for stable isotope and trace elements was undertaken along the growth axis of the sample, where the initial precipitation of calcium carbonate was thought

to have occurred, to avoid sampling of regions which have undergone chemical evolution from initial depositional conditions. Where a change in sample growth axis was apparent in 2-dimensions, a corresponding change in the position of the milling axis was performed. High-resolution sub-sampling was undertaken using a 0.8mm tungsten carbide drill bit on a New Wave Research MicroMill, with samples fixed to a stage with 3-dimensional (x-y-z) adjustment capabilities.

Sub-sample powders were collected using an acid cleaned spatula and placed directly into 2 ml centrifuge vials, before the surface of the sample was blown with compressed air to clean the surface of the sample prior to moving onto the next sub-sample collection. The width of a sample trench was always greater than the depth into the sample, for which there are more unknowns, reducing the likelihood of mixing. When undertaking high-resolution milling, a notch was drilled into the sample, usually every 10 sub-samples, so that the resulting time or depth-series record could be referenced against the physical sample.

3.2 Sample Characterisation

High-resolution scanning

Prior to sub-sampling, samples were imaged using a high-resolution scanner to ensure a full catalogue of samples prior to geochemical sampling procedures.

XRD

X-ray powder diffraction (XRD) was performed in-house by Katherine Clayton in the XRD laboratory in the Department of Earth Sciences, Oxford. Aliquots of milled carbonate powders of $\sim$0.25 mg were analysed using the method described in detail in Day et al. (2021). In summary, samples were mixed with ethanol and deposited on a zero-background single crystal silicon substrate before being analysed using a PANalytical Empyrean Series 2 powder diffractometer, operating at 40 kV and 40 mA

with a Co Ka source. HighScore software was subsequently used to detect peaks and calculate % of minerals based on user-selected best fit mineral candidates.

Thin sections

Sample thin sections were cut by Matthew Beverley-Smith in the rock preparation suite in the Department of Earth Sciences, Oxford. A rough billet of sample was first cut using a continuous rim diamond saw and water lubrication before being dried using a low temperature warming plate. Samples were impregnated using epoxy resin in a vacuum chamber before being ground and lapped using a diamond grinder. Samples were then mounted to frosted glass slides using epoxy resin and mounting jigs, and sectioned using a petrothin trim saw and grinder. Slides were then lapped using lapping machines and vacuum jigs, and hand lapped to 30 microns. Finally, slides were cleaned and covered using UV resin and glass coverslips.

3.3 Stable Isotope Analysis

For samples presented in Chapter 4, 30-60 μg of carbonate powder was analysed for oxygen and carbon stable isotopes using a Thermo Scientific Delta V isotope ratio mass spectrometer (IRMS) coupled to a Kiel IV carbonate device at the University of Oxford. Sample measurements were calibrated with NBS-18 and NBS-19 bracketing standards and reacted with 100% H_3PO_4 at 71 °C. For samples presented in Chapters 5 and 6, 120-160 μg of carbonate powder was analysed for oxygen and carbon stable isotopes using a Thermo Delta V Advantage gas source mass spectrometer, fitted with a Gas Bench II peripheral. Within the Gas Bench II sample block, the powdered samples, in 12 mL He-flushed exetainers (Labco), are reacted with 100% phosphoric acid at 72°C.

In both cases, accuracy and precision were checked against an in-house secondary marble standard's (NOCZ) long-term average, included in all runs, with long-term standard deviations in Gas Bench II runs of $\delta^{18}O = 0.09‰$ and $\delta^{13}C = 0.06‰$ (1σ,

n=120) and in Kiel IV runs of $\delta^{18}O = 0.07‰$ and $\delta^{13}C = 0.05‰$ (1σ).

The relative $^{13}C/^{12}C$ values are reported in the conventional $\delta^{13}C$ (‰) notation, relative to the Vienna Pee Dee Belemnite (V-PDB), by assigning a value of +1.95‰ exactly to NBS-19. The relative $^{18}O/^{16}O$ values are reported in the conventional $\delta^{18}O$ (‰) notation, relative to V-PDB, on a normalised scale such that the $\delta^{18}O$ of NBS-19 is -2.2‰.

For measurements of aragonite $\delta^{18}O$, IUPAC guidelines were followed to account for the difference in acid fractionation factor applicable to the calcite bracketing standards (NBS-18 and NBS-19) and the aragonite samples. The aragonite acid fractionation factors from Kim et al. (2007), calcite acid fractionation factors from Kim and O'Neil (1997), and the method/software of Kim et al. (2015) were used for normalising the stable isotope data of these two different carbonate mineralogies.

Between uses, exetainers were washed thoroughly via submersion and ultrasonication 4 times for 5 minutes in deionised water. Clean vials were dried in an oven for > 24 hours at 40°C to ensure the evaporation of all H_2O prior to the next use.

3.4 U-Th Dating

3.4.1 U-Th Theory

An in-depth discussion of the U-Th dating of secondary carbonates can be found in Richards and Dorale (2003) and references therein. Here, a shorter introduction into the relevant theories is presented so as to directly aid interpretations of U-Th results presented in data chapters of this thesis.

U-Th disequilibrium dating, also referred to as ^{230}Th or ^{238}U-^{234}U-^{230}Th dating, allows the chronological placement through geological time of some of Earth's natural processes (Kaufman and Broecker, 1965; Ivanovich, 1992; Bourdon, 2003; van Calsteren and Thomas, 2006; Hellstrom, 2006). It is fundamental for understanding the links between the timing of climate change and global climate system mechanisms (Henderson,

2006), from a few years to in excess of 600 kyrs (Cheng et al., 2013). The technique has been applied to numerous terrestrial carbonate proxy archives to temporally locate evidence of both local and regional environmental and climatic change, including speleothems, travertines, corals, tufa and lacustrine carbonates (Mason and Henderson, 2010; Wendt et al., 2021) and may be applied up until the point at which daughter and parent radionuclides in the decay chain reach secular equilibrium, at approximately 600 kyrs. "Secular equilibrium" describes a steady state in which the activity of both the parent and daughter nuclides are equal. Time elapsed since the deposition of a sample is subsequently calculated by measuring the degree to which different daughter isotopes along a decay chain have returned to secular equilibrium (Chen et al., 2020; Figure 3.1).

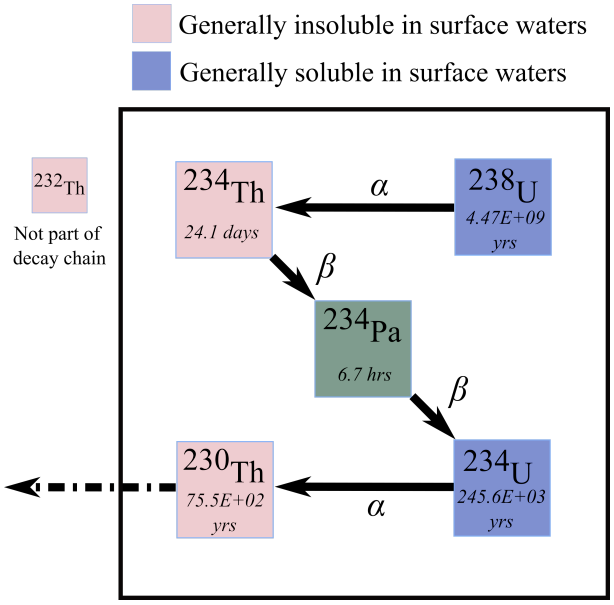


Figure 3.1: **U-Th Decay Chain.** Cartoon of the portion of the ^{238}U decay chain relevant for U-Th dating, adapted from Chen et al. (2020). The half-lives found in Cheng et al. (2013) and Chen et al. (2020) are annotated next to each isotope, and the type of particle emitted during radioactive decay (an α or β particle) are labelled as appropriate. The dashed black line indicates that ^{230}Th is not the end of the decay chain, which continues until the stable ^{206}Pb.^{232}Th is not part of this decay chain and pink and blue box colours refer to the insolubility and solubility of each radionuclide respectively.

A key assumption to U-Th chronology is that there is no thorium incorporated into the crystal structure during chemical deposition, meaning that $^{230}\text{Th} = 0$ at time zero. This is due to the relative insolubility of thorium (Th) into water (Figure 3.1), which

occurs in the terrestrial environment mainly in the 4+ oxidation state (Scholz and Hoffmann, 2008), ensuring that all measured ^{230}Th is ingrown from decaying uranium (U). U on the other hand is readily mobilized in the meteoric environment (Richards and Dorale, 2003), occurring mainly at the Earth's surface in the soluble U^{6+} form (Scholz and Hoffmann, 2008), and therefore *is* incorporated into speleothem crystal structures upon formation, from which ^{230}Th is produced via the decay of ^{234}U (Figure 3.1). A sample can be corrected for any initial ^{230}Th which has not been produced from radiogenic decay by measuring the ^{232}Th concentration during analysis and correcting for ^{230}Th with a chosen ^{230}Th/^{232}Th ratio, usually using an a-priori estimate for bulk earth (Wedepohl, 1995).

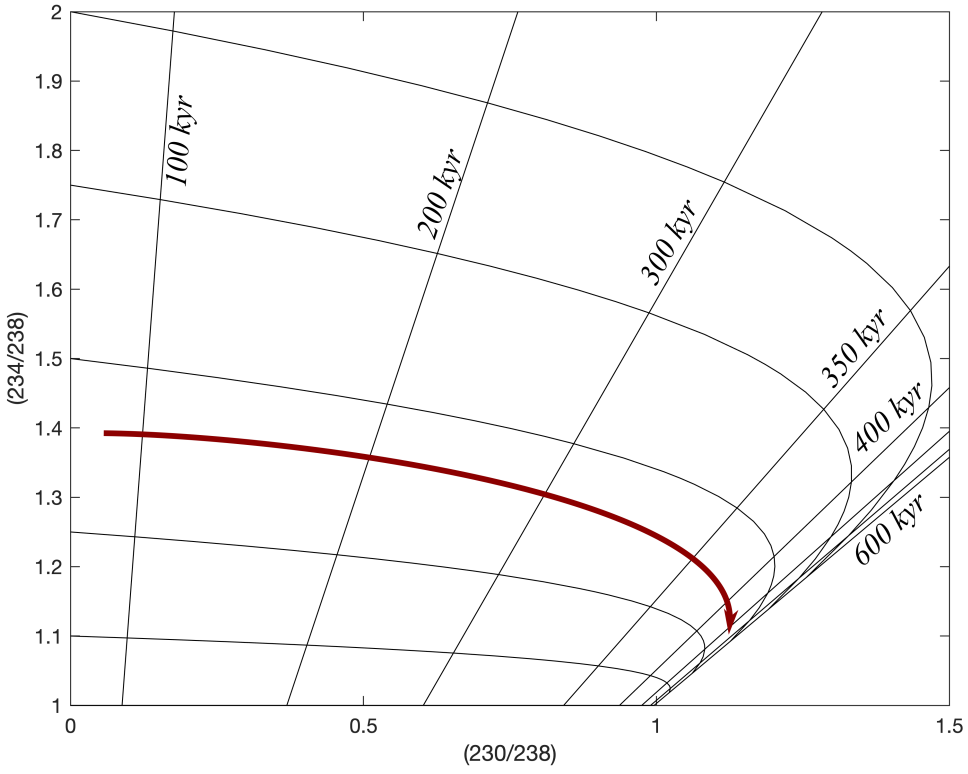


Figure 3.2: **U-Th Closed-system Decay**. Plot of the isotopic evolutions of (^{230}Th/^{238}U) and (^{234}U/^{238}U) activity ratios provided a system remains closed. Closed-system ^{234}U decay into ^{230}Th occurs from a starting (^{234}U/^{238}U) value following the horizontal decay curves, as exhibited by horizontal black lines. A typical decay trajectory is shown by the red arrow. Vertical black isochrons represent (^{230}Th/^{238}U)-(^{234}U/^{238}U) values that calculate to constant time periods, several examples are annotated.

The measured activity ratio of (^{230}Th/^{238}U) and (^{234}U/^{238}U) may then be used to determine the time elapsed since the initial chemical precipitation of the carbonate (Sauvet et al., 2017) by rearranging Equation 3.1 for t (Figure 3.2).

$$(\frac{230}{238}) = (1 - \exp^{-\lambda_{230}t}) + (((\frac{234}{238}) - 1) * (\frac{\lambda_{230}}{\lambda_{230} - \lambda_{234}}) * (1 - \exp^{((\lambda_{234} - \lambda_{230}) * t)})) \quad (3.1)$$

where

$\lambda_{Isotope} = \frac{ln(2)}{T_{1/2_{Isotope}}}$

and the half-lives ($T_{1/2_{Isotope}}$) of isotopes ^{230}Th, ^{232}Th, ^{234}U and ^{238}U are those found in Cheng et al. (2013).

The ratio of (^{234}U/^{238}U) is often given in the δ^{234}U notation, reported in ‰ relative to the ratio at secular equilibrium, equal to one, where:

$$\delta^{234}U = ((\frac{^{234}U}{^{238}U}) - 1) * 1000 \quad (3.2)$$

From a measured δ^{234}U value ($\delta^{234}\mathrm{U}_{\mathrm{measured}}$), the initial δ^{234}U of a sample ($\delta^{234}\mathrm{U}_{\mathrm{initial}}$) can be calculated with knowledge of the time that has elapsed since deposition, by re-arranging the equation:

$$\delta^{234}U_{measured} = (\delta^{234}U_{initial}) \exp^{-\lambda_{234}t} \quad (3.3)$$

These equations are only valid if two assumptions hold; (1) there is no initial ^{230}Th in the sample at the time of formation, or any incorporation can be corrected for, and (2) the system remains 'closed' after deposition. If not, the resulting age may be substantially biased and without significance (Scholz and Hoffmann, 2008).

A system remaining 'closed' means that there is no post-depositional addition or loss of either U or Th. A system can become 'open' as a result of several factors. Non-carbonate sediments such as organic matter or Fe-Mn hydroxides can absorb onto carbonate surfaces (Ames et al., 1983), acting as a separate source of U which is then

more susceptible to subsequent post-depositional loss or mobilization (Alam and Cheng, 2014) than U which is bound within the carbonate lattice (Chen et al., 2020). U loss may occur from thin or exposed carbonate deposits, as the U may be partially eliminated in wet media due to its solubility in water (Sauvet et al., 2017), a leaching process which would artificially increase the age of a deposit as there is now more Th as a ratio to U than would have occurred naturally from decay. In occurrences of U loss, it would therefore be expected that lower U concentrations measured in sub-samples would correlate with older ages (Borsato, 2003).

Post diagenesis U addition may also occur, from a U source which has a different δ^{234}U value than the original deposit (Ayling et al., 2017). In a similar fashion to the initial absorption of non-carbonate sediments, organic matter and oxides can be introduced to carbonates long after initial deposition, via fluid flow (Chen et al., 2020). A diagnostic feature of U addition would be a positive or negative correlation between a samples measured δ^{234}U and ^{238}U concentration, depending on if the post diagenetic U addition was of higher or lower δ^{234}U values than the original solution. Understanding post-diagenetic impacts on samples is therefore critical for U-Th interpretations, as paleoclimate information is of restricted value without accurate chronological constraints on the period in which it was recorded.

3.4.2 Chemistry methods

Sample mass

The mass used for each U-Th analysis depends on the age and ^{238}U concentration of the sample being processed. Nu-Instrument Multicollector-Inductively-Coupled-Plasma-Mass-Spectrometer (MS-ICP-MS) precision depends largely on counting statistics, and so a compromise between destructive sub-sampling and achieving a high enough ^{238}U and ^{230}Th voltage during MC-ISP-MS analysis is required. For older samples, particularly those with higher ^{238}U concentration, less sample mass is required as there is more ingrown ^{230}Th. When performing U-Th on new samples, for which there is

no prior knowledge of the sample's age or Th concentration, initial ICP-MS measurements were made to gain knowledge as to the ^{238}U concentration of the sample. Due to high static interference associated with using teflon beakers and powdered carbonate powders, weighing was triplicated or until reproducible masses were observed.

Spiking

Once powdered, calcite samples were dissolved in quartz distilled ($\mathbf{\Delta}$) nitric acid ($\mathbf{\Delta}HNO_3$), and spiked with a mixed ^{229}Th—^{236}U solution (Robinson et al., 2004), facilitating the measurements of $^{238}U/^{236}U$ and $^{230}Th/^{229}Th$. This is required as, during column chemistry, Th and U have a ∼70% and ∼50% yield respectively, although this can vary. Therefore, the measured $^{230}Th/^{238}U$ of the sample during MC-ICP-MS is impacted by the respective yield during column chemistry. By spiking samples with a known mass and ratio of ^{229}Th—^{236}U solution, which are non-natural radionuclides, measured isotopic ratios can be corrected via isotope dilution back to the correct ratios to allow for sample age calculation.

The mass of spike used for each U-Th analysis was dependent on the mass of sample being analysed (and subsequent expected ng of U present in the sample), the δ^{234}U of the sample, and the sample's age (if known). Spike addition was optimised to give a $^{230}Th/^{229}Th$ ratio between 0.06 and 0.77, and a $^{238}U/^{236}U$ ratio of < 138, to match thorium standards Mac-1 or This-2 used in MC-ICP-MS analysis.

All spiking was undertaken gravimetrically rather than volumetrically, which allowed for a much higher degree of accuracy. Due to the acidity of the spike solution (which is diluted in 2M HNO_3), 1-3 mL of MQ H_2O was added to samples (including analytical blanks) prior to spike addition, to reduce the effervescence of the reaction with the powdered carbonate.

Column Chemistry

All column chemistry was completed under clean laboratory conditions in the University of Oxford. Tyvek suits, lab clogs and non-powdered gloves were worn to reduce contamination. All work, with the exception of sample weighing and spiking, was completed under balanced laminar flow conditions, over-pressured with a class 1000 hepa-filtered air. Acid reagents ($\mathbf{\Delta}HNO_3$ and $\mathbf{\Delta}HCl$) used for sample dissolution, dilution and preparation were quartz distilled in-house from reagent grade. H_2O used for sample chemistry and reagent dilution was 18.2 MΩ (MQ) Millipore water, deionised using a MilliQ-element water polisher. Teflon beakers used for chemistry were cleaned before use using a standard procedure designed in-house (Appendix II Figure 5) using a range of reagent and distilled grade acids. Biorad AG1-X8 resin used for the chemical separation of U and Th was also cleaned using an in-house procedure (Appendix II Figure 5) to reduce potential contamination, with successive MQ and $\mathbf{\Delta}HCl$ washes. Biorad columns were rinsed with MQ and soaked in 2M $\mathbf{\Delta}HCl$ between uses. Pipette tips used for sample chemistry and acid dilution were rinsed prior to use using MQ water and a dilute (<1M) form of the acid being subsequently pipetted.

Sample dissolution and column chemistry was completed following the procedures outlined in Appendix II Figure 6, and the U and Th fractions were separated following procedures adapted from Edwards et al. (1987). This separation is important for MC-ICP-MS analysis as it removes the carbonate matrix which can impact instrument mass bias (Mason and Henderson, 2010) and allowed for the separate analysis of U and Th.

Blanks

For each 9 samples put through column chemistry and MC-ICP-MS analysis, at least 1 analytical blank was run alongside and subject to the same procedures throughout. This allows for monitoring of potential contamination from external Th and U which would impact on age calculations. Blank data for all analyses are provided in Appendix II Table 1.

3.4.3 MC-ICP-MS analysis

U and Th isotopes were measured using a Nu Plasma multicollector inductively coupled plasma mass spectrometer (MC-ICP-MS) at Oxford University, following the procedures described further in Vaks et al. (2013). The Nu plasma used ('P2') is coupled with a DSN100 desolvator and equipped with a collector array of 12 Faraday collectors and 3 ion counters. U measurements were performed using Faraday cups for ^{238}U, ^{236}U and ^{235}U and ion counters for ^{234}U. Dynamic Th measurements were performed based on the methods described in Mason and Henderson (2010), using a combination of Faraday cups and ion counters to allow for simultaneous measurements of ^{235}U-^{232}Th-^{230}Th and ^{238}U-^{235}U-^{229}Th.

All errors are reported as 2 s.e. (twice the standard deviation divided by the square root of the number of measurements). Subsequently, uncertainty reduces with the number of measurements made and so U was typically measured 50 times and Th 75 times. The external reproducibility of CRM-145 throughout U runs is a significant control on the final analytical uncertainty resulting from MC-ICP-MS analysis, with lower U voltages and insufficiently tuned instruments resulting in higher analytical uncertainties, and so several standards were run prior to samples to assess the reproducibility of CRM-145 ratios.

3.4.4 Corrections

Several corrections, detailed in Mason and Henderson (2010) and Thomas (2006) are applied to MC-ICP-MS measurements, including mass bias, abundance sensitivity and ion counter gain. Mass bias is corrected internally using the standard CRM-145 ^{238}U/^{235}U value, which is assumed to be 137.88. During Th measurements, ion counter gain is corrected for using the ^{238}U/^{235}U from Faraday (^{238}U) and ion counter (^{235}U) measurements.

Abundance sensitivity is corrected based on the half-mass dynamic measurements at 236.5, 235.5, 234.5 and 233.5 on the ion-counter during the initial part of the U

measurement, and based on the half-mass dynamic measurements at 230.5, 229.5 and 228.5 on the ion-counter during the final part of the Th measurement (Vaks et al., 2013).

A significant correction for U/Th chronology is for the detrital contamination of Th (i.e. not in-grown). This can be calculated by measuring the ^{232}Th concentration in a sample (which is not part of the ^{238}U-^{234}U-^{230}Th decay chain), and using an a-priori estimate of ^{230}Th/^{232}Th to correct for non-authigenic ^{230}Th. The level of correction therefore strongly depends on the chosen value for the initial ^{230}Th/^{232}Th used, specified as applied in each data chapter of this thesis.

3.4.5 Data processing

Individual ages and 95% confidence intervals were calculated using an in-house Monte Carlo script (DONKEY) that incorporates chemical blank errors, analytical uncertainties and the chosen initial ^{230}Th/^{232}Th ratio. The half-lives used for age calculations are those reported in Cheng et al. (2013), and ages are calculated based on the standard ^{230}Th/^{238}U equation (Equation 3.1; Kaufman and Broecker (1965)), derived in Richards and Dorale (2003).

Chapter 4

North-West Saharan Holocene rainfall driven by interhemispheric temperature differences

Contents

4.1 Abstract 65

4.2 Main Text 66

4.3 Additional Information 74

Statement of Authorship

This chapter presents the abstract and main text of the manuscript "North-West Saharan Holocene rainfall driven by interhemispheric temperature differences", submitted to Science Advances. The supplementary material of the manuscript is presented in Appendix III of this thesis. Manuscript authors are as listed; Hamish O. Couper, Christopher C. Day, Julia J. Barrott, Stacy A. Carolin, Ben Lovett, Abdeljalil Bouzouggar, Nick Barton and Gideon M. Henderson.

Cave sites presented in the manuscript were first visited and introduced by Julia J. Barrott (Barrott, 2014), with fieldwork undertaken alongside Christopher C. Day, Ben Lovett, Abdeljalil Bouzouggar and Gideon M. Henderson. Julia J. Barrott collected data for the age models and stable isotope records of stalagmites ASD-1 and MM.

Within the remit of this thesis, I re-interpret these records and add further U-Th and stable isotope data on existing samples. I re-process ASD-1 stable isotope data to correct for analytical aragonite acid fractionation, thus presenting a more accurate record to compare to other proxies. I also added an additional U-Th data point to the very top of ASD-1 to improve our chronological constraints on the stalagmite growth period. I generated a third high-resolution age model (10 ages) and a low-resolution stable isotope record from stalagmite KFT-1, to complement ASD-1 data and confirm that oxygen isotopes are describing regional climate signals rather than in-cave processes.

Subsequently, I interpreted stalagmite data alongside archaeological and regional proxy records, before writing and generating figures for the manuscript and supplementary materials in collaboration with my supervisor, Dr. Christopher Day. Gideon M. Henderson, Stacy A. Carolin, Nick Barton and Julia J. Barrott were all involved in data interpretation as well as editing the final manuscript.

4.1 Abstract

There is abundant evidence of wetter conditions in the Sahara during the early- to mid-Holocene, but a paucity of high-resolution spatial and temporal rainfall reconstructions, which has impeded the robust understanding of climate and archaeology. New stalagmite records from inland, north-west Sahara demonstrate increased rainfall between 8.7-4.3 kyr BP. The location, timing and oxygen isotopes of this stalagmite-growth demonstrate that subtropical rainfall occured, after the decline of the West African Monsoon, in response to increased North-South interhemispheric temperature anomalies. This rainfall supported a significant increase in the region's population during the Neolithic. Improved habitability and increased recharge to rivers flowing south through the Sahara will have facilitated connections, during a key period in the development of land use and animal production.

4.2 Main Text

There is abundant observational evidence that regions in today's Sahara experienced vastly wetter conditions in the early to mid-Holocene (Gasse, 2000; Tierney et al., 2011; Skinner and Poulsen, 2016). But there is a lack of high-resolution spatial and temporal palaeoclimate-records, which leads to an overly generalised representation of 'Saharan' climate, and to significant discrepancies between climate patterns and mechanisms proposed in the literature. The most widely discussed source of increased rainfall is the intensification, and northwards expansion, of the West African Monsoon (WAM), although studies disagree on fundamental details such as the northern limit of monsoonal rain, whether this extended beyond 30°N (Pausata et al., 2017; Tierney et al., 2017a; Sha et al., 2019; Dallmeyer et al., 2020) or remained between 10-20°N (Dallmeyer et al., 2020). The source of mid-Holocene moisture at subtropical latitudes (>30°N) is particularly uncertain, with a substantial range of northern limits to increased rainfall suggested in observational evidence and model simulations (Kuhlmann et al., 2004; Renssen et al., 2006; Pausata et al., 2016; Sha et al., 2019; Dallmeyer et al., 2020), and ongoing discrepancies between proxy and modelled data (Pausata et al., 2020). Alternative, non-monsoonal mechanisms proposed for subtropical rainfall include tropical plumes exporting moisture northwards (Knippertz et al., 2003a; Skinner and Poulsen, 2016; Dallmeyer et al., 2020), or a southward shift of the Mediterranean winter precipitation system (Cheddadi et al., 2021). To date palaeo-observations have not been able to distinguish which of these mechanisms provided moisture.

Many palaeo-observations are limited by the spatial and temporal resolution inherent to the individual archives. River- and surface-water, for example, may be supplied by distant rainfall, via surface or groundwater flow, making these proxies unfit for resolving precise locations of increased Saharan rainfall in the past. Additionally, an offset in timing exists between rainfall increase and the appearance of persistent surface-water bodies, as it can take hundreds of years for groundwater levels to rise sufficiently to feed the surface-water bodies featured in palaeo-hydrology reconstruction studies (Lézine et

al., 2011). An alternative terrestrial archive, that has not previously been used in the north-west Sahara, is speleothem carbonate (secondary calcium carbonate that forms in caves, including stalagmites). Stalagmites are uniquely capable of directly recording periods in arid locations when local rainfall levels rise above a threshold level (Vaks et al., 2010), and can be precisely dated with U-Th approaches. They are therefore ideally suited for determining the precise location and timing of past rainfall in the Sahara.

Here we produce stalagmite-based palaeo-rainfall reconstructions from an area close to the north-western boundary of the Sahara (Figure 4.1, box 'NW-Sahara', ∼30°N) that has a current lack of palaeo-hydrology (e.g., lake presence) records. We compare these new stalagmite palaeo-rainfall reconstructions with 183 surface palaeo-hydrology records from the south-west Sahara (Figure 4.1, box 'SW-Sahara', ∼20°N) to address climate trends and mechanisms.

The north-west Sahara (Figure 4.1, box 'NW-Sahara', ∼30°N) is bordered by the high Atlas mountains, which impede winter Atlantic and Mediterranean rains from reaching the region (Ait Brahim et al., 2016). Average annual rainfall in the region today is low at $<$ 160 mm/yr (Appendix III), and the net water balance (i.e. precipitation - evaporation) is substantially below the 300-350 mm/yr previously established as required for speleothem growth (Vaks et al., 2010). Approximately 40% of the local rainfall is rain sourced from the tropics during transition seasons (October-November, February-March), travelling northward in the form of Tropical-Plumes, with this mechanism also known as Tropical-Extratropical Interactions (Knippertz et al., 2003a; Knippertz, 2003, 2007). Tropical Plume (TP) rainfall requires a source of convective moisture in the tropics, which feeds a northwards mid-level moisture flux over northern Africa, with subsequent upper-level divergence or orographic rainfall in the north-west Sahara region (Knippertz, 2007). Tropical plumes already supply irregular rainfall to the north-west Sahara in recent decades, with moisture sourced from mesoscale convective clusters over tropical West Africa, or over the adjacent Atlantic Ocean (Knippertz

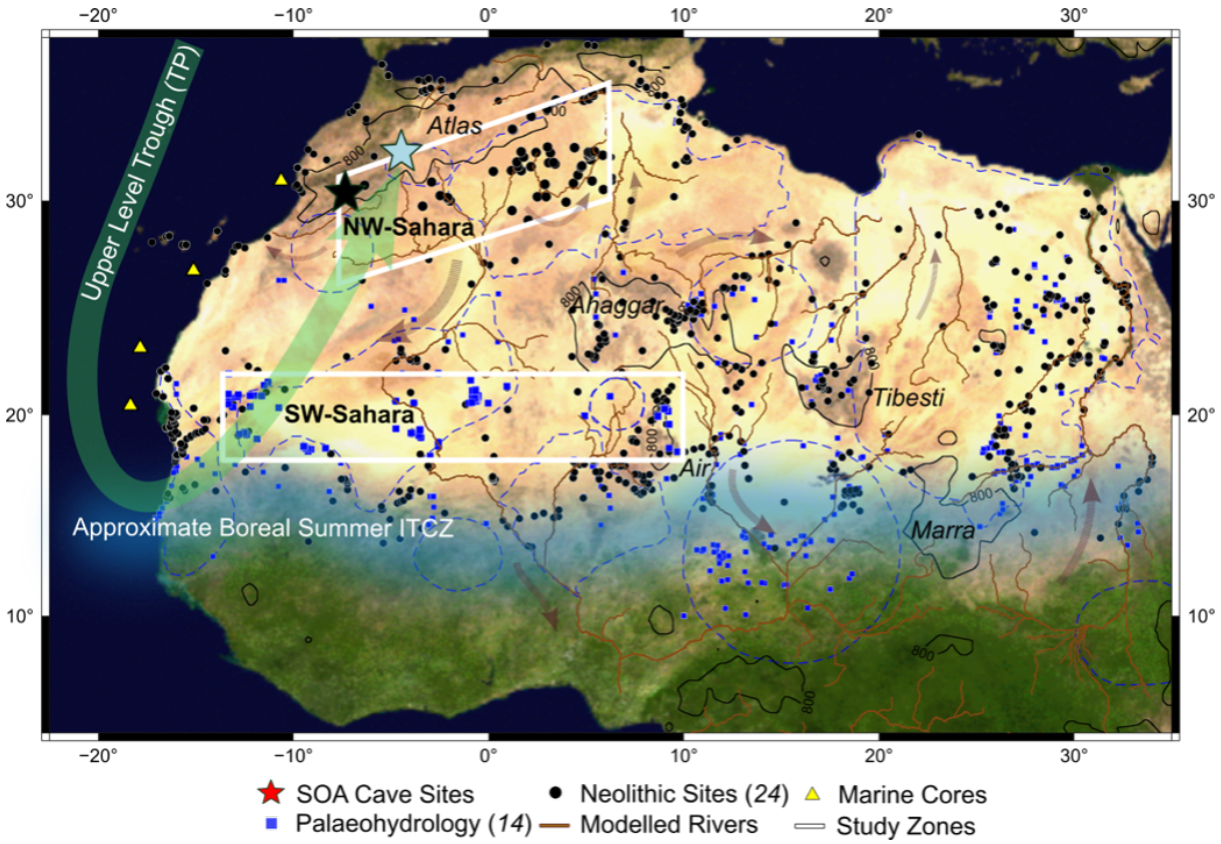


Figure 4.1: **AHP Manuscript Figure 1**: **Satellite image of north Africa, with north-west and south-west Saharan regions (white boxes) used to compare the timing of increased-rainfall, surface hydrology, and archaeology.** Stars are cave sites from this study. Black lines are 800m altitude contours. Brown lines are topographically-defined surface water flows modelled using NASA SRTM3 data and Topotoolbox2 (Schwanghart and Scherler, 2014). Brown arrows summarise the general directions of river flow. Dashed pale blue lines are approximate limits of known aquifers (Lézine et al., 2011). The green arrow is an example upper-level trough trajectory associated with modern TP-rainfall events (Knippertz, 2003). The blue shaded area is the approximate boreal summer ITCZ extent, based on vegetation coverage. Black dots are radiocarbon dated Neolithic sites compiled by (Manning and Timpson, 2014). Blue squares are radiocarbon dated surface hydrology records compiled by Lézine et al., (2011).

et al., 2003a; Knippertz, 2003, 2007).

In contrast, the south-west Saharan region (∼20°N) forms the modern southern boundary of the desert, and is just beyond the reach of regular summer monsoonal rainfall. It also has low rainfall, $<$ 130 mm/yr (Appendix III), the result of irregular, northwards excursions of summer West African Monsoon (WAM) rainfall (Drobinski et al., 2009; Cornforth, 2012; Dallmeyer et al., 2020). Past increased rainfall within this south-west region is caused by a more northerly position of the WAM frontal rain band driven by insolation changes (Gasse, 2000; Kuhlmann et al., 2004; Hély et al., 2014; Dallmeyer et al., 2020). Surface palaeo-hydrology evidence of wetter conditions at ∼20°N first appears around 11 kyr BP (Lézine et al., 2011), with the maximum number of surface-water records in the period 10.5-7.5 kyr BP, followed by a significant decrease in surface water at ∼7.5 kyr BP, and a further decrease at ∼5 kyr BP (Figure 4.2B). As changes in surface hydrology are typically delayed relative to changes in rainfall amount (Lézine et al., 2011), rainfall in the south-west Sahara likely decreased in two steps earlier than 7.5 kyr BP and 5 kyr BP.

We found and U-Th dated stalagmites in three caves in the north-west Sahara (30-32°N, 7.5-4.4°E, Appendix III Figure S1), with overlapping growth in the period 8.7-4.3 kyr BP (Figure 4.2A; Appendix III), and low age uncertainty (average 2σ uncertainty is 59 years, Appendix III Table S1). The combined growth periods of the stalagmites provide direct evidence of rainfall greater than 300 mm/year, and increased vegetation on the surface. The onset of increased rainfall was at least 2000 years later, and the termination of this rainfall occurred at least 700 years later, than in the south-west Sahara (Figure 4.1, box SW-Sahara, ∼20°N).

High rainfall in the north-west Sahara, ending significantly later in the north-west Sahara than in the south-west Sahara (Figure 4.2B), rules out the northward expansion of the WAM as the cause of increased rainfall at ∼30°N. A monsoonal mechanism would require increased rainfall ending first in the north, as the monsoonal frontal rain band retreated southwards at the end of the humid period. These new north-west Sahara

stalagmite growth records provide evidence against this mechanism.

We instead propose the coupling of an existing mechanism (Tropical Plumes; TP) with northwards shifts of the Atlantic Intertropical Convergence Zone (ITCZ) to explain the increased rainfall in the north-west Sahara during the early-to-mid Holocene. We suggest that northward shifts of the ITCZ, characterised by warmer northern hemisphere temperatures relative to the southern hemisphere (Schneider et al., 2014), increased moisture supplied to the northwards mid-level moisture flux, fuelling increased TP-rainfall.

This coupled ITCZ-TP mechanism supplying increased rainfall to the north-west Sahara is supported by two lines of evidence. Firstly, by the growth history of multiple speleothems in the north-west Sahara, with speleothem growth coeval with periods when the northern hemisphere is more than ∼0.8℃ warmer than the southern hemisphere (Figure 4.2A). Secondly, by the speleothem oxygen isotopes from the Anti-Atlas stalagmites. Anti-Atlas caves are located midway between the Atlantic climate zone (dominated by winter Atlantic-sourced rainfall) and the South-of-Atlas climate zone (dominated by TP rainfall), as defined independently by modern meteorological studies (Knippertz, 2003) (Appendix III Figure S1). This midway position of the Anti-Atlas caves means that the average rainfall that fed them will have oxygen isotopes falling on a mixing line between the South-of-Atlas oxygen isotope values (constrained by one cave from this study; Ksar cave) and the coastal oxygen isotope values (constrained by Wintimdouine cave (Sha et al., 2019)). When TP-rainfall is enhanced (reduced) by a more northerly (southerly) ITCZ, the Anti-Atlas oxygen isotope values shift towards the South-of-Atlas (Atlantic) oxygen isotope values (Figure 4.3A). This is further demonstrated by comparison of the Anti-Atlas oxygen isotopes with the North-South temperature anomaly, with the temperature anomaly controlling the latitudinal position of the ITCZ. Anti-Atlas oxygen isotopes shift towards more negative TP-rainfall isotopic values as the N-S temperature anomaly increases, and back towards less negative Atlantic rainfall isotopic values as the temperature anomaly decreases (Figure 4.3).

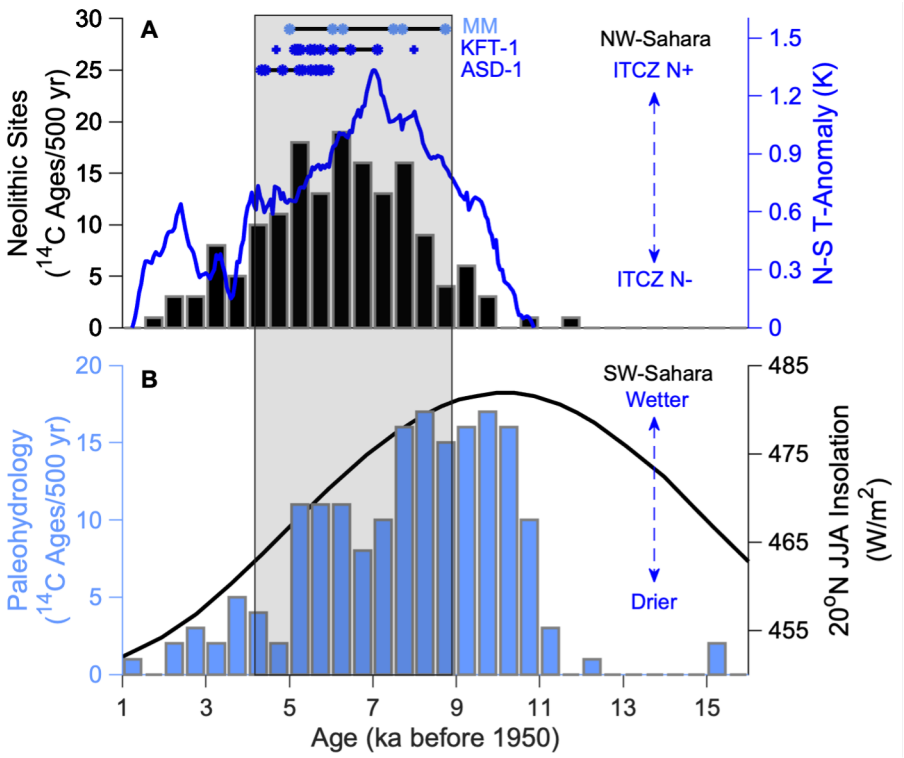


Figure 4.2: **AHP Manuscript Figure 2**: **Timing and abundance of palaeo-environmental and archaeological records from north-west and south-west Sahara (white boxes Figure 4.1)**. (A) Stalagmite and archaeology records from NW-Sahara. Pale blue dots, dark blue dots, and dark blue crosses denote U-Th ages from stalagmite samples MM, KFT-1 & ASD-1, and miscellaneous stalagmite-pieces respectively. The grey-shaded rectangle highlights enhanced rainfall in the NW-Sahara from stalagmite chronology. Black bar charts denote the number of ^{14}C ages from Neolithic archaeological sites (Manning and Timpson, 2014), in 500-year bins. The blue curve is the North-South interhemispheric temperature anomaly (Schneider et al., 2014). (B) Palaeo-hydrology and insolation from the SW-Sahara. Blue bar charts denote the number of palaeo-hydrology records in 500-year bins from (Sha et al., 2019). Black line is the 20°N June insolation curve, calculated with (Berger and Loutre, 1991; Huybers, 2006).

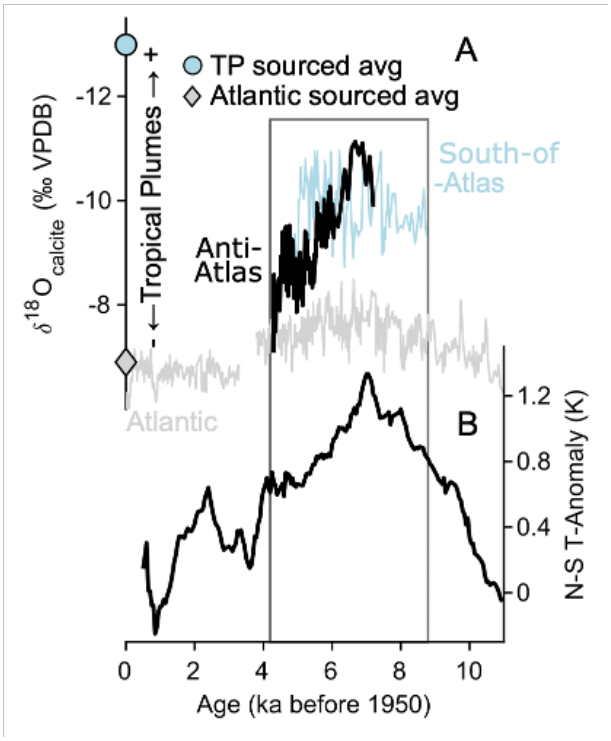


Figure 4.3: **AHP Manuscript Figure 3: Anti-Atlas (AA) stalagmite oxygen isotopes responding to tropical-plume (TP) rainfall-amount**. (A) Blue curve plots oxygen isotopes from inland, South-of-Atlas, stalagmite 'MM'. Grey line plots oxygen isotopes from an Atlantic coast stalagmite (Sha et al., 2019). Black line plots oxygen isotopes from Anti-Atlas stalagmites, located midway between the South-of-Atlas and Atlantic sites, with oxygen isotopes on a mixing line between oxygen isotopes dominated by TP-sourced (pale-blue circle) and Atlantic sourced rainfall (grey diamond) (Appendix III). Black rectangle highlights the period of enhanced rainfall in the NW-Sahara from stalagmite chronology. (B) Black line is the calculated North-South temperature anomaly (Schneider et al., 2014).

This provides us with a sensitive indicator of increased TP-rainfall, fed by northwards ITCZ migrations. A continentality effect on oxygen isotopes is not seen at these cave sites, as evidenced by periods of overlapping oxygen isotopes between Wintimdouine & Anti-Atlas caves, and between Anti-Atlas & Ksar caves (Figure 4.3A), despite hundreds of kilometres separating these sites (Appendix III Figure S1).

The precise location and timing of the new stalagmite records also allow assessment of the relationship between rainfall change and human habitation in the north-west Sahara region. An early, pioneering study into connections between North African demography and climate (Manning and Timpson, 2014) demonstrates the difficulty of interpreting archaeology and demography with insufficiently resolved environmental

data. At the time of its publication, a lack of records and lack of recognition of the spatial heterogeneity of the loosely termed 'Saharan' climate allowed the authors of this early record to propose a thousand-year lag of demography relative to atmospheric climate change. Here we demonstrate significant differences in the timing of wet periods within distinct regions of the western Sahara. Considering only locations in the north-west Saharan region of the dataset of (Manning and Timpson, 2014) indicates a strong agreement between periods of stalagmite growth and archaeological finds (as shown in Figure 4.2A). Of the 160 Holocene Neolithic site radiocarbon (^{14}C) ages in this region 80% fall within the 8.7-4.3 kyr BP period. This suggests that increased rainfall supported improved habitability within this region.

North-south Sahara connectivity is key to understanding the dispersal of human evolution from its centre in sub-Saharan Africa. To the north of sub-Saharan Africa the Sahara impedes connections and exchanges. Periods of significant north-south connectivity across the western Sahara have been inferred from zoo-geographical evidence, including the trans-Saharan distribution of numerous aquatic species (Drake et al., 2011). Until now, however, there lacked certainty regarding the timing of these wet periods, particularly in the north-western desert.

Stalagmite growth from three different cave sites presented here suggests that rainfall levels increased regionally along the southern foothills of the Atlas Mountains, which fits with meteorological data demonstrating the impact of modern TP-rainfall at locations from Ouarzazate (∼7°W) to beyond Béchar (∼2°W). Enhanced rainfall in this region recharged major aquifers and increased recharge to rivers flowing southwards through the Sahara (Heiß et al., 2020), c.f. topographically modelled rivers using TopoToolbox (Schwanghart and Scherler, 2014) in Figure 4.1. Improved habitability and the increased recharge to rivers flowing south through the Sahara will have greatly facilitated connections, and encouraged movement, by people across the Sahara, during a key period in the development of land use and animal production (Barich et al., 2014; Dunne et al., 2018; Phelps et al., 2020; Broich et al., 2021). The new speleothem-

growth and oxygen isotope evidence, presented here, of a coupled ITCZ-TP mechanism for exporting moisture from the tropics to the north-western Sahara, provides a significant new perspective on the underlying controls of Saharan climate. This has global implications as the importance of dust export from the Sahara to the north Atlantic is increasingly recognised for climate systems as distant and as significant as the Asian monsoon (Griffiths et al., 2020), and ENSO (Pausata et al., 2017). This novel mechanism provides an additional supply of moisture to the north Sahara, without requiring the disputed extension of the West African Monsoon as far north as the subtropics.

4.3 Additional Information

In Appendix III, the supplementary information for this manuscript is presented. In addition, a figure is presented providing further evidence for the robustness of ASD-1 in recording variations in the average annual position of the ITCZ, using comparisons between Anti-Atlas δ^{18}O and records of Cariaco basin Ti%, a tropical recorder of northern hemisphere ITCZ position.

Statement of Authorship for joint/multi-authored papers for PGR thesis

To appear at the end of each thesis chapter submitted as an article/paper

The statement shall describe the candidate's and co-authors' independent research contributions in the thesis publications. For each publication there should exist a complete statement that is to be filled out and signed by the candidate and supervisor **(only required where there isn't already a statement of contribution within the paper itself).**

Title of Paper	North-West Saharan Holocene rainfall driven by interhemispheric temperature differences
Publication Status	□Published □ Accepted for Publication ☒**Submitted for Publication** □Unpublished and unsubmitted work written in a manuscript style
Publication Details	Submitted to Science Advances

Student Confirmation

Student Name:	Hamish Couper		
Contribution to the Paper	I performed all geochemical analyses on sample KFT-1, as well as additional U-Th and stable isotope analyses on sample ASD-1. I interpreted the data and generated all figures for the manuscript I wrote the manuscript, and accompanying supplementary information, in collaboration with my supervisors.		
Signature	H Couper.	Date	18/04/2022

Supervisor Confirmation

By signing the Statement of Authorship, you are certifying that the candidate made a substantial contribution to the publication, and that the description described above is accurate.

Supervisor name and title: Dr. Christopher Day		
Supervisor comments I confirm that Hamish Couper made a substantial contribution to the article "North-West Saharan Holocene rainfall driven by interhemispheric temperature differences" by Couper et al., and that this is entirely appropriate material for a thesis chapter.		
Signature	Date	18/04/2022

This completed form should be included in the thesis, at the end of the relevant chapter.

Chapter 5

Regionally extensive periods of increased rainfall during the last 450 kyrs defined by northern Saharan stalagmites

Contents

5.1 Introduction 78

5.2 Climate and cave settings 80

5.2.1 Grar Cave 81

5.2.2 Maqlae Cave 84

5.2.3 Other caves 86

5.3 Methods 86

5.3.1 XRD 86

5.3.2 U-Th Dating 87

5.3.3 Stable isotope analysis 88

5.4 Results 89

5.4.1 XRD 89

5.4.2 U-Th Chronology 89

5.4.3 OxCal Age Model 95

5.4.4 High-resolution stable isotope records 96

5.5 Discussion 98

5.5.1 Timing of SOA rainfall throughout the past 450 kyrs 98

5.5.2 The African Humid Period 103

5.6 Conclusion 106

Acknowledgments

Acknowledgments in this chapter are made to Christopher Day for measuring speleothem stable isotopes, to Katherine Clayton for performing XRD analyses and to Matthew Beverley-Smith for making sample thin sections.

Abstract

Presently, the Sahara is arid, with very low precipitation rates and high evapotranspiration. However, this has not always been the case, with known past increases in rainfall, although the timing and spatial extent of direct rainfall is not well-defined in non-coastal regions. Here, fossil stalagmites were collected from cave sites in Algeria at the northern limits of the central Saharan Atlas Mountains, to assess periods of increased rainfall throughout the middle to late Pleistocene. High-precision U-Th chronology reveals numerous periods of increased rainfall leading to speleothem growth, including robust evidence for formation at 386-378 kyr BP (MIS 11), 316-310 kyr BP (MIS 9), 155-145 kyr BP (MIS 6), 80-74 kyr BP (MIS 5a) and 8-5 kyr BP (MIS 1). This chronology correlates with periods of speleothem growth in stalagmites located in the Moroccan High- and Anti-Atlas Mountains, implying that increases in north Saharan rainfall are regional on the desert side of the Atlas range between 7°W-1°E and 30-33°N. These data robustly increase the temporal resolution of records of direct, local rainfall, and provide key information as to the minimum geographic extent of increased rainfall in the north-west Sahara. High-resolution stable isotope records from this study during the African Humid Period suggests a tropical plume moisture source during the mid-Holocene across the breadth of the southern Atlas range, whilst differences in $\delta^{18}O$ between distinct stalagmite growth periods implies variations in the amount of tropical rainfall. Importantly, this research presents the South of Atlas zone as a unique and significant Saharan region, from which the activation of perennial southward flowing river systems was critical for human migration and development.

5.1 Introduction

The Saharan Atlas Mountains, central Algeria, are at a climatic crux, situated at the border between the hyper-arid Sahara and the Mediterranean climate zone of northern Algeria. On both short- and long-term timescales, there is significant climate change which impacts local human populations, migration, water resources and dust export from the region (Larrasoaña et al., 2013; Hadour et al., 2020; Derdour et al., 2018; Melalih and Mazour, 2021).

Compared to the Mediterranean coastlines of North Africa, and regions west of the Atlas Mountain ranges, which both receive predominantly winter rainfall, the most significant proportion of annual rainfall in the Algerian Saharan Atlas falls during transition season months (spring and autumn), suggested to result from tropical plumes (TPs; Knippertz (2003); Figure 5.1), implying a modern connection between the northern Sahara and the tropics. Elucidating how climate mechanisms transporting rainfall to these regions in the present day reacted to changing global and local parameters throughout the geological past is vital for understanding how rainfall amount in the region varies, and for accurately predicting future changes (Karssene et al., 2017; Bouderbala, 2019; Pausata et al., 2020).

Throughout the geological past, there are known to have been periods in which regional rainfall has increased in North Africa (DeMenocal et al., 2000; McGee et al., 2013; Skonieczny et al., 2015; Pausata et al., 2020), recharging major regional aquifers (Edmunds et al., 2003) and potentially acting as 'windows of opportunity' for human migration (Drake et al., 2011; Scerri et al., 2014; Bae et al., 2017). The most commonly cited cause of rainfall maxima is associated with increased boreal summer insolation, leading to a strengthening and expansion of the West African Monsoon (WAM) system (Renssen et al., 2006; Sha et al., 2019; Lüning and Vahrenholt, 2019; Nicholson et al., 2020). A recent study (Chapter 4) introduced the concept of changes in inter-hemispheric temperatures being important for increased rainfall in north-west Africa, with increased temperature anomalies between the north and southern hemisphere lead-

ing to more northerly average intertropical convergence zone (ITCZ) positioning (Chapter 4). This phenomenon allows for increased moisture transport via TPs, leading to orographic rainfall in the western parts of the South of Atlas (SOA) region.

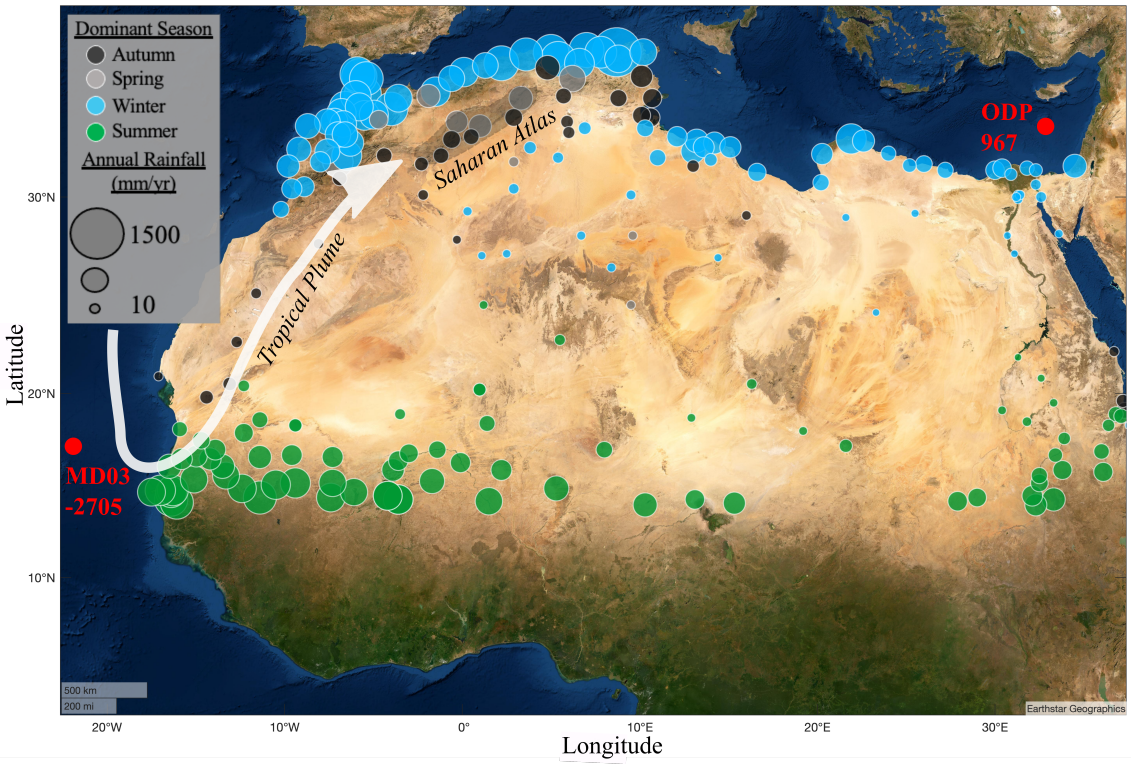


Figure 5.1: **Saharan Atlas Location and Climatology.** North African GHCN-M meteorological station rainfall amounts and dominant season plotted on a high-resolution satellite image. Data sourced from http://climexp.knmi.nl (Trouet and Oldenborgh, 2013). Bubble size represents annual rainfall amount, ranging between 10 and 1542 mm/yr. Bubble colour represents the dominant season in which rainfall occurs; blue = winter, green = summer, black = autumn, grey = spring. A typical tropical plume trajectory is marked as a white arrow (Knippertz, 2003) and the location of the Saharan Atlas range is marked in a grey shaded area. Red circles denote the locations of marine records MD03-2705 (Skonieczny et al., 2019) and ODP 967 (Trauth et al., 2021), used as part of interpretations.

Whilst there is extensive proxy evidence for past increased rainfall in North Africa (Gasse, 2000; DeMenocal et al., 2000; Kröpelin et al., 2008; Watrin et al., 2009; Chandan and Peltier, 2020), records do not act as direct evidence for increased local rainfall, instead representing distal moisture sources or regionally integrated signals (Adkins et al., 2006; Krinner et al., 2012). Speleothem deposits on the other hand offer robust indicators of paleo-rainfall at a cave site in presently arid regions. Currently, north-west

African speleothem data currently comes from either the far north (Genty et al., 2006; Ruan et al., 2016; Hoffmann et al., 2016b) or west (Sha et al., 2019; Wassenburg et al., 2016; Ait Brahim et al., 2017), in most cases situated close to coastlines and limited to growth during the most recent 20 kyrs (Figure 5.2). A stalagmite record from northeast Africa (El-Shenawy et al., 2018) extends further back through time, but is located $>$ 3000 km and several degrees of latitude south from study sites presented here. An unpublished stalagmite record (MegaMite (MM)) from the desert side of the High Atlas Mountains (Ksar Cave; Barrott (2014)) identified numerous periods of increased rainfall in the SOA throughout the last 400 kyrs. However, whilst offering direct evidence of rainfall, the record acts as a single data point and requires corroboration from other records to confirm regional rainfall patterns.

There therefore remains a paucity of Saharan paleo-archives which have high-precision chronology that provides local information regarding the occurrence of rainfall. Fieldwork in 2020 targeted two areas with known limestone geology, 350 and 550 km east of Ksar cave (Barrott, 2014), a significant distance from coastlines and south of the Saharan Atlas Mountain range, placing them within the Sahara in regions with insufficient rainfall for contemporary speleothem growth. Here, U-Th chronology and stable isotope records are presented from samples collected from these sites to further investigate the climate of the Saharan Atlas during the past 400 kyrs.

5.2 Climate and cave settings

Caves are located on the desert side of the Saharan Atlas orographic belt (Figure 5.2), at the boundary between the hyper-arid Sahara to the south and the semi-arid Hautes Plaines to the north, situated between a hot (BWh) and cold (BWk) desert climate classification (Peel et al., 2007). Annual rainfall is $<$ 170 mm/yr, insufficient for modern speleothem growth. Caves are at the head of major southward-flowing rivers, south of which lies some of the richest neolithic archaeology sites in north-west Africa (Manning and Timpson 2014), with numerous radiocarbon dated sites (Figure 5.2).

Sites are protected from winter rainfall via topographic barriers and distance from the Atlantic and Mediterranean coastlines, and are dominated by transition season (Spring and Autumn) rainfall associated with TPs (Figure 5.1; Knippertz, 2003).

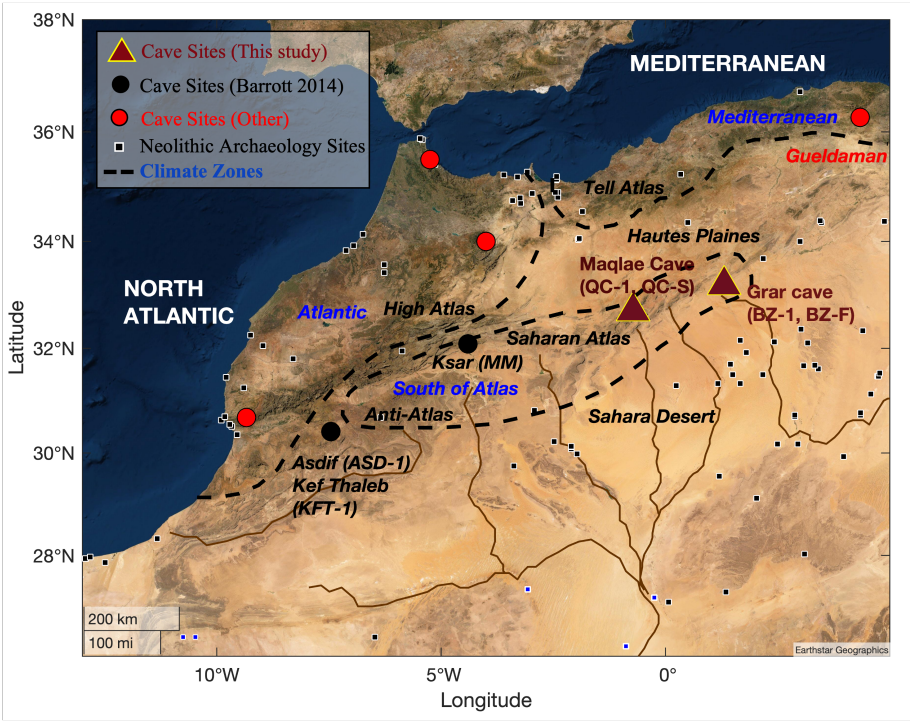


Figure 5.2: **North-west Africa Field Sites.** Expanded satellite map of north-west Africa with cave sites from this study, Barrott (2014) and other studies plotted. Maroon triangles with yellow borders mark cave sites first presented in this study, black circles from Barrott (2014) and red circles are other records (Ruan et al., 2016; Wassenburg et al., 2016; Sha et al., 2019; Ait Brahim et al., 2019). Moroccan climate zones (Atlantic, Mediterranean, South of Atlas) defined in (Knippertz et al., 2003a) are marked using dashed black lines, whilst brown lines indicate modelled rivers from satellite imagery (Schwanghart and Scherler, 2014). Archaeological Neolithic sites are marked as black squares with white borders (Manning and Timpson 2014).

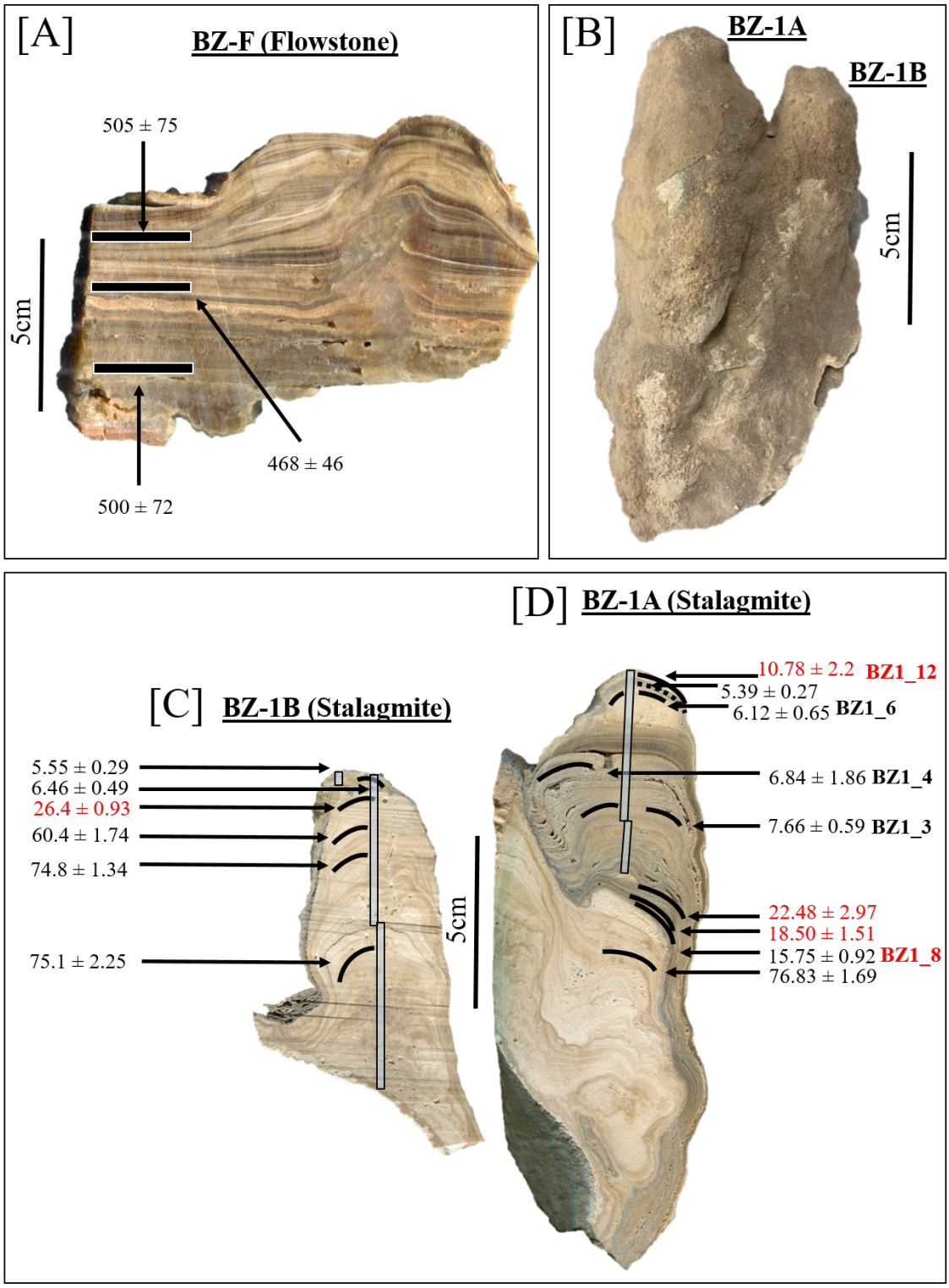
5.2.1 Grar Cave

Grar cave is located in the southern foothills of the Saharan Atlas (33.2°N, 1.3°E), at an altitude of 974 masl, 10 km northeast of the village of Brezina (Figure 5.2). The cave is $>$ 350 km from the closest point to the Mediterranean coast and 550 km from Ksar Cave (Barrott, 2014). Annual precipitation at the El Aliod meteorological station, 80 km from Grar cave, averages 124 mm/yr, similar to ERA5 reanalysis estimates at

Brezina of 146 mm/yr, falling in the bi-modal distribution diagnostic of the SOA region (Appendix I Figure 4). Further descriptions of the cave setting are found in Chapter 2 of this thesis.

Stalagmites BZ-1A and BZ-1B (Figure 5.3) were collected as a conjoined sample, ∼150m into the cave from a 3m high shelf. The sample is ∼20cm long at its greatest extent. The conjoined stalagmites were separated and subsequently cut along their central growth sections to produce BZ-1A (larger) and BZ-1B (smaller), both consisting of different internal structures (Figure 5.3). Also analysed from this cave was BZ-F, a flowstone totalling $>$ 2m in height from which the entire length was sampled across 14 pieces. The top piece, consisting of the most recent formation, is reported on here.

Figure 5.3: **Grar Cave Speleothem Scans and U-Th Ages.** High-resolution scans of the three speleothem samples discussed from Grar Cave. Note the varying distance scales between scans. [A] Scan of the top section of flowstone BZ-F. [B] Image of the conjoined stalagmite samples BZ-1A and BZ-1B, prior to cutting [C] Scan of stalagmite BZ-1B [D] Scan of stalagmite BZ-1A. It is notable that the bottom half of BZ-1A corresponds to the majority of BZ-1B growth, with similar crystal colouring and laminae. The top half of BZ-1A is not represented in BZ-1B to the same extent. On each scan, the positions of U-Th trenches and resultant U-Th age results (expressed in kyr BP) are annotated. Ages with significant ^{232}Th contamination ($>$ 5 ppb) are marked in red. The second age from the top on BZ-1A is marked with a dashed line as it was drilled from the top of the sample inwards, prior to cutting the sample in half, and so this location is not exact. Sub-samples annotated in black (BZ1_6, BZ1_4 and BZ1_3) identify those used in calculating an initial thorium ratio with which to correct Grar cave ages, whilst those annotated in red (BZ1_12, BZ1_8) identify anomalous ages discussed in the text. Stable isotope trenches for BZ-1A and BZ-1B are marked as pale blue rectangles down the central growth axes of the samples.

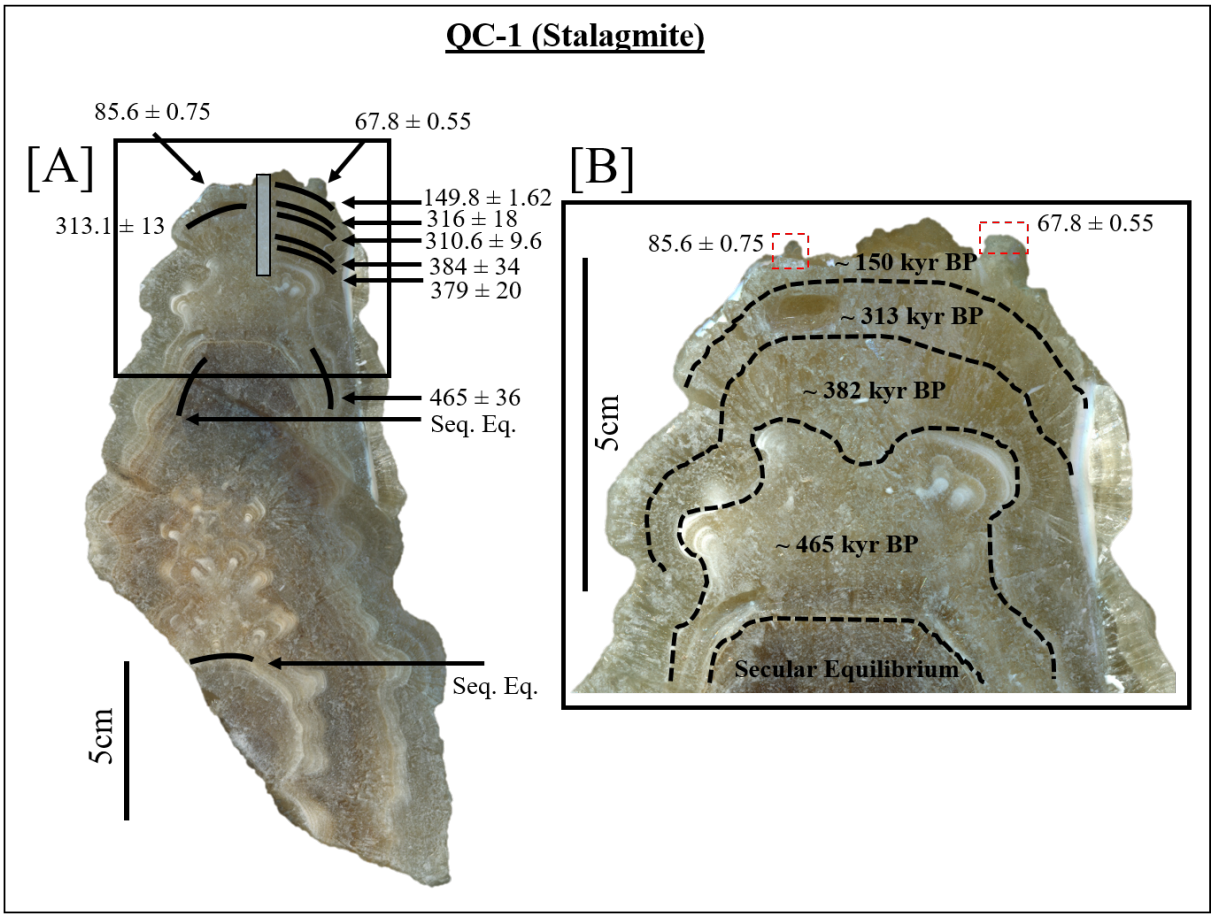

[A]
BZ-F (Flowstone)
505 ± 75
5cm
468 ± 46
500 ± 72
[B]
BZ-1A
BZ-1B
5cm
[C]
BZ-1B (Stalagmite)
5.55 ± 0.29
6.46 ± 0.49
26.4 ± 0.93
60.4 ± 1.74
74.8 ± 1.34
75.1 ± 2.25
5cm
[D]
BZ-1A (Stalagmite)
10.78 ± 2.2 BZ1_12
5.39 ± 0.27
6.12 ± 0.65 BZ1_6
6.84 ± 1.86 BZ1_4
7.66 ± 0.59 BZ1_3
22.48 ± 2.97
18.50 ± 1.51
15.75 ± 0.92 BZ1_8
76.83 ± 1.69

5.2.2 Maqlae Cave

Maqlae Cave is located at 32.7°N, 0.7°W, at an altitude of 1180 masl. The cave is situated 350 km east of Ksar cave (Barrott, 2014) and 200 km west of Grar cave, found in a limestone quarry with near vertical dipping bedrock. Mean annual precipitation in Ain Sefra (an oasis city 20 km west of Maqlae cave) is 170mm/yr, although high-rainfall years can lead to annual precipitation exceeding 400mm and flash floods (Derdour et al., 2018). Speleothem deposition is extensive throughout the cave. Further descriptions of the cave setting are found in Chapter 2 of this thesis.

Samples collected included QC-1 and QC-S (Figure 5.4), of which QC-1 is a stalagmite and QC-S is a small stalactite. Samples consist of clean high-density calcite with numerous changes in colouration.

Figure 5.4: **Maqlae Cave Speleothem Scans and U-Th Ages.** High-resolution scans of the two speleothem samples discussed from Maqlae Cave. Note the varying distance scales between scans. [A] Scan of the entire QC-1 stalagmite sample. [B] Zoomed in scan of the top of QC-1, as per the box in sub-plot A. Suggested hiatus lines are drawn as dashed black lines and the average age for intermediate growth between lines is annotated. Red dashed squares at the top of the scan denote the nodules from which the top two ages are taken. [C] Scan of the entire QC-S stalactite sample. [D] Zoomed in scan of the bottom of QC-S, as per the box in sub-plot C. The arrow indicates increasing ages towards the centre of the sample. On each scan, positions of U-Th trenches, annotated along with U-Th ages (expressed in kyr BP), are annotated. The location of the stable isotope trench for QC-1 is marked as a pale blue rectangle down the central growth axes of the samples. Faint lines can be seen within the calcite of both samples.


QC-1 (Stalagmite)
[A]
85.6 ± 0.75
67.8 ± 0.55
313.1 ± 13
149.8 ± 1.62
316 ± 18
310.6 ± 9.6
384 ± 34
379 ± 20
465 ± 36
Seq. Eq.
Seq. Eq.
5cm
[B]
85.6 ± 0.75
67.8 ± 0.55
~ 150 kyr BP
~ 313 kyr BP
~ 382 kyr BP
~ 465 kyr BP
Secular Equilibrium
5cm
QC-S (Stalactite)
[C]
436 ± 36
Seq. Eq.
312 ± 18
155 ± 1.9
145 ± 1.6
227 ± 3.3
5cm
[D]
Increasing age
1cm

5.2.3 Other caves

Other caves not visited within the remit of this study, but of significance to the interpretations of U-Th and stable isotope records presented here, include Ksar cave (stalagmite MM), Asdif cave (stalagmite ASD-1) and Kef Thaleb cave (stalagmite KFT-1) from the High- and Anti-Atlas mountains of Morocco (Barrott, 2014). Of direct comparability, stalagmite MM from Ksar cave (Barrott, 2014) is located ∼350km west of Maqlae cave, also in a presently arid region (< 150mm/yr rainfall; Chapter 4) with no contemporary speleothem formation, and exhibits numerous periods of U-Th chronology during the past 400 kyrs.

The only other stalagmite record from Algeria found along the northern Mediterranean coastline of North Africa (Figure 5.2) is Gueldaman cave (Ruan et al., 2016). However, this site is considerably further north of the Atlas Mountains and has contemporary speleothem growth caused by rainfall that is likely from Mediterranean sources (Ruan et al., 2016). Furthermore, two coeval mid-Holocene stalagmite $\delta^{18}O$ records from the cave are not reproducible and are suggested to be impacted upon by evaporation and disequilibrium processes. Therefore, this site is not well suited for comparison to SOA speleothem records or for understanding significant changes in past rainfall amount.

5.3 Methods

5.3.1 XRD

Aliquots of milled carbonate powders of ∼0.25 mg were analysed at the University of Oxford using the method described in detail in Day et al. (2021), summarised in Chapter 3 of this thesis.

5.3.2 U-Th Dating

Samples were sliced in half in-house using a water-cooled band saw and placed in an oven at 20°C for 24 hours prior to sub-sampling to allow evaporation of H_2O from the sample surface. Stalagmite QC-1 was slabbed to facilitate attachment to a micro-mill prior to sub-sampling. Samples for U-Th chronology were hand-drilled for QC-S and initial QC-1 ages, whilst a New Wave MicroMill was used to mill the U-Th samples from stalagmites BZ-1A and BZ-1B, as well as subsequent QC-1 ages. Powdered carbonate samples were dissolved in $\mathbf{\Delta}HNO_3$ and spiked with a mixed $^{229}Th-^{236}U$ spike (Robinson et al., 2004; Mason and Henderson, 2010), and the U and Th fractions were separated following chemical procedures adapted from Edwards et al. (1987) (further described in Chapter 3 of this thesis). A $^{230}Th/^{232}Th$ ratio of 5.38 ppm + 5.38 ppm / - 4.84 ppm (Wang et al., 2019) was used to correct Maqlae cave samples for detrital Th contamination, and 11.8 ± 4.6 ppm for Grar cave, chosen via the method described below.

Initial thorium correction for Grar cave samples

Applying a bulk earth initial $^{230}Th/^{232}Th$ ratio of 5.38 ppm + 5.38 ppm / - 4.84 ppm (Wang et al., 2019) to correct Grar cave ages for detrital thorium contamination resulted in a number of age inversions in sample BZ-1A, for which there is significant ^{232}Th contamination in several sub-samples. Sub-samples BZ1_3 (depth = 45 mm), BZ1_4 (depth = 30.5 mm) and BZ1_6 (depth = 6.5 mm) (Figure 5.3) exhibit an age inversion not within analytical uncertainty, where BZ1_4 is calculated to be older than BZ1_3 despite being closer to the top of the stalagmite (Table 5.1). This is as a result of higher ^{232}Th concentrations in BZ1_4 (4.1 ppb) compared to BZ1_3 (1 ppb) and BZ1_6 (1.3 ppb) which results in a larger allochthonous ^{230}Th addition to the sample during correction. This is in opposition to the fundamental requirement of stalagmite growth that, under closed-system conditions, formation must be from older to younger up the sample.

Low ^{238}U concentrations and small sample sizes in BZ-1A made it unfeasible to generate an isochron age to determine initial ^{230}Th/^{232}Th (Fairchild and Baker 2012; Carolin et al., 2016). Therefore, to get an a-priori constraint on initial thorium, a method was devised whereby a range of initial ^{230}Th/^{232}Th ratios were used to allow the age of BZ1-4 to vary within the maximum analytical uncertainties of the ages above and below it. The range of ages was calculated using the (^{234}U/^{238}U), (^{230}Th/^{238}U) and (^{232}Th/^{238}U) activity ratios of each sub-sample and decay equations presented in Chapter 3. A maximum and minimum ^{230}Th/^{232}Th ratio which subsequently allows BZ1_4 to vary within analytical uncertainty of BZ1_6 and BZ1_3 is calculated as 16.4 and 7.2 ppm. Resultantly, a mean^{230}Th/^{232}Th ratio and range of 11.8 ± 4.6 ppm is calculated; a uniform distribution was used between these bounds. This is within error of the range applied to Maqlae cave samples (Wang et al., 2019), and of other bulk earth estimates of ^{230}Th/^{232}Th (Kaufman and Broecker, 1965; Wedepohl, 1995). All ages from Grar cave were corrected using this ^{230}Th/^{232}Th initial ratio for consistency, with uncertainty applied to the final age.

Sub-samples with ^{232}Th concentrations > 5 ppb still gave erroneous chronology and were subsequently removed from chronological interpretations due to being too 'dirty' (marked in red in Table 5.1). These ages occurred after or near hiatuses and so may have had Th incorporated with anomalous^{230}Th/^{232}Th ratios, such as via Saharan dust, soil or bat guano.

5.3.3 Stable isotope analysis

A trench was milled from stalagmites BZ-1A, BZ-1B and QC-1 using a NewWave Micro-mill to a depth of 500 μm in each sample. Each stable isotope sample was then produced by extending this trench by 300 μm, 500 μm and 100 μm for samples BZ-1A, BZ-1B and QC-1 respectively to produce continuous sampling along the growth axis (Figure 5.3 and 5.4). In the top section of BZ-1B, a second stable isotope trench was milled to corroborate with the original trench record due to uncertainty over the location of the

growth axis (Figure 5.3). For all samples, 50-80 μg of carbonate powder was analysed for oxygen and carbon stable isotopes using a Thermo Scientific Delta V IRMS fitted with a GasBench II peripheral (further described in Chapter 3).

Accuracy and precision were checked using an in-house secondary standard's long-term average, NOCZ, included in all runs. Long-term δ^{13}C and δ^{18}O measurements of NOCZ averages 2.19‰ ± 0.05‰ and -1.9‰ ± 0.07 ‰. NOCZ measurements within BZ-1A and QC-1 stable isotope runs averaged δ^{18}O of -1.93‰ ± 0.07‰ and δ^{13}C of 2.16‰ ± 0.04‰ (1σ, n=23), within the long-term NOCZ values. Two anomalous measurements during the stable isotope analysis of BZ-1B gave a higher standard deviation for δ^{18}O of 0.27‰ (1σ, n=14), although absolute values are still correct and this slightly lower precision does not inhibit general interpretations.

5.4 Results

5.4.1 XRD

XRD analysis revealed all samples to be calcite in mineralogy (Appendix IV Figure 16).

5.4.2 U-Th Chronology

U-Th data and corrected ages are presented in Tables 5.1 and 5.2. All ages are expressed relative to the year 1950 CE (i.e. years before present (BP)). High ^{232}Th concentrations in Grar cave speleothems result in significant corrections in some cases, and the most precise ages were obtained from stalagmite QC-1 due to low ^{232}Th concentrations.

Chronology

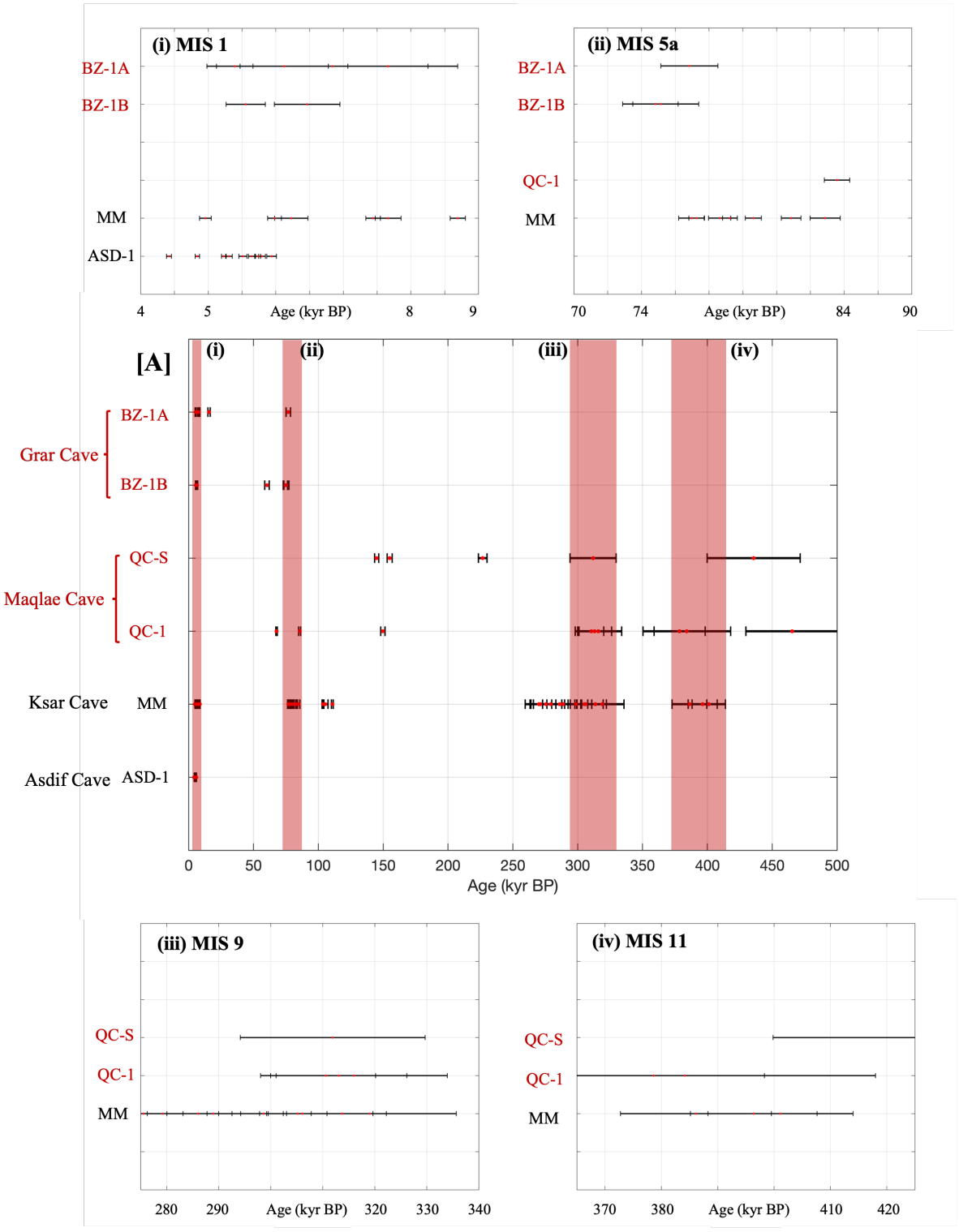
Corrected U-Th ages of the calcite collected from Grar cave (samples BZ-1A, BZ-1B and BZ-F) largely fall in two distinct periods; MIS 1 and MIS 5a (Figure 5.3; Table 5.1), correlating with growth periods observed in MM and ASD-1 (Figure 5.5; Barrott, 2014).

Sample BZ-1A is 150 mm in length. Between 45 mm and 4 mm from the top of BZ-1A, ages range between 7.7 ± 0.6 kyr BP and 5.4 ± 0.3 kyr BP (Figure 5.3), identifying a significant period of mid-Holocene growth coinciding with the African Humid Period (AHP). Sub-sample BZ1_12 was sampled from the very top of the stalagmite and produced an out of sequence age of 10.8 ± 2.2 kyr BP (Table 5.1). Whilst sub-sample BZ1_8 has <5 ppb ^{232}Th and corrects to within stratigraphic order, erroneous ages above this sub-sample means that robust interpolation between this age and mid-Holocene growth isn't possible without further chronology. Therefore, the Holocene growth of BZ-1A and subsequent stable isotope record can only be robustly interpreted until the well constrained age of 7.7 ± 0.6 kyr BP (BZ1_3), although earlier Holocene, and potentially older, growth is likely.

Sample BZ-1B is 90 mm in length. Between 51 and 15 mm from the top of BZ-1B, ages range between 75 ± 2.1 kyr and 60 ± 1.6 kyr BP, although more U-Th chronology is required to confirm how continuous growth is after 74 kyr BP (21.5 mm depth), with a considerably higher extension rate between sub-samples BZ2_2 and BZ2_4 than BZ2_4 and BZ2_1. There is no clear evidence for a hiatus at this time, however. Two ages at the top of the sample of 6.5 ± 0.5 kyr BP and 5.6 ± 0.3 kyr BP indicate a small section of mid-Holocene growth.

Three ages from the top piece of flowstone BZ-F are 468 ± 46, 500 ±72 and 505 ±75 kyr BP.

Figure 5.5: **South of Atlas Speleothems U-Th Ages.** U-Th results of samples presented in this study, and those presented in Barrott (2014). [A] Centre: U-Th results from all samples across the past 500 kyrs. From top to bottom, samples plotted are from Grar, Maqlae, Ksar and Asdif caves. Stalagmites annotated in black, MM and ASD-1, are from Ksar and Asdif cave respectively (Figure 5.2) (Barrott, 2014); these samples were not collected as part of this study but are directly comparable. Stalagmites labelled in dark red are those first presented in this study. Red shaded vertical bars labelled (i) to (iv) denote periods of time within analytical uncertainty that speleothem formation is occurring coevally in at least 2 caves. Plots (i) to (iv) subsequently illustrate these highlighted periods in more detail, with only samples that are growing during them annotated on the y-axis. The associated marine isotope stage (MIS) which each of these periods is also noted.


(i) MIS 1
BZ-1A
BZ-1B
MM
ASD-1
4
5
Age (kyr BP)
8
9
(ii) MIS 5a
BZ-1A
BZ-1B
QC-1
MM
70
74
Age (kyr BP)
84
90
[A]
(i)
(ii)
(iii)
(iv)
Grar Cave
BZ-1A
BZ-1B
Maqlae Cave
QC-S
QC-1
Ksar Cave
MM
Asdif Cave
ASD-1
0
50
100
150
200
250
300
350
400
450
500
Age (kyr BP)
(iii) MIS 9
QC-S
QC-1
MM
280
290
Age (kyr BP)
320
330
340
(iv) MIS 11
QC-S
QC-1
MM
370
380
Age (kyr BP)
410
420

Corrected ages from Maqlae cave range between 465 ± 36 kyr BP and 68 ± 0.5, with five further ages in secular equilibrium (Figure 5.4; Table 5.2). There is robust evidence for speleothem growth during MIS 5a, MIS 9 and MIS 11, all correlating with growth periods observed in MM from Ksar cave (Figure 5.5; Barrott, 2014).

Ages from stalactite QC-S confirm periods of speleothem growth in Maqlae cave as suggested by stalagmite QC-1. Three ages milled from the outer edge of the sample to the centre produced chronological ages; 145 ± 1.6, 155 ± 1.9 and 311 ± 18 kyr BP, all of which are coeval with QC-1 ages. Therefore, in addition to MIS 5a, 9 and 11, speleothems from Maqlae cave also provide robust evidence for rainfall during MIS 6, with three reproducible ages centred around 150 kyr BP.

U-Th chronology from samples presented here, combined with records from Morocco (Barrott, 2014), now provides robust evidence for at least four periods of increased rainfall which are reproduced across numerous sites in the SOA (Figure 5.5); 401-379 kyr BP (Marine Isotope Stage (MIS) 11), 316-310 kyr BP (MIS 9), 85-74 kyr BP (MIS 5a) and 8-5 kyr BP (MIS 1).

Further chronology suggests the possibility for increased rainfall during MIS 6 (155-145 kyr BP), although this is only represented at Maqlae cave and so is less robust as a regionally extensive period of rainfall. Two further periods of MM formation between 119-110 kyr BP (MIS 5c-5d) and 250 kyr BP (MIS 8) are also only observed at Ksar cave, and not in the Saharan- or Anti-Atlas.

U-Th ages at 16 kyr BP (MIS 2), ∼65 kyr BP (MIS 4), 226 kyr BP (MIS 7), 247 kyr BP (MIS7/8) and between 465-500 kyr BP (MIS 12/13) are individual ages which are not reproduced either within or between caves, thus not considered robust enough for interpretations.

Distance (mm)	Sample ID	238 (ppb)	232 (ppb)	(230/238)	2s error	(234/238)	2s error	(232/238)	2s error	Uncorr Age (kyr BP)	Corrected Age (kyr BP)	2s error (kyr BP)
BZ-1A												
1.5	BZ1_12	85	7.4	0.1717	0.0036	1.2084	0.0142	2.8E-02	2.8E-04	16.64	10.78	2.2
4.0	BZ_1_A	99	0.7	0.0641	0.0020	1.2101	0.0071	2.3E-03	2.3E-05	5.93	5.39	0.3
6.5	BZ1_6	77	1.3	0.0775	0.0046	1.1996	0.0138	5.4E-03	1.6E-04	7.27	6.12	0.7
30.5	BZ1_4	56	4.1	0.1242	0.0031	1.2099	0.0103	2.4E-02	1.8E-04	11.77	6.84	1.9
45.0	BZ1_3	60	1.0	0.0949	0.0038	1.2132	0.0110	5.7E-03	9.3E-05	8.86	7.66	0.6
63.5	BZ1_9	163	18.9	0.2945	0.0033	1.2072	0.0135	3.8E-02	3.5E-04	30.24	22.48	3.0
66.0	BZ1_2	104	6.2	0.2250	0.0029	1.2032	0.0106	1.9E-02	1.4E-04	22.44	18.50	1.5
67.5	BZ1_8	103	3.5	0.1841	0.0031	1.2009	0.0141	1.1E-02	1.4E-04	18.07	15.75	0.9
81.0	BZ1_7	54	1.45	0.6245	0.0074	1.1948	0.0148	8.9E-03	1.5E-04	78.65	76.83	1.7
BZ-1B												
2.0	BZ_1_B	80	0.6	0.0664	0.0023	1.2188	0.0070	2.4E-03	2.3E-05	6.10	5.55	0.3
3.0	BZ2_8	74	1.3	0.0833	0.0023	1.2283	0.0189	5.6E-03	8.8E-05	7.64	6.46	0.5
7.5	BZ2_3	170	5.2	0.2849	0.0044	1.2334	0.0113	1.0E-02	1.1E-04	28.40	26.38	0.9
15.0	BZ2_1	78	3.9	0.5443	0.0068	1.2129	0.0077	1.6E-02	1.1E-04	63.66	60.44	1.7
21.5	BZ2_4	116	2.5	0.6049	0.0060	1.1834	0.0107	6.9E-03	9.3E-05	76.27	74.83	1.3
51.0	BZ2_2	53	1.5	0.6134	0.0111	1.1919	0.0135	9.1E-03	1.6E-04	76.98	75.14	2.3
BZF												
1.0	BZF_A	391	1.3	1.0130	0.0049	1.0167	0.0039	1.1E-03	8.7E-06	505.87	505.64	75
25.0	BZF_B	1160	0.1	1.0141	0.0045	1.0205	0.0036	3.7E-05	9.9E-07	468.37	468.36	45.6
50.0	BZF_C	263	0.03	0.9967	0.0043	1.0053	0.0040	3.3E-05	4.6E-06	500.05	500.05	72.1

Table 5.1: **Grar Cave U-Th Results.** U-Th results from Grar cave speleothems. Sub-samples which have ^{232}Th concentrations $>$ 5 ppm are marked in red. Ages are corrected for initial thorium using 230/232 atomic ratios cited in the text.

Distance (mm)	Sample ID	238 (ppb)	232 (ppb)	(230/238)	2s error	(234/238)	2s error	(232/238)	2s error	Uncorr. Age (kyr BP)	Corrected Age (kyr BP)	2s error
QC-1												
Top	QC1_H	146	0.24	0.6337	0.0031	1.3366	0.0057	5.4E-04	2.0E-05	67.89	67.8	0.6
Top	QC1_E	116	0.32	0.7525	0.0039	1.3432	0.0058	9.1E-04	2.1E-05	85.72	85.6	0.8
2.0	QC1A	136	0.10	1.0196	0.0040	1.3074	0.0055	2.5E-04	1.4E-05	149.88	149.8	1.6
6.5	QC1_G	55	0.03	1.1929	0.0109	1.1986	0.0137	1.6E-04	7.3E-05	316.08	316	18
8.0	QC_1_2020T	67	0.03	1.2066	0.0086	1.2113	0.0075	1.3E-04	1.8E-05	313.15	313	13.1
10.0	QC1B	77	0.02	1.2221	0.0058	1.2253	0.0053	8.8E-05	2.8E-05	310.67	310.6	9.6
15.0	QC1_F	44	0.02	1.1710	0.0109	1.1521	0.0134	1.5E-04	7.2E-05	384.23	384.2	33.8
21.0	QC1C	45	0.02	1.1707	0.0061	1.1537	0.0056	1.5E-04	4.2E-05	378.70	378.6	19.7
29.0	QC1_D	133	0.04	1.1446	0.0042	1.1160	0.0049	9.8E-05	1.9E-05	465.43	465.4	35.6
55.0	QC_1_2020M	81	0.03	1.1231	0.0081	1.0777	0.0087	1.2E-04	3.0E-05	Sec. Eq.	Sec. Eq.	Sec. Eq.
160.0	QC_1_2020B	67	0.09	1.0164	0.0071	1.0147	0.0055	4.4E-04	1.3E-05	Sec. Eq.	Sec. Eq.	Sec. Eq.
QC-S												
Bottom	QC_S	152	0.17	1.1408	0.0039	1.2416	0.0043	3.5E-04	7.7E-06	226.86	226.8	3.3
Top	QC_S2	101	0.24	1.0033	0.0042	1.0162	0.0043	7.8E-04	7.8E-06	435.85	435.8	35.6
Outer	QCS_A	222	0.15	0.9923	0.0045	1.2956	0.0057	2.2E-04	1.7E-05	145.05	145	1.6
Inner 1	QCS_B	164	0.53	1.0493	0.0054	1.3205	0.0060	1.0E-03	3.3E-05	155.24	155.2	1.9
Inner 2	QCS_C	95	0.10	1.0985	0.0104	1.1252	0.0125	3.5E-04	6.4E-05	312.01	312	17.8
Inner 3	QCS_D	68	0.09	1.0294	0.0100	1.0240	0.0119	4.5E-04	8.8E-05	Sec. Eq.	Sec. Eq.	Sec. Eq.

Table 5.2: **Maqlae Cave U-Th Results.** U-Th results from Maqlae cave speleothems. A $^{230}Th/^{232}Th$ ratio of 5.38 ppm + 5.38 ppm / - 4.84 ppm (Wang et al., 2019) was used to correct ages for detrital thorium.

5.4.3 OxCal Age Model

An OxCal (version 4.3) age model (Bronk Ramsey, 2008; Bronk Ramsey, 2009; Bronk Ramsey and Lee, 2013) is presented for the Holocene section of BZ-1A (Figure 5.6). The mean age model and 68% and 95% confidence ranges were produced using the P-Sequence Poisson-process deposition model [k0 = 1 cm−1, log10(k/k0) = U(−2,2)] (Bronk Ramsey and Lee, 2013). The sample was only modelled down to sub-sample BZ1_3 (7.66 kyr BP), below which interpolation cannot be robustly undertaken. Individual ages and 95% confidence intervals are also modelled for each depth gradation down the stalagmite, each corresponding to a stable isotope data point. An age model was not generated for sample QC-1 due to significantly smaller periods of growth between its hiatus lines, or BZ-1B due to a low density of U-Th ages completed on the sample.

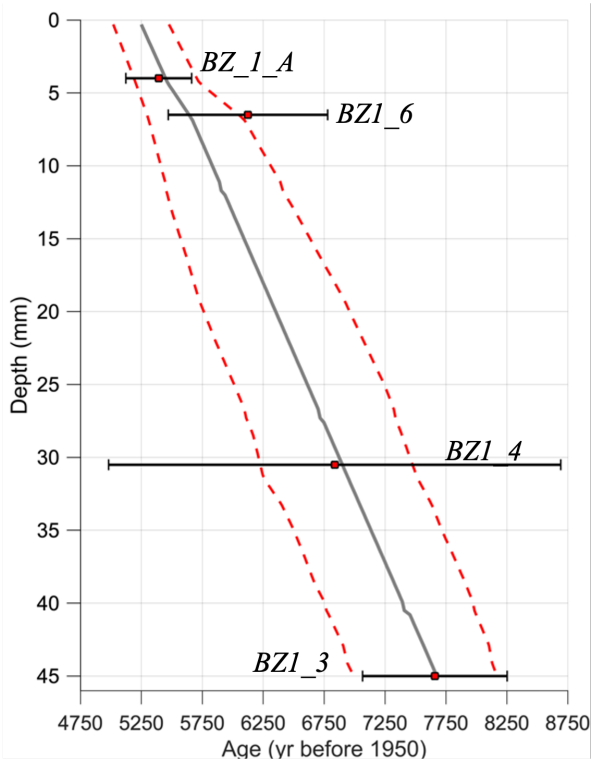


Figure 5.6: **BZ-1A OxCal Age Model**. OxCal age model of the Holocene section of BZ-1A. The mean (black line) and 95% confidence limits (dashed red line) are plotted, along with the 4 calculated ages from sub-samples and associated uncertainty. Higher ^{232}Th concentration associated with sub-sample BZ1_4 results in the larger associated uncertainty after the initial Th correction. The age model is extrapolated to 0mm depth (top of the stalagmite) to allow for temporal association of stable isotope measurements.

5.4.4 High-resolution stable isotope records

The stable isotope records of stalagmites BZ-1A, BZ-1B and QC-1 are plotted against distance from the top of the stalagmite, defined as 'depth' (Figure 5.7). Stalagmite BZ-1A has average δ^{13}C and δ^{18}O values of -5.9 ‰ and -6.9 ‰, respectively, compared to slightly higher values of -4.7 ‰ and -6.5 ‰ in BZ-1B. In both cases, there are large shifts in isotope values, up to 10 ‰ in δ^{13}C and 4 ‰ in δ^{18}O. A correlation between δ^{13}C and δ^{18}O in BZ-1A (r^2 = 0.64) is largely controlled by the top 30 mm of the sample, in which both δ^{13}C and δ^{18}O shift to significantly higher values (Figure 5.7).

The overall range of δ^{13}C and δ^{18}O is much smaller for QC-1. δ^{13}C and δ^{18}O average -8.7 ‰ and -9.3 ‰ respectively, fluctuating by up to 4 ‰ in both cases. For the top 200 mm of the sample, the correlation coefficient between δ^{13}C and δ^{18}O is 0.75. For the bottom 100 mm of the sample, δ^{13}C and δ^{18}O have a correlation coefficient of 0.33. Abrupt changes in stable isotopes align with possible hiatus events in the sample growth history, as annotated (Figure 5.7). Two periods of low variability form two isotope 'plateaus', centred around 75- and 175-mm depth. These plateaus coincide with MIS 9 and MIS 11 respectively, with δ^{18}O approximately 1 ‰ lower during the latter period (Figure 5.7).

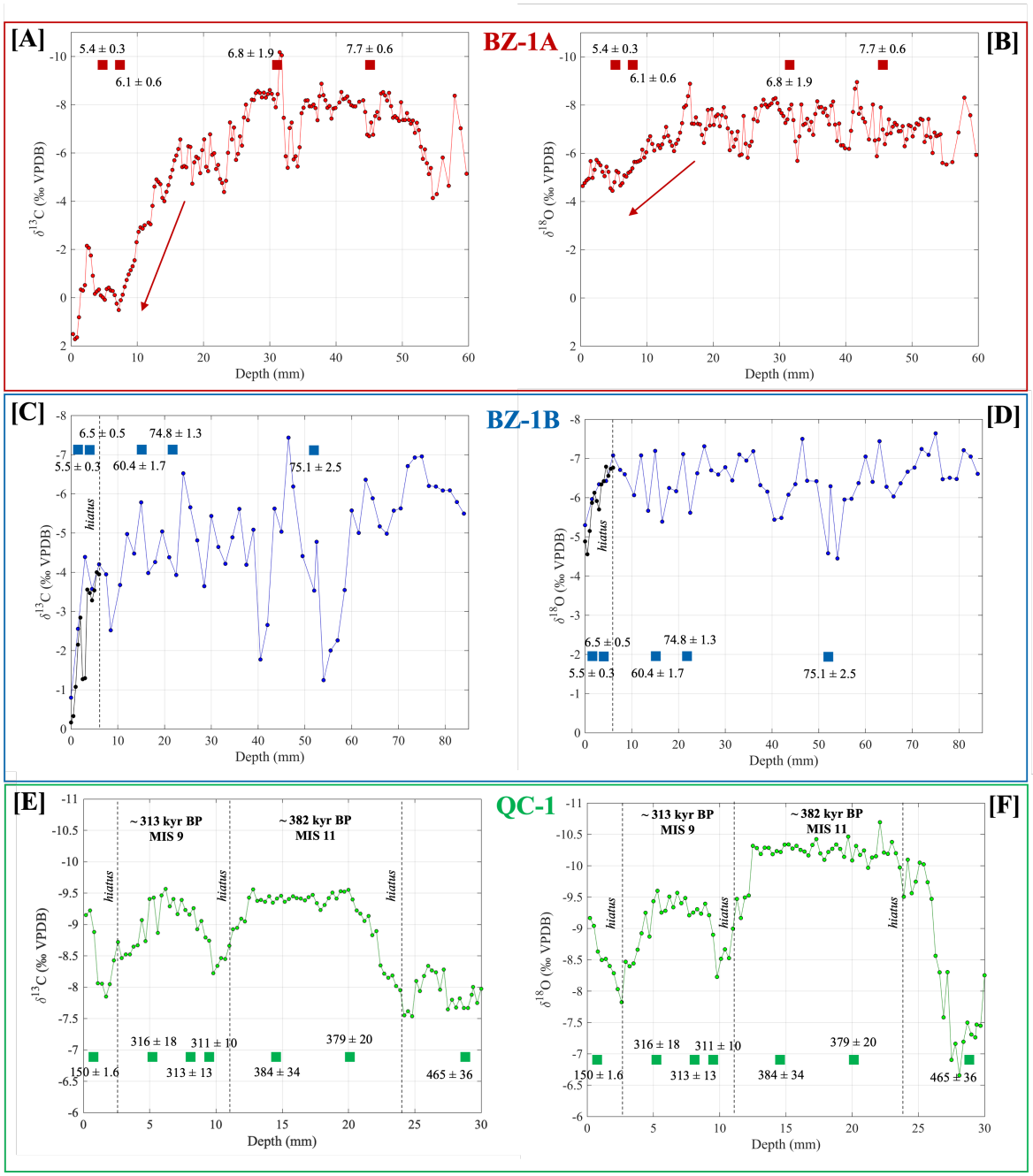


Figure 5.7: **Ksour Stalagmite Stable Isotope Records**. Stable isotope records for all Ksour speleothems sampled at high-resolution. Within individual stalagmite records, the y-axis are to the same scale and all are plotted against distance from the top of the stalagmite (depth). Annotated are the location (depth from top of stalagmite) and resultant ages from U-Th trenches. Ages are reported in kyr BP. Plots [A] and [B] are BZ-1A (red) δ^{13}C and δ^{18}O respectively. The arrow illustrates a trends towards heavier isotope values in the top 20mm of the sample. Plots [C] and [D] are BZ-1B (blue) δ^{13}C and δ^{18}O respectively. A second, offset, stable isotope trench at the top of BZ-1B agrees closely with original data, plotted in black. The dashed black line represents a hiatus lamina observed on the sample. Plots [E] and [F] are QC-1 (green) δ^{13}C and δ^{18}O respectively. Proposed hiatus lines on QC-1 are drawn with dashed black lines and correspond with shifts in stable isotope values.

5.5 Discussion

5.5.1 Timing of SOA rainfall throughout the past 450 kyrs

The most robust and reproducible periods of speleothem formation across SOA cave sites, inferring increased rainfall, all occur during northern hemisphere interglacials and interstadials (Lisiecki and Raymo, 2005, Figure 5.8), in agreement with the timings of other proxy records (Tierney et al., 2017a; Pausata et al., 2017; Sha et al., 2019; Drake et al., 2022). Periods of growth during MIS 1, 5a, 9 and 11 are observed across numerous cave sites in the SOA region, with MIS 1 and 5a being the best represented periods, both observed in 3 caves to date (Figure 5.5). It is important to note that a lack of speleothem growth does not necessarily indicate arid conditions, as there are numerous reasons as to why a stalagmite may cease formation (Fairchild and Baker 2012). Instead, the occurrence of speleothem growth *does* robustly indicate conditions of sufficient rainfall, without which it would not occur. Whilst MIS 1, MIS 9 and MIS 11 are all known periods of increased moisture availability in the Sahara (Geyh and Thiedig, 2008; Tierney et al., 2017b; Drake et al., 2022), evidence for SOA rainfall is a significant step forwards in providing the first indications as to *where* rainfall occurred, likely replenishing groundwater and supplying central Sahara lakes via the major southwards-flowing rivers evident from the Ksour Mountains (Figure 5.2).

Robust observations of SOA speleothem formation occurring across 3 caves during interstadial MIS 5a (Schellmann et al., 2004), and a lack of SOA speleothem growth during either interglacial maxima MIS 5e or MIS 7 (Figure 5.8), challenges the paradigm that Saharan rainfall increases are regionally occurring during each interglacial maxima (Larrasoaña et al., 2003), agreeing with recent observations (Skonieczny et al., 2019). MIS 5e, the Eemian, is suggested to have had a warmer northern hemisphere than MIS 1, the Holocene (Turner, 2000; Nicholson et al., 2022; Larrasoaña et al., 2013, Nicholson et al., 2022), and MIS 7 has lower benthic foraminifera δ^{18}O than MIS 5a (during which SOA speleothem growth *is* observed), suggestive of a warmer northern

hemisphere at this time. Both MIS 5e and MIS 7 are well-represented in Saharan paleoclimate records and modelling studies (Osborne et al., 2008; Geyh and Thiedig, 2008; Herold and Lohmann, 2009; Caley et al., 2011; Ehrmann et al., 2017; Henselowsky et al., 2021) and speleothem growth in eastern North Africa has supported the notion of increased WAM rainfall at these times (El-Shenawy et al., 2018). In fact, a greater increase in river discharge (Trauth et al., 2021) and reduction in dust export (Skonieczny et al., 2019) is observed during MIS 5e and MIS 7 than during MIS 1 (and 9 or 11 in the case of river discharge recorded in ODP 967), during which SOA speleothem formation *is* observed (Figure 5.8).

Therefore, although a lack of speleothem growth does not necessarily indicate arid conditions, the complete lack of robust evidence for speleothem formation during MIS 5e and MIS 7 across all cave sites is notable, inferring an absence of sufficiently increased effective precipitation in the SOA during these periods. MIS 5e and MIS 7 both coincide with the highest eccentricity and precession amplitude of the last 500 kyrs (Figure 5.8) and so it may be that there is a threshold of one of these parameters above which there is still a strengthening of the WAM causing rainfall at lower latitudes, but not a more northwards mean ITCZ position, and the moisture transport processes which brings rainfall to the SOA does not occur (Singarayer and Burrough, 2015).

Growth in Northern Oman and Egyptian speleothems (Fleitmann et al., 2003; El-Shenawy et al., 2018) during MIS 5e and MIS 7 (Figure 5.8) further support this, exhibiting that mechanisms of monsoonal maxima, which are suggested to lead to increased rainfall in Oman and eastern North Africa, are not the dominant control for SOA rainfall. Furthermore, a notable lack of stalagmite growth in eastern North Africa (28°N) during MIS 1 (the African Humid Period; El-Shenawy et al., 2018) compared to growth in three caves in the SOA, also supports the notion that the WAM is not regionally reaching sub-tropical latitudes at this time and that SOA rainfall is occurring instead due to TPs (Chapter 4).

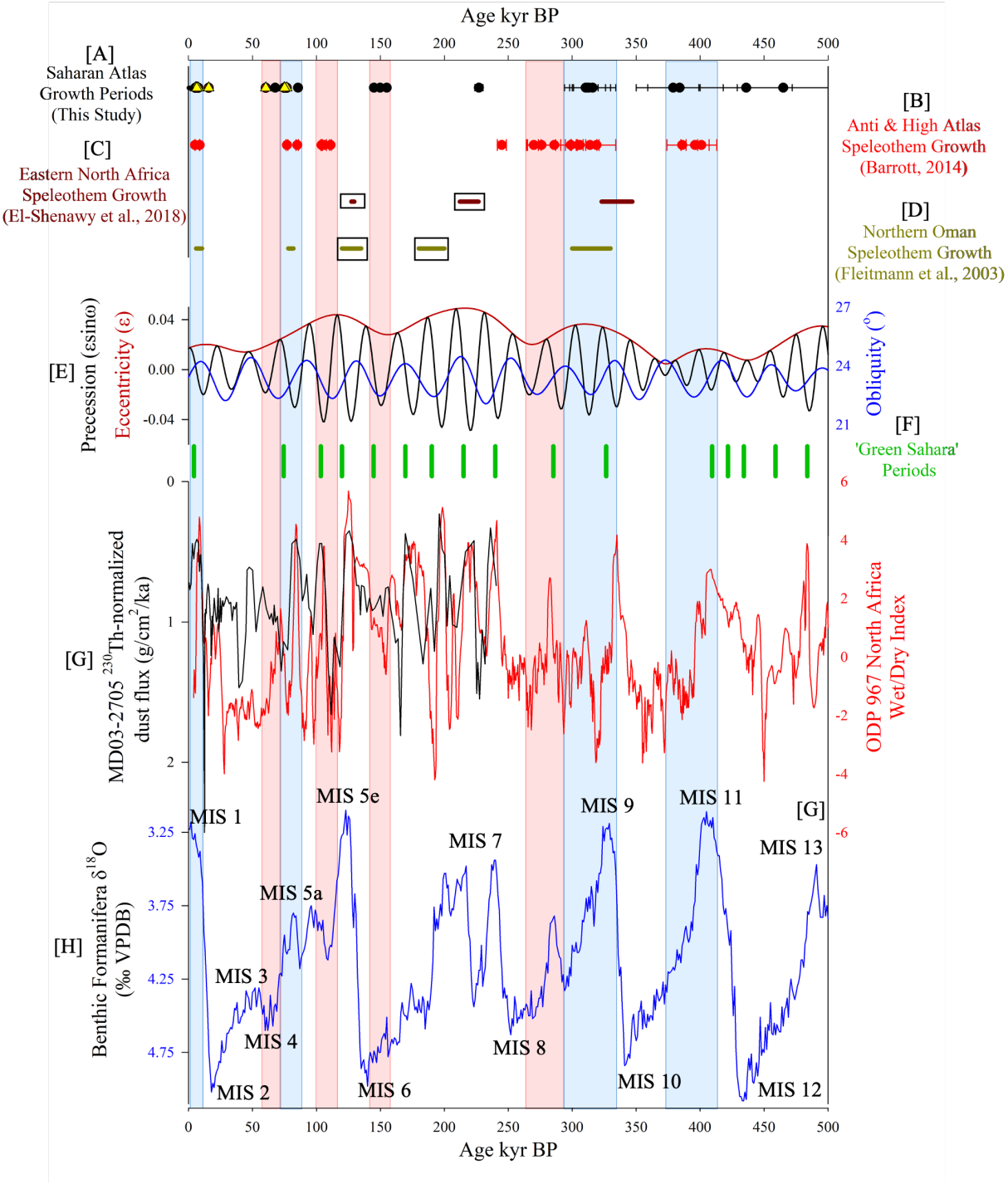

Age kyr BP
[A]
Saharan Atlas
Growth Periods
(This Study)
[B]
Anti & High Atlas
Speleothem Growth
(Barrott, 2014)
[C]
Eastern North Africa
Speleothem Growth
(El-Shenawy et al., 2018)
[D]
Northern Oman
Speleothem Growth
(Fleitmann et al., 2003)
[E]
Precession (εsinω)
Eccentricity (ε)
Obliquity (°)
[F]
'Green Sahara'
Periods
[G]
MD03-2705 230Th-normalized
dust flux (g/cm2/ka)
ODP 967 North Africa
Wet/Dry Index
[H]
Benthic Formanifera δ18O
(‰ VPDB)
MIS 1
MIS 2
MIS 3
MIS 4
MIS 5a
MIS 5e
MIS 6
MIS 7
MIS 8
MIS 9
MIS 10
MIS 11
MIS 12
MIS 13
[G]
Age kyr BP

Figure 5.8: **Paleoclimate Stack Plot**. Stack plot of major indicators of North Africa humidity and data presented in this study. Blue shaded areas represent the most robust periods of increased SOA rainfall, with evidence for speleothem growth across numerous cave sites. Red shaded areas represent periods of more than one U-Th age, but from single caves (periods not reproduced across numerous caves). From top to bottom: [A] Black (yellow) markers and uncertainties are U-Th data from Maqlae (Grar) caves, collectively identified as 'Saharan Atlas' growth periods. [B] Red markers and uncertainties are U-Th data from Asdif, Ksar and Kef Thaleb caves, in the Anti- and High-Atlas (Barrott, 2014). [C] Stalagmite growth periods in eastern North Africa (El-Shenawy et al., 2018). There is no evidence for growth during MIS 1 whereas growth during MIS 5e and MIS 7 (highlighted by a box) is not replicated in SOA speleothems [D] Stalagmite growth periods in Northern Oman (Fleitmann et al., 2003). Growth during MIS 5e and MIS 7 (highlighted by a box) is not replicated in SOA speleothems. [E] Orbital parameters (eccentricity (red), obliquity (blue), precession (black). [F] Green lines indicate 'Green Sahara' periods as identified by sapropel records (Larrasoaña et al., 2013). [G] Marine records of variations in dust export from core MD03-2705 (black line; Skonieczny et al., 2019) and the 'wet/dry index' as represented in sapropel ODP 967 (red line; Trauth et al., 2021), from the North Atlantic and Mediterranean respectively. There is good agreement as to when increased 'humidity' is occurring in both records between 50-250 kyr BP. [H] The blue curve is the global benthic plot (Lisiecki and Raymo, 2005) with lower values representing reduced ice cover associated with northern hemisphere interglacials and interstadials. Major Marine Isotope Stages (MIS) are annotated.

Sporadic glacial rainfall

Whilst SOA cave sites are largely protected from contemporary Atlantic and Mediterranean climate regimes by distance and topography (Figure 5.2), Sultan et al. (1997) suggested that the North Atlantic storm track strengthens and shifts southwards during northern hemisphere glacials (Abouelmagd et al., 2012), delivering winter rainfall from west to east across North Africa. Three U-Th ages are observed in Maqlae cave during MIS 6, between 155 and 145 kyr BP, coinciding with some of the coldest northern hemisphere conditions of the past 500 kyrs (Figure 5.8), suggesting the potential for increased rainfall in the SOA via these non-tropical mechanisms.

Maqlae cave has the least topography between itself and the Mediterranean Sea (Appendix IV Figure 17), potentially making the site more conducive to receiving increased winter rainfall during glacial periods. It is notable also that chronology during glacial sub-stages is not as reproducible across cave systems, appearing to be more sporadic in

nature, perhaps suggesting that whilst winter rainfall may have caused variable growth at some sites, increased rainfall was not as regional or significant as during interglacial or interstadials (Prell and Kutzbach, 1987; Blanchet et al., 2021).

Furthermore, north-west Africa is suggested to have been wetter during the Last Glacial Maximum (LGM), approximately 20 kyrs BP (Scheff et al., 2017; McGee, 2020), with increased topsoil moisture and more positive precipitation-evaporation in the sub-tropics. The lack of stalagmite growth at any site during this time supports the notion that generally not enough direct winter rainfall reaches the southern limits of the Atlas Mountains in the modern day or during past periods of strengthened westerlies, and that significant increases in winter rainfall would largely be limited to regions north of the Atlas Mountains.

Non-homogenous North African rainfall

The timing of SOA speleothem growth presented here highlights that 'Green Sahara' and 'wet/dry' interpretation of marine core and sapropel records, as well as general interpretations of lacustrine and speleothem records as being evidence for increased rainfall across the entire North African region, is too generalised. Whilst North Atlantic records of dust export (MD03-2705; Skonieczny et al., 2019) and Mediterranean sapropel records (ODP 967; Trauth et al., 2021; 5.1) agree well for large periods of the last 250 kyrs, and are valuable indicators of regional changes in North African humidity and dust export, there are numerous 'wet' periods defined in these proxies which are not represented in SOA stalagmite growth (Figure 5.8).

More direct, local proxy evidence of rainfall is required across key locations of North Africa to ascertain a true picture of when and where rainfall directly increased. Particularly valuable would be evidence for where rainfall occurred during MIS 5e and MIS 7, for which there is extensive evidence for North African humidity but no apparent rainfall in the SOA, inferring that groundwater was not being replenished in the Atlas Mountains and southward-flowing rivers were not active.

5.5.2 The African Humid Period

The mid-Holocene African Humid Period (AHP) is the most recent increase in regional North African rainfall, with vast evidence for wet conditions and increased habitability between ∼10 and ∼4 kyr BP (McGee et al., 2013; Manning and Timpson, 2014; Pausata et al., 2020). The importance of TPs in delivering moisture to the SOA region during the AHP was presented in Chapter 4, a process also occurring in the present day (Knippertz (2003); Figure 5.1). U-Th chronology and high-resolution stable isotope records from stalagmite BZ-1A further supports this interpretation in the SOA region.

BZ-1A grew continuously between at least 7.7 and 5.4 kyr BP (Figure 5.3; Table 5.1). This chronology agrees with the beginning of formation of speleothem samples further east in the SOA (Figure 5.2); MM (8.8 kyr BP), KFT-1 (7.2 kyr BP) and ASD-1 (6 kyr BP), suggesting a homogenous moisture source. Furthermore, cessation of BZ-1A growth occurs at 5.3 kyr BP, prior to the ending of stalagmites growth in MM (4°W, 4.8 kyr BP) and ASD-1 (7°W, 4.2 kyr BP), suggesting an east to west drying at the end of the AHP in the SOA.

The high-resolution δ^{18}O record of BZ-1A also supports a TP-source of rainfall during the AHP. There are similarities between the BZ-1A and MM δ^{18}O records (Figure 5.9), which is hypothesised to be supplied only by TP rainfall (Chapter 4). Both records exhibit a noisy δ^{18}O record with abrupt and short-lived changes, but with a flat longer term average and a trend to higher isotopic values at the end of growth. Absolute δ^{18}O values are ∼3‰ higher in BZ-1A, although the strong altitudinal control on δ^{18}O in the Atlas region (Ait Brahim et al., 2016) and large variation in δ^{18}O associated with TP events (Cappy, 2007) may contribute to this.

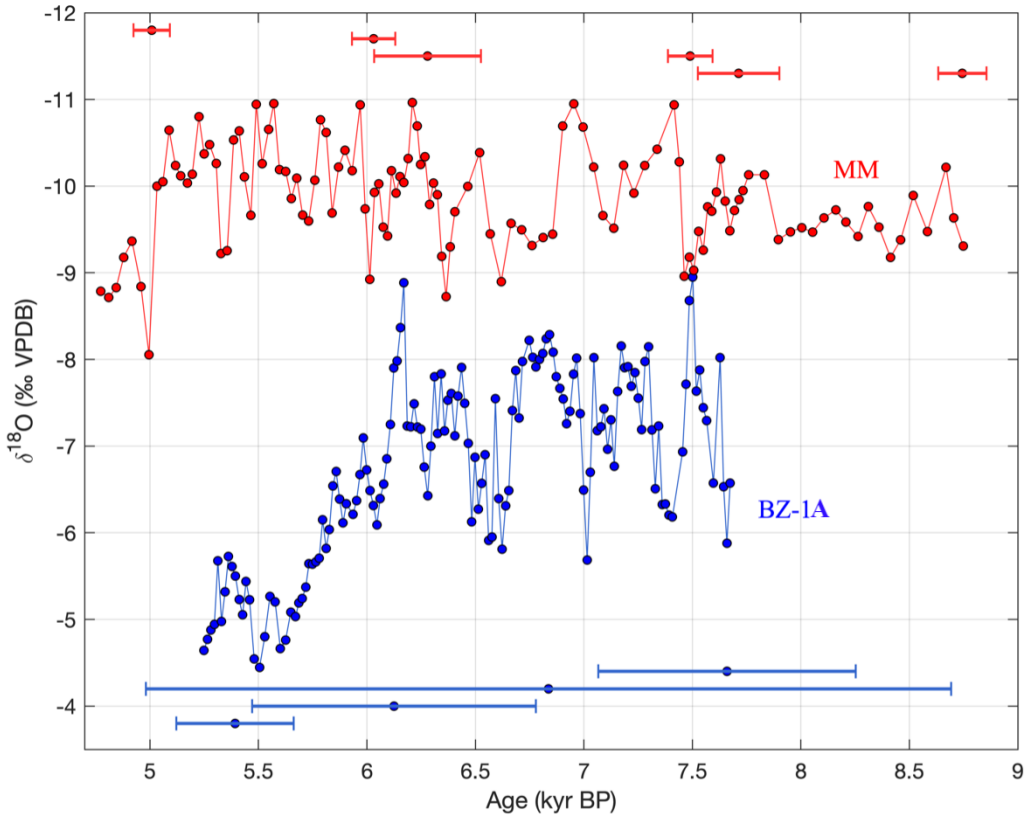


Figure 5.9: **MM vs BZ-1A δ^{18}O records**. MM (red) and BZ-1A (blue) δ^{18}O records. Ages and associated uncertainties are also plotted. Both records exhibit a largely untrended, flat record with large and sudden shifts. A shift to higher values in BZ-1A is more pronounced than in MM at the end of growth. The samples conceivably stop growing within uncertainty of one another, and further growth down BZ-1A which cannot yet be robustly interpolated may represent earlier growth, closer to the start of MM.

Furthermore, the δ^{13}C record of BZ-1A may provide indications into levels of rainfall and vegetation occurrence above Grar cave (Owen et al., 2018). BZ-1A being the furthest east and most northerly SOA sample growing during the AHP (Figure 5.2) makes it likely most sensitive to changes in moisture availability. A higher north-south temperature anomaly (Schneider et al., 2014), indicative of a more northerly mean ITCZ position, correlates with the lowest δ^{13}C values in BZ-1A at 7 kyr BP (Figure 5.10), which can be interpreted as indicating peak moisture availability (Fairchild and Baker 2012; Owen et al., 2018). These proxies also correlate with the lowest Anti-Atlas (ASD-1 and KFT-1 combined; Appendix III Figure 9) δ^{18}O values, indicative of the

highest proportion of TP rainfall in the SOA (Chapter 4). From 7 kyr BP, there is then a clear shift towards higher δ^{18}O and δ^{13}C, and lower N-S T-Anomaly values which is coeval across each record, suggesting drier conditions and reduced vegetation amount above Grar cave, as the ITCZ shifts southwards and TP rainfall occurrence reduces in the SOA. These changes are not represented in the BZ-1A δ^{18}O record, suggesting that factors such as moisture source, cave temperature and kinetic processes were unchanged at this site.

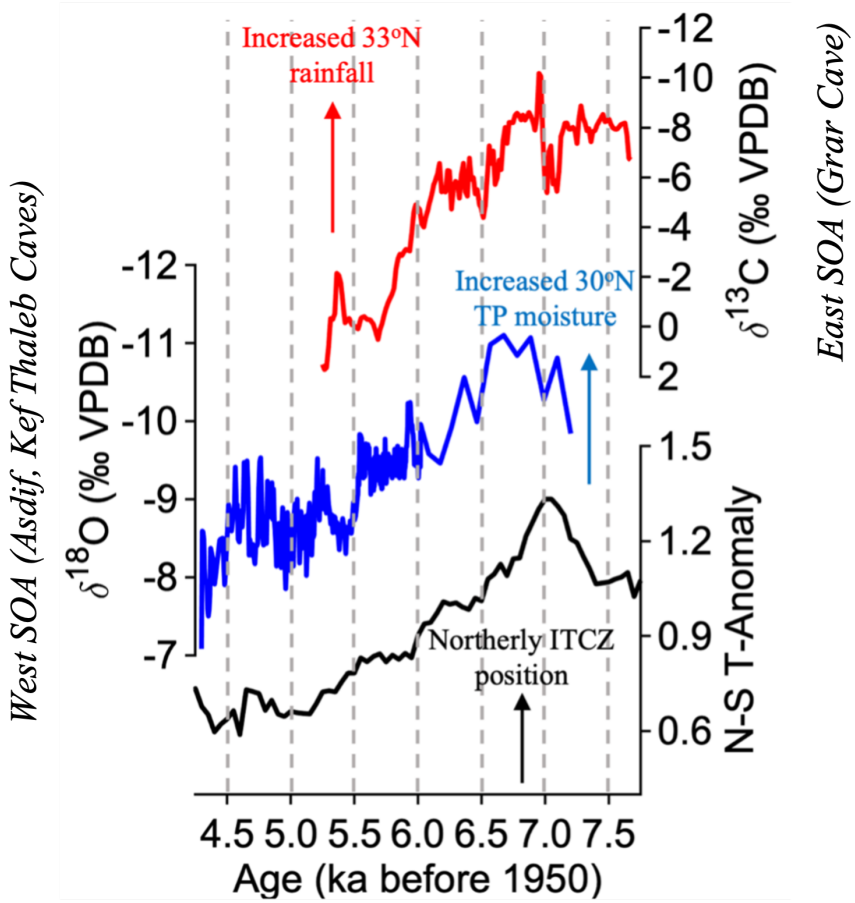


Figure 5.10: **BZ-1A δ^{13}C, Anti-Atlas δ^{18}O and N-S Temperature Anomaly**. Top (red): δ^{13}C record from BZ-1A, inferring drying (reduced rainfall) towards the end of the AHP. Middle (blue): Anti-Atlas δ^{18}O record (Chapter 4), inferring reduced tropical plume moisture in the SOA towards the end of the AHP. Bottom (black): N-S T-Anomaly (Schneider et al., 2014), inferring that a more northerly position of the ITCZ average annual position is supporting increased levels of rainfall at Grar cave and TP moisture at the Anti-Atlas caves.

These data provide robust evidence for a regional TP moisture source across the breadth of the SOA region during the AHP. Whilst the spread of archaeological evidence

across the SOA (Manning and Timpson, 2014) was used to draw these conclusions in Chapter 4, here direct evidence of increased rainfall as far east as 1.2°E is provided by stalagmite growth, subsequently supplying the southward flowing rivers observed from satellite imagery (Figure 5.2). This supports archaeological comparisons made in Chapter 4, by which speleothem growth can be used as evidence of supporting increased Neolithic populations across the entire SOA region (Manning and Timpson, 2014), suggesting that the chronology of stalagmite growth defines highly important periods of time for hominid migration and cultural exchange (Scerri et al., 2014).

Continued tropical plume rainfall during the middle to late Pleistocene

A recurring mechanism of TP moisture in the SOA across time periods is supported further by consistent differences in stalagmite δ^{18}O occurring between older time periods across cave sites. Average δ^{18}O is 1‰ higher during MIS 5a than MIS 1 in both Ksar and Grar caves, and 1‰ lower during MIS 11 than MIS 9 in both Ksar and Maqlae caves. Differences in average δ^{18}O may be recording the amount of TP rainfall which is occurring during each time period, shown to be an important control on TP δ^{18}O in the modern day (Cappy, 2007; Chapter 1), This corroboration of changes in δ^{18}O across cave sites 100s of kms apart supports the notion that regional controls, such as moisture source, are impacting speleothem δ^{18}O, rather than in-cave processes (Treble et al., 2022).

5.6 Conclusion

These data provide clear evidence as to the regional extent of past increases in rainfall between 7°W and 1°E and 30-33°N in the SOA region, across numerous time periods and lasting thousands of years. U-Th chronology suggest that the largest increases in rainfall are broadly occurring during northern hemisphere interglacials, but that they are not tied uniquely to maximum interglacial conditions. There is clear evidence for a TP-source of moisture during the AHP across the SOA, whilst a lack of consistent

agreement between SOA rainfall and rainfall in regions where monsoonal maxima are shown to be the controlling factor on rainfall (Fleitmann et al., 2003; El-Shenawy et al., 2018), suggests that TP, rather than monsoonal, rainfall is an ongoing source of moisture in the SOA throughout the middle to late Pleistocene.

This research exhibits the SOA as an important and unique region for how expansive periods of increased North African rainfall are. The SOA is critical to the extent to which periods of increased rainfall covered North Africa due to the topographic characteristics of the region allowing for rainfall at the northern extremes of the desert, where the West African Monsoon front likely cannot reach, filling lakes and expanding the influenced area of increased humidity from just being southern, monsoon-fed regions (Shanahan et al., 2015). Rainfall here is not only the final piece in connecting watercourses across the desert (Drake et al., 2011), but also leads to aquifer recharge and defines increased human activity.

Chapter 6

Secondary carbonates record increased local rainfall in the central Sahara during MIS 11

Contents

6.1 Introduction 111

6.2 Study Site 113

6.3 Methods 116

6.3.1 XRD Analysis 116

6.3.2 U-Th Dating 118

6.3.3 OxCal Age Model 120

6.3.4 Stable Isotope Analysis 120

6.3.5 Calcium Isotope Analysis 121

6.3.6 Clumped Isotope paleo-thermometry 122

6.4 Results 122

6.4.1 XRD 122

6.4.2 U-Th 122

6.4.3 Stable Isotopes 130

6.4.4 Calcium Isotopes 132

6.4.5 Clumped Isotope paleo-thermometry 134

6.5 Discussion 135

6.5.1 Calcite Chronology 135

6.5.2 Saharan rainfall during MIS 11 137

6.5.3 Moisture Sources 140

6.5.4 Paleoclimate Significance 144

6.6 Conclusion 146

Acknowledgments

Acknowledgments in this chapter are made to Christopher Day for performing all calcium isotope analysis and measuring speleothem stable isotopes, to Alvaro Fernandez for performing clumped isotope paleo-thermometry analysis, to Katherine Clayton for performing XRD analyses and to Matthew Beverley-Smith for making sample thin sections.

Abstract

There is little to no direct evidence of past increased rainfall in the central Sahara, resulting in geographic and temporal constraints as to when rainfall occurred away from coastlines or regions of high topography. This chapter introduces new U-Th, stable isotope, calcium isotope and clumped isotope data from well-laminated speleothem-like central Saharan secondary calcite deposits, collected from the southern edge of the Tademaït Plateau in central Algeria. 36 U-Th ages suggest complex open-system impacts on calcite across the plateau, but more reliable chronology from sample TPB1 provides evidence for the occurrence of a period of increased rainfall centred around 409 kyr BP. This growth coincides with a major northern hemisphere interglacial, MIS 11, and is coeval with stalagmite growth in samples MegaMite (MM) and QC-1, located at the northernmost limits of the Sahara. These data provide the first evidence of secondary carbonate deposition from this region forming from direct, local rainfall rather than simply as a result of increased surface moisture availability. High-resolution stable isotope records from TPB1 and MM exhibit similarities whilst coeval changes with northern hemisphere sea surface temperatures and other orbitally controlled paleoclimate proxies suggest a consistent tropical control on rainfall at the northern extent of the Sahara, and interconnected rainfall between 28 and 32°N during MIS 11.

6.1 Introduction

The Sahara is known to have experienced past periods of increased rainfall and perennial surface water coverage (Ritchie et al., 1985; McGee et al., 2013; Pausata et al., 2016; Grant et al., 2017; Blanchet et al., 2021), largely associated with increased tropical rainfall during interglacials (Adkins et al., 2006; Burrough and Thomas, 2013; Tierney et al., 2017a; Pausata et al., 2020).

Presently, terrestrial and marine paleoclimate proxies are limited by (i) integrating environmental change over large regions (Adkins et al., 2006) (ii) chronological constraints of OSL and ^{14}C techniques compared to U-Th dating prior to time periods $>$ 50 kyr BP, (iii) potential bias for recording the most recent period of increased rainfall due to the overwriting of previous records and (iv) the delayed onset between rainfall occurring and it being recorded in proxies (Lézine et al.,2011). Chapter 5 of this thesis presented new stalagmite records from the Algerian Saharan Atlas, alongside records from Barrott (2014) (MegaMite (MM)) which significantly improves the temporal and spatial coverage of proxies of direct rainfall at the northern limits of the desert (Figure 6.1). However, distinct uncertainties remain as to where and when direct rainfall fell in the *central* portions of the Sahara, for which the majority of terrestrial proxies are currently indirect indicators.

Here, well-laminated, speleothem-like central Saharan secondary calcite deposits are presented, from the southern edge of the Tademaït Plateau, central Algeria. The scatter of U-Th data suggests that not all calcite has remained under closed-system conditions since deposition. Subsequently, a number of criteria are applied to assess for open-system behaviour and excessive "geologic scatter" (Ludwig and Paces, 2002; Chen et al., 2020), with remaining chronology from sample TPB1 providing evidence for the occurrence of a period of increased rainfall centred around 409 kyr BP, coincident with Marine Isotope Stage (MIS) 11. This chapter presents field and data interpretations which provide robust evidence for this period of increased rainfall, and discusses the paleoclimatic significance of results.

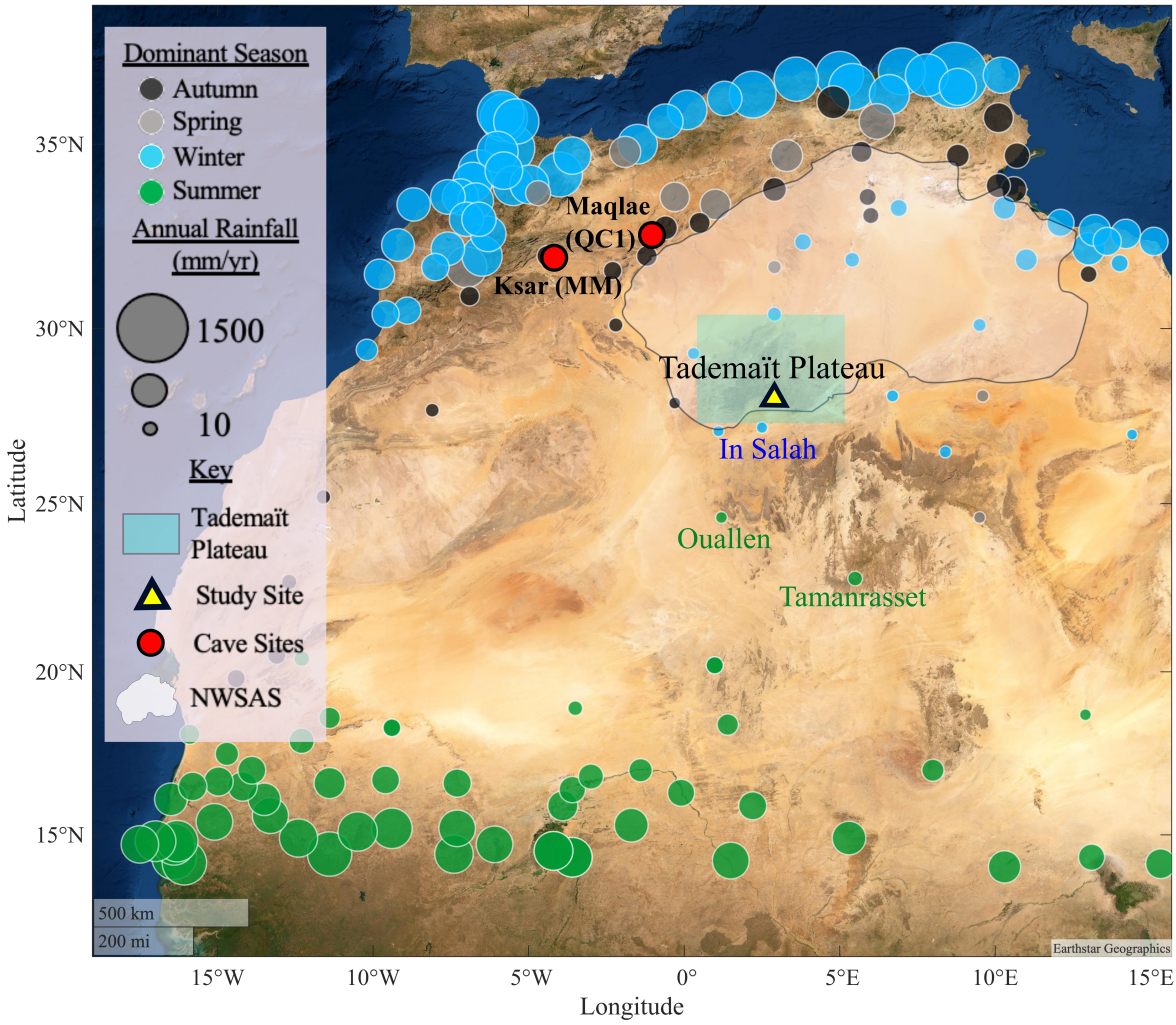


Figure 6.1: **Tademaït Plateau and Modern Climate**. North African GHCN-M meteorological station rainfall amounts and dominant season plotted on a high-resolution satellite image (blue = winter, green = summer, black = autumn, grey = spring). Data sourced from http://climexp.knmi.nl (Trouet and Oldenborgh, 2013). Saharan cave sites at the northern extent of the desert (Ksar cave; Barrott (2014), Maqlae cave; Chapter 5) are plotted as red circles. Stalagmite names are noted in parenthesis. The shaded white area represents the extent of the NWSAS groundwater system, made up of the Complex Terminal and Continental Intercalaire aquifers. The names of three relevant Global Historical Climatology Network-Monthly (GHCN-M) climate stations are annotated, for which In Salah (blue) average monthly rainfall between 1905-2018 is dominated by rainfall during boreal winter, and Ouallen and Tamanrasset (green) average monthly rainfall between 1925-2018 is dominated by rainfall during boreal summer. The blue shaded square identifies the location of the Tademaït Plateau (Figure 6.2).

Marine Isotope Stage 11

Alongside MIS 1 and 5e, MIS 11 is suggested to have been the warmest interglacial to have occurred during the last 800 kyrs (Howard, 1997; Lisiecki and Raymo, 2005). Similar orbital forcing conditions have raised MIS 11 as being the interglacial most analogous to the Holocene (Loutre and Berger, 2003; Dickson et al., 2009; Candy et al., 2014) and the most applicable in understanding future climate conditions (Maiorano et al., 2013). Furthermore, the length of MIS 11, in some cases suggested to be $>$ 30 kyrs, has driven interest in the period due to it being longer in duration than all subsequent interglacials (Kandiano et al., 2012; Kleinen et al., 2014). Therefore, observations of where rainfall occurred in the Sahara during MIS 11 would provide key insights into how Saharan climate may change in the future, and the potential causes for changes in rainfall amount in the centre of the desert.

6.2 Study Site

Few elevated carbonate outcrops, necessary for secondary carbonate deposition, are found in the central Sahara within geopolitically accessible regions. One suitable region however, to which fieldwork was undertaken, is the Tademaït Plateau; an elevated, northwards dipping discontinuous carbonate landform, the southern extent of which (27-28°N, 1-3°E) lies ∼900m from the Mediterranean Sea and over ∼1000m from Atlantic coastlines (Figure 6.1).

The top of the plateau is formed from a carbonate (limestone) bedrock at an elevation of ∼750masl. Two large aquifers are located in the region (Moulla et al., 2012); the Complex Terminal (CT) and Continental Intercalaire (CI) aquifers, together forming the north-west Sahara Aquifer System (NWSAS; Figure 6.1). Secondary calcite was found *in-situ* exclusively at the highest point on the plateau (Figure 6.2B), from which surface and sub-surface water flows away, suggesting that calcite formation is driven by local rainfall, and can therefore be used as a local indicator for periods of past rainfall

and aquifer recharge. Further geological, field and geomorphological details of this site are presented in Chapter 2.

Modern Climate

The southern Tademaït plateau region receives $<$ 30mm of annual rainfall and is within a BWh (hot, arid desert) Köppen climate classification (Chen and Chen, 2013). When observing GHCN-M station rainfall data, it is apparent that the plateau lies north of the northerly modern day WAM influenced limit. Due south, in Tamanrasset (22.8°N, 1378masl) and Ouallen (24.6°N, 347 masl), there is a clear WAM influence shown by increased summer rainfall, compared to the sites north of 27°N, such as In Salah, which have a minimum in rainfall during the summer and instead increased winter precipitation (Figure 6.1; Appendix V Figure 18). Between Ouallen and Tamanrasset, there is a difference in annual rainfall of 1mm/35m of altitude change, similar to that as between In Salah and the top of the Tademaït plateau (1mm/29m), suggestive of an altitude control on rainfall in the central Sahara.

Samples

Calcite samples were collected from the plateau in either crystal geode or laminated 'block'/flowstone form (Figure 6.3). *In-situ* calcite was found solely in the carbonate bedrock in the top ∼70m of the plateau (Figure 6.2). Out of situ samples were collected from various upper sections of paleo-rivers. Further descriptions of samples can be found in Chapter 2.

In summary, calcite geodes were collected exclusively *in-situ*, predominantly from two locations; 'Levels' and Aïn Guetterra, but were observed across the plateau (Figure 6.2). Geodes collected from the 'Levels' field site are labelled as such that, for example, sample "L1G1" was collected from 'level 1', at the highest altitude on the plateau, and sample "L4G1" was collected from 'level 4', at a lower altitude. Seven geode samples are reported on here (Figure 6.3A, B). Block calcite, hereafter referred to as flowstones, is

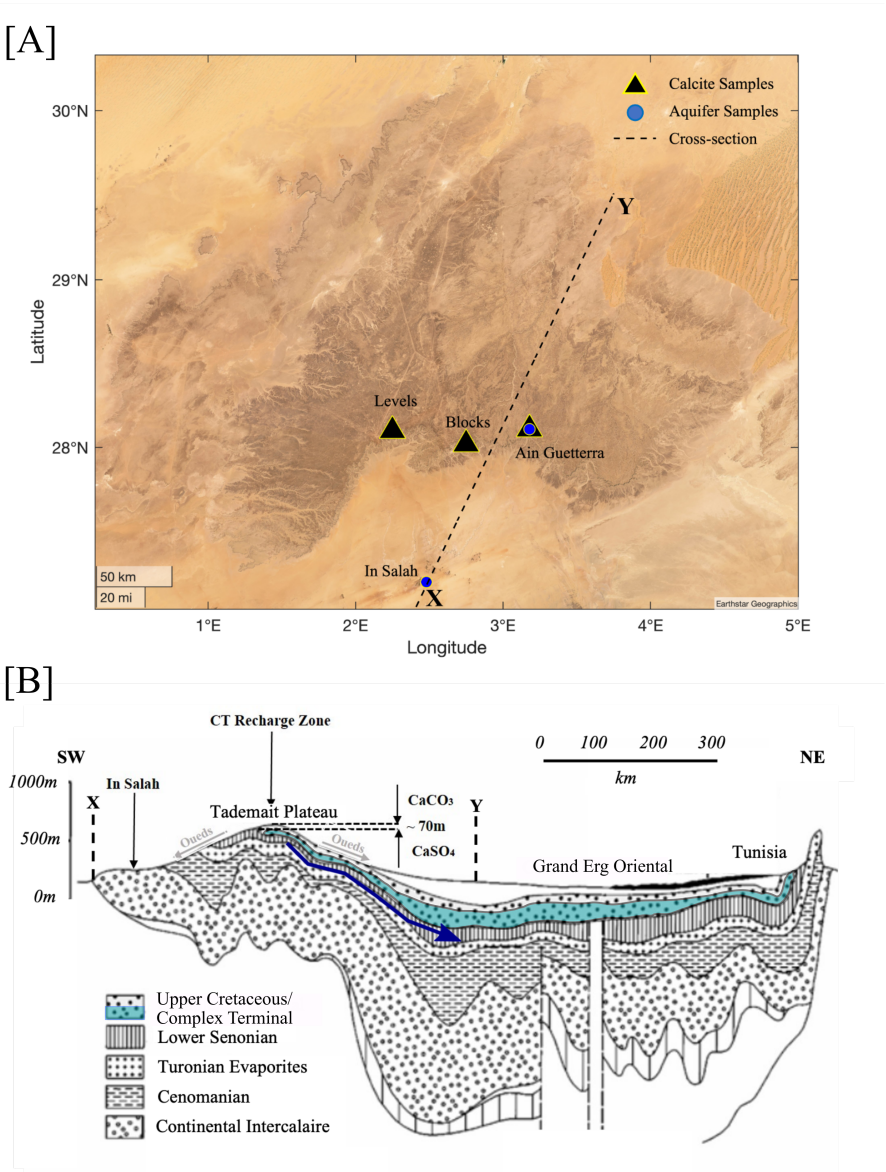


Figure 6.2: **The Tademaït Plateau**. [A] Satellite image of the Tademaït Plateau, as per the box in Figure 6.1. Surrounding desert sand can be observed around the dark weathered carbonate top of the plateau. Locations of the collection points of calcite and aquifer samples are plotted as black triangles and blue circles respectively. The dashed line represents the cross section plotted in subplot B. The location "Blocks" identifies where samples TPB1-TPB4 were collected from (Figure 6.3) and the location "Levels" identifies where the calcite geodes discussed in the text were collected from. [B] Cross-section of the Tademaït Plateau adapted from Edmunds et al. (2003). Geological units are annotated. The CT aquifer can be observed at the top of the plateau, shaded in blue, and the CI aquifer at the bottom. The general sub-surface flow of the CT is annotated by a dark blue arrow, towards the Grand Erg Oriental (Nadhira and Omar, 2019). The locations of black dashed lines annotated as X and Y correlate with the black dashed line plotted in A.

up to 4cm thick and 10cm wide. Samples are formed from dense, clean calcite crystals and are clearly laminated (Figure 6.3). These samples were collected out-of-situ from paleo-rivers extending from the top of the carbonate plateau. Flowstone samples are hypothesised to have originally been in-situ in the carbonate bedrock, as observed in the field (Figure 6.3F, G), and to have been washed downstream during periods of plateau erosion. Four flowstone samples are presented here, labelled TPB1 (largest) to TPB4 (smallest) (Figure 6.3; TPB4 is not discussed further in the text and is therefore not shown here).

Aquifer Water

Five water samples were collected from two locations in the field (Figure 6.2A). Three samples are reported on from In Salah (250 masl), an oasis city, ∼70km south of the Tademaït Plateau and two samples are reported on from Aïn Guetterra (600 masl), a natural spring found near the top of the plateau.

6.3 Methods

Sample Preparation

Calcite flowstones were sliced in half using a diamond tipped cutting wheel or band saw along their thickest plane, revealing clearly structured lamina and numerous changes in calcite density and colouration (Figure 6.3). Sample TPB1 was set in resin prior to cutting, to reduce the risk of loose individual crystals coming off the sample. From calcite geodes, whole crystals were removed and individually cleaned with deionised H_2O and 2M $\mathbf{\Delta}HNO_3$ prior to analysis (Figure 6.3A; inset).

6.3.1 XRD Analysis

Aliquots of milled carbonate powders of ∼0.25 mg were analysed at the University of Oxford using the method described in detail in Day et al. (2021), summarised in

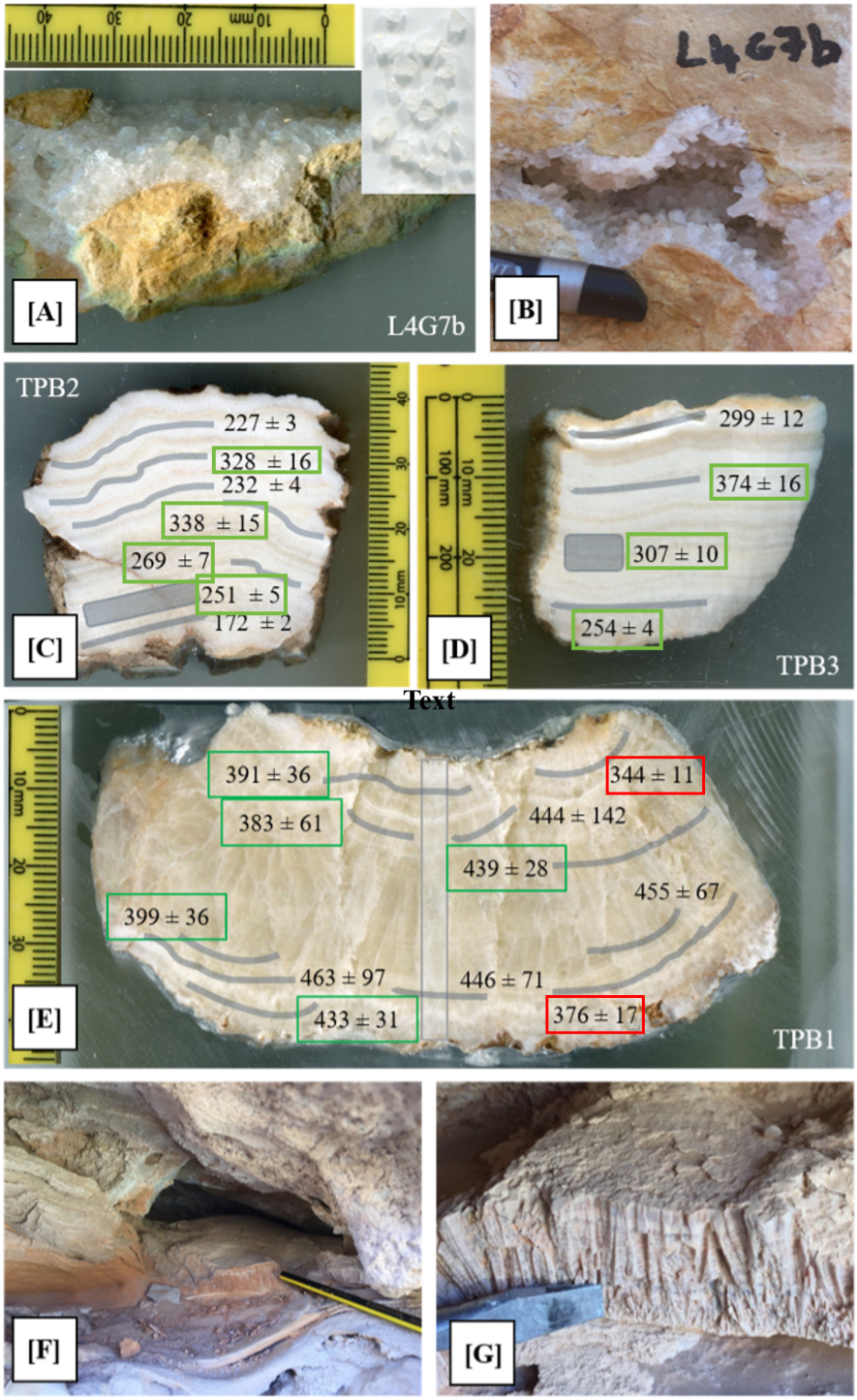


Figure 6.3: **Calcite Samples from the Tademaït Plateau.** Scans and field images of Tademaït Plateau calcite. [A] and [B] are of geode sample L4G7b, scanned and in-situ in the field respectively. The inset image on A is a collection of calcite crystals after being cleaned prior to U-Th analysis. [C], [D] and [E] are scans of TPB2, TPB3 and TPB1 respectively, with U-Th ages and uncertainties annotated. Green boxes around ages in E represent final ages used for the age model of TPB1 and in C and D represent ages which are in stratigraphic order and have similar $\delta^{234}U_{(i)}$ values. Red boxes around ages represent sub-samples with anomalously high $\delta^{234}U_{(i)}$ values. [F] and [G] are field images of other calcite flowstones observed in small cavities resembling caves, but not collected due to significant alteration or contamination.

Chapter 3 of this thesis.

6.3.2 U-Th Dating

Clear laminations in flowstone samples allowed them to be milled for U-Th along individual laminae using a NewWave MicroMill, whilst geode crystals were individually cleaned prior to U-Th analysis to ensure the removal of bedrock. In total, eleven U-Th ages were milled and analysed along various lamina from sample TPB1, with masses ranging from 50-400 mg, coded TPB1_1 to TPB1_11. Samples TPB2, 3 and 4 have had seven, four and three sub-samples respectively measured on them, and the calcite geodes have had a further eleven sub-samples measured, across seven geode samples.

Carbonate samples were dissolved in $\mathbf{\Delta}HNO_3$ as either powdered aliquots or whole calcite crystals. Sub-samples were spiked with a mixed ^{229}Th—^{236}U solution, and the U and Th fractions were separated following chemical procedures adapted from Edwards et al. (1987), further described in Chapter 3 of this thesis.

Open system behaviour

U-Th ages either not in stratigraphic order on a sample, or within analytical error of neighbouring ages, may be indicating either mixing of growth periods or open-system behaviour (Hoffmann et al., 2016a). Open-system behaviour can result from sample dissolution and re-precipitation, recrystallisation from aragonite to calcite polymorphs, alpha recoil processes or other post-depositional uranium addition (Richards and Dorale, 2003). Further information into the potential causes of open-system behaviour are found in Chapter 3. Subsequent radionuclide addition or loss which is not a result of radiogenic decay of U into Th leads to an incorrect calculation of sample age (Chen et al., 2020). The most susceptible material for post-depositional loss or addition of radionuclides are outer layers of samples that have been exposed to moisture (Richards and Dorale, 2003), suggesting that the calcite flowstones collected from paleo-rivers extending from the Tademaït plateau may be at risk.

A number of criteria can be investigated to ensure that a sample has formed and continued to preside under closed-system decay, and thus can be used as the basis of U-Th interpretations, to avoid the cherry picking of final chronological information (Chen et al., 2020). Ideally, calculated ages must be either in stratigraphic order, with younger samples towards the 'top' of a sample, or within error of one another if analytical uncertainty is high or the samples extension rate is higher than the range associated with 95% confidence limits of ages. If this initial criteria does not hold, and there is no reasonable evidence as to why ages may not be in stratigraphic order (via sub-sampling issues such as lamina mixing), then potential open-system impacts can be investigated using radionuclide concentrations and isotopic ratios of sub-samples.

When a sample first forms, U is incorporated into the secondary carbonate with a set ratio of ($^{234}U/^{238}U$), often given in the $\delta^{234}U$ notation, reported in ‰, and is discussed in those terms here, where:

$$\delta^{234}U = ((\frac{^{234}U}{^{238}U}) - 1) * 1000 \tag{6.1}$$

From a measured $\delta^{234}U$ value ($\delta^{234}U_{(m)}$), the initial $\delta^{234}U$ of a sample ($\delta^{234}U_{(i)}$) can be calculated with knowledge of the time that has elapsed since deposition, by rearranging the equation:

$$\delta^{234}U_{(m)} = (\delta^{234}U_{(i)}) \exp^{-\lambda_{234}t} \tag{6.2}$$

The internal consistency of initial $\delta^{234}U$ ($\delta^{234}U_{(i)}$) in a sample which grew continuously or during one period is subsequently an indicator of closed-system behaviour (Richards and Dorale, 2003). Anomalous $\delta^{234}U_{(i)}$ values are indicative of diagenetic addition of U.

A further diagnostic indicator of open-system behaviour is a strong correlation between ^{238}U concentration ($^{238}U_{conc}$) and raw age (Age_{raw}) or measured $\delta^{234}U$ values ($\delta^{234}U_{(m)}$) within a sample (Thompson et al., 2003; Rowe et al., 2015; Ayling et al.,

2017). Under closed-system decay, Age_{raw} should be independent of $^{238}U_{conc}$, as $\delta^{234}U$ at formation should be consistent irrespective of the amount of U incorporated, and $^{238}U_{conc}$ does not subsequently vary as radiogenic decay progresses, owing to the long half-life of ^{238}U (Cheng et al., 2013). A positive (negative) relationship between $^{238}U_{conc}$ and $\delta^{234}U_{(m)}$would imply a post-depositional addition of high (low) $\delta^{234}U$ uranium, to a sample (Rowe et al., 2015). Different sources such as groundwater submersion or meteoric rainfall erosion may have different $\delta^{234}U$ inputs, and so post-depositional controls are likely complex and changing through time for old samples subject to significant water interactions.

6.3.3 OxCal Age Model

OxCal was used to generate an age model of sample TPB1. A poisson-sequence deposition model was selected (Bronk Ramsey, 2008; Bronk Ramsey, 2009; Bronk Ramsey and Lee, 2013), with an interpolation rate of 5 depth^{-1} and poisson parameter k(o) value of 300 depth^{-1}, to increase the rigidity of the model. The selected log10($k/k_{(o)}$) value was U(-2,2).

6.3.4 Stable Isotope Analysis

Individual stable isotope measurements were completed on calcite geodes (n=31) as well as low-resolution records on blocks TPB2 (n=13), TPB3 (n=11), TPB4 (n=4) and a high-resolution record on block TPB1 (n=69). A continuous trench of sub-sample powders was milled from flowstone TPB1 using a NewWave Micro-mill at a 500 μm resolution and to a depth of 300 μm. Samples TPB2, 3 and 4 and geodes were milled by hand using a Dremel dentist drill fitted with a 0.85mm diameter drill bit. Carbonate stable isotope methods are further described in Chapter 3 of this thesis. NOCZ (secondary standard) measurements within Tademaït Plateau calcite stable isotope runs averaged $\delta^{18}O$ of -1.94‰ ± 0.07‰ and $\delta^{13}C$ of 2.2‰ ± 0.04‰ (1σ, n=14), within the long-term NOCZ values.

Aquifer H_2O hydrogen and oxygen stable isotopes were measured on the same Delta V IRMS using a Thermo Scientific Gasbench II gas preparation and introduction system as carbonate samples. The relative $^{18}O/^{16}O$ values are reported in the conventional $\delta^{18}O$ (‰) notation, relative to V-SMOW, on a normalised scale such that the $\delta^{18}O$ of IA-RO63 is -0.41‰. The relative ^{2}H values are reported in the conventional δD (‰) notation, relative to V-SMOW, on a normalised scale such that the δD of IA-RO63 is 11.26‰. Water calibration standards and evenly scattered secondary standards were used for water analyses. Long-term measurements of OxDw (secondary standard) averages -7.55‰ ± 0.15‰ for $\delta^{18}O$ and -49.42‰ ± 0.85‰ for δD. OxDw measurements within Tademaït Plateau aquifer water runs averaged $\delta^{18}O$ of -7.51‰ ± 0.05‰ (1σ, n=3) and δD of -48.94‰ ± 0.71‰, within the expected long-term values.

6.3.5 Calcium Isotope Analysis

Calcium isotope analysis was performed by Christopher Day at the University of Oxford. Sub-samples were milled using a hand operated Dremel dentist drill fitted with a 0.85mm diameter drill bit. Samples measured were all from the Levels location on the plateau (Figure 6.2A). Sub-samples were milled from two bedrock samples (L1BR, L4BR) and three calcite geodes (L1G4b, L2G1a, L4G7b). Powders were stored in acid leached 2mL polypropylene centrifuge tubes and aliquots of $CaCO_3$ (200–650 µg) were dissolved in 2M $\mathbf{\Delta}HNO_3$ and purified using an automated Ca–Sr separation method (PrepFAST MC, Elemental Scientific), using the methods described in Lechleitner et al. (2021). Ca-isotope ratios were analysed at the University of Oxford using a Nu Instruments MC-ICP-MS, following the method of Reynard et al. (2011). $\delta^{44/42}$Ca was calculated using:

$$\delta^{44/42}Ca(‰) = (\frac{(^{44}Ca/^{42}Ca)_{sample}}{(^{44}Ca/^{42}Ca)_{standard}} - 1) * 1000$$

(Hippler et al., 2003) and is reported normalised to NIST-SRM-915a. Secondary standards HPSnew (in-house standard) and NIST-SRM-915b (purified alongside the samples) were used to determine accuracy and external precision. Measured values

for purified SRM 915b were $\delta^{44/40}$Ca = 0.71 ± 0.08‰ (2se, n=10), which match values obtained by TIMS (thermal ionization mass spectrometry) of 0.72 ± 0.04 ‰ (2se; Heuser and Eisenhauer, 2008). Uncertainty on Ca-isotope data is quoted as the t-distribution-derived 95 % confidence interval on the mean of repeat measurements calculated using either the standard deviation on all repeat measurements on each sample or the standard deviation on all secondary standard analyses, whichever is greater (Lechleitner et al., 2021).

6.3.6 Clumped Isotope paleo-thermometry

Clumped isotope thermometry was performed by Alvaro Fernandez at the University of Bergen with a ThermoFisher Scientific MAT 253 mass spectrometer coupled to a Kiel IV carbonate preparation device. Sub-samples of 1.2-2 mg were milled using a hand operated Dremel dentist drill fitted with a 0.85mm diameter drill bit from geode calcite sample L4G7b (Figure 6.3A, B). Each measurement consists of 8–12 analyses of sample aliquots of 150–200 μg each and are measured alongside several carbonate standards which are used to correct sample data (Meckler et al., 2015). Details of the analytical method are described by Meckler et al. (2014).

6.4 Results

6.4.1 XRD

Crystal geodes and flowstones are all calcite ($CaCO_3$), with some smaller blocks shown to be high in magnesium ($CaCO_3$•Mg) (Appendix V Figures 19 and 16).

6.4.2 U-Th

In total, thirty-six ages were collected from calcite samples (Figure 6.3; Table 6.1); eleven ages from geodes with an average age uncertainty of ± 5% (range 1.5-7%), fifteen from smaller calcite flowstones with average uncertainty of ± 2.7% (range 1-5%)

and eleven ages from TPB1 with average uncertainty of ± 12% (range 3-32%). The majority of ages appear to have been impacted by open-system behaviour or mixing across time periods, as exhibited by the scatter of ages and samples not satisfying the assumptions of U-Th dating (Chen et al., 2020).

Detrital ^{232}Th contamination in Tademaït Plateau calcite is low, averaging 1.5 ppb. In all cases, a bulk Earth ^{230}Th/^{232}Th ratio of 5.38 ppm + 5.38 ppm / - 4.84 ppm (Wang et al., 2019) was used to correct ages for detrital thorium, although this correction was often negligible. Results are plotted in (^{230}Th/^{238}U)-(^{234}U/^{238}U) space (Figure 6.4).

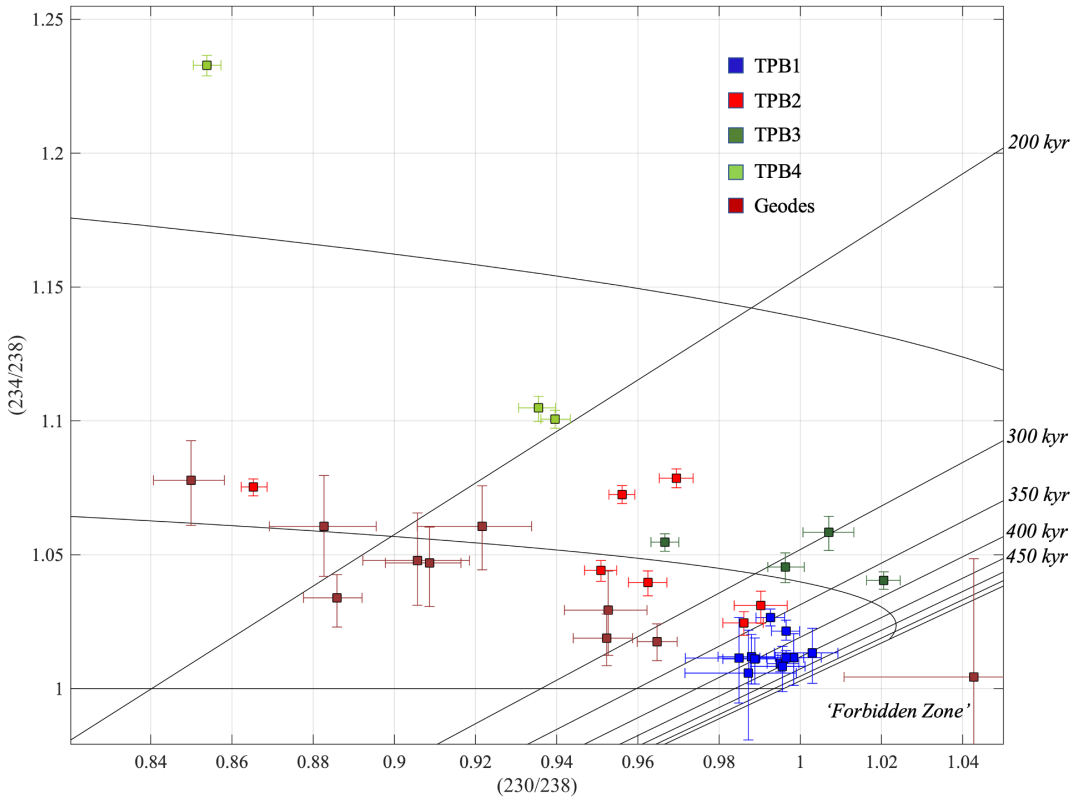


Figure 6.4: **U-Th Activity Ratio Data.** U-Th isotope results from Tademaït Plateau calcite plotted in (^{230}Th/^{238}U)-(^{234}U/^{238}U) space with 95% confidence intervals. Data is uncorrected for initial Th. All TPB1 (blue) samples are clustered within error of one another in the bottom right of the figure, closest to secular equilibrium. Only one sample (GTCU1) extends into the 'forbidden zone', suggesting secular equilibrium, although 95% confidence intervals do cross back into disequilibrium zones. Isochrons are calculated using decay equations presented in Chapter 3 of this thesis, and half-lives presented in Cheng et al. (2013).

Distance (mm)	Sample ID	238 conc (ppb)	(230/238)	2s error	(234/238)	2s error	(232/238)	2s error	232/230 (atomic)	δ^{234}U (m)	δ^{234}U (i)	Uncorr. Age (kyr BP)	Corr. Age (kyr BP)	2s Error
TPB1														
2	TPB10	127	0.993	0.004	1.027	0.003	0.027	0.00012	5120	26.5	70.6	347	344	11
4	TPB7	155	0.988	0.007	1.012	0.009	0.001	0.00002	225	11.9	35.9	391	391	39
11	TPB5	136	0.987	0.014	1.006	0.021	0.0002	0.00004	29	5.8	20.2	444	444	143
11	TPB6	116	0.985	0.013	1.011	0.016	0.0004	0.00006	76	11.4	33.6	383	383	61
19	TPB9	133	0.995	0.004	1.009	0.003	0.009	0.00004	1625	9.3	32.3	440	439	28
25	TPB3	146	0.996	0.007	1.008	0.008	0.0001	0.00001	23	8.3	29.9	455	455	67
26	TPB4	152	0.989	0.007	1.011	0.009	0.002	0.00002	307	11.0	34.0	399	399	36
30	TPB8	182	0.996	0.003	1.021	0.004	0.002	0.00001	381	21.4	61.9	377	376	17
31	TPB2	162	0.998	0.008	1.012	0.010	0.0007	0.00003	137	11.5	40.4	446	446	71
34	TPB1	159	1.003	0.008	1.013	0.010	0.004	0.00004	681	13.3	49.2	463	463	97
35	TPB11	160	0.996	0.005	1.011	0.003	0.002	0.00001	315	11.4	38.8	433	433	31
TPB2														
5	TPB2_c	116	0.956	0.003	1.072	0.003	0.009	0.00004	1730	72.5	137.7	228	227	3
8	TPB2_b	178	0.990	0.007	1.031	0.006	0.003	0.00002	521	31.1	78.5	329	328	16
14	TPB2_e	105	0.969	0.004	1.079	0.004	0.005	0.00003	930	78.6	151.4	233	232	4
20	TPB2_f	217	0.986	0.005	1.025	0.004	0.001	0.00002	273	24.5	63.6	338	338	16
29	TPB2_g	168	0.962	0.005	1.040	0.005	0.001	0.00003	221	39.6	84.8	270	269	8
32	TPB2_a	158	0.951	0.004	1.044	0.004	0.002	0.00001	397	44.2	89.7	251	251	5
34	TPB2_d	176	0.865	0.003	1.075	0.003	0.001	0.00001	314	75.3	122.2	172	172	2
TPB3														
1	TPB3_a	175	1.007	0.006	1.058	0.006	0.001	0.00002	195	58.4	135.4	299	299	12
11	TPB3_c	126	1.021	0.004	1.040	0.003	0.005	0.00002	871	40.4	116.1	374	374	15
19	TPB3_b	154	0.996	0.004	1.045	0.006	0.002	0.00001	430	45.4	107.9	307	307	10
25	TPB3_d	156	0.967	0.003	1.055	0.003	0.001	0.00001	238	54.7	112.1	255	254	5
3	TPB_4	250	0.935	0.005	1.105	0.005	0.029	0.00018	5728	104.8	104.9	192	190	4
5	TPB4_1	177	0.854	0.003	1.233	0.004	0.248	0.00106	54035	232.8	232.9	122	97	24
6	TPB4_2	263	0.940	0.004	1.101	0.003	0.083	0.00041	16513	100.6	100.7	197	188	8

Table 6.1: U-Th results from Tademaït Plateau calcite flowstones. Sub-samples highlighted red from TPB1 are those with anomalously high $\delta^{234}U_{(i)}$values. Sub-samples highlighted green from TPB1 are those used in final interpretations, as per the text. A $^{230}Th/^{232}Th$ ratio of 5.38 ppm + 5.38 ppm / - 4.84 ppm (Wang et al., 2019) was used to correct ages for detrital thorium.

Geodes

Geodes are very low in ^{238}U concentration, averaging 18ppb. Despite being old, geodes also average only 0.25ppt of ^{230}Th, compared to average ^{232}Th concentrations of 1.4ppb, giving an average atomic ^{232}Th/^{230}Th ratio of ∼5000 (Table 6.2).

Eleven ages span between 104 and 304 kyr BP, with an average 2σ uncertainty of 11 kyrs. There is significant variation in age within individual geodes, such as sample L1G1 producing three ages of 187, 208 and 268 kyr BP. Due to the geodes not being laminated, there is no indication as to which crystals should be older or younger. Thus, both mixing of time periods or open-system behaviour could be the reason for the spread of ages within individual samples. However, a lack of correlation between $^{238}U_{conc}$ and $\delta^{234}U_{(m)}$ or Age_{raw} in the three ages from L1G1 means that there is currently no clear evidence for open-system diagenesis influencing these samples.

Flowstones

Flowstone calcite is higher in ^{238}U concentration than the geodes, averaging 150 ppb. Generally, ages with smaller sub-samples masses had significantly higher errors associated with them ($>$ 80 kyrs), resulting from counting statistics and high analytical uncertainties during MC-ICP-MS analysis. ^{232}Th is generally very low in flowstone samples (^{232}Th/^{230}Th averages 380, except for sub-sample TPB1_10 which is $>$ 5000), with ages corrected by $<$ 3 kyrs, suggesting that ages from these samples aren't significantly influenced by initial Th corrections. Higher ^{232}Th concentrations (^{232}Th/^{230}Th $>$ 5000) and limited chronology from sample TPB4 limit interpretations on this sample.

Samples TPB2 and TPB3 have corrected ages ranging between 172 and 374 kyr BP (2σ error of 2-17 kyr). In both cases, there are several ages which are not in stratigraphic order or within error of neighbouring ages, suggestive of open-system impacts. When only considering sub-samples from TPB2 and TPB3 which show consistent δ^{234}U(i) values, ages *are* chronological on the sample, compared to ages with significantly different $\delta^{234}U_{(i)}$ which do not sit stratigraphically (Figure 6.3). $\delta^{234}U_{(i)}$ is therefore giving initial

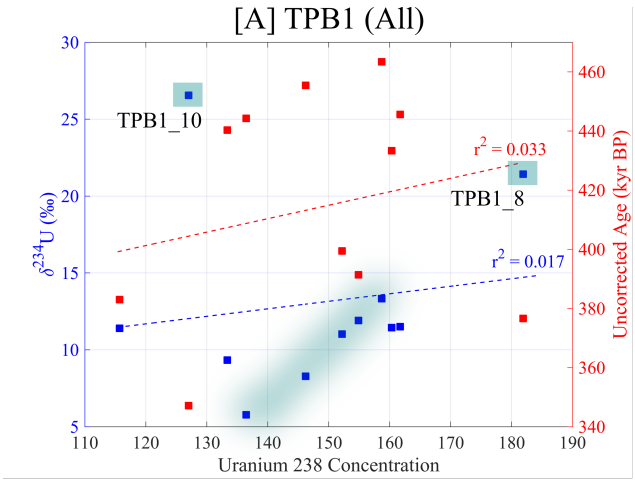
Stal ID	Sample ID	238 conc (ppb)	(230/238)	2s error	(234/238)	2s error	(232/238)	2s error	232/230 (atomic)	δ^{234}U (m)	Uncorr. Age (kyr BP)	Corr. Age (kyr BP)	2s Error
Geodes													
L1G1	L1G1_1	14	0.883	0.013	1.061	0.019	0.014	0.00017	2931	60.6	188	187	9
L1G1	L1G1_2	17	0.909	0.009	1.047	0.015	0.031	0.00030	6323	46.9	213	208	10
L1G1	L1G1_3	15	0.953	0.010	1.029	0.016	0.028	0.00028	5549	29.3	273	268	19
L1G2	L1G2	16	0.850	0.009	1.078	0.016	0.070	0.00067	15339	77.8	164	151	9
L1G3	L1G3	31	0.965	0.005	1.018	0.007	0.045	0.00024	8675	17.5	312	303	14
L1G4b	L1G4b_1	29	0.952	0.007	1.019	0.010	0.004	0.00003	810	18.9	289	289	15
L1G4b	L1G4b_2	21	0.886	0.007	1.034	0.010	0.006	0.00004	1290	33.9	207	206	6
L4G7b	L4G7b_B	11	0.906	0.013	1.048	0.017	0.009	0.00010	1846	47.9	211	210	14
L4G7b	L4G7b_C	14	0.714	0.006	1.141	0.006	0.003	0.00006	816	140.6	104	104	2
L4G7b	L4G7b2	14	0.922	0.014	1.061	0.016	0.054	0.00052	10944	60.6	213	207	14
GTCU1	GTCU1-C3	5	1.043	0.032	1.004	0.044	0.004	0.00014	683	Out Of Range	Out Of Range	Out Of Range	n/a

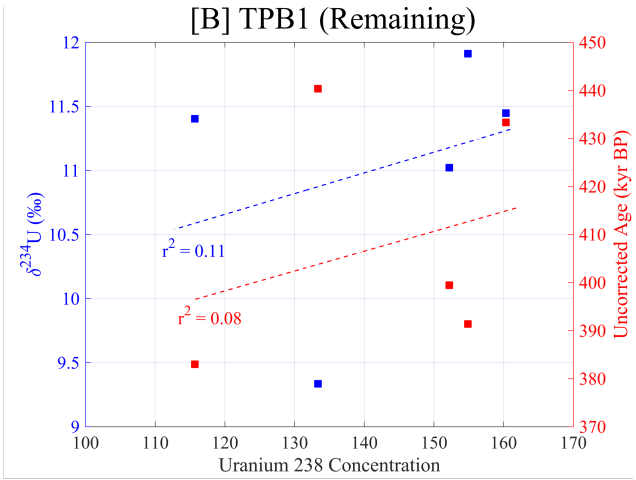
Table 6.2: U-Th results from Tademaït Plateau calcite geodes. A $^{230}Th/^{232}Th$ ratio of 5.38 ppm + 5.38 ppm / - 4.84 ppm (Wang et al., 2019) was used to correct ages for detrital thorium.

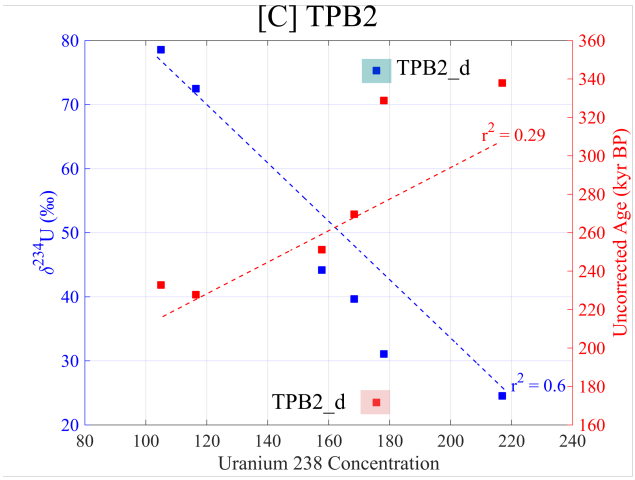
indications that portions of TPB2 and 3 are closed-system. Despite this, for example in TPB3, stratigraphic ages are $\sim$ 1cm apart and incorporate $>$ 50 kyrs of growth (Figure 6.3) meaning that it is likely that, even without open-system impacts, the sample grew either very slowly or with numerous hiatuses, and that mixing of growth periods will be occurring during sub-sampling, making paleoclimate interpretations difficult.

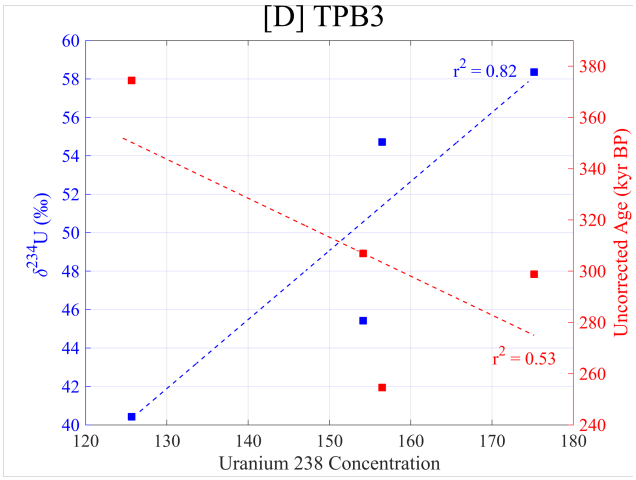
TPB3 exhibits a negative ($r^2 = 0.5$) relationship between Age_{raw} and $^{238}U_{conc}$ (Figure 6.5), compared to TPB2 which exhibits a positive relationship ($r^2 = 0.3$, rising to 0.8 when not including TPB2_d, which appears anomalous). These relationships again suggest that both TPB2 and TPB3 appear to be impacted upon by open-system behaviour. This is exhibited further by correlations between measured $\delta^{234}U$ ($\delta^{234}U_{(m)}$) and $^{238}U_{conc}$ (Ayling et al., 2017), for which there is a positive and negative relationship in TPB3 and TPB2 respectively, again indicative of open-system controls. This implies a post-depositional addition of high $\delta^{234}U$ uranium to TPB2 and low $\delta^{234}U$ uranium to TPB2 (Rowe et al., 2015), suggesting a complex nature of open-system behaviour on Tademaït Plateau calcite.

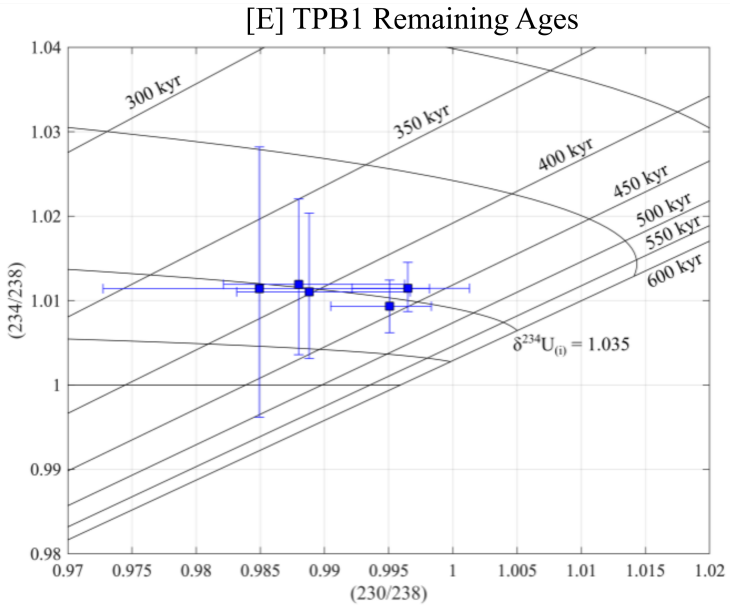
Figure 6.5: **U-Th Isotopic Data.** U-Th isotopic data from calcite flowstones TPB1, TPB2 and TPB3. [A] TPB1 Age_{raw} and $\delta^{234}U_{(m)}$ plotted against sample $^{238}U_{conc}$. Sub-samples TPB1_8 and _10 which have anomalous $\delta^{234}U_{(m)}$ (and subsequent $\delta^{234}U_{(i)}$) are shaded. The long shaded area highlights five ages which are exhibiting a relationship between $\delta^{234}U_{(m)}$ and $^{238}U_{conc}$ [B] TPB1 Age_{raw} and $\delta^{234}U_{(m)}$ plotted against sample $^{238}U_{conc}$ for the five remaining TPB1 ages once sub-samples with high $\delta^{234}U(i)$ and significant errors are removed. [C] TPB2 Age_{raw} and $\delta^{234}U_{(m)}$ plotted against sample $^{238}U_{conc}$, exhibiting negative and positive correlations respectively. Sub-sample TPB2_d, which appears to be anomalous in both correlations, is shaded. [D] TPB3 Age_{raw} and $\delta^{234}U_{(m)}$ plotted against sample $^{238}U_{conc}$ exhibiting positive and negative correlations respectively. [E] Five remaining TPB1 ages once sub-samples with high $\delta^{234}U(i)$ and significant errors are removed, in ($^{230}Th/^{238}U$)-($^{234}U/^{238}U$) space with isochrons plotted. These ages fall within 95% confidence intervals along an evolution line from a $\delta^{234}U(i)$ of approximately 1.035, suggestive of closed-system decay.


[A] TPB1 (All)
TPB1_10
TPB1_8
r2 = 0.033
r2 = 0.017
δ234U (‰)
Uncorrected Age (kyr BP)
Uranium 238 Concentration


[B] TPB1 (Remaining)
r2 = 0.11
r2 = 0.08
δ234U (‰)
Uncorrected Age (kyr BP)
Uranium 238 Concentration


[C] TPB2
TPB2_d
TPB2_d
r2 = 0.29
r2 = 0.6
δ234U (‰)
Uncorrected Age (kyr BP)
Uranium 238 Concentration


[D] TPB3
r2 = 0.82
r2 = 0.53
δ234U (‰)
Uncorrected Age (kyr BP)
Uranium 238 Concentration


[E] TPB1 Remaining Ages
300 kyr
350 kyr
400 kyr
450 kyr
500 kyr
550 kyr
600 kyr
δ234U(i) = 1.035
(234/238)
(230/238)

Sample TPB1 produced ages ranging between 344 ± 12 kyr and 463 ± 100 kyr BP, with an average corrected age of 416 kyr BP and average uncertainty of 55 kyrs. Measured δ^{234}U varies between 5.8 and 13.3 ‰, excluding two anomalously high values of 21.4 and 26.5 ‰ in sub-samples TPB1_8 and _10 respectively (Figure 6.5). These sub-samples were milled close to the weathered edge of TPB1 (Figure 6.3), suggesting a higher risk of open-system behaviour the further ages are sampled from the more protected central portions. In juxtaposition to TPB2 and TPB3, and despite large analytical uncertainty, ages in TPB1 do generally lie stratigraphically, with younger ages towards the top of the sample (r^2= 0.33; Appendix V Figure 20).

TPB1 also does not exhibit open-system behaviour as strongly, and data suggests that the sample is largely closed-system, with some anomalous analyses. The fine crystalline structure of samples TPB2 and TPB3, as can be observed under thin section (Appendix V Figure 21), may be more conducive to open-system impacts compared to the large, denser crystals which make up TPB1 (Chen et al., 2020). This is exhibited by the fact that nine out of eleven TPB1 ages are within analytical uncertainty of one another, rising to all samples when not including $\delta^{234}U_{(i)}$ sub-samples greater than 1 standard deviation from the mean (TPB1_8 and _10). TPB1 exhibits no relationship (r^2 = 0.03) between Age_{raw} and $^{238}U_{conc}$ when considering all data, although there is a potential correlation between five of the ages when considering $\delta^{234}U_{(m)}$ and $^{238}U_{conc}$ (Figure 6.5A). Despite this, the fact that ages remain within error of one another, compared to ∼100 kyr age reversals in TPB2, suggests that diagenesis is not as significant.

U-Th analysis of TPB1 is clearly complex, with at times significant analytical uncertainty that may be associated with "geologic scatter". In other words, the accuracy and precision of dates may be impacted by geologic factors not accounted for in typical uncertainty calculations (Ludwig and Paces, 2002; Chen et al., 2020). Despite this, there are several ages with well-constrained ages and consistent isotopic ratios. Subsequently, ages with anomalous $\delta^{234}U_{(i)}$ and very high analytical errors (> 80 kyrs in either direction) are discounted temporarily to test how well constrained chronology on

the sample may be with enough analyses. Five ages remain after doing this, which; (i) do not exhibit a strong relationship between $^{238}U_{conc}$ and $\delta^{234}U_{(m)}$ or Age_{raw} (Figure 6.5B), (ii) have the most consistent $\delta^{234}U_{(i)}$values (only sub-samples between 30-40‰ remain, Table 6.1), an indication of closed-system decay (Richards and Dorale, 2003) and (iii) fall along a horizontal evolution line describing closed-system decay (Figure 6.5E). Therefore, there is robust evidence that TPB1 chronology is less impacted upon by open-system diagenesis and is identifying a single continuous period of growth.

6.4.3 Stable Isotopes

Significant stable isotope variation is observed within individual samples. In general, greater magnitude variation is observed in $\delta^{13}C$ than $\delta^{18}O$, varying across all samples by 7.5 ‰ and 5.4 ‰ respectively (TPB2, 3 and 4 data presented in Appendix V Figure 22). The high-resolution TPB1 record varies between -13.2 ‰ and -8.1 ‰ (average -11.8 ‰) for $\delta^{18}O$ and between -9.3 ‰ and -2.4 ‰ (average of -6.4 ‰) for $\delta^{13}C$ (Figure 6.6).

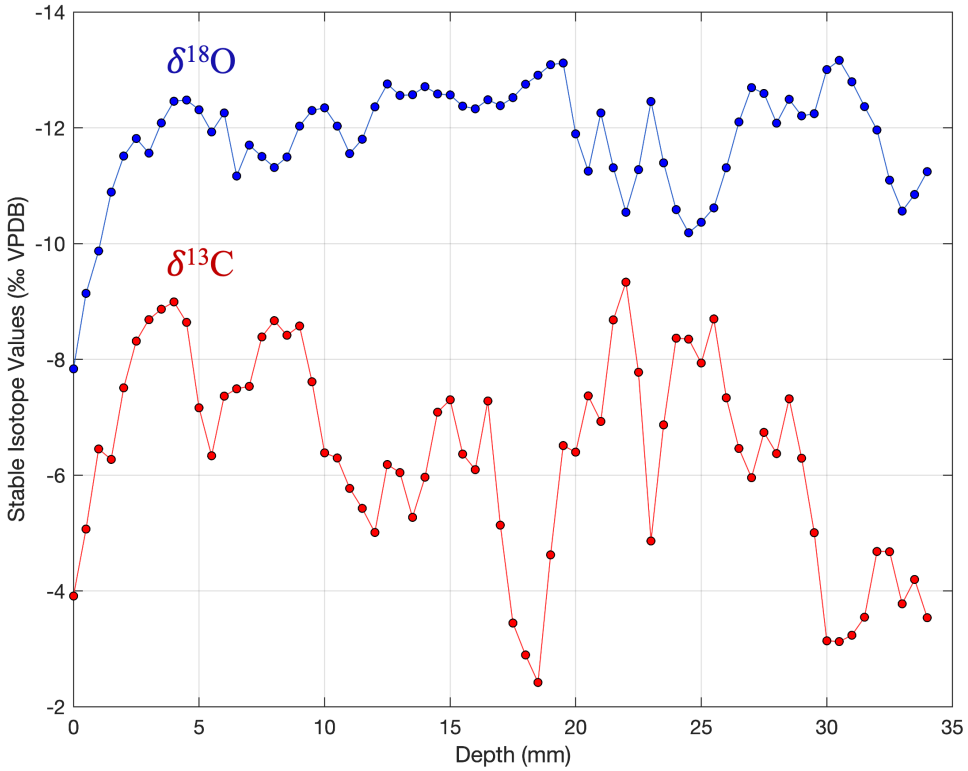


Figure 6.6: **TPB1 Stable Isotope Records**. High-resolution stable isotope records (blue = δ^{18}O, red = δ^{13}C) from flowstone TPB1 against depth from the top of the samples (Figure 6.3). Larger amplitude variations are observed in δ^{13}C whilst both records shift consistently to heavier values in the top 4mm of the sample. There is a low (r^2 = 0.03) correlation coefficient between the two records.

Stable isotope analysis of aquifer water indicates the presence of two groundwater bodies (Table 6.3). From Aïn Guetterra, average measured δ^{18}O values of -6.5 ‰ (VSMOW) are almost identical to that of -6.6 ‰ reported in Guendouz et al. (2003) from Complex Terminal aquifer waters. Average measured δ^{18}O values from In Salah of -8.1 ‰ (VSMOW) is close to that of -8.02 ‰ reported in Edmunds et al. (2003) from Continental Intercalaire aquifer water, confirming the presence of the two aquifer bodies.

Aquifer	Field Site	Measured δ^{18}O	Literature δ^{18}O	Measured δD	Literature δD	Reference
Complex Terminal	Aïn Guet-terra	- 6.47 ± 0.57 ‰	- 6.59 ± 1.07 ‰	- 48 ± 1.3 ‰	- 57 ± 6.6 ‰	Guendouz et al. (2003)
Continental Intercalaire	In Salah	- 8.14 ± 0.21 ‰	- 8.02 ± 0.57 ‰	- 63 ± 0.7 ‰	- 60 ± 4.8 ‰	Edmunds et al. (2003)

Table 6.3: **Aquifer Isotopic Values.** δ^{18}O and δD results from Tademaït Plateau aquifer water measurements compared to literature values. Two and three measurements were made from Aïn Guetterra and In Salah samples respectively. Values are reported to ± 1 standard deviation

6.4.4 Calcium Isotopes

Here, samples are discussed such that calcite geodes collected from 'Level 1' of the Levels field site on the plateau (Figure 6.2) are annotated as 'L1', geodes from 'Level 2' as 'L2' and geodes from 'Level 4' as 'L4'. The calcium isotope ($\delta^{44/42}$Ca) ratios of bedrock and calcite, combined with calcite stable carbon isotope (δ^{13}C) ratios (Figure 6.7), are suggestive of prior calcite precipitation (PCP) and the progressive formation of calcite from solution, such as that expected from carbonate precipitation in a traditional karstic environment. 'F' values (where F defines the fraction of calcite remaining in solution) are calculated from measured $\delta^{44/42}$Ca using the equation:

$$\delta^{44/42}Ca = \delta^{44/42}Ca_o + 1000(\alpha F^{(\alpha-1)} - 1)$$

where $\alpha = 0.99937 \pm 0.00003$ (Owen et al., 2016), $\delta^{44/42}$Ca = the measured $\delta^{44/42}$Ca value and $\delta^{44/42}\mathrm{Ca_o}$ = the starting $\delta^{44/42}$Ca value of solution when F=1.

In short, a solution will take on the $\delta^{44/42}$Ca value of dissolved bedrock (Owen et al., 2016), as illustrated (Figure 6.7A). Subsequently, calcite forms from F=1 (all calcium remains in solution) initially with a $\delta^{44/42}$Ca value via the fractionation factor above. As progressive precipitation of calcite occurs (PCP), the value of F decreases (less calcium remains in solution) and the $\delta^{44/42}$Ca of calcite shifts to higher values. This can be observed as higher $\delta^{44/42}$Ca values in L4 than L1 and L2, which are within error.

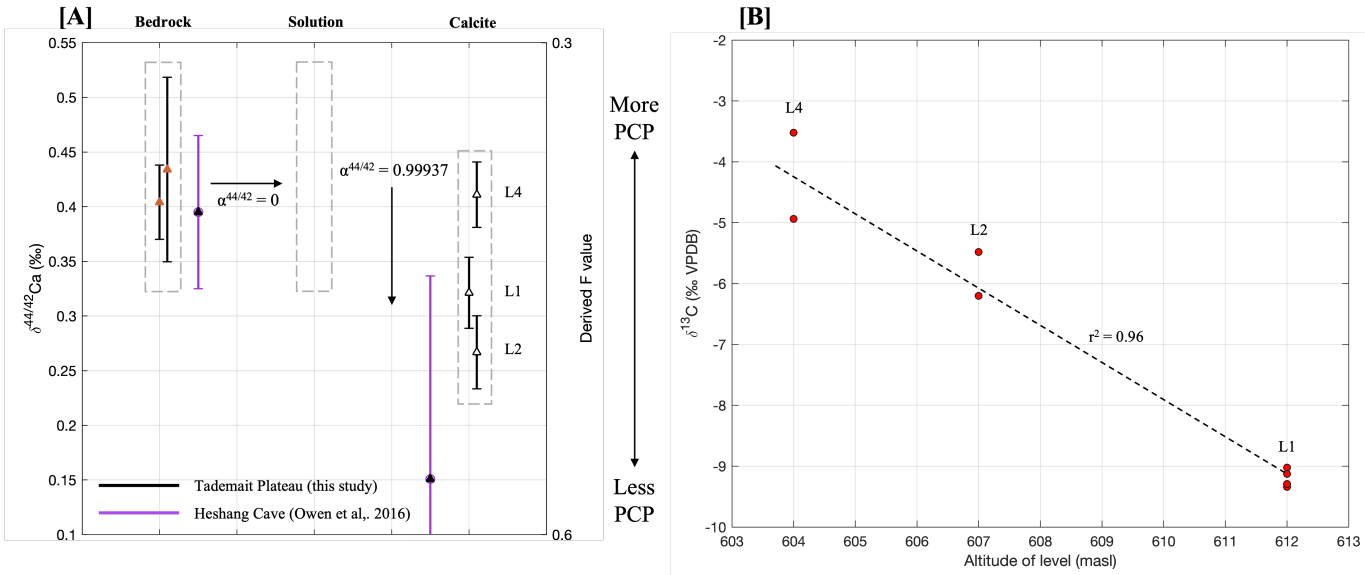


Figure 6.7: **Levels Calcite $\delta^{44/42}$Ca and δ^{13}C Data.** [A] $\delta^{44/42}$Ca isotope results from Levels geode calcite. α (fractionation factors) are taken from Owen et al. (2016) whom argue that initial solution $\delta^{44/42}$Ca values are equal to bedrock $\delta^{44/42}$Ca. L4 has a higher $\delta^{44/42}$Ca value than L1 and L2, indicative of more PCP having occurred prior to calcite formation. Purple bars are the mean and 2 standard deviations of measured $\delta^{44/42}$Ca in Heshang cave bedrock and stalagmite HS4 calcite. [B] 'Levels' calcite geode δ^{13}C against sample altitude. Higher altitudes are closer to the top of the plateau, associated with lower δ^{13}C values indicative of less PCP having occurred prior to calcite formation at L1. Annotations of 'L1' to 'L4' indicate the level from which calcite was collected.

This data is therefore suggesting that calcite geodes at L1 and L2, nearest the top of the plateau, formed with a larger proportion of calcium remaining in solution than calcite at L4, at ∼8-10m lower altitude, indicating a PCP control (Owen et al., 2016).

Values are similar to bedrock and calcite $\delta^{44/42}$Ca values from a stalagmite from Heshang cave, China (Owen et al., 2016; Figure 6.7), providing confidence that values observed on the Tademaït Plateau are similar to that measured in conventional speleothems. The higher (lower) $\delta^{44/42}$Ca (F) values in Tademaït calcite than Heshang cave are unsurprising considering the more arid conditions at the Tademaït Plateau, leading to more significant PCP occurrence.

Furthermore, there are shifts in calcite δ^{13}C of ∼5‰ between L1 and L4, with significantly higher values observed with increased depth from the top of the plateau ($r^2 = 0.96$). This is again suggestive of PCP via the preferential degassing of the lighter isotope, ^{12}C, during initial calcite formation (Owen et al., 2018) with shifts to higher δ^{13}C values occurring with progressive formation, corroborating with $\delta^{44/42}$Ca trends.

These magnitude of changes and overall trends in $\delta^{44/42}$Ca and δ^{13}C are not indicative of secondary calcite which has all formed from a homogenous starting solution, such as that which may be expected from a well-mixed aquifer. Instead, these trends provide further evidence for the formation of secondary calcite from meteoric water travelling from the top of the plateau downwards (Figure 6.8).

6.4.5 Clumped Isotope paleo-thermometry

Clumped isotope thermometry analysis of geode sample L4G7b calculated two Δ_{47} calibrated formation temperatures of 26.2 ± 2.4°C and 30.1 ± 5.6°C. This formation temperature closely agrees with contemporary mean annual temperatures measured at the In Salah GHCN-M station (Figure 6.1), which averages 26.4°C. Whilst these temperatures are also similar to shallow aquifer water temperatures (Guendouz et al., 2003), they are significantly cooler than deep, geothermal water (Edmunds et al., 2003), supporting the evidence for surface meteoric moisture being the source for calcite formation

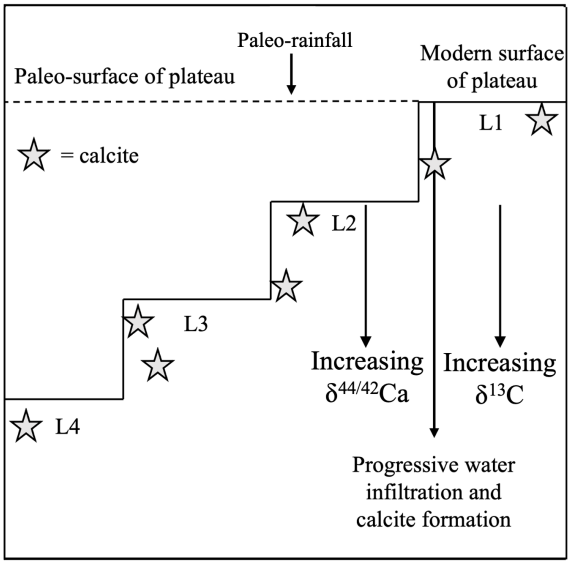


Figure 6.8: **Cartoon Representation of Levels Calcite Formation**. Cartoon representation of the theorised formation of calcite at the Levels location on the Tademaït Plateau. Both $\delta^{44/42}$Ca and δ^{13}C values increase with depth from the top of the plateau, suggestive of a PCP control and the progressive formation of calcite from the top of the plateau downwards.

on the plateau.

6.5 Discussion

6.5.1 Calcite Chronology

Depending on (i) the amount of diagenesis samples are experiencing (i.e. the extent to which the addition or loss of radionuclides have shifted a sample from its starting conditions) and (ii) the amount of sub-sample mixing within geode samples, there are likely numerous periods of increased rainfall and subsequent calcite formation throughout the past 400 kyrs. Whilst the exact timing of each of these periods cannot yet be quantified, the most robust ages are sourced from a single flowstone block, TPB1.

Including all analyses, TPB1 has a mean age and standard error of 416 ± 23 kyr BP to 95% confidence intervals. After the removal of ages with anomalous $\delta^{234}U_{(i)}$ and large (> 80 kyrs) analytical uncertainty, five ages remain with a mean age and standard error of 409 ± 23 kyr BP. The result of a similar mean age and standard error after applying

the criteria of which ages not to include in chronological interpretations, combined with remaining ages being consistent with closed-system behaviour, provides more confidence that this is the true age of TPB1 (Chen et al., 2020). There is, therefore, robust evidence that TPB1 was deposited during Marine Isotope Stage (MIS) 11 (Lisiecki and Raymo, 2005). An age-depth model from these five ages (Bronk Ramsey, 2009; Appendix V Figure 23) suggest that TPB1 growth occurred between 434 and 398 kyr BP.

This period of growth is coeval with the occurrence of MIS 11 in numerous other proxies (Candy et al., 2014). Observations of increased rainfall during MIS 11 are made in tropical West Africa (Rousseau, 2003), whilst Lake Megafezzan (27°N, 13°E) was dated to have been at its fullest extent (Armitage et al., 2007; Geyh and Thiedig, 2008; Drake et al., 2022). Helmke et al. (2008) note a pronounced increase in vegetation cover in north-west Africa for ∼25 kyrs from 420 kyr BP onwards, suggesting that peak wet conditions occurred at 409 kyr BP and identifying a likely influence of the West African Monsoon (WAM) and reduction in trade wind intensity. This is coeval with sapropel S11 (Kroon et al., 1998) for which maximum wet conditions are centred around 407 kyr BP. Peak North Atlantic SSTs are also between 410 and 400 kyr BP (Voelker et al., 2010) and model data suggests up to a 400 mm/yr increase in annual precipitation between 10-30°N (CLIMBER2-LPJ; Kleinen et al., 2014) across North Africa at 416 kyr BP, associated with the WAM.

MIS 11 is split roughly into two interstadials (MIS 11a, MIS 11c) and one stadial (MIS 11b) (Zhao et al., 2019). Whilst the transition into interstadial MIS 11c is suggested to have occurred from ∼430 kyr BP (Candy et al., 2014), there is no consistent pattern for the occurrence of stadials and interstadials MIS 11b and 11a, with some studies having proposed numerous abrupt climate events occurring prior to the onset of MIS 10 (Voelker et al., 2010).

Significantly, MIS 11 is also observed in stalagmites MegaMite (MM) from Ksar cave, and QC-1 from Maqlae cave (Figure 6.1), located in the southern foothills of southern Morocco (Barrott, 2014) and the Saharan Atlas (Chapter 5) respectively. Growth in

MM is modelled to be between 404 and 386 kyr BP, and averages 382 ± 34 kyr BP in QC-1. These samples therefore provide direct evidence for rainfall at the northern extent of the Sahara, towards the end of the interglacial, and later than the onset of TPB1 formation. Whilst there are numerous conditions for speleothem growth, this later onset of MM and QC-1 formation would suggest a later onset of rainfall at the northern extent of the Sahara, compared to earlier growth in the central regions of the desert.

6.5.2 Saharan rainfall during MIS 11

TPB1, QC-1 and MM δ^{18}O values are all consistent with carbonate precipitation from a meteoric moisture source. The depleted nature of the values (averages of -11.8‰ (TPB1), -10.2‰ (QC-1) and -9.6‰ (MM)) are indicative of long-distance moisture transport or strong Rayleigh fractionation (El-Shenawy et al., 2018; Henselowsky et al., 2021). Here, only the δ^{18}O records of TPB1 and MM are compared with other proxies, as whilst there is MIS 11 growth in QC-1 with similarly depleted δ^{18}O values, growth is very limited and subsequent constraints on stalagmite growth rate is poor within the period (Chapter 5).

MM δ^{18}O exhibits remarkably similar records to North Atlantic SSTs (Voelker et al., 2010; Figure 6.9). Warmer northern hemisphere SSTs are associated with increased ocean heat transport between the southern and northern hemispheres (McGee et al., 2014) and a resultantly more northerly zoned ITCZ (Marshall et al., 2014). Therefore, the close correlation between MM δ^{18}O and North Atlantic SSTs may be indicating an increase in tropical plume (TP) rainfall at the northern limits of the Sahara during MIS 11, for which a more northerly mean ITCZ (as identified by increased northern hemisphere SSTs) is a trigger (Chapter 4). Furthermore, during the Holocene, a high temperature anomaly between the north and south hemispheres (which leads to increased rainfall at Ksar cave and MM formation) is associated also with a strengthened Atlantic meridional overturning circulation (AMOC) (McGee et al., 2014). Whilst there is not

an equivalent north-south temperature anomaly during MIS 11, a "vigorous" AMOC is usually inferred during this period (Kandiano et al., 2017), suggesting that the same cause of rainfall at Ksar cave may apply.

Similar shifts to those observed in MM δ^{18}O and North Atlantic SSTs are exhibited in Lake Baikal %BiSil (a northern hemisphere temperature proxy) and Sanbao cave stalagmite δ^{18}O (a proxy for Asian Summer Monsoon (ASM) strength), both of which respond to orbital variations (Figure 6.9), suggests a regional fingerprint of MIS 11 in paleoclimate proxies, with close teleconnections between insolation, boreal tropical monsoon strength and ITCZ position. A shift to cooler and drier conditions is observed in all proxies between ∼398-392 kyr BP, coinciding with the stadial MIS 11b, as defined by Zhao et al. (2019) (Figure 6.9).

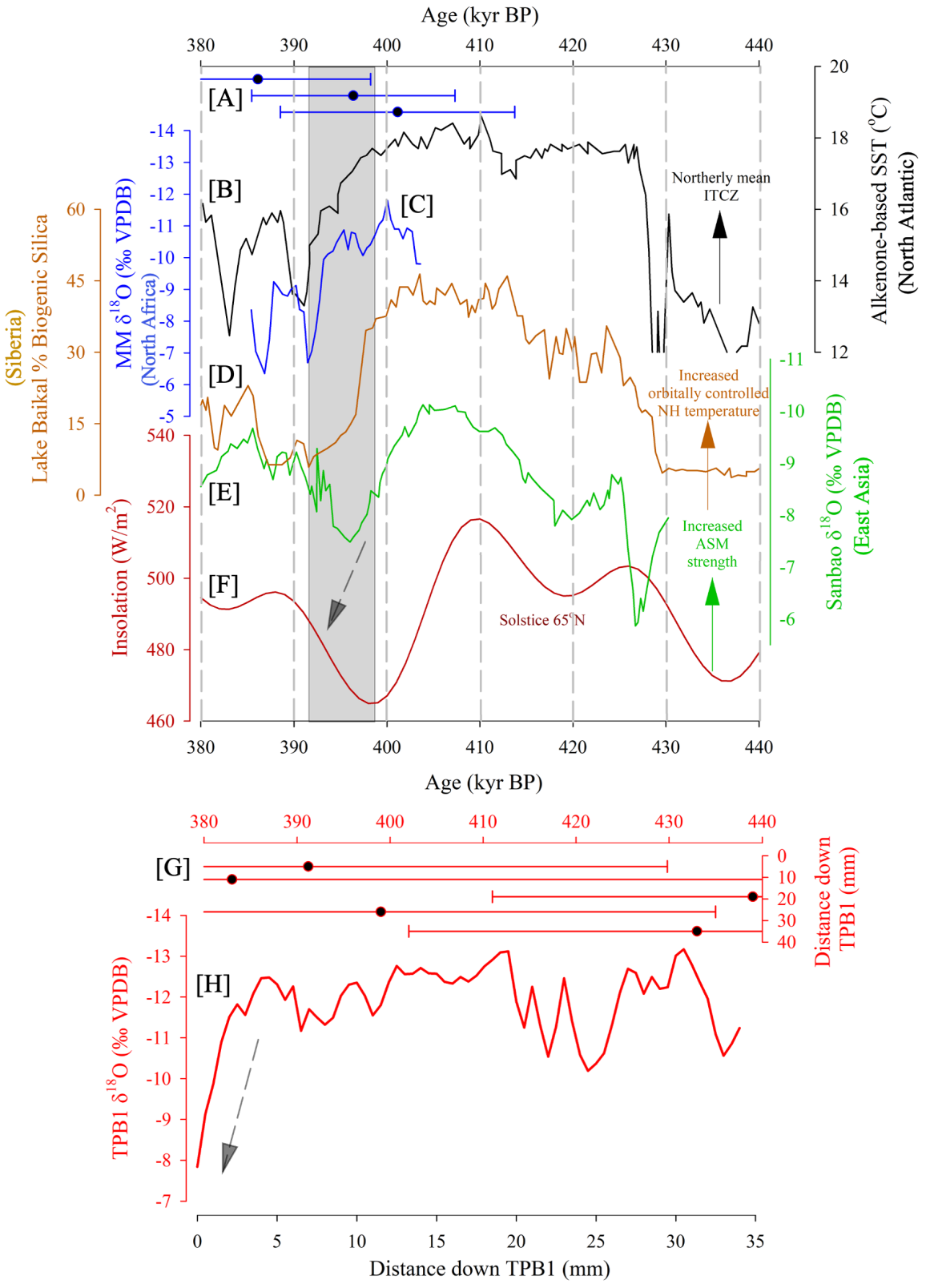

Age (kyr BP)
380
390
400
410
420
430
440
[A]
[B]
[C]
[D]
[E]
[F]
[G]
[H]
Northerly mean ITCZ
Alkenone-based SST (°C)
(North Atlantic)
MM δ18O (‰ VPDB)
(North Africa)
(Siberia)
Lake Baikal % Biogenic Silica
Increased orbitally controlled NH temperature
Increased ASM strength
Sanbao δ18O (‰ VPDB)
(East Asia)
Insolation (W/m2)
Solstice 65°N
Distance down TPB1 (mm)
TPB1 δ18O (‰ VPDB)

Figure 6.9: **MIS 11 Paleoclimate Proxies.** Paleoclimate proxies and orbital parameters during MIS 11. From top to bottom: [A] Black circles with red error bars are unmodelled MM U-Th ages. [B] The grey line is Alkenone-based sea surface temperatures (SSTs) at 39°N in the North Atlantic (Voelker et al., 2010). [C] Blue line; MM δ^{18}O (Ksar cave) [D] Brown line, Lake Baikal % biogenic silica, an orbitally controlled temperature proxy at 52-56°N (Prokopenko et al., 2006; Candy et al., 2014). [E] Green line; composite Sanbao cave δ^{18}O (Cheng et al., 2016; Zhao et al., 2019), a proxy for orbitally controlled changes in Asian Summer Monsoon (ASM) strength. [F] Maroon line, July 21st (boreal solstice) insolation at 65°N (Berger and Loutre, 1991). [G] Black circles with red error bars are unmodelled TPB1 U-Th ages plotted against distance from the top of the sample (y-axis). [H] TPB1 δ^{18}O plotted against distance from the top of the sample (x-axis). The grey bar indicates the approximate timing of stadial MIS 11b as defined in Zhao et al. (2019), during which a shift to drier and colder conditions occurs in all proxies, as indicated by the grey arrow. The equivalent grey arrow in [H] may indicate a similar shift to drier conditions in TPB1, prior to a cessation in formation.

Due to the chronological constrains of the sample, it is not viable to plot TPB1 on the same age time-series plot (Figure 6.9), and so it is instead compared as a depth plot. Ages suggest that the TPB1 record could theoretically sit at any point on the x-axis and subsequently may have viable comparisons with records of North Atlantic SST, Lake Baikal %BiSil or MM δ^{18}O, subsequently limiting interpretations which may be made into the controls and source of rainfall at the Tademaït plateau. However, a shift is also observed to values suggesting colder and drier conditions observed in all proxies at ∼400 kyr BP is also observed at the end of the TPB1 δ^{18}O record, potentially indicating a coeval representation of stadial MIS 11b. Furthermore, the flat top of the TPB1 record is similar to the middle sections of the North Atlantic SST and Lake Baikal %BiSil records, also suggesting regional similarities between proxies.

6.5.3 Moisture Sources

Whilst it is difficult to de-convolute the exact sources of rainfall which leads to TPB1 and MM formation, several viable mechanisms exist. Previous work (Chapter 4) suggests that it is unlikely that the WAM front reached as far north as 32°N, where MM formed, and that increased moisture transport via TPs are a likely source of rainfall

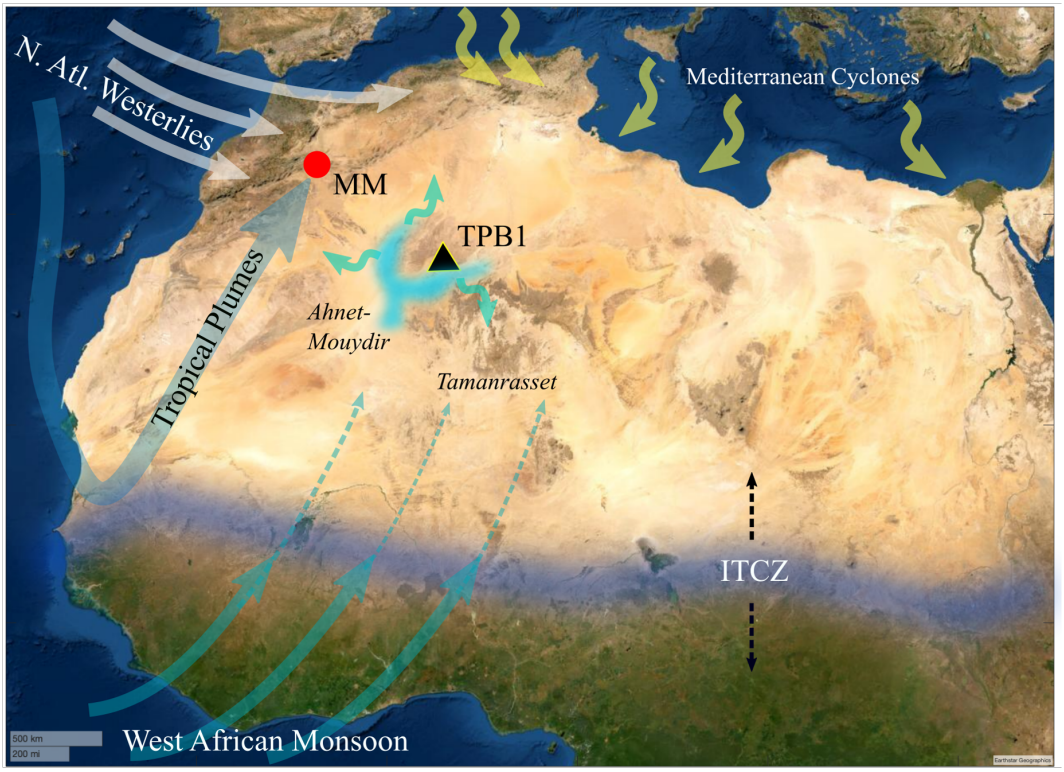


Figure 6.10: **North Africa (Paleo)Rainfall Mechanisms.** Cartoon representation for the different potential mechanisms of rainfall in North Africa and at the Tademaït Plateau, plotted against a satellite image of North Africa. North Atlantic westerlies and Mediterranean cyclones are drawn as white and yellow arrows respectively. The modern approximate northern extent of the ITCZ is represented by a shaded dark blue band at 15°N. An approximate extent of Lake Ahnet (Ahnet-Mouydir) is drawn as a shaded blue area, approximated from Drake et al. (2022). The location of Tamanrasset, which receives a dominant proportion of WAM rainfall in the modern-day, is annotated with dashed blue lines extending from the modern WAM range representing this northerly transport of contemporary moisture. The location of Ksar cave is plotted as a red dot and annotated with the sample name 'MM', with the proposed upper-level trough moisture trajectory of tropical plumes drawn (Knippertz et al., 2003b).

at this latitude, as in the modern day (Knippertz, 2003). Agreements between MM δ^{18}O and North Atlantic SSTs, which may be used as a proxy for mean ITCZ position, support this (Figure 6.9). However, the lack of evidence for this mechanism during contemporary rainfall events at the Tademaït plateau, combined with reduced orographic uplift compared to at the Atlas Mountains, suggesting alternate climate mechanisms were required for the rainfall which led to TPB1 formation during MIS 11.

There is evidence for contemporary WAM-sourced rainfall at Tamanrasset (23°N), ~600 km south of the Tademaït Plateau (Figure 6.1). Therefore, an approximately 5°

shift in the northerly influence of the WAM system, a conservative extension proposed widely in modelling studies (Kuhlmann et al., 2004) and suggested by isotopic analysis from Megalake Darfur (Drake et al., 2022), could conceivably directly increase WAM rainfall at the plateau. A direct WAM rainfall source at the Tademaït Plateau, and TP rainfall source at Ksar cave, would suggest a tropical moisture source in both cases via two mechanisms.

There is also potential that non-contemporary sources of rainfall occurred at the plateau during periods of increased moisture availability. It is known that a large surface water body, referred to as Lake Ahnet or the Ahnet-Mouydir basin, existed just south of the Tademaït plateau during the mid-Holocene (Lézine et al.,2011; Drake et al., 2022). Modelling studies have suggested that moisture recycling from terrestrial water bodies was important during humid periods in bringing rainfall to more northerly regions (Krinner et al., 2012). Rainfall at the Tademaït Plateau may therefore have occurred via local evaporation and precipitation processes from these terrestrial water bodies, similar to that observed in other modern day micro-climates (Saranya et al., 2021). This mechanism would require earlier rainfall in the Atlas mountains, from which rising groundwater levels and river flow to the central Sahara would lead to the formation of Lake Ahnet. Drake et al. (2022) summarised the importance of southward flowing rivers from increased Atlas Mountain rainfall in flooding the Ahnet-Mouydir basin and some limited U-Th chronology of speleothem growth at Maqlae cave between ∼460 and 430 kyr BP (Chapter 5), prior to the onset of TPB1 formation, may support this hypothesis. However, a current lack of reliable chronology from Lake Ahnet means this cannot be confirmed (Drake et al., 2022).

Finally, Sultan et al. (1997) amongst others postulate that an Atlantic source of precipitation can be inferred from stable isotope data of both fossil groundwater and U-Th dated travertine deposits from the Western Desert, Egypt, with rain occurring from west to east via westerly air masses travelling from the North Atlantic during periods of southward-shifted and strengthened winter westerlies (Alfy et al., 1997). However,

this is considered an unlikely source of rainfall at the Tademaït plateau during MIS 11 due to chronology being during a major interglacial. Lower δ^{18}O values are coeval with increased summer insolation and strengthened monsoon systems in ASM regions (Zhao et al., 2019), suggesting that sub-tropical westerlies would not be in a phase of increased strength or southwards positioning.

These comparisons show that numerous moisture sources may be influencing the TPB1 and MM δ^{18}O records, and it is not currently possible to identify the moisture source at the Tademaït plateau during periods of increased rainfall. Modern climate observations suggest that WAM and TP rainfall are respectively a likely cause at the Tademaït plateau and Ksar cave, although moisture recycling may have also contributed. The homogeneity of oxygen isotopes in other Tademaït Plateau calcite blocks (Appendix V Figure 22), which likely did not all grow during MIS 11, suggests that the mechanism bringing rainfall to the region is a recurring phenomenon at the Tademaït Plateau.

Environmental conditions between 28-32°N during MIS 11

Despite chronological uncertainties, similarities also exist between TPB1 and MM δ^{13}C records (Figure 6.11). The extent to which δ^{13}C values vary can be impacted upon by numerous variables makes interpretations complex, including prior degassing and carbonate precipitation in the karst, changes in overlying soil vegetation, atmospheric and soil pCO2 and the extent and open/closed-system nature of bedrock dissolution (Owen et al., 2018). Despite this, Hellstrom et al. (2020) demonstrated the robustness of flowstone samples in indicating surface vegetation and soil cover, whilst numerous studies have shown the responsiveness of stalagmites in recording vegetation (Yin et al., 2017; Lechleitner et al., 2017; Fohlmeister et al., 2020). Subsequently, similar variations in TPB1 and MM δ^{13}C may be representing coeval or equivalent variations in vegetation cover and environmental conditions at the top of the Tademaït Plateau and above Ksar cave. MIS 11 is thought to have been influenced by numerous abrupt climate events

(Candy et al., 2014), which may be being represented in the large changes of up to 8‰ in both TPB1 and MM δ^{13}C. Whilst it is difficult to be certain about the controls on δ^{13}C without trace element or calcium isotope analysis, the similarities between the magnitude of change in δ^{13}C between the records may be the first proxy evidence for coeval environmental conditions between 28-32°N during MIS 11, such as changing vegetation amount or type, corroborating with model results (Pausata et al., 2020).

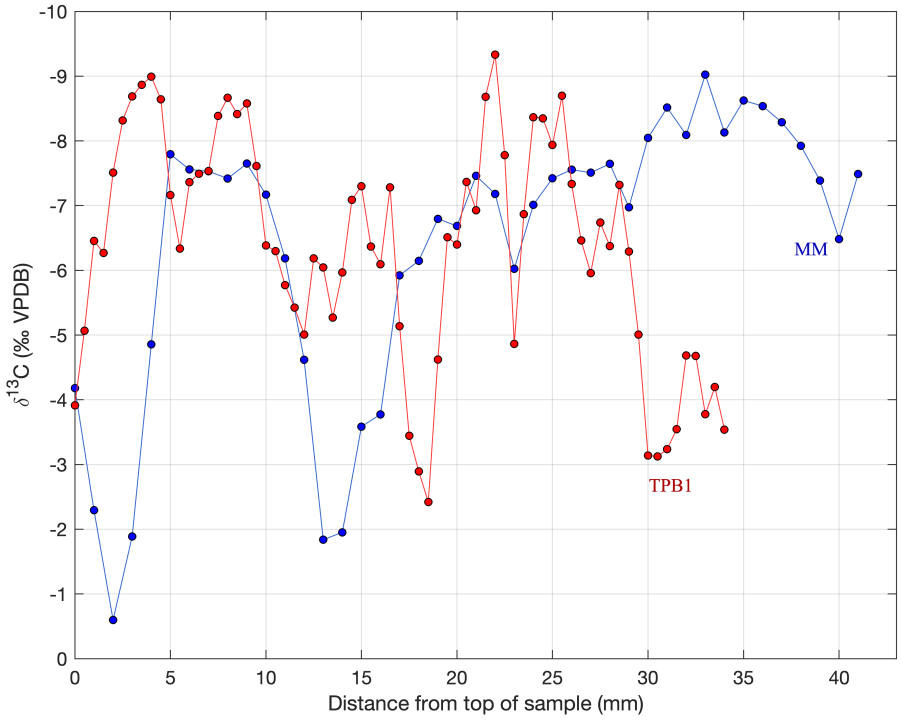


Figure 6.11: **TPB1 and MM δ^{13}C Records.** TPB1 (red) and MM (blue) δ^{13}C records plotted against depth (mm) from the top of the respective samples. The physical amount of growth in each sample during MIS 11 is similar (35mm in TPB1, 40mm in MM). Absolute changes in δ^{13}C in both records is almost identical, with slightly higher values of ∼ -1‰ observed in MM towards the end of growth (2mm from the top of the sample). Variations of 5‰ are observed in both records at similar distances from the top of the sample, particularly between ∼5 and 25 mm.

6.5.4 Paleoclimate Significance

These data provide the first direct evidence for coeval rainfall across large portions of the Sahara (between at least 28-32°N) during periods of increased north-west Africa rainfall.

Direct rainfall at the Tademaït Plateau is of significance due to its role as a recharge zone for the Complex Terminal and Continental Intercalaire aquifers. Using fractionation factors expressed in Kim and O'Neil (1997) (Chapter 1), clumped isotope thermometry formation temperatures (which agree with average local temperatures from the area), and measured δ^{18}O (VSMOW) in aquifer water (the best approximation for paleo-rainfall at the plateau), the calculated range of calcite δ^{18}O (VPDB) is comparable to the measured δ^{18}O range in the calcite. This provides evidence that rainfall which is replenishing the CT and CI aquifers at the recharge zone of the Tademaït Plateau, is also leading to the chemical deposition of the calcite observed. Whilst this may also suggest that calcite itself formed sub-aqueously from aquifer water, this is considered unlikely due to the morphology of the calcite blocks, evidence provided by δ^{13}C and $\delta^{44/42}$Ca data, and the fact that water drains away from the southern edge of the plateau, meaning it is unlikely that a sustained sub-aqueous environment existed.

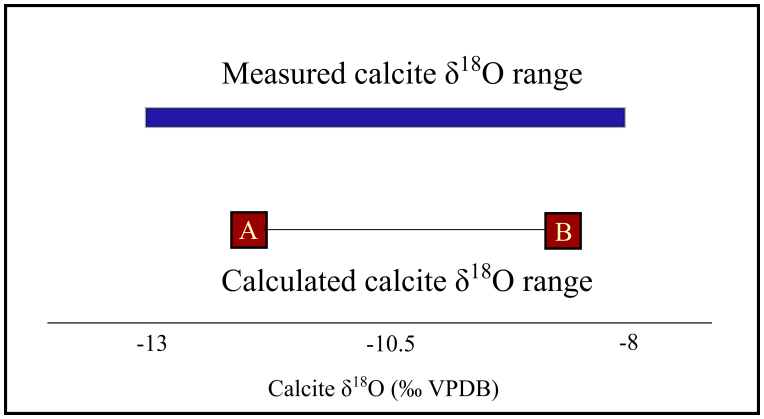


Figure 6.12: **Measured and calculated δ^{18}O Variations**. Cartoon representation of the measured δ^{18}O range in Tademaït Plateau calcite (blue bar) compared to the calculated δ^{18}O range expected from measured clumped isotope thermometry temperatures and aquifer δ^{18}O values (black line and red squares). End members A and B represent the calculated calcite δ^{18}O using maximum and minimum measured clumped isotope temperatures and aquifer δ^{18}O values. For A: Clumped Isotope temperature = 30.1°C, Aquifer δ^{18}O = -8.39 ‰. For B: Clumped Isotope temperature = 26.2°C, Aquifer δ^{18}O = -6.06 ‰. Fractionation factors from Kim and O'Neil (1997) were used for the calculation.

Subsequently, the U-Th chronology of closed system calcite samples from the plateau is giving information into the timing of periods of aquifer recharge. This offers potential

for vastly improving the understanding of the rate and timing of major Saharan aquifer recharge, should further closed-system U-Th chronology be attained from the plateau, throughout the late Quaternary. Currently, the timings of aquifer replenishment are largely unknown due to ^{14}C limitations of dating water and the discharge of water from older periods of aquifer recharge into the oceans, but is of great importance for modern-day human populations living in the region and relying on these water sources (Khezzani and Bouchemal, 2018).

6.6 Conclusion

The results presented here offer significant evidence for a sustained period of increased local rainfall during MIS 11, not only at the northern and southern limits of the Sahara, but in the very centre of the desert where both tropical and North Atlantic sourced moisture does not presently reach in great volume. Whilst it is evident that increased rainfall occurred at the Tademaït Plateau during MIS 11, it is not currently possible to identify the source or precise timing of the rainfall within the interglacial at the centre of the Sahara, and a number of mechanisms may have acted to bring rainfall to the Tademaït Plateau. Nonetheless, this research gives strong potential for reconstructing further periods of increased rainfall in the central Sahara, offering insight into the occurrence and cause of rainfall here, and subsequently the frequency of major aquifer recharge in the presently hyper-arid central Sahara.

Chapter 7

Sub-monthly African Humid Period trace element records

Contents

7.1 Introduction 150

7.1.1 Trace elements as a stalagmite proxy 152

7.2 Methods 153

7.2.1 Sub-sampling 153

7.2.2 Trace element analysis 154

7.2.3 Stable isotope analysis 154

7.3 Results and discussion 155

7.4 Conclusion 159

Acknowledgments

Acknowledgments in this chapter are made to Christopher Day for measuring speleothem stable isotopes, and to Phil Holdship for performing trace element analysis.

Abstract

This chapter presents a new high-resolution trace element record across the entire growth history of stalagmite ASD-1, from southern Morocco, along with two sub-monthly trace element and stable isotope records from separate growth sections of the stalagmite. These records are presented as further evidence for changes in the availability of moisture and seasonality of rainfall in the South of Atlas region during the African Humid Period. Whilst not included in the manuscript presented in Chapter 4, these data provide robust initial evidence for the potential of using trace element variations in tracking changes in rainfall during the AHP in southern Morocco, for which information is currently limited, thus contributing further important theoretical interpretations of past climate.

7.1 Introduction

Whilst Chapters 4 to 6 of this thesis present important advances as to the timing and potential source of rainfall in the South of Atlas (SOA) during past periods of increased rainfall, the extent to which rainfall amount varied *within* these periods has not been extensively assessed. This chapter therefore provides the first indications into how trace elements may be applied in SOA speleothems and what interpretations may be drawn from this proxy. Stalagmite ASD-1 was collected from Asdif cave in the Anti-Atlas Mountains of southern Morocco, and formed between 6 and 4.3 kyr BP during the mid-Holocene African Humid Period (AHP) (Barrott, 2014). The U-Th and stable isotope data collected from ASD-1 is presented in Chapter 4 of this thesis combined with data from stalagmite KFT-1 (collected from Kef Thaleb cave, $<$ 10 km from Asdif cave) as evidence for increased tropical plume rainfall across the SOA range during the AHP. Here, data from ASD-1 are briefly examined in more detail prior to the presentation of three new trace element records, including two ultra-high-resolution (sub-monthly) records, which provide further detail into potential changes in rainfall amount and cyclicity at Asdif cave during the AHP, and the potential controls on the sample's δ^{13}C record, which is not presented in Chapter 4.

Stalagmite ASD-1, aragonitic in mineralogy, can be split into two distinct periods of growth separated by dark lamina in the middle of the sample (Figure 7.1). The lower section of ASD-1, forming between 6.0 and 5.5 kyr BP, averages an extension rate of 180 μm/yr, δ^{18}O values of -9.5 ‰ and δ^{13}C values of -4.5 ‰. The upper section on the other hand, forming between 5.5 and 4.3 kyr BP, exhibits a slower extension rate of 49 μm/yr, higher δ^{18}O values of -8.6 ‰ and higher δ^{13}C values of -3.5 ‰. Initial interpretations suggested that the lower (older) section of ASD-1 formed during wetter conditions which transitions to a significant reduction in effective precipitation at the site after 5.5 kyr BP (Barrott, 2014), corresponding with a reduction in growth rate of the sample and a shift to higher δ^{18}O and δ^{13}C values. This agrees with the interpretations made in Chapter 4, in which a consistent reduction in tropical plume

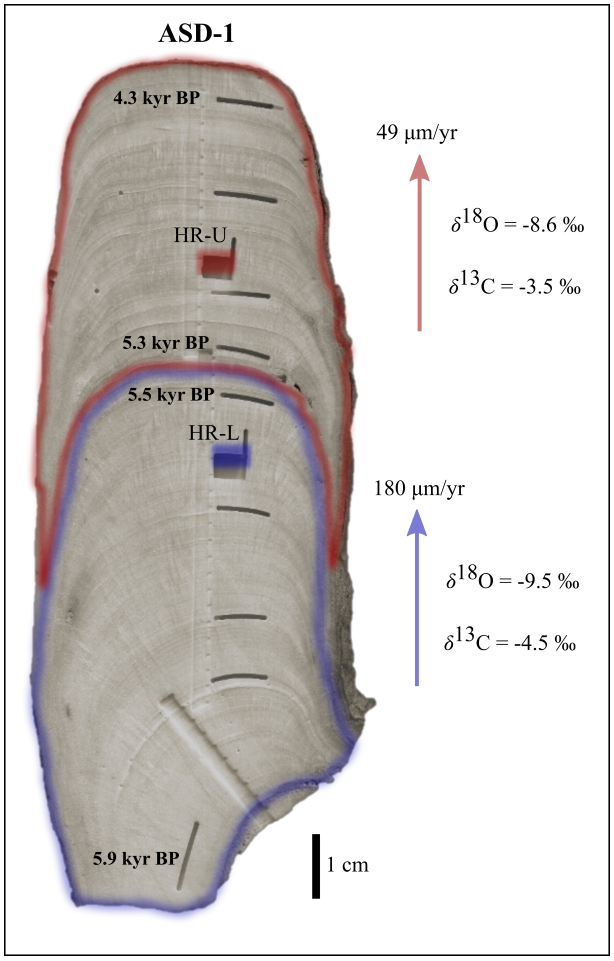


Figure 7.1: **Summary of ASD-1 Proxies**. Figure of ASD-1. The upper half of the stalagmite is bordered by a red line and the lower half by a blue line. Values of average extension rate, δ^{18}O and δ^{13}C values for each section are annotated. Locations from which the ultra-high-resolution trace element analyses are marked by red and blue shaded areas in the upper (HR_U) and lower (HR_L) half respectively.

rainfall throughout the mid-Holocene is inferred, likely resulting in progressively more arid conditions towards the end of ASD-1 formation. This shift in ASD-1 occurring at ∼5.5 kyr BP is coeval with a suggested abrupt increase in terrigenous flux from North Africa, observed in marine core records (Adkins et al., 2006; McGee et al., 2013).

However, whilst $\delta^{18}O$ interpretations show that there is a reduction in the proportion of tropical plume rainfall throughout the AHP in the Anti-Atlas, there are multiple factors which may impact upon speleothem $\delta^{13}C$ (Owen et al., 2018) and growth rate, with higher and slower values respectively not necessarily indicating reduced rainfall amount (Fairchild and Baker, 2012). Potential changes in rainfall amount throughout the AHP were therefore further investigated using trace element U/Ca ratios and $\delta^{13}C$ values of stalagmite ASD-1.

7.1.1 Trace elements as a stalagmite proxy

Trace element analysis in speleothems is increasing applied as a proxy for changes in rainfall amount above a cave (Day and Henderson, 2013; Jamieson et al., 2016; Owen et al., 2018; Vansteenberge et al., 2020). Certain elements (X) have a strong partitioning between fluid H_2O and solid $CaCO_3$ phases, and therefore are preferentially incorporated into secondary carbonates' crystal lattice as a proportion of calcium (Ca) (Lechleitner et al., 2016). The extent to which elements are preferentially incorporated is dependent on their distribution coefficients (D(X)), with higher values indicating increased incorporation of elements into the solid phase during carbonate precipitation (Day and Henderson, 2013; Wassenburg et al., 2016).

During periods of reduced moisture input to a karst system, water will take longer to percolate from the surface into the cave, leading to increased progressive degassing of CO_2, and subsequent prior precipitation of calcium carbonate, taking place in the karst above the cave. Uranium (U) for example has been shown to have a high partition coefficient into aragonite (Jamieson et al., 2016; $D(U) = 3.74 \pm 1.13$), meaning it is preferentially incorporated into the crystal lattice, a chemical characteristic which

makes aragonite stalagmites good targets for U-Th chronology. The amount of U in a stalagmite is therefore sensitive to the percentage of aragonite already precipitated from solution (%cp), by which increased prior aragonite precipitation (PAP), typically during drier environmental conditions, results in lower U/Ca ratios in the stalagmite. Changes in stalagmite U/Ca can thus be used, in conjunction with other environmental proxies such as δ^{13}C, as an indicator in changes in the amount of PAP, and subsequently rainfall amount, happening above a cave.

7.2 Methods

7.2.1 Sub-sampling

ASD-1 was sampled on a NewWave micro-mill at two sections along its growth axis (Figure 7.1); one period during when the speleothem was growing slower, after 5.5 kyr BP (HR_U) and one for during more rapid growth, prior to 5.5 kyr BP (HR_L). Powders were milled from a sampling trench of 3mm depth and 5mm width, at a sampling resolution of just 5μm. Using the high-precision U-Th chronology from ASD-1, it can be estimated that this resolution corresponds to approximately 30 samples per year in the lower faster growing section, and approximately 10 samples per year during upper slower growth. Sufficient sub-samples were milled to cover a 3-year period in each instance to gain an insight into the seasonality of hydrology, equating to 90 and 30 samples for the lower and upper sections respectively. It is noted however that ASD-1 may have been growing significantly faster or slower in the < 0.5 mm sections in which sampling was undertaken, and there is subsequent uncertainty as to how many years worth of stalagmite growth may actually have been sampled.

Sub-samples analysed for trace elements were collected from the samples surface using isopropanol alcohol-cleaned aluminium tools, and stored directly in acid leached polypropylene centrifuge tubes. From each sub-sample, 20-60μg was transferred into glass KIEL vials for stable isotope analysis, and the remaining powder was left in 2mL

acid-leached centrifuge vials for dissolution and subsequent trace element analysis. Sub-sampling masses < 250µg was difficult and so in some cases, not enough powder was collected, resulting in some missing analyses.

Furthermore, a full-section trace element record was constructed for ASD-1, consisting of 148 measurements from base to top, equating to a sub-decadal resolution in the lower section and sub-centennial resolution in the slower growing upper half. Trace element analysis was always carried out on aliquots of the same sub-samples used for stable isotope analysis to allow for direct comparisons between proxies.

7.2.2 Trace element analysis

An aliquot of the sub-sample was dissolved in 2% **Δ**HNO3, using a mass which matched to an approximate calcium (Ca) concentration of 15-20ppm in a volume of 2.2 mL. Sub-samples were analysed on a PerkinElmer NexION 350D ICP-MS (Inductively Coupled Plasma Mass Spectrometer). Helium was used as a collision gas in the cell for kinetic energy discrimination (KED) and multi-element calibration standards were run alongside the sub-samples, supplied from single element high-purity standards whose concentrations were certified against NIST Spectrometric Standard Solutions. A stock of each standard was diluted using the ESI prepFAST dilution system between 2 and 150 times to create calibration standards over a wide concentration range to cover the varying elemental concentrations in the samples. The concentration of U is reported as molar ratios relative to the major element Ca, and the analytical uncertainty is reported as twice the relative standard deviation of a number of monitor standards (U/Ca = ±6%; n = 7).

7.2.3 Stable isotope analysis

The methods for stable isotope analysis of the whole section (low-resolution) ASD-1 record can be found in the supplementary information of Chapter 4 or Barrott (2014). For the ultra-high-resolution analysis, 20-60 µg of carbonate powder was analysed for

oxygen and carbon stable isotopes using a Thermo Scientific Delta V isotope ratio mass spectrometer (IRMS) coupled to a Kiel IV carbonate device at the University of Oxford, Department of Earth Sciences (further described in Chapter 3). Accuracy and precision were checked using an in-house marble secondary standard's long-term average, NOCZ, included in all runs, for which long-term δ^{13}C and δ^{18}O measurements averages 2.19‰ ± 0.05‰ and -1.9‰ ± 0.07 ‰. NOCZ measurements within ultra-high-resolution ASD-1 stable isotope runs averaged δ^{13}C of 2.20‰ ± 0.04‰ and δ^{18}O of -1.85‰ ± 0.07‰ (1σ, n=7), within the long-term NOCZ values.

7.3 Results and discussion

As a result of the high associated D(X) between U and Ca (Jamieson et al., 2016), U/Ca is likely the most responsive elemental ratio in ASD-1 to changes in PAP and subsequent moisture availability. Subsequently, in these initial interpretations, U/Ca and δ^{13}C variations are the focus of the discussion.

There is a strong anti-correlation between U/Ca and δ^{13}C prior to 5.5 kyr BP (r^2 = 0.47), with lower δ^{13}C values (wetter) trending towards higher U/Ca values (wetter), suggesting a homogenous control on both proxies before 5.5 kyr BP, best explained by changes in the amount of PAP (Figure 7.2). Whilst some parts of the records remain anti-correlated after 5.5 kyr BP, such as at the very end of growth, there is no clear correlation (r^2 = 0.03) between U/Ca and δ^{13}C at this time. This lack of correlation after 5.5 kyr BP is coincident with a convergence in the long-term trends of the two proxies as δ^{13}C shifts to higher isotopic values, suggesting drying, and U/Ca also trends towards higher values, although in this case suggesting wetter conditions (Figure 7.2). This may suggest a breakdown in PAP controlling long-term variation in one or both proxies, with potentially other sources of U impacting on U/Ca values such as increased dust flux into the cave (Frumkin and Stein, 2004), or δ^{13}C becoming more responsive to factors such as increased bedrock dissolution (Owen et al., 2018).

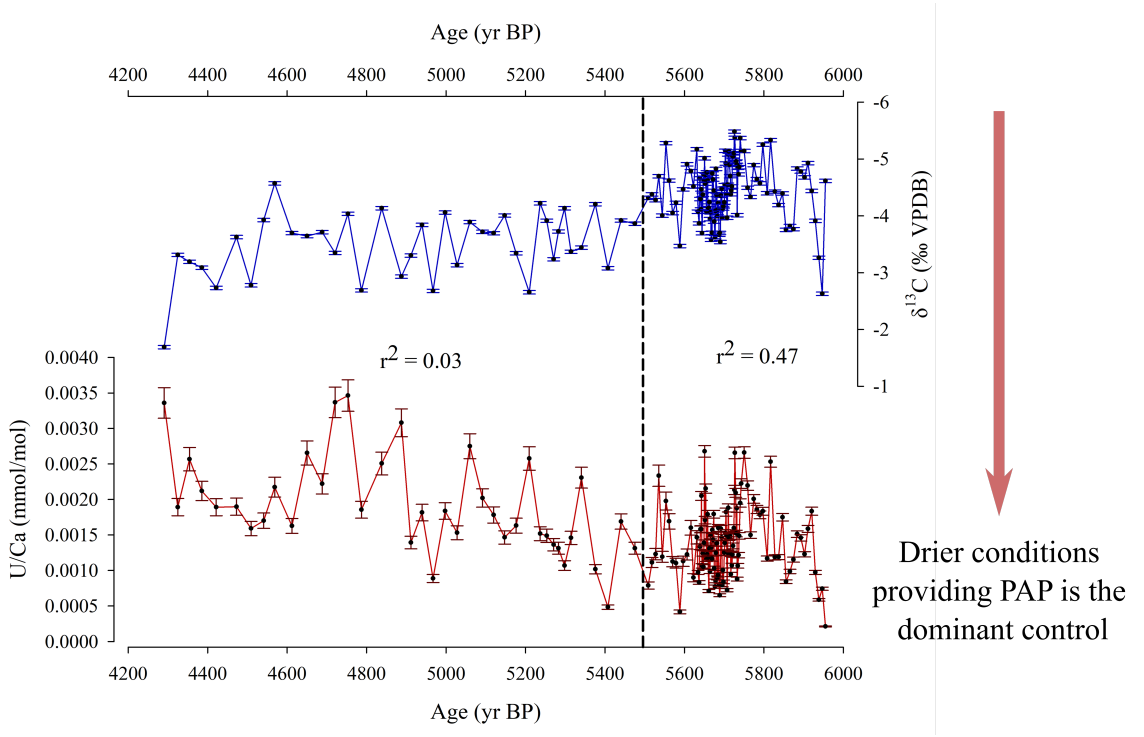


Figure 7.2: **Full section ASD-1 Trace Element Record.** Full section ASD-1 U/Ca (red) and δ^{13}C (blue) records. Higher (lower) values in U/Ca (δ^{13}C) represent generally wetter conditions. There is a high correlation coefficient between the two proxies prior to 5.5 kyr BP, with a breakdown in the relationship in the younger section of the record. The boundary between these two distinct growth periods is marked by the dashed black line.

In the lower, faster growing section of ASD-1, U/Ca from ultra-high-resolution analysis exhibits cyclicity between high (peaks of ∼0.0021 mmol/mol) and low (troughs of ∼0.0016 mmol/mol) values, with three troughs representing drier conditions during growth and two clear peaks representing wetter conditions (Figure 7.3). There is no overall trend in the data, suggesting stable overall environmental conditions. The clear cyclicity between peaks and troughs in U/Ca are potentially suggesting annual or seasonal cyclicity of wet-dry periods prior to 5.5 kyr BP in ASD-1, indicating reliable and cyclical changes in the input of water above the cave. δ^{13}C generally anti-correlates with U/Ca (except for the lower values at 350 μm depth), with lower δ^{13}C during periods of higher U/Ca indicating a PAP control. The less clear cyclicity in δ^{13}C compared to U/Ca may be expected due to the greater number of controls which can impact on a samples δ^{13}C, which may be dominantly controlled by PAP but still influenced by

other factors (Owen et al., 2018).

In the upper, slower growing section, the occurrence of annual cycles is not evident. Instead, both proxies exhibit a general trend towards drier conditions (lower U/Ca and higher δ^{13}C) across the period of formation (Figure 7.3). These data suggest that PAP may still be the dominant control on δ^{13}C and U/Ca over short timescales, exhibited by a strong anti-correlation ($r^2 = 0.67$), but not over longer timescales, shown by lack of correlation in the low-resolution data after 5.5. kyr BP (Figure 7.2). The lack of cyclicity in either variable suggests either (i) non-continuous stalagmite growth, with the stalagmite only growing for short periods, for example during one season, (ii) the stalagmite is growing continuously, but much slower, as suggested by U-Th data, with no clear wet and dry seasonality or (iii) the stalagmite was growing faster than expected across the sampling period, and analysis covers less of a temporal range than expected and so observations of cyclicity was not possible. Together, the strong anti-correlation in high-resolution analysis and lack of correlation in low-resolution analysis may suggest non-continuous growth of ASD-1 after 5.5 kyr BP, where PAP is a dominant control on δ^{13}C and U/Ca during the short periods that the stalagmite is growing, but separate factors are impacting the long-term trends of each variable.

These trace element data provide the first evidence for the potential of tracking changes in moisture availability in the SOA during the AHP. There appears to be a clear shift from cyclical wet-dry conditions prior to 5.5 kyr BP, in which PAP is the dominant control on U/Ca and δ^{13}C values, to slower formation after this time where the two proxies diverge and environmental interpretations become more convoluted. A breakdown in the relationship between δ^{13}C and U/Ca may suggest less continuous stalagmite growth after 5.5 kyr BP, associated with the reduced occurrence of tropical plume rainfall towards the end of the AHP (Chapter 4).

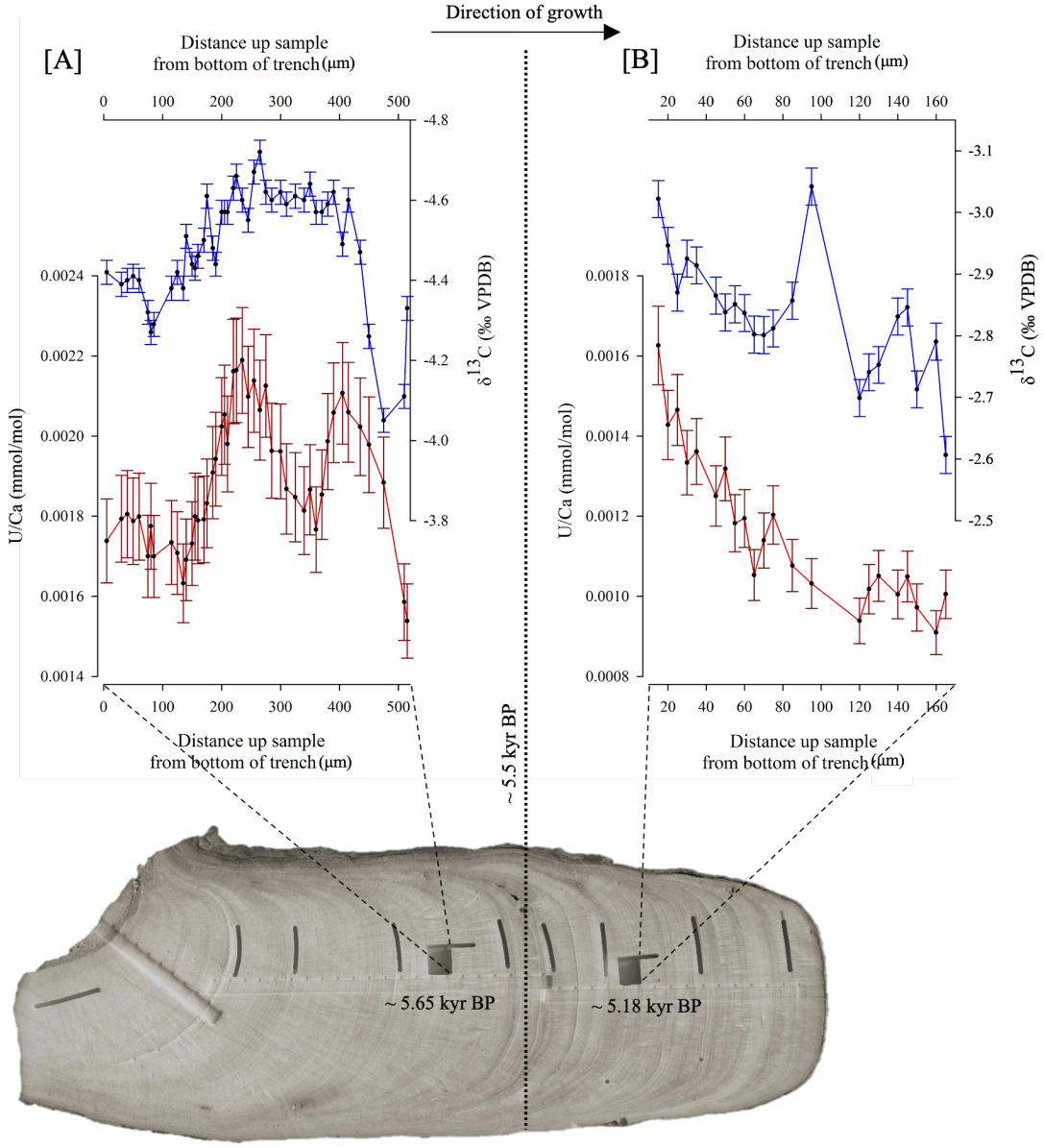


Figure 7.3: **Ultra-high-resolution ASD-1 Trace Element Records.** Ultra-high-resolution U/Ca and δ^{13}C records for ASD-1 plotted above a high-resolution scan of the stalagmite. [A] Lower ultra-high-resolution record, milled at approximately 5.65 kyr BP at a temporal resolution of just over one sample per two weeks, over a total period of approximately 3 years. U/Ca exhibits clear cyclicity between peaks and troughs. δ^{13}C generally anti-correlates with U/Ca except for the lower values at 350 µm depth [B] Upper ultra-high-resolution record, milled at approximately 5.18 kyr BP at a temporal resolution of just under one sample per month, over a total period of approximately 3 years. Both U/Ca and δ^{13}C exhibit a general trend towards drier conditions up the sample, with no apparent cyclicity.

7.4 Conclusion

The analysis of sub-annual and seasonal records within stalagmites is continually being advanced as a powerful resource of information (Baldini et al., 2021). Whilst the results in this chapter are preliminary in nature, they offer robust evidence for the use of X/Ca analyses in further understanding changes in rainfall amount and the controls on environmental proxies in SOA stalagmites. The coincidence of major changes in numerous geochemical proxies in ASD-1 across 5.5 kyr BP supports past interpretations of a regional shift in climate conditions on the North African continent at this time (Adkins et al., 2006; McGee et al., 2013), although the continuation of ASD-1 growth after 5.5 kyr BP does not support this age as being the "end" of the AHP.

The application of additional geochemical measurements, such as calcium isotopes, in a multi-proxy approach in instances where interpretations are complex, for example during the divergence of $\delta^{13}C$ and U/Ca in the upper section of ASD-1, would also increase the robustness of interpretations. Furthermore, applying techniques such as laser ablation to ASD-1 to observe when cyclicity does and does not occur across the stalagmites growth history would vastly increase the robustness of interpretations.

Chapter 8

Conclusions

Contents

8.1 Summary 162

8.1.1 Climate variability during the African Humid Period 163

8.1.2 Improved temporal coverage of north-west Sahara rainfall . . 163

8.1.3 Records of direct rainfall in the central Sahara 164

8.1.4 Potential for sub-annual measurements of paleo-hydrology in the northern Sahara 164

8.2 "Green Sahara" periods 165

8.3 The South of Atlas 166

8.4 Future work 166

8.1 Summary

The aim of this research was to increase the spatial and temporal coverage of high-resolution and absolute-dated terrestrial paleoclimate archives from the northern and central Sahara, with the aim of better understanding the mechanisms, extent and timing of past increased rainfall. Fieldwork across northern and central regions of the Algerian Sahara, and subsequent geochemical analysis of numerous collected speleothem and secondary carbonate samples, has made great strides in progressing knowledge in this area.

New cave sites from the Saharan Atlas have added to a longitudinally extensive coverage of direct rainfall paleoclimate records across the Atlas Mountain Range. Numerous periods of speleothem growth are observed in caves 100s of kms apart, providing robust evidence for periods of regionally increased rainfall in north-west Africa. In the central Sahara, the first evidence for local rainfall occurring in the middle of the desert is presented, providing evidence that direct increases in rainfall occurred in presently hyper-arid environments, rather than just distal moisture sources causing an increase in moisture availability in these regions. Furthermore, interpretations and additional data on samples collected previously (Barrott, 2014) have robustly characterised the African Humid Period at the northern extent of the desert.

This research has therefore thoroughly begun to address the ever-increasing need for improving the spatial coverage of well-dated paleoclimate proxy data for which chronology is unequivocal evidence of increased rainfall at that site, so as to better understand where and when rainfall directly occurred in the past. It has also introduced several suggestions for the need to better characterise periods of increased North African rainfall at discrete locations, rather than extrapolating periods of increased humidity across the continent.

8.1.1 Climate variability during the African Humid Period

Moroccan stalagmite records from the north-west Sahara demonstrate increased rainfall between 8.7-4.3 kyr BP (Chapter 4). The location, timing and oxygen isotopes of this stalagmite-growth demonstrate that subtropical rainfall occurs in response to increasing North-South interhemispheric temperature anomalies, after the decline of the West African Monsoon, and that this increased rainfall supports a rapid increase in the region's population. This work identifies the coupling of an existing mechanism, Tropical Plumes (TP), with northwards shifts of the Atlantic Intertropical Convergence Zone (ITCZ), to explain the increased rainfall in the north-west Sahara during the early-to-mid Holocene.

Further high-resolution stable isotope records from the Saharan Atlas (Chapter 5), situated east from Moroccan samples, during the African Humid Period suggests that the TP moisture source during the mid-Holocene occurred across the breadth of the South of Atlas range, supplying major southward-flowing rivers and encouraging movement of people, during a key period in the Holocene development of land use and animal production.

8.1.2 Improved temporal coverage of north-west Sahara rainfall

High-precision U-Th chronology of stalagmites from the Saharan Atlas reveals numerous periods of increased rainfall leading to speleothem growth (Chapter 5), including robust evidence for formation at 386-378 kyr BP (MIS 11), 316-310 kyr BP (MIS 9), 155-145 kyr BP (MIS 6), 80-62 kyr BP (MIS 5a) and 8-5 kyr BP (MIS 1). This chronology correlates with periods of speleothem growth in the stalagmites MegaMite and ASD-1, located in the Moroccan High- and Anti-Atlas Mountains respectively, implying that increases in north Saharan rainfall are regional on the desert side of the Atlas range between 7°W-1°E and 30-33°N. Furthermore, whilst there are numerous controls which may impact upon speleothem $\delta^{18}O$, consistent values between cave sites and across different time-periods point towards homogenous moisture sources in the SOA region

during periods of increased rainfall, likely tropical plumes.

These data provide important evidence for multiple periods of increased rainfall across north-west Africa during the past 450 kyrs, robustly increasing the temporal resolution of records of direct, local rainfall, and providing key information as to the minimum geographic extent of increased rainfall across the northern Sahara.

8.1.3 Records of direct rainfall in the central Sahara

Research at the Tademaït plateau, in the very centre of the Sahara, provides the first significant evidence for the potential of middle to late Pleistocene paleoclimate information being sourced from terrestrial, speleothem-like secondary carbonate deposits from the central Sahara (Chapter 6). The results presented offer significant evidence for a sustained period of increased rainfall during MIS 11, not only at the northern or southern limits of the Sahara, but in the heart of the desert, where both tropical and North Atlantic sourced moisture does not presently reach in great volume. This gives potential for reconstructing further periods of increased rainfall in this region, offering insight into the occurrence, timing and frequency of major aquifer recharge in the presently hyper-arid central Sahara.

8.1.4 Potential for sub-annual measurements of paleo-hydrology in the northern Sahara

Ultra-high-resolution (sub-monthly) trace element analysis from a well-dated southern Morocco stalagmite (Chapter 7) provides evidence for the potential of gaining insights into the seasonality or cyclicity of north-west African paleoclimate during periods of increased rainfall. These results are preliminary, but offer robust evidence for the use of trace elements in a multi-proxy approach for developing our understanding of the nuances of climate within stalagmite growth periods.

8.2 "Green Sahara" periods

Recent work has begun to acknowledge the range of microclimates across the North African landscape in a paleoclimate context (Pausata et al., 2020), which leads to suggestions that interpretations should move away from all-encompassing terms such as "Green Sahara", and towards a better understanding of changes in local rainfall at discrete locations. This work further highlights this requirement to move away from describing increased humidity in North Africa in such general terms. Whilst there are similarities in when periods of increased moisture availability are occurring, such as largely being observed during northern hemisphere interglacial and interstadial periods, this thesis exhibits the discrepancies in the spatial and temporal extent to which increases in humidity occurs. For example;

(1) The AHP does not appear to have followed a simple suggested latitudinal increase and decrease in rainfall between 12 and 5.5 kyr BP, caused by a northward and southwards migration of the West African Monsoon (WAM) system. Instead, different moisture sources and climate systems are acting at discrete locations.

(2) The Eemian period (MIS 5e, ∼120 kyr BP) cannot be interpreted as a blanket increase in North African rainfall, more significant than the AHP, because there is simply no observation of rainfall at this time in the SOA region.

(3) Sapropel observations off the coast of northeast Africa do not always correspond with increased rainfall in the north-west of the continent, suggesting that numerous periods of strengthened WAM rainfall in the south (leading to increased terrestrial discharge into the Mediterranean) are not necessarily associated with a more northerly mean ITCZ position, which would lead to rainfall in the South of Atlas.

These nuances are important because an overly extrapolated interpretation of increased rainfall or moisture availability across large swathes of the Sahara restricts the robustness with which climate models can reproduce past environments and rainfall changes, explaining some of the discrepancies which already exist between model and proxy data. Furthermore, constraints on future changes in rainfall are less accurate if

our understanding of where rainfall occurred in the past under certain climate conditions is flawed.

Instead of the continued discussions about "Green Sahara" conditions, it is important to attain further direct indicators of local rainfall at discrete and strategic locations across North Africa to move towards a more complete picture of Saharan paleoclimate.

8.3 The South of Atlas

This work also highlights the South of Atlas (SOA) as being an important and unique region for how expansive periods of increased North African rainfall are. Already from contemporary rainfall observations, the region is evidently unique in when during the year rainfall is occurring, and is the only area of North Africa in which rainfall does not fall into the unimodal winter or summer dominated climate patterns observed at the continent's extremes. This work identifies that this uniqueness likely translates directly into past climates, with sites on the desert side of the Atlas range not only protected from Atlantic and Mediterranean moisture sources, but also at a high enough topography to trigger tropical plume rainfall, allowing for tropical-sourced rainfall at the very northern limits of the Sahara.

Based on the positioning of caves, and subsequent evidence of rainfall via speleothem formation at the heads of numerous major southwards-flowing rivers, the SOA is likely a critical zone of rainfall for allowing rivers to flow into the central Sahara, filling lakes and expanding the influenced area of increased humidity from just being southern, monsoon-fed regions (Shanahan et al., 2015; Drake et al., 2022).

8.4 Future work

As per the conclusions of this work, further absolute-dated evidence of direct, local rainfall at discrete locations in North Africa are required to better characterise periods of increased rainfall across the region. The Tademaït Plateau, and regions of continuous

karstic rock further east (Appendix I Figure 1), offer potential for reconstructing records of direct rainfall in the centre of the desert, particularly if in-situ samples which have not interacted with water post-deposition can be attained. Also, further samples from the Saharan Atlas, perhaps along a north-south transect through the region, would allow for a better understanding as to the northerly and easterly extent to which tropical plume rainfall occurs, and the occurrence of glacial winter rainfall in regions less protected by topographic boundaries, as observed at Maqlae cave.

Additional work may also still be undertaken on samples already collected. At the Tademaït Plateau, if open-system diagenesis was caused by submersion by groundwater, then analysis of the ($^{234}U/^{238}U$) ratios of this water would allow for modelling of potential uranium addition to calcite via this source, and the correction of samples to pre-diagenesis conditions. Numerous collected samples are also still yet to be analysed from Maqlae and Grar cave, including several stalagmites which will no doubt continue to characterise the extent and robustness of the time periods in which increased rainfall is appearing to occur. Further back through time, a large stalagmite, QC-L, from Maqlae cave has $>$ 1 metre of formation during periods $>$ 500 kyrs BP, whilst from the flowstone BZ-F from Grar cave only the very top section of the $>$ 2m tall flowstone has been analysed, producing U-Th ages of $\sim$500 kyrs. This is suggesting that large amounts of speleothem formation in the Saharan Atlas are ancient, offering a unique opportunity to investigate much earlier Pleistocene climates using U-Pb chronology.

There are almost endless field excursions, analyses and interpretations which may be made into North African speleology and paleoclimate. Most importantly for the future of work in this area is to be based first around improving the spatial coverage of chronology which shows direct rainfall at strategic locations, so that a picture may be built as to where to best direct attention and time for future research.

Bibliography

Aberkane, K., Rabhi, M., 2022. Industrie lithique et cadre culturel du site archéologique" Grotte d'Amoura"(Atlas saharien oriental, Djelfa). Algerian Scientific Journal Platform .

Abouelmagd, A., Sultan, M., Milewski, A., Kehew, A.E., Sturchio, N.C., Soliman, F., Krishnamurthy, R.V., Cutrim, E., 2012. Toward a better understanding of palaeoclimatic regimes that recharged the fossil aquifers in North Africa: Inferences from stable isotope and remote sensing data. Palaeogeography, Palaeoclimatology, Palaeoecology 329-330, 137–149. doi:10.1016/j.palaeo.2012.02.024.

Adkins, J., DeMenocal, P., Eshel, G., 2006. The "African humid period" and the record of marine upwelling from excess 230Th in Ocean Drilling Program Hole 658C. Paleoceanography 21. doi:10.1029/2005PA001200.

Al-Gamal, S.A., 2011. An assessment of recharge possibility to North-Western Sahara Aquifer System (NWSAS) using environmental isotopes. Journal of Hydrology 398, 184–190. doi:10.1016/j.jhydrol.2010.12.004.

Alam, M.S., Cheng, T., 2014. Uranium release from sediment to groundwater: Influence of water chemistry and insights into release mechanisms. Journal of Contaminant Hydrology 164, 72–87. doi:10.1016/j.jconhyd.2014.06.001.

Alfy, Z., Crombie, M.K., Arvidson, R.E., Sturchio, N.C., El Alfy, Z., Zeid, K.A., 1997. Age and isotopic constraints on Pleistocene pluvial episodes in the Western Desert, Egypt Related papers Age and isotopic constraints on Pleistocene pluvial episodes in the Western Desert, Egypt. Technical Report.

Ames, L.L., McGarrah, J.E., Walker, B.A., 1983. Sorption of Trace Constituents from

Aqueous Solutions onto Secondary Minerals. I. Uranium. Clays and Clay Minerals 31, 321–334. doi:10.1346/CCMN.1983.0310501.

Ansmann, A., Tesche, M., Althausen, D., Müller, D., Seifert, P., Freudenthaler, V., Heese, B., Wiegner, M., Pisani, G., Knippertz, P., Dubovik, O., 2008. Influence of Saharan dust on cloud glaciation in southern Morocco during the Saharan Mineral Dust Experiment. Journal of Geophysical Research 113, D04210. doi:10.1029/2007JD008785.

Armitage, S.J., Drake, N.A., Stokes, S., El-Hawat, A., Salem, M.J., White, K., Turner, P., McLaren, S.J., 2007. Multiple phases of North African humidity recorded in lacustrine sediments from the Fazzan Basin, Libyan Sahara. Quaternary Geochronology 2, 181–186. doi:10.1016/j.quageo.2006.05.019.

Atsawawaranunt, K., Comas-Bru, L., Amirnezhad Mozhdehi, S., Deininger, M., Harrison, S.P., Baker, A., Boyd, M., Kaushal, N., Ahmad, S.M., Ait Brahim, Y., Arienzo, M., Bajo, P., Braun, K., Burstyn, Y., Chawchai, S., Duan, W., Hatvani, I.G., Hu, J., Kern, Z., Labuhn, I., Lachniet, M., Lechleitner, F.A., Lorrey, A., Pérez-Mejías, C., Pickering, R., Scroxton, N., 2018. The SISAL database: a global resource to document oxygen and carbon isotope records from speleothems. Earth System Science Data 10, 1687–1713. doi:10.5194/essd-10-1687-2018.

Ayalon, A., Bar-Matthews, M., Sassb, E., 1998. Rainfall-recharge relationships within a karstic terrain in the Eastern Mediterranean semi-arid region, Israel: δ18O and δD characteristics. Technical Report.

Ayling, B.F., Eggins, S., McCulloch, M.T., Chappell, J., Grün, R., Mortimer, G., 2017. Uranium uptake history, open-system behaviour and uranium-series ages of fossil Tridacna gigas from Huon Peninsula, Papua New Guinea. Geochimica et Cosmochimica Acta 213, 475–501. doi:10.1016/j.gca.2017.06.037.

Bae, C.J., Douka, K., Petraglia, M.D., 2017. On the origin of modern humans: Asian perspectives. doi:10.1126/science.aai9067.

Baker, A., Mariethoz, G., ComasâBru, L., Hartmann, A., Frisia, S., Borsato, A., Treble,

P.C., Asrat, A., 2021. The Properties of Annually Laminated Stalagmites - A Global Synthesis. Reviews of Geophysics 59. doi:10.1029/2020RG000722.

Baker, A.R., Kelly, S.D., Biswas, K.F., Witt, M., Jickells, T.D., 2003. Atmospheric deposition of nutrients to the Atlantic Ocean. Geophysical Research Letters 30. doi:10.1029/2003GL018518.

Baldini, J.U., Lechleitner, F.A., Breitenbach, S.F., van Hunen, J., Baldini, L.M., Wynn, P.M., Jamieson, R.A., Ridley, H.E., Baker, A.J., Walczak, I.W., Fohlmeister, J., 2021. Detecting and quantifying palaeoseasonality in stalagmites using geochemical and modelling approaches. Quaternary Science Reviews 254, 106784. doi:10.1016/j.quascirev.2020.106784.

Baldini, L.M., McDermott, F., Baldini, J.U.L., Fischer, M.J., Möllhoff, M., 2010. An investigation of the controls on Irish precipitation δ18O values on monthly and event timescales. Climate Dynamics 35, 977–993. doi:10.1007/s00382-010-0774-6.

Barich, B., Lucarini, G., Hamdan MA, Hassan FA, 2014. From Lake to Sand. The Archaeology of Farafra Oasis Western desert, Egypt. All'Insegna del Giglio.

Barrott, J., 2014. Reconstructing North-West African palaeoclimate from speleothem geochemistry: past climate variability and implications for human history. Ph.D. thesis. University of Oxford.

Berger, A., Loutre, M., 1991. Insolation values for the climate of the last 10 million years. Quaternary Science Reviews 10, 297–317. doi:10.1016/0277-3791(91)90033-Q.

Blanchet, C.L., Osborne, A.H., Tjallingii, R., Ehrmann, W., Friedrich, T., Timmermann, A., Brückmann, W., Frank, M., 2021. Drivers of river reactivation in North Africa during the last glacial cycle. Nature Geoscience 14, 97–103. doi:10.1038/s41561-020-00671-3.

Boos, W.R., Korty, R.L., 2016. Regional energy budget control of the intertropical convergence zone and application to mid-Holocene rainfall. Nature Geoscience 9, 892–897. doi:10.1038/ngeo2833.

Borsato, A., 2003. Open-system alpine speleothems: implications for U-series dating and paleoclimate reconstructions. Studi Trent. Sci. Nat., Acta Geol 80, 71–83.

Bosmans, J.H., Drijfhout, S.S., Tuenter, E., Hilgen, F.J., Lourens, L.J., 2015. Response of the North African summer monsoon to precession and obliquity forcings in the EC-Earth GCM. Climate Dynamics 44, 279–297. doi:10.1007/s00382-014-2260-z.

Bouderbala, A., 2019. The impact of climate change on groundwater resources in coastal aquifers: case of the alluvial aquifer of Mitidja in Algeria. Environmental Earth Sciences 78. doi:10.1007/s12665-019-8702-5.

Bourdon, B., 2003. Introduction to U-series Geochemistry. Reviews in Mineralogy and Geochemistry 52, 1–21. doi:10.2113/0520001.

Bouzouggar, A., Humphrey, L.T., Barton, N., Parfitt, S.A., Balzan, L.C., Schwenninger, J.L., Hajraoui, M.A.E., Nespoulet, R., Bello, S.M., 2018. 90,000 year-old specialised bone technology in the Aterian Middle Stone Age of North Africa. PLoS ONE 13. doi:10.1371/journal.pone.0202021.

Brahim, Y.A., Bouchaou, L., Sifeddine, A., Beraaouz, E.H., Wanaim, A., Cheng, H., 2019. Hydro-climate characteristics of the karst system of Wintimdouine cave (Western High Atlas, Morocco): monitoring and implications for paleoclimate research. Environmental Earth Sciences 78, 508. doi:10.1007/s12665-019-8496-5.

Brahim, Y.A., Bouchaou, L., Sifeddine, A., Khodri, M., Reichert, B., Cruz, F.W., 2016. Elucidating the climate and topographic controls on stable isotope composition of meteoric waters in Morocco, using station-based and spatially-interpolated data. Journal of Hydrology 543, 305–315. doi:10.1016/j.jhydrol.2016.10.001.

Brahim, Y.A., Cheng, H., Sifeddine, A., Wassenburg, J.A., Cruz, F.W., Khodri, M., Sha, L., Pérez-Zanón, N., Beraaouz, E.H., Apaéstegui, J., Guyot, J.L., Jochum, K.P., Bouchaou, L., 2017. Speleothem records decadal to multidecadal hydroclimate variations in southwestern Morocco during the last millennium. Earth and Planetary Science Letters 476, 1–10. doi:10.1016/j.epsl.2017.07.045.

Broccoli, A.J., Dahl, K.A., Stouffer, R.J., 2006. Response of the ITCZ to North-

ern Hemisphere cooling. Geophysical Research Letters 33, n/a–n/a. doi:10.1029/2005GL024546.

Broich, M., Potì, A., Linstädter, J., Gibaja, J.F., Mazzucco, N., Conesa, M.V., Mikdad, A., Weniger, G.C., 2021. The early and middle holocene lithic industries of ifri nâetsedda (eastern rif, morocco). African Archaeological Review 38, 49–71. doi:10.1007/s10437-020-09377-8.

Burrough, S.L., Thomas, D.S.G., 2013. Central southern Africa at the time of the African Humid Period: A new analysis of Holocene palaeoenvironmental and palaeoclimate data. doi:10.1016/j.quascirev.2013.08.001.

Caley, T., Malaizé, B., Revel, M., Ducassou, E., Wainer, K., Ibrahim, M., Shoeaib, D., Migeon, S., Marieu, V., 2011. Orbital timing of the Indian, East Asian and African boreal monsoons and the concept of a 'global monsoon'. Quaternary Science Reviews 30, 3705–3715. doi:10.1016/j.quascirev.2011.09.015.

van Calsteren, P., Thomas, L., 2006. Uranium-series dating applications in natural environmental science. Earth-Science Reviews 75, 155–175. doi:10.1016/j.earscirev.2005.09.001.

Camps, G., 1990. Des incertitudes de l'art aux erreurs d'Hérodote. La faune des temps néolithiques et protohistoriques de l'Afrique du Nord. Comptes-rendus des séances de l année - Académie des inscriptions et belles-lettres 134, 35–57. doi:10.3406/crai.1990.14809.

Candy, I., Schreve, D.C., Sherriff, J., Tye, G.J., 2014. Marine Isotope Stage 11: Palaeoclimates, palaeoenvironments and its role as an analogue for the current interglacial. doi:10.1016/j.earscirev.2013.09.006.

Cappy, S., 2007. Hydrogeological Characterization of the Upper Drâa Catchment: Morocco.

Carolin, S.A., Cobb, K.M., Lynch-Stieglitz, J., Moerman, J.W., Partin, J.W., Lejau, S., Malang, J., Clark, B., Tuen, A.A., Adkins, J.F., 2016. Northern Borneo stalagmite records reveal West Pacific hydroclimate across MIS 5 and 6. Earth and Planetary

Science Letters 439, 182–193. doi:10.1016/j.epsl.2016.01.028.

Carolin, S.A., Ersek, V., Roberts, W.H., Walker, R.T., Henderson, G.M., 2019. Drying in the Middle East During Northern Hemisphere Cold Events of the Early Glacial Period. Geophysical Research Letters 46, 14003–14010. doi:10.1029/2019GL084365.

Chandan, D., Peltier, W.R., 2020. African Humid Period Precipitation Sustained by Robust Vegetation, Soil, and Lake Feedbacks. Geophysical Research Letters 47. doi:10.1029/2020GL088728.

Cheddadi, R., Carré, M., Nourelbait, M., François, L., Rhoujjati, A., Manay, R., Ochoa, D., Schefuß, E., 2021. Early holocene greening of the sahara requires mediterranean winter rainfall. Proceedings of the National Academy of Sciences 118. doi:10.1073/pnas.2024898118.

Chen, C.Y., McGee, D., Woods, A., Pérez, L., Hatfield, R.G., Edwards, R.L., Cheng, H., Valero-Garcés, B.L., Lehmann, S.B., Stoner, J.S., Schwalb, A., Tal, I., Seltzer, G.O., Tapia, P.M., Abbott, M.B., Rodbell, D.T., 2020. U-Th dating of lake sediments: Lessons from the 700 ka sediment record of Lake Junín, Peru. Quaternary Science Reviews 244, 106422. doi:10.1016/j.quascirev.2020.106422.

Chen, D., Chen, H.W., 2013. Using the Köppen classification to quantify climate variation and change: An example for 1901-2010. Environmental Development 6, 69–79. doi:10.1016/j.envdev.2013.03.007.

Cheng, H., Edwards, R.L., Shen, C.C., Polyak, V.J., Asmerom, Y., Woodhead, J., Hellstrom, J., Wang, Y., Kong, X., Spötl, C., Wang, X., Alexander, E.C., 2013. Improvements in 230Th dating, 230Th and 234U half-life values, and U-Th isotopic measurements by multi-collector inductively coupled plasma mass spectrometry. Earth and Planetary Science Letters 371-372, 82–91. doi:10.1016/j.epsl.2013.04.006.

Cheng, H., Edwards, R.L., Sinha, A., Spötl, C., Yi, L., Chen, S., Kelly, M., Kathayat, G., Wang, X., Li, X., Kong, X., Wang, Y., Ning, Y., Zhang, H., 2016. The Asian monsoon over the past 640,000 years and ice age terminations. Nature 534, 640–646. doi:10.1038/nature18591.

Cheng, H., Zhang, H., Zhao, J., Li, H., Ning, Y., Kathayat, G., 2019. Chinese stalagmite paleoclimate researches: A review and perspective. Science China Earth Sciences 62, 1489–1513. doi:10.1007/s11430-019-9478-3.

Cornforth, R., 2012. Overview of the West African Monsoon. Weather 67, 59–65. doi:10.1002/wea.1896.

Cuthbert, M.O., Baker, A., Jex, C.N., Graham, P.W., Treble, P.C., Andersen, M.S., Ian Acworth, R., 2014. Drip water isotopes in semi-arid karst: Implications for speleothem paleoclimatology. Earth and Planetary Science Letters 395, 194–204. doi:10.1016/j.epsl.2014.03.034.

Dallmeyer, A., Claussen, M., Lorenz, S.J., Shanahan, T., 2020. The end of the African humid period as seen by a transient comprehensive Earth system model simulation of the last 8000 years. Climate of the Past 16, 117–140. doi:10.5194/cp-16-117-2020.

Darling, W.G., Sorensen, J.P.R., Newell, A.J., Midgley, J., Benhamza, M., 2018. The age and origin of groundwater in the Great Western Erg sub-basin of the North-Western Sahara aquifer system: Insights from Krechba, central Algeria. Applied Geochemistry 96, 277–286. doi:10.1016/j.apgeochem.2018.07.016.

Day, C.C., Henderson, G.M., 2013. Controls on trace-element partitioning in cave-analogue calcite. Geochimica et Cosmochimica Acta 120, 612–627. doi:10.1016/j.gca.2013.05.044.

Day, C.C., Pogge von Strandmann, P.A., Mason, A.J., 2021. Lithium isotopes and partition coefficients in inorganic carbonates: Proxy calibration for weathering reconstruction. Geochimica et Cosmochimica Acta 305, 243–262. doi:10.1016/j.gca.2021.02.037.

DeMenocal, P., Ortiz, J., Guilderson, T., Adkins, J., Sarnthein, M., Baker, L., Yarusinsky, M., 2000. Abrupt onset and termination of the African Humid Period:. Quaternary Science Reviews 19, 347–361. doi:10.1016/S0277-3791(99)00081-5.

Derdour, A., Bouanani, A., Babahamed, K., 2018. Modelling rainfall runoff relations using HEC-HMS in a semi-arid region: Case study in Ain Sefra watershed, Ksour

Mountains (SW Algeria). Journal of Water and Land Development 36, 45–55. doi:10.2478/jwld-2018-0005.

Dickson, A.J., Beer, C.J., Dempsey, C., Maslin, M.A., Bendle, J.A., McClymont, E.L., Pancost, R.D., 2009. Oceanic forcing of the Marine Isotope Stage 11 interglacial. Nature Geoscience 2, 428–433. doi:10.1038/ngeo527.

Drake, N.A., Blench, R.M., Armitage, S.J., Bristow, C.S., White, K.H., 2011. Ancient watercourses and biogeography of the Sahara explain the peopling of the desert. Earth, Atmospheric and Planetary Sciences URL: www.pnas.org/cgi/doi/10.1073/pnas.1012231108, doi:10.1073/pnas.1012231108/-/DCSupplemental.

Drake, N.A., Breeze, P., Parker, A., 2013. Palaeoclimate in the Saharan and Arabian Deserts during the Middle Palaeolithic and the potential for hominin dispersals. Quaternary International 300, 48–61. doi:10.1016/j.quaint.2012.12.018.

Drake, N.A., Candy, I., Breeze, P., Armitage, S.J., Gasmi, N., Schwenninger, J.L., Peat, D., Manning, K., 2022. Sedimentary and geomorphic evidence of Saharan megalakes: A synthesis. Quaternary Science Reviews 276. doi:10.1016/j.quascirev.2021.107318.

Draoui, A., Bendella, M., Ferré, B., Benhamou, M., Abdelkrim, M.B., Benyoucef, M., 2022. The Lower Cretaceous "Continental Intercalaire" around Tidikelt (Central Sahara, Algeria): Sedimentology, palaeontology and ichnology. Journal of African Earth Sciences 185. doi:10.1016/j.jafrearsci.2021.104396.

Drobinski, P., Bastin, S., Janicot, S., Bock, O., Dabas, A., Delville, P., Reitebuch, O., Sultan, B., 2009. On the late northward propagation of the west African monsoon in summer 2006 in the region of Niger/Mali. Journal of Geophysical Research Atmospheres 114. doi:10.1029/2008JD011159.

Dunne, J., di Lernia, S., Chłodnicki, M., Kherbouche, F., Evershed, R.P., 2018. Timing and pace of dairying inception and animal husbandry practices across Holocene North Africa. Quaternary International 471, 147–159. doi:10.1016/j.quaint.2017.06.062.

Edmunds, W.M., Guendouz, A.H., Mamou, A., Moulla, A., Shand, P., Zouari, K., 2003. Groundwater evolution in the Continental Intercalaire aquifer of southern Algeria and Tunisia: trace element and isotopic indicators. Technical Report. URL: www.elsevier.com/locate/apgeochem.

Edwards, R.L., Chen, J.H., Ku, T.L., Wasserburg, G.J., 1987. Precise Timing of the Last Interglacial Period from Mass Spectrometric Determination of Thorium-230 in Corals. Science 236, 1547–1553. doi:10.1126/science.236.4808.1547.

Ehrmann, W., Schmiedl, G., Beuscher, S., Krüger, S., 2017. Intensity of african humid periods estimated from saharan dust fluxes. PLoS ONE 12. doi:10.1371/journal.pone.0170989.

Ehrmann, W., Seidel, M., Schmiedl, G., 2013. Dynamics of late quaternary north african humid periods documented in the clay mineral record of central aegean sea sediments. Global and Planetary Change 107, 186–195. doi:10.1016/j.gloplacha.2013.05.010.

El-Shenawy, M.I., Kim, S.T., Schwarcz, H.P., Asmerom, Y., Polyak, V.J., 2018. Speleothem evidence for the greening of the Sahara and its implications for the early human dispersal out of sub-Saharan Africa. Quaternary Science Reviews 188, 67–76. doi:10.1016/j.quascirev.2018.03.016.

Elliot, T., Bonotto, D.M., Andrews, J.N., 2014. Dissolved uranium, radium and radon evolution in the Continental Intercalaire aquifer, Algeria and Tunisia. Journal of Environmental Radioactivity 137, 150–162. doi:10.1016/j.jenvrad.2014.07.003.

Fairchild, I., Baker, A., 2012. Speleothem science: from process to past environments. Wiley-Blackwell.

Fink, A.H., Knippertz, P., 2003. An extreme precipitation event in southern Morocco in spring 2002 and some hydrological implications. Weather 58, 371–377. doi:10.1256/wea.61.03A.

Fleitmann, D., Burns, S.J., Mangini, A., Mudelsee, M., Kramers, J., Villa, I., Neff, U., Al-Subbary, A.A., Buettner, A., Hippler, D., Matter, A., 2007. Holocene ITCZ and

Indian monsoon dynamics recorded in stalagmites from Oman and Yemen (Socotra). Quaternary Science Reviews 26, 170–188. doi:10.1016/j.quascirev.2006.04.012.

Fleitmann, D., Burns, S.J., Neff, U., Mangini, A., Matter, A., 2003. Changing moisture sources over the last 330,000 years in Northern Oman from fluid-inclusion evidence in speleothems. Quaternary Research 60, 223–232. doi:10.1016/S0033-5894(03)00086-3.

Fohlmeister, J., 2012. A statistical approach to construct composite climate records of dated archives. Quaternary Geochronology 14, 48–56. doi:10.1016/j.quageo.2012.06.007.

Fohlmeister, J., Arps, J., Spötl, C., Schröder-Ritzrau, A., Plessen, B., Günter, C., Frank, N., Trüssel, M., 2018. Carbon and oxygen isotope fractionation in the water-calcite-aragonite system. Geochimica et Cosmochimica Acta 235, 127–139. doi:10.1016/j.gca.2018.05.022.

Fohlmeister, J., Voarintsoa, N.R.G., Lechleitner, F.A., Boyd, M., Brandtstätter, S., Jacobson, M.J., L. Oster, J., 2020. Main controls on the stable carbon isotope composition of speleothems. Geochimica et Cosmochimica Acta 279, 67–87. doi:10.1016/j.gca.2020.03.042.

Ford, D., Williams, P., 2013. Karst Hydrogeology and Geomorphology. Wiley.

Frohlich, L., Knippertz, P., Fink, A.H., Hohberger, E., 2013. An Objective Climatology of Tropical Plumes. Journal of Climate 26, 5044–5060. doi:10.1175/JCLI-D-12-00351.1.

Frumkin, A., Stein, M., 2004. The SaharaâEast Mediterranean dust and climate connection revealed by strontium and uranium isotopes in a Jerusalem speleothem. Earth and Planetary Science Letters 217, 451–464. doi:10.1016/S0012-821X(03)00589-2.

Gaetani, M., Messori, G., Zhang, Q., Flamant, C., Pausata, F.S.R., 2017. Understanding the mechanisms behind the northward extension of the west african monsoon during the mid-holocene URL: www.ametsoc.org/PUBSReuseLicenses, doi:10.1175/JCLI-D-16-0299.1.s1.

Gasse, F., 2000. Hydrological changes in the African tropics since the Last Glacial Maximum. Quaternary Science Reviews 19, 189–211. doi:10.1016/S0277-3791(99)00061-X.

Genty, D., Blamart, D., Ghaleb, B., Plagnes, V., Causse, C., Bakalowicz, M., Zouari, K., Chkir, N., Hellstrom, J., Wainer, K., Bourges, F., 2006. Timing and dynamics of the last deglaciation from European and North African δ13C stalagmite profiles-comparison with Chinese and South Hemisphere stalagmites. Quaternary Science Reviews 25, 2118–2142. doi:10.1016/j.quascirev.2006.01.030.

Geyh, M.A., Thiedig, F., 2008. The Middle Pleistocene Al Mahrúqah Formation in the Murzuq Basin, northern Sahara, Libya evidence for orbitally-forced humid episodes during the last 500,000 years. Palaeogeography, Palaeoclimatology, Palaeoecology 257, 1–21. doi:10.1016/j.palaeo.2007.07.001.

Gibert, C., Vignoles, A., Contoux, C., Banks, W.E., Barboni, D., Boisserie, J.R., Chavasseau, O., Fluteau, F., Guy, F., Noûs, C., Otero, O., Sepulchre, P., Souron, A., Ramstein, G., 2022. Climate-inferred distribution estimates of mid-to-late Pliocene hominins. Global and Planetary Change 210. doi:10.1016/j.gloplacha.2022.103756.

Glueck, M.F., Stockton, C.W., 2001. Reconstruction of the North Atlantic Oscillation, 1429-1983. International Journal of Climatology 21, 1453–1465. doi:10.1002/joc.684.

Goncalves, J., Petersen, J., Deschamps, P., Hamelin, B., Baba-Sy, O., 2013. Quantifying the modern recharge of the "fossil" Sahara aquifers. Geophysical Research Letters 40, 2673–2678. doi:10.1002/grl.50478.

Grant, K.M., Rohling, E.J., Westerhold, T., Zabel, M., Heslop, D., Konijnendijk, T., Lourens, L., 2017. A 3 million year index for North African humidity/aridity and the implication of potential pan-African Humid periods. Quaternary Science Reviews 171, 100–118. doi:10.1016/j.quascirev.2017.07.005.

Griffiths, M.L., Johnson, K.R., Pausata, F.S.R., White, J.C., Henderson, G.M., Wood,

C.T., Yang, H., Ersek, V., Conrad, C., Sekhon, N., 2020. End of Green Sahara amplified mid- to late Holocene megadroughts in mainland Southeast Asia. Nature Communications 11. doi:10.1038/s41467-020-17927-6.

Guendouz, A., Moulla, A., Edmunds, W.M., Shand, P., Poole, J., Zouari, K., Mamou, A., 1998. PALAEOCLIMATIC INFORMATION CONTAINED IN GROUNDWATERS OF THE GRAND ERG ORIENTAL, NORTH AFRICA.

Guendouz, A., Moulla, A.S., Edmunds, W.M., Zouari, K., Shand, P., Mamou, A., 2003. Hydrogeochemical and isotopic evolution of water in the Complexe Terminal aquifer in the Algerian Sahara. Hydrogeology Journal 11, 483–495. doi:10.1007/s10040-003-0263-7.

Hadour, A., Mahé, G., Meddi, M., 2020. Watershed based hydrological evolution under climate change effect: An example from North Western Algeria. doi:10.1016/j.ejrh.2020.100671.

Hamed, Y., Ahmadi, R., Hadji, R., Mokadem, N., Dhia, H.B., Ali, W., 2014. Groundwater evolution of the Continental Intercalaire aquifer of Southern Tunisia and a part of Southern Algeria: Use of geochemical and isotopic indicators. Desalination and Water Treatment 52, 1990–1996. doi:10.1080/19443994.2013.806221.

Haug, G.H., Hughen, K.A., Sigman, D.M., Peterson, L.C., RoÌhl, U., 2001. Southward migration of the intertropical convergence zone through the holocene. Science 293, 1304–1308. doi:10.1126/science.1059725.

Heiß, L., Bouchaou, L., Tadoumant, S., Reichert, B., 2020. Multi-tracer approach for assessing complex aquifer systems under arid climate: Case study of the River Tata catchment in the Moroccan Anti-Atlas Mountains. Applied Geochemistry 120. doi:10.1016/j.apgeochem.2020.104671.

Hellstrom, J., 2006. U-Th dating of speleothems with high initial 230Th using stratigraphical constraint. Quaternary Geochronology 1, 289–295. doi:10.1016/j.quageo.2007.01.004.

Hellstrom, J., Sniderman, K., Drysdale, R., Couchoud, I., Hartland, A., Pearson, A.,

Bajo, P., 2020. Speleothem growth intervals reflect New Zealand montane vegetation response to temperature change over the last glacial cycle. Scientific Reports 10. doi:10.1038/s41598-020-58317-8.

Helmke, J.P., Bauch, H.A., Röhl, U., Kandiano, E.S., 2008. Uniform climate development between the subtropical and subpolar Northeast Atlantic across marine isotope stage 11. Technical Report. URL: www.clim-past.net/4/181/2008/.

Hely, C., Lézine, A.M., Contributors, A., 2014. Holocene changes in African vegetation: tradeoff between climate and water availability. Climate of the Past 10, 681–686. doi:10.5194/cp-10-681-2014.

Henderson, G.M., 2006. Caving In to New Chronologies. Science 313, 620–622. doi:10.1126/science.1128980.

Henselowsky, F., Eichstädter, R., Schröder-Ritzrau, A., Herwartz, D., Almoazamy, A., Frank, N., Kindermann, K., Bubenzer, O., 2021. Speleothem growth phases in the central Eastern Desert of Egypt reveal enhanced humidity throughout MIS 5. Quaternary International doi:10.1016/j.quaint.2021.05.006.

Herold, M., Lohmann, G., 2009. Eemian tropical and subtropical African moisture transport: An isotope modelling study. Climate Dynamics 33, 1075–1088. doi:10.1007/s00382-008-0515-2.

Hersbach, H., Bell, B., Berrisford, P., Hirahara, S., Horányi, A., MuñozâSabater, J., Nicolas, J., Peubey, C., Radu, R., Schepers, D., Simmons, A., Soci, C., Abdalla, S., Abellan, X., Balsamo, G., Bechtold, P., Biavati, G., Bidlot, J., Bonavita, M., Chiara, G., Dahlgren, P., Dee, D., Diamantakis, M., Dragani, R., Flemming, J., Forbes, R., Fuentes, M., Geer, A., Haimberger, L., Healy, S., Hogan, R.J., Hólm, E., Janisková, M., Keeley, S., Laloyaux, P., Lopez, P., Lupu, C., Radnoti, G., Rosnay, P., Rozum, I., Vamborg, F., Villaume, S., Thépaut, J., 2020. The ERA5 global reanalysis. Quarterly Journal of the Royal Meteorological Society 146, 1999–2049. doi:10.1002/qj.3803.

Heuser, A., Eisenhauer, A., 2008. The Calcium Isotope Composition (δ44/40Ca) of NIST SRM 915b and NIST SRM 1486. Geostandards and Geoanalytical Research

32, 311–315. doi:10.1111/j.1751-908X.2008.00877.x.

Hippler, D., Schmitt, A.D., Gussone, N., Heuser, A., Stille, P., Eisenhauer, A., Nägler, T.F., 2003. Calcium isotopic composition of various reference materials and seawater. Geostandards and Geoanalytical Research 27, 13–19. doi:10.1111/j.1751-908X.2003.tb00709.x.

Hoffmann, D.L., Pike, A.W., García-Diez, M., Pettitt, P.B., Zilhão, J., 2016a. Methods for U-series dating of CaCO3 crusts associated with Palaeolithic cave art and application to Iberian sites. Quaternary Geochronology 36, 104–119. doi:10.1016/j.quageo.2016.07.004.

Hoffmann, D.L., Rogerson, M., SpÃ¶tl, C., Luetscher, M., Vance, D., Osborne, A.H., Fello, N.M., Moseley, G.E., 2016b. Timing and causes of north african wet phases during the last glacial period and implications for modern human migration. Scientific Reports 6, 36367. doi:10.1038/srep36367.

Hopcroft, P.O., Valdes, P.J., 2019. Paleoclimate-conditioning reveals a North Africa land-atmosphere tipping point URL: https://doi.org/10.1073/pnas.2108783118, doi:10.1073/pnas.2108783118/-/DCSupplemental.

Hopcroft, P.O., Valdes, P.J., Harper, A.B., Beerling, D.J., 2017. Multi vegetation model evaluation of the Green Sahara climate regime. Geophysical Research Letters 44, 6804–6813. doi:10.1002/2017GL073740.

Howard, W.R., 1997. A warm future in the past. Nature 388, 418–419. doi:10.1038/41201.

Hublin, J.J., Ben-Ncer, A., Bailey, S.E., Freidline, S.E., Neubauer, S., Skinner, M.M., Bergmann, I., Le Cabec, A., Benazzi, S., Harvati, K., Gunz, P., 2017. New fossils from Jebel Irhoud, Morocco and the pan-African origin of Homo sapiens. Nature 546, 289–292. doi:10.1038/nature22336.

Huybers, P., 2006. Early Pleistocene Glacial Cycles and the Integrated Summer Insolation Forcing. Science 313, 508–511. doi:10.1126/science.1125249.

Jamieson, R.A., Baldini, J.U., Brett, M.J., Taylor, J., Ridley, H.E., Ottley, C.J.,

Prufer, K.M., Wassenburg, J.A., Scholz, D., Breitenbach, S.F., 2016. Intra- and inter-annual uranium concentration variability in a Belizean stalagmite controlled by prior aragonite precipitation: A new tool for reconstructing hydro-climate using aragonitic speleothems. Geochimica et Cosmochimica Acta 190, 332–346. doi:10.1016/j.gca.2016.06.037.

Jimenez, G., 2010. Travertine from Egypt' s Western Desert: a terrestrial record of North African paleohydrology and paleoclimate during the late Pleistocene.

Johnston, V.E., Borsato, A., Frisia, S., Spötl, C., Hellstrom, J.C., Cheng, H., Edwards, R.L., 2021. Last interglacial hydroclimate in the Italian Prealps reconstructed from speleothem multi-proxy records (Bigonda Cave, NE Italy). Quaternary Science Reviews 272. doi:10.1016/j.quascirev.2021.107243.

Kandiano, E.S., Bauch, H.A., Fahl, K., Helmke, J.P., Röhl, U., Pérez-Folgado, M., Cacho, I., 2012. The meridional temperature gradient in the eastern North Atlantic during MIS 11 and its link to the ocean-atmosphere system. Palaeogeography, Palaeoclimatology, Palaeoecology 333-334, 24–39. doi:10.1016/j.palaeo.2012.03.005.

Kandiano, E.S., Meer, M.T.J.V.D., Schouten, S., Fahl, K., Damsté, J.S.S., Bauch, H.A., 2017. Response of the North Atlantic surface and intermediate ocean structure to climate warming of MIS 11. Scientific Reports 7. doi:10.1038/srep46192.

Karssene, Y., Chammem, M., Khorchani, T., Li, F., 2017. Inter-Research Science Center Global warming drives changes in carnivore communities in the North Sahara Desert 72, 153–162. doi:10.2307/26394304.

Kathayat, G., Sinha, A., Tanoue, M., Yoshimura, K., Li, H., Zhang, H., Cheng, H., 2021. Interannual oxygen isotope variability in Indian summer monsoon precipitation reflects changes in moisture sources. Communications Earth & Environment 2. doi:10.1038/s43247-021-00165-z.

Kaufman, A., Broecker, W., 1965. Comparison of Th and C Ages for Carbonate Materials from Lakes Lahontan and Bonneville. Technical Report 16.

Kaufman, D., McKay, N., Routson, C., Erb, M., Dätwyler, C., Sommer, P.S., Heiri,

O., Davis, B., 2020a. Holocene global mean surface temperature, a multi-method reconstruction approach. Scientific Data 7. doi:10.1038/s41597-020-0530-7.

Kaufman, D., McKay, N., Routson, C., Erb, M., Davis, B., Heiri, O., Jaccard, S., Tierney, J., Dätwyler, C., Axford, Y., Brussel, T., Cartapanis, O., Chase, B., Dawson, A., de Vernal, A., Engels, S., Jonkers, L., Marsicek, J., Moffa-Sánchez, P., Morrill, C., Orsi, A., Rehfeld, K., Saunders, K., Sommer, P.S., Thomas, E., Tonello, M., Tóth, M., Vachula, R., Andreev, A., Bertrand, S., Biskaborn, B., Bringué, M., Brooks, S., Caniupán, M., Chevalier, M., Cwynar, L., Emile-Geay, J., Fegyveresi, J., Feurdean, A., Finsinger, W., Fortin, M.C., Foster, L., Fox, M., Gajewski, K., Grosjean, M., Hausmann, S., Heinrichs, M., Holmes, N., Ilyashuk, B., Ilyashuk, E., Juggins, S., Khider, D., Koinig, K., Langdon, P., Larocque-Tobler, I., Li, J., Lotter, A., Luoto, T., Mackay, A., Magyari, E., Malevich, S., Mark, B., Massaferro, J., Montade, V., Nazarova, L., Novenko, E., PaÅil, P., Pearson, E., Peros, M., Pienitz, R., Płóciennik, M., Porinchu, D., Potito, A., Rees, A., Reinemann, S., Roberts, S., Rolland, N., Salonen, S., Self, A., Seppä, H., Shala, S., St-Jacques, J.M., Stenni, B., Syrykh, L., Tarrats, P., Taylor, K., van den Bos, V., Velle, G., Wahl, E., Walker, I., Wilmshurst, J., Zhang, E., Zhilich, S., 2020b. Author Correction: A global database of Holocene paleotemperature records. Scientific Data 7, 246. doi:10.1038/s41597-020-00584-1.

Khezzani, B., Bouchemal, S., 2018. Variations in groundwater levels and quality due to agricultural over-exploitation in an arid environment: the phreatic aquifer of the Souf oasis (Algerian Sahara). Environmental Earth Sciences 77. doi:10.1007/s12665-018-7329-2.

Kim, S.T., Coplen, T.B., Horita, J., 2015. Normalization of stable isotope data for carbonate minerals: Implementation of IUPAC guidelines. Geochimica et Cosmochimica Acta 158, 276–289. doi:10.1016/j.gca.2015.02.011.

Kim, S.T., O'Neil, J.R., 1997. Equilibrium and nonequilibrium oxygen isotope effects in synthetic carbonates.

Kim, S.T., O'Neil, J.R., Hillaire-Marcel, C., Mucci, A., 2007. Oxygen isotope fraction-

ation between synthetic aragonite and water: Influence of temperature and Mg2+ concentration. Geochimica et Cosmochimica Acta 71, 4704–4715. doi:10.1016/j.gca.2007.04.019.

Kipfer, R., Aeschbach-Hertig, W., Peeters, F., Stute, M., 2002. Noble Gases in Lakes and Ground Waters. Reviews in Mineralogy and Geochemistry 47, 615–700. doi:10.2138/rmg.2002.47.14.

Kleinen, T., Hildebrandt, S., Prange, M., Rachmayani, R., Müller, S., Bezrukova, E., Brovkin, V., Tarasov, P.E., 2014. The climate and vegetation of Marine Isotope Stage 11 - Model results and proxy-based reconstructions at global and regional scale. Quaternary International 348, 247–265. doi:10.1016/j.quaint.2013.12.028.

Knippertz, P., 2003. Tropical-Extratropical Interactions Causing Precipitation in Northwest Africa: Statistical Analysis and Seasonal Variations. Monthly Weather Review 131, 3069–3076. doi:10.1175/1520-0493(2003)131<3069:TICPIN>2.0.CO;2.

Knippertz, P., 2007. Tropical-extratropical interactions related to upper-level troughs at low latitudes. Dynamics of Atmospheres and Oceans 43, 36–62. doi:10.1016/j.dynatmoce.2006.06.003.

Knippertz, P., Christoph, M., Speth, P., 2003a. Long-term precipitation variability in Morocco and the link to the large-scale circulation in recent and future climates. Meteorology and Atmospheric Physics 83, 67–88. doi:10.1007/s00703-002-0561-y.

Knippertz, P., Fink, A.H., Reiner, A., Speth, P., 2003b. Three late summer/early autumn cases of tropical-extratropical interactions causing precipitation in northwest africa. Monthly Weather Review 131, 116–135. doi:10.1175/1520-0493(2003)131<0116:TLSEAC>2.0.CO;2.

Knippertz, P., Martin, J.E., 2005. Tropical plumes and extreme precipitation in subtropical and tropical West Africa. Quarterly Journal of the Royal Meteorological Society 131, 2337–2365. doi:10.1256/qj.04.148.

Kowalski, K., Gaisler, J., Bessam, H., 1986. Annual Life Cycle of Cave Bats in Northern Algeria Cherifa ISSAAD & Hassen KSANTINI. Technical Report.

Krinner, G., Lézine, A.M., Braconnot, P., Sepulchre, P., Ramstein, G., Grenier, C., Gouttevin, I., 2012. A reassessment of lake and wetland feedbacks on the North African Holocene climate. doi:10.1029/2012GL050992.

Kroon, D., Alexander, I., Little, M., Lourens, L., Matthewson, A., Robertson, A., Sakamoto, T., 1998. 4. OXYGEN ISOTOPE AND SAPROPEL STRATIGRAPHY IN THE EASTERN MEDITERRANEAN DURING THE LAST 3.2 MILLION YEARS 1. Technical Report.

Kröpelin, S., Verschuren, D., Lézine, A.M., Eggermont, H., Cocquyt, C., Francus, P., Cazet, J.P., Fagot, M., Rumes, B., Russell, J.M., Darius, F., Conley, D.J., Schuster, M., Suchodoletz, H.V., Engstrom, D.R., 2008. Climate-Driven Ecosystem Succession in the Sahara: The Past 6000 Years.

Kuhlmann, H., Meggers, H., Freudenthal, T., Wefer, G., 2004. The transition of the monsoonal and the N Atlantic climate system off NW Africa during the Holocene. Geophysical Research Letters 31. doi:10.1029/2004GL021267.

Lachniet, M.S., 2009. Climatic and environmental controls on speleothem oxygen-isotope values. Quaternary Science Reviews 28, 412–432. doi:10.1016/j.quascirev.2008.10.021.

Larrasoana, J.C., Roberts, A.P., Rohling, E.J., 2013. Dynamics of Green Sahara Periods and Their Role in Hominin Evolution. PLoS ONE 8. doi:10.1371/journal.pone.0076514.

Larrasoana, J.C., Roberts, A.P., Rohling, E.J., Winklhofer, M., Wehausen, R., 2003. Three million years of monsoon variability over the northern Sahara. Climate Dynamics 21, 689–698. doi:10.1007/s00382-003-0355-z.

Lechleitner, F.A., Baldini, J.U., Breitenbach, S.F., Fohlmeister, J., McIntyre, C., Goswami, B., Jamieson, R.A., van der Voort, T.S., Prufer, K., Marwan, N., Culleton, B.J., Kennett, D.J., Asmerom, Y., Polyak, V., Eglinton, T.I., 2016. Hydrological and climatological controls on radiocarbon concentrations in a tropical stalagmite. Geochimica et Cosmochimica Acta 194, 233–252. doi:10.1016/j.gca.2016.08.039.

Lechleitner, F.A., Breitenbach, S.F., Cheng, H., Plessen, B., Rehfeld, K., Goswami, B., Marwan, N., Eroglu, D., Adkins, J., Haug, G., 2017. Climatic and in-cave influences on δ18O and δ13C in a stalagmite from northeastern India through the last deglaciation. Quaternary Research 88, 458–471. doi:10.1017/qua.2017.72.

Lechleitner, F.A., Day, C.C., Kost, O., Wilhelm, M., Haghipour, N., Henderson, G.M., Stoll, H.M., 2021. Stalagmite carbon isotopes suggest deglacial increase in soil respiration in western Europe driven by temperature change. Climate of the Past 17, 1903–1918. doi:10.5194/cp-17-1903-2021.

LeGrande, A.N., Schmidt, G.A., 2006. Global gridded data set of the oxygen isotopic composition in seawater. Geophysical Research Letters 33. doi:10.1029/2006GL026011.

Lezine, A.M., Hély, C., Grenier, C., Braconnot, P., Krinner, G., 2011. Sahara and Sahel vulnerability to climate changes, lessons from Holocene hydrological data. Quaternary Science Reviews 30, 3001–3012. doi:10.1016/j.quascirev.2011.07.006.

Lionello, P., Malanotte-Rizzoli, P., Boscolo, R., Alpert, P., Artale, V., Li, L., Luterbacher, J., May, W., Trigo, R., Tsimplis, M., Ulbrich, U., Xoplaki, E., 2006. The Mediterranean climate: An overview of the main characteristics and issues, pp. 1–26. doi:10.1016/S1571-9197(06)80003-0.

Lisiecki, L.E., Raymo, M.E., 2005. A Pliocene-Pleistocene stack of 57 globally distributed benthic δ 18O records. Paleoceanography 20, 1–17. doi:10.1029/2004PA001071.

Loutre, M., Berger, A., 2003. Marine Isotope Stage 11 as an analogue for the present interglacial. Global and Planetary Change 36, 209–217. doi:10.1016/S0921-8181(02)00186-8.

Lu, Z., Miller, P.A., Zhang, Q., Zhang, Q., Wårlind, D., Nieradzik, L., Sjolte, J., Smith, B., 2018. Dynamic Vegetation Simulations of the Mid Holocene Green Sahara. Geophysical Research Letters 45, 8294–8303. doi:10.1029/2018GL079195.

Ludwig, K., Paces, J., 2002. Uranium-series dating of pedogenic silica and carbonate,

Crater Flat, Nevada. Geochimica et Cosmochimica Acta 66, 487–506. doi:10.1016/S0016-7037(01)00786-4.

Luning, S., Vahrenholt, F., 2019. Holocene Climate Development of North Africa and the Arabian Peninsula, pp. 507–546. doi:10.1007/978-3-319-96794-3_14.

M, I., RS, H., 1992. Uranium-series Disequilibrium: Applications to Earth, Marine, and Environmental Sciences. Oxford.

Madi, M., Meddi, M., Boutoutaou, D., Pulido-Bosch, A., 2016. Assessment of aquifer vulnerability using a geophysical approach in hyper-arid zones. A case study (In Salah region, Algeria). Arabian Journal of Geosciences 9. doi:10.1007/s12517-016-2489-4.

Maiorano, P., Tarantino, F., Marino, M., Lange, G.J.D., 2013. Paleoenvironmental conditions at Core KC01B (Ionian Sea) through MIS 13-9: Evidence from calcareous nannofossil assemblages. Quaternary International 288, 97–111. doi:10.1016/j.quaint.2011.12.007.

Manning, K., Timpson, A., 2014. The demographic response to holocene climate change in the Sahara. Quaternary Science Reviews 101, 28–35. doi:10.1016/j.quascirev.2014.07.003.

Mao, X., Wang, H., Feng, L., 2018. 14C age reassessment of groundwater from the discharge zone due to cross-flow mixing in the deep confined aquifer. Journal of Hydrology 560, 572–581. doi:10.1016/j.jhydrol.2018.03.052.

Marcott, S.A., Shakun, J.D., Clark, P.U., Mix, A.C., 2013. A Reconstruction of Regional and Global Temperature for the Past 11,300 Years. Science 339, 1198–1201. doi:10.1126/science.1228026.

Markowska, M., Baker, A., Andersen, M.S., Jex, C.N., Cuthbert, M.O., Rau, G.C., Graham, P.W., Rutlidge, H., Mariethoz, G., Marjo, C.E., Treble, P.C., Edwards, N., 2016. Semi-arid zone caves: Evaporation and hydrological controls on δ18O drip water composition and implications for speleothem paleoclimate reconstructions. Quaternary Science Reviews 131, 285–301. doi:10.1016/j.quascirev.2015.10.024.

Marshall, J., Donohoe, A., Ferreira, D., McGee, D., 2014. The ocean's role in setting the mean position of the Inter-Tropical Convergence Zone. Climate Dynamics 42, 1967–1979. doi:10.1007/s00382-013-1767-z.

Mason, A.J., Henderson, G.M., 2010. Correction of multi-collector-ICP-MS instrumental biases in high-precision uranium-thorium chronology. International Journal of Mass Spectrometry 295, 26–35. doi:10.1016/j.ijms.2010.06.016.

McGee, D., 2020. GlacialâInterglacial Precipitation Changes. Annual Review of Marine Science 12, 525–557. doi:10.1146/annurev-marine-010419-010859.

McGee, D., DeMenocal, P.B., Winckler, G., Stuut, J.B.W., Bradtmiller, L.I., 2013. The magnitude, timing and abruptness of changes in North African dust deposition over the last 20,000 yr. Earth and Planetary Science Letters 371-372, 163–176. doi:10.1016/j.epsl.2013.03.054.

McGee, D., Donohoe, A., Marshall, J., Ferreira, D., 2014. Changes in ITCZ location and cross-equatorial heat transport at the Last Glacial Maximum, Heinrich Stadial 1, and the mid-Holocene. Earth and Planetary Science Letters 390, 69–79. doi:10.1016/j.epsl.2013.12.043.

Meckler, A.N., Affolter, S., Dublyansky, Y.V., Krüger, Y., Vogel, N., Bernasconi, S.M., Frenz, M., Kipfer, R., Leuenberger, M., Spötl, C., Carolin, S., Cobb, K.M., Moerman, J., Adkins, J.F., Fleitmann, D., 2015. Glacial-interglacial temperature change in the tropical West Pacific: A comparison of stalagmite-based paleo-thermometers. Quaternary Science Reviews 127, 90–116. doi:10.1016/j.quascirev.2015.06.015.

Meckler, A.N., Ziegler, M., Millán, M.I., Breitenbach, S.F., Bernasconi, S.M., 2014. Long-term performance of the Kiel carbonate device with a new correction scheme for clumped isotope measurements. Rapid Communications in Mass Spectrometry 28, 1705–1715. doi:10.1002/rcm.6949.

Melalih, A., Mazour, M., 2021. Analysis of water and soil conservation techniques at the Ain Sefra arid watershed (Ksour Mountains, southwest Algeria). Environmental Monitoring and Assessment 193. doi:10.1007/s10661-020-08842-w.

Messori, G., Gaetani, M., Zhang, Q., Zhang, Q., Pausata, F.S., 2019. The water cycle of the mid-Holocene West African monsoon: The role of vegetation and dust emission changes. International Journal of Climatology 39, 1927–1939. doi:10.1002/joc.5924.

Michael, L., 2008. ATLAS OF THE GREAT CAVES AND THE KARST OF AFRICA.

Middleton, N.J., Goudie, A.S., 2001. Saharan dust: sources and trajectories. Transactions of the Institute of British Geographers 26, 165–181. doi:10.1111/1475-5661.00013.

Moulla, A.S., Guendouz, A., Cherchali, M.E., Chaid, Z., Ouarezki, S., 2012. Updated geochemical and isotopic data from the Continental Intercalaire aquifer in the Great Occidental Erg sub-basin (south-western Algeria). Quaternary International 257, 64–73. doi:10.1016/j.quaint.2011.08.038.

Muschitiello, F., Zhang, Q., Sundqvist, H.S., Davies, F.J., Renssen, H., 2015. Arctic climate response to the termination of the African Humid Period. Quaternary Science Reviews 125, 91–97. doi:10.1016/j.quascirev.2015.08.012.

Nadhira, S., Omar, S., 2019. Hydrogeochemical characterization of the Complexe Terminal aquifer system in hyper-arid zones: the case of wadi Mya Basin, Algeria. Arabian Journal of Geosciences 12. doi:10.1007/s12517-019-4917-8.

Naimi, M.N., Cherif, A., 2021. Inventory and assessment of significant scientific Algerian geoheritage: Case of remarkable geosites from Orania (Western Algeria). International Journal of Geoheritage and Parks 9, 13–29. doi:10.1016/j.ijgeop.2020.09.001.

Newell, A.J., Kirby, G.A., Sorensen, J.P.R., Milodowski, A.E., 2015. The Cretaceous Continental Intercalaire in central Algeria: Subsurface evidence for a fluvial to aeolian transition and implications for the onset of aridity on the Saharan Platform. Palaeogeography, Palaeoclimatology, Palaeoecology 438, 146–159. doi:10.1016/j.palaeo.2015.07.023.

Nicholson, S.L., Hosfield, R., Groucutt, H.S., Pike, A.W.G., Burns, S.J., Matter, A., Fleitmann, D., 2022. A climatic evaluation of the southern dispersal route during

MIS 5e. Quaternary Science Reviews 279. doi:10.1016/j.quascirev.2022.107378.

Nicholson, S.L., Pike, A.W.G., Hosfield, R., Roberts, N., Sahy, D., Woodhead, J., Cheng, H., Edwards, R.L., Affolter, S., Leuenberger, M., Burns, S.J., Matter, A., Fleitmann, D., 2020. Pluvial periods in Southern Arabia over the last 1.1 million-years. Quaternary Science Reviews 229. doi:10.1016/j.quascirev.2019.106112.

Osborne, A.H., Vance, D., Rohling, E.J., Barton, N., Rogerson, M., Fello, N., 2008. A humid corridor across the Sahara for the migration of early modern humans out of Africa 120,000 years ago. Technical Report. URL: https://www.pnas.org.

Owen, R., Day, C.C., Henderson, G.M., 2018. CaveCalc: A new model for speleothem chemistry & isotopes. Computers and Geosciences 119, 115–122. doi:10.1016/j.cageo.2018.06.011.

Owen, R.A., Day, C.C., Hu, C.Y., Liu, Y.H., Pointing, M.D., Blättler, C.L., Henderson, G.M., 2016. Calcium isotopes in caves as a proxy for aridity: Modern calibration and application to the 8.2 kyr event. Earth and Planetary Science Letters 443, 129–138. doi:10.1016/j.epsl.2016.03.027.

Pausata, F.S., Gaetani, M., Messori, G., Berg, A., Maia de Souza, D., Sage, R.F., DeMenocal, P.B., 2020. The Greening of the Sahara: Past Changes and Future Implications. doi:10.1016/j.oneear.2020.03.002.

Pausata, F.S., Messori, G., Zhang, Q., 2016. Impacts of dust reduction on the northward expansion of the African monsoon during the Green Sahara period. Earth and Planetary Science Letters 434, 298–307. doi:10.1016/j.epsl.2015.11.049.

Pausata, F.S., Zhang, Q., Muschitiello, F., Lu, Z., Chafik, L., Niedermeyer, E.M., Stager, J.C., Cobb, K.M., Liu, Z., 2017. Greening of the Sahara suppressed ENSO activity during the mid-Holocene. Nature Communications 8. doi:10.1038/ncomms16020.

Peel, M.C., Finlayson, B.L., Mcmahon, T.A., 2007. Hydrology and Earth System Sciences Updated world map of the Köppen-Geiger climate classification. Technical Report. URL: www.hydrol-earth-syst-sci.net/11/1633/2007/.

Phelps, L.N., Broennimann, O., Manning, K., Timpson, A., Jousse, H., Mariethoz, G., Fordham, D.A., Shanahan, T.M., Davis, B.A., Guisan, A., 2020. Reconstructing theÂ climatic niche breadth of land use for animal production during the African Holocene. Global Ecology and Biogeography 29, 127–147. doi:10.1111/geb.13015.

Prell, W.L., Kutzbach, J.E., 1987. Monsoon variability over the past 150,000 years. Journal of Geophysical Research 92, 8411. doi:10.1029/JD092iD07p08411.

Prokopenko, A.A., Hinnov, L.A., Williams, D.F., Kuzmin, M.I., 2006. Orbital forcing of continental climate during the Pleistocene: a complete astronomically tuned climatic record from Lake Baikal, SE Siberia. Quaternary Science Reviews 25, 3431–3457. doi:10.1016/j.quascirev.2006.10.002.

Quade, J., Dente, E., Armon, M., Ben Dor, Y., Morin, E., Adam, O., Enzel, Y., 2018. Megalakes in the Sahara? A Review. doi:10.1017/qua.2018.46.

Raj, J., Bangalath, H.K., Stenchikov, G., 2019. West African Monsoon: current state and future projections in a high-resolution AGCM. Climate Dynamics 52, 6441–6461. doi:10.1007/s00382-018-4522-7.

Ramsey, C.B., 2008. Deposition models for chronological records. Quaternary Science Reviews 27, 42–60. doi:10.1016/j.quascirev.2007.01.019.

Ramsey, C.B., 2009. Bayesian Analysis of Radiocarbon Dates. Radiocarbon 51, 337–360. doi:10.1017/S0033822200033865.

Ramsey, C.B., Lee, S., 2013. Recent and Planned Developments of the Program OxCal. Radiocarbon 55, 720–730. doi:10.1017/s0033822200057878.

Renssen, H., Brovkin, V., Fichefet, T., Goosse, H., 2006. Simulation of the Holocene climate evolution in Northern Africa: The termination of the African Humid Period. Quaternary International 150, 95–102. doi:10.1016/j.quaint.2005.01.001.

Reynard, L., Day, C., Henderson, G., 2011. Large fractionation of calcium isotopes during cave-analogue calcium carbonate growth. Geochimica et Cosmochimica Acta 75, 3726–3740. doi:10.1016/j.gca.2011.04.010.

Richards, D.A., Dorale, 2003. Uranium-series Chronology and Environmental Ap-

plications of Speleothems. Reviews in Mineralogy and Geochemistry 52, 407–460. doi:10.2113/0520407.

Ritchie, J.C., Eyles, C.H., Haynes, C.V., 1985. Sediment and pollen evidence for an early to mid-Holocene humid period in the eastern Sahara. Nature 314, 352–355. doi:10.1038/314352a0.

Robinson, L.F., Belshaw, N.S., Henderson, G.M., 2004. U and Th concentrations and isotope ratios in modern carbonates and waters from the Bahamas. Geochimica et Cosmochimica Acta 68, 1777–1789. doi:10.1016/j.gca.2003.10.005.

Rogerson, M., Dublyansky, Y., Hoffmann, D., Luetscher, M., Töchterle, P., Spötl, C., 2019. Enhanced mediterranean water cycle explains increased humidity during mis 3 in north Africa. Climate of the Past 15, 1757–1769. doi:10.5194/cp-15-1757-2019.

Rousseau, D.D., 2003. The continental record of stage 11: A review, in: Geophysical Monograph Series. Blackwell Publishing Ltd. volume 137, pp. 213–222. doi:10.1029/137GM15.

Rowe, P.J., Turner, J.A., Andrews, J.E., Leeder, M.R., Calsteren, P.V., Thomas, L., 2015. Uranium-thorium dating potential of the marine bivalve Lithophaga lithophaga. Quaternary Geochronology 30, 80–89. doi:10.1016/j.quageo.2015.08.003.

Ruan, J., Kherbouche, F., Genty, D., Blamart, D., Cheng, H., Dewilde, F., Hachi, S., Edwards, R.L., Régnier, E., Michelot, J.L., 2016. Evidence of a prolonged drought ca. 4200 yrBP correlated with prehistoric settlement abandonment from the Gueldaman GLD1 Cave, Northern Algeria. Climate of the Past 12, 1–4. doi:10.5194/cp-12-1-2016.

Sahnouni, M., van der Made, J., Everett, M., 2010. Early North Africa: Chronology, ecology, and hominin behavior: Insights from Ain Hanech and El-Kherba, northeastern Algeria. doi:10.1016/j.quaint.2009.07.016.

Saranya, P., Krishnakumar, A., Sinha, N., Kumar, S., Krishnan, K.A., 2021. Isotopic signatures of moisture recycling and evaporation processes along the Western Ghats orography. Atmospheric Research 264. doi:10.1016/j.atmosres.2021.105863.

Sauvet, G., Bourrillon, R., Conkey, M., Fritz, C., Gárate-Maidagan, D., Vilá, O.R., Tosello, G., White, R., 2017. Uranium thorium dating method and palaeolithic rock art. Quaternary International 432, 86–92. doi:10.1016/j.quaint.2015.03.053.

Scerri, E.M., Drake, N.A., Jennings, R., Groucutt, H.S., 2014. Earliest evidence for the structure of Homo sapiens populations in Africa. Quaternary Science Reviews 101, 207–216. doi:10.1016/j.quascirev.2014.07.019.

Scerri, E.M.L., 2017. The North African Middle Stone Age and its place in recent human evolution. Evolutionary Anthropology: Issues, News, and Reviews 26, 119–135. doi:10.1002/evan.21527.

Scheff, J., Seager, R., Liu, H., Coats, S., 2017. Are Glacials Dry? Consequences for Paleoclimatology and for Greenhouse Warming. Journal of Climate 30, 6593–6609. doi:10.1175/JCLI-D-16-0854.1.

Schellmann, G., Radtke, U., Potter, E.K., Esat, T., McCulloch, M., 2004. Comparison of ESR and TIMS U/Th dating of marine isotope stage (MIS) 5e, 5c, and 5a coral from Barbadosâimplications for palaeo sea-level changes in the Caribbean. Quaternary International 120, 41–50. doi:10.1016/j.quaint.2004.01.005.

Schilling, J., Freier, K.P., Hertig, E., Scheffran, J., 2012. Climate change, vulnerability and adaptation in North Africa with focus on Morocco. Agriculture, Ecosystems and Environment 156, 12–26. doi:10.1016/j.agee.2012.04.021.

Schneider, T., 2001. Analysis of Incomplete Climate Data: Estimation of Mean Values and Covariance Matrices and Imputation of Missing Values. Journal of Climate 14, 853–871. doi:10.1175/1520-0442(2001)014<0853:AOICDE>2.0.CO;2.

Schneider, T., Bischoff, T., Haug, G.H., 2014. Migrations and dynamics of the intertropical convergence zone. doi:10.1038/nature13636.

Scholz, D., Hoffmann, D., 2008. (230)Th/U-dating of fossil corals and speleothems.

Schwanghart, W., Scherler, D., 2014. Short Communication: TopoToolbox 2 - MATLAB-based software for topographic analysis and modeling in Earth surface sciences. Earth Surface Dynamics 2, 1–7. doi:10.5194/esurf-2-1-2014.

Sha, L., Brahim, Y.A., Wassenburg, J.A., Yin, J., Peros, M., Cruz, F.W., Cai, Y., Li, H., Du, W., Zhang, H., Edwards, R.L., Cheng, H., 2019. How Far North Did the African Monsoon Fringe Expand During the African Humid Period? Insights From Southwest Moroccan Speleothems. Geophysical Research Letters 46, 14093–14102. doi:10.1029/2019GL084879.

Shanahan, T.M., Mckay, N.P., Hughen, K.A., Overpeck, J.T., Otto-Bliesner, B., Heil, C.W., King, J., Scholz, C.A., Peck, J., 2015. The time-transgressive termination of the African humid period. Nature Geoscience 8, 140–144. doi:10.1038/ngeo2329.

Singarayer, J.S., Burrough, S.L., 2015. Interhemispheric dynamics of the African rainbelt during the late Quaternary. Quaternary Science Reviews 124, 48–67. doi:10.1016/j.quascirev.2015.06.021.

Skinner, C.B., Poulsen, C.J., 2016. The role of fall season tropical plumes in enhancing Saharan rainfall during the African Humid Period. Geophysical Research Letters 43, 349–358. doi:10.1002/2015GL066318.

Skonieczny, C., Mcgee, D., Winckler, G., Bory, A., Bradtmiller, L.I., Kinsley, C.W., Polissar, P.J., Pol-Holz, R.D., Rossignol, L., Malaizé, B., 2019. Monsoon-driven Saharan dust variability over the past 240,000 years. URL: https://www.science.org, doi:10.1126/sciadv.aav1887.

Skonieczny, C., Paillou, P., Bory, A., Bayon, G., Biscara, L., Crosta, X., Eynaud, F., Malaizé, B., Revel, M., Aleman, N., Barusseau, J.P., Vernet, R., Lopez, S., Grousset, F., 2015. African humid periods triggered the reactivation of a large river system in Western Sahara. Nature Communications 6. doi:10.1038/ncomms9751.

Slingo, A., Ackerman, T.P., Allan, R.P., Kassianov, E.I., McFarlane, S.A., Robinson, G.J., Barnard, J.C., Miller, M.A., Harries, J.E., Russell, J.E., Dewitte, S., 2006. Observations of the impact of a major Saharan dust storm on the atmospheric radiation balance. Geophysical Research Letters 33, L24817. doi:10.1029/2006GL027869.

Smith, B.J., 1978. Aspect-Related Variations in Slope Angle Near Béni Abbès, Western Algeria. Geografiska Annaler: Series A, Physical Geography 60, 175–180. doi:10.

1080/04353676.1978.11879972.

Sultan, M., Sturchio, N., Hassan, F.A., Hamdan, M.A.R., Mahmood, A.M., Alfy, Z.E., Stein, T., 1997. Precipitation Source Inferred from Stable Isotopic Composition of Pleistocene Groundwater and Carbonate Deposits in the Western Desert of Egypt. Quaternary Research 48, 29–37. doi:10.1006/qres.1997.1907.

Tabor, C., Otto-Bliesner, B., Liu, Z., 2020. Speleothems of South American and Asian Monsoons Influenced by a Green Sahara. Geophysical Research Letters 47. doi:10.1029/2020GL089695.

Tarki, M., Dassi, L., Hamed, Y., Jedoui, Y., 2011. Geochemical and isotopic composition of groundwater in the Complex Terminal aquifer in southwestern Tunisia, with emphasis on the mixing by vertical leakage. Environmental Earth Sciences 64, 85–95. doi:10.1007/s12665-010-0820-z.

Thomas, A., 2006. Variations in past and present ocean circulation assessed with U-series nuclides. Ph.D. thesis. University of Oxford.

Thompson, W.G., Spiegelman, M.W., Goldstein, S.L., Speed, R.C., 2003. An open-system model for U-series age determinations of fossil corals. Earth and Planetary Science Letters 210, 365–381. doi:10.1016/S0012-821X(03)00121-3.

Thorncroft, C.D., Nguyen, H., Zhang, C., Peyrille, P., 2011. Annual cycle of the West African monsoon: Regional circulations and associated water vapour transport. Quarterly Journal of the Royal Meteorological Society 137, 129–147. doi:10.1002/qj.728.

Tierney, J.E., DeMenocal, P.B., Zander, P.D., 2017a. A climatic context for the out-of-Africa migration. Geology 45, 1023–1026. doi:10.1130/G39457.1.

Tierney, J.E., Lewis, S.C., Cook, B.I., LeGrande, A.N., Schmidt, G.A., 2011. Model, proxy and isotopic perspectives on the East African Humid Period. Earth and Planetary Science Letters 307, 103–112. doi:10.1016/j.epsl.2011.04.038.

Tierney, J.E., Pausata, F.S.R., deMenocal, P.B., 2017b. Rainfall regimes of the green sahara. Science Advances 3. doi:10.1126/sciadv.1601503.

Trauth, M.H., Asrat, A., Cohen, A.S., Duesing, W., Foerster, V., Kaboth-Bahr, S., Kraemer, K.H., Lamb, H.F., Marwan, N., Maslin, M.A., Schäbitz, F., 2021. Recurring types of variability and transitions in the 620 kyr record of climate change from the Chew Bahir basin, southern Ethiopia. Quaternary Science Reviews 266. doi:10.1016/j.quascirev.2020.106777.

Treble, P.C., Baker, A., Abram, N.J., Hellstrom, J.C., Crawford, J., Gagan, M.K., Borsato, A., Griffiths, A.D., Bajo, P., Markowska, M., Priestley, S.C., Hankin, S., Paterson, D., 2022. Ubiquitous karst hydrological control on speleothem oxygen isotope variability in a global study. Communications Earth & Environment 3. doi:10.1038/s43247-022-00347-3.

Trouet, V., Oldenborgh, G.J.V., 2013. Knmi climate explorer: A web-based research tool for high-resolution paleoclimatology. Tree-Ring Research 69, 3–13. doi:10.3959/1536-1098-69.1.3.

Turner, C., 2000. The Eemian interglacial in the North European plain and adjacent areas. Geologie en Mijnbouw/Netherlands Journal of Geosciences 79, 217–231. doi:10.1017/s0016774600023660.

Vaks, A., Bar-Matthews, M., Matthews, A., Ayalon, A., Frumkin, A., 2010. Middle-Late Quaternary paleoclimate of northern margins of the Saharan-Arabian Desert: Reconstruction from speleothems of Negev Desert, Israel. Quaternary Science Reviews 29, 2647–2662. doi:10.1016/j.quascirev.2010.06.014.

Vaks, A., Gutareva, O.S., Breitenbach, S.F.M., Avirmed, E., Mason, A.J., Thomas, A.L., Osinzev, A.V., Kononov, A.M., Henderson, G.M., 2013. Speleothems Reveal 500,000-Year History of Siberian Permafrost. Science 340, 183–186. doi:10.1126/science.1228729.

Vaks, A., Mason, A.J., Breitenbach, S.F., Kononov, A.M., Osinzev, A.V., Rosensaft, M., Borshevsky, A., Gutareva, O.S., Henderson, G.M., 2020. Palaeoclimate evidence of vulnerable permafrost during times of low sea ice. Nature 577, 221–225. doi:10.1038/s41586-019-1880-1.

Vansteenberge, S., de Winter, N.J., Sinnesael, M., Xueqin, Z., Verheyden, S., Claeys, P., 2020. Benchtop μXRF as a tool for speleothem trace elemental analysis: Validation, limitations and application on an Eemian to early Weichselian (125-97â¯ka) stalagmite from Belgium. Palaeogeography, Palaeoclimatology, Palaeoecology 538, 109460. doi:10.1016/j.palaeo.2019.109460.

Voelker, A.H.L., Rodrigues, T., Billups, K., Oppo, D., McManus, J., Stein, R., Hefter, J., Grimalt, J.O., 2010. Variations in mid-latitude North Atlantic surface water properties during the mid-Brunhes (MIS 9-14) and their implications for the thermohaline circulation. Climate of the Past 6, 531–552. doi:10.5194/cp-6-531-2010.

Wang, J.K., Johnson, K.R., Borsato, A., Amaya, D.J., Griffiths, M.L., Henderson, G.M., Frisia, S., Mason, A., 2019. Hydroclimatic variability in Southeast Asia over the past two millennia. Earth and Planetary Science Letters 525, 115737. doi:10.1016/j.epsl.2019.115737.

Wang, Z., Chen, S., Wang, Y., Zhao, K., Liang, Y., Cheng, H., Shao, Q., Wang, X., Zhang, J., Wang, Q., Zhai, X., Edwards, R.L., 2022. A high-resolution stalagmite record from Luoshui Cave, Central China over the past 23.5 kyr. Quaternary Science Reviews 282, 107443. doi:10.1016/j.quascirev.2022.107443.

Wassenburg, J.A., Immenhauser, A., Richter, D.K., Niedermayr, A., Riechelmann, S., Fietzke, J., Scholz, D., Jochum, K.P., Fohlmeister, J., Schröder-Ritzrau, A., Sabaoui, A., Riechelmann, D.F., Schneider, L., Esper, J., 2013. Moroccan speleothem and tree ring records suggest a variable positive state of the North Atlantic Oscillation during the Medieval Warm Period. Earth and Planetary Science Letters 375, 291–302. doi:10.1016/j.epsl.2013.05.048.

Wassenburg, J.A., Scholz, D., Jochum, K.P., Cheng, H., Oster, J., Immenhauser, A., Richter, D.K., Häger, T., Jamieson, R.A., Baldini, J.U., Hoffmann, D., Breitenbach, S.F., 2016. Determination of aragonite trace element distribution coefficients from speleothem calciteâaragonite transitions. Geochimica et Cosmochimica Acta 190, 347–367. doi:10.1016/j.gca.2016.06.036.

Watrin, J., Lezine, A.M., Hely, C., 2009. Plant migration and plant communities at the time of the âgreen Saharaâ. Comptes Rendus Geoscience 341, 656–670. doi:10.1016/j.crte.2009.06.007.

Wedepohl, K., 1995. The composition of the continental crust. Geochimica et Cosmochimica Acta 59, 1217–1232. doi:10.1016/0016-7037(95)00038-2.

Wendt, K.A., Li, X., Edwards, R.L., 2021. Uranium-Thorium Dating of Speleothems. Elements 17, 87–92. doi:10.2138/gselements.17.2.87.

Yin, J.J., Li, H.C., Rao, Z.G., Shen, C.C., Mii, H.S., Pillutla, R.K., Hu, H.M., Li, Y.X., Feng, X., 2017. Variations of monsoonal rain and vegetation during the past millennium in Tiangui Mountain, North China reflected by stalagmite δ18O and δ13C records from Zhenzhu Cave. Quaternary International 447, 89–101. doi:10.1016/j.quaint.2017.06.039.

Zhang, G., Cook, K.H., 2014. West African monsoon demise: Climatology, interannual variations, and relationship to seasonal rainfall. Journal of Geophysical Research 119, 10,175–10,193. doi:10.1002/2014JD022043.

Zhao, X., Cheng, H., Sinha, A., Zhang, H., Baker, J.L., Chen, S., Kong, X., Wang, Y., Edwards, R.L., Ning, Y., Zhao, J., 2019. A High-Resolution Speleothem Record of Marine Isotope Stage 11 as a Natural Analog to Holocene Asian Summer Monsoon Variations. Geophysical Research Letters 46, 9949–9957. doi:10.1029/2019GL083836.

Appendices

Additional figures, data and text which is referred to in the main text of chapters throughout this thesis are presented here, in the same order as throughout the thesis. Appendix III is the supplementary information associated with the manuscript presented in Chapter 4, submitted as is to Science Advances. Age models, stable isotope records and trace element data used for interpretations in this thesis are presented in full in the "Additional_Documents.zip" file uploaded along with this thesis.

Appendix I

Appendix figures associated with Chapter 2.



Figure 1: Map of North Africa karst (whymap.org). Light blue and dark blue shading identifies regions of discontinuous and continuous carbonate karstic geology respectively. The location of the Tademaït Plateau, within discontinuous carbonates, is annotated.

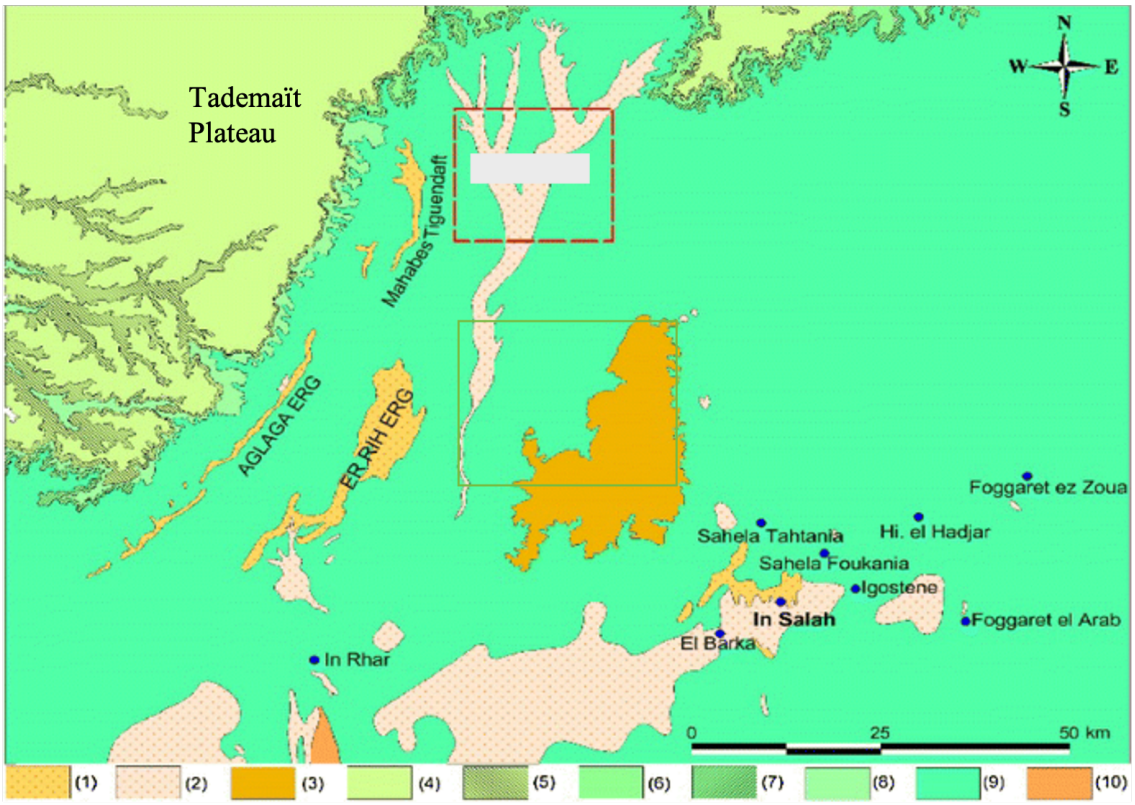


Figure 2: Geologic map of the southern extent of the Tademaït Plateau taken from Madi et al. (2016). Geological units coloured in the legend relate to the following facies (taken from the figure caption of Madi et al. (2016); (1) Dunes, (2) recent quaternary: clayey sand alluvium, (3) tertiary continental: clay and sandstone, (4) upper Senonian: limestone, (5) lower Senonian: clay gypsum, (6) Turonian: dolomite and chalk, (7) Cenomanian: dolomite, (8) Cenomanian and Turonian: dolomite and clay, (9) Lower Cretaceous: clay, sandstone, gravel, and sand, (10) Lower Visean Carboniferous: clay

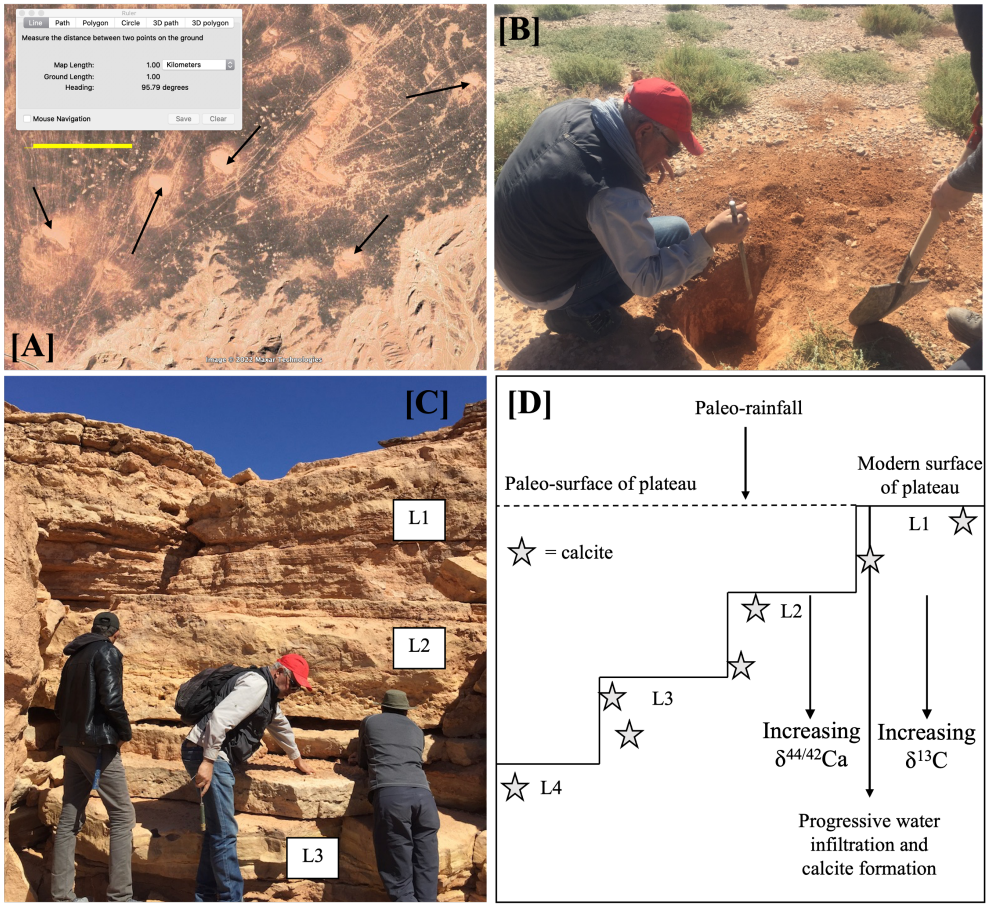


Figure 3: [A] Satellite image of the Tademaït Plateau with apparent doline (sinkhole) features annotated with arrows. A scale bar of 1 km is drawn in yellow. [B] Field image of authors and collaborators digging holes into soil at one of the doline features. Soil was damp past ∼20 cm and had significant vegetation compared to the other regions of the plateau [C] Field image of authors and collaborators at the Levels location on the plateau (Figure 2.2), collecting calcite geodes from "L3". [D] Cartoon representation of the theorised formation of calcite at the Levels location on the plateau, as supported by calcium and carbon isotope analysis (Chapter 6).

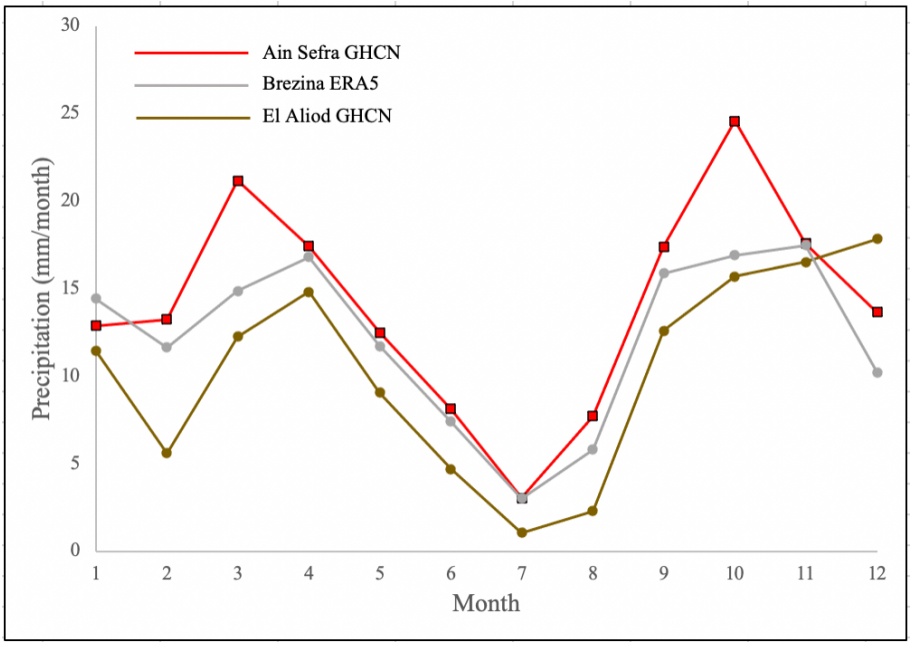


Figure 4: GHCN-M rainfall amounts at sites in the South of Atlas, exhibiting the characteristic peaks during transition seasons (Spring and Autumn). Data sourced from http://climexp.knmi.nl (Trouet and Oldenborgh, 2013). Annual modern rainfall amounts are plotted from climate stations at Ain Sefra (red) and El Aliod (brown) and calculated from ERA-5 reanalysis data at Brezina, the closest site to Grar cave (grey). The bi-modal distribution of rainfall characteristic of the South of Atlas (SOA) region, with peaks during spring and/or autumn, is most apparent in Ain Sefra but is apparent in all annual rainfall records.

Appendix II

Appendix figures associated with Chapter 3.

Biorad columns cleaning protocol

1) 1-2 hrs immersed in 8M reagent grade HNO3, unheated.

2) 3-4 hrs immersed in reagent grade 6M HCl, unheated

3) Overnight and leave in 2M HCl, distilled grade, in 1L polypropylene bottle with wide cap

Biorad resin cleaning protocol

1) Use 100-200 mesh resin only

2) In a clean and designated bottle, add approximately 10-20% resin. Use a funnel and gently tap the resin into the bottle.

3) Fill the bottle with MQ, shake and let the resin settle before decanting as much water as possible. Repeat until the water is clear and no more foam is forming (repeat at least 3 times).

4) Add water to approximately ¾ of the bottle and add 20-50ml distilled HCl and shake. Decant after settling is complete.

5) Repeat water washes 3-4x.

6) Add water and a small amount of distilled HCl to acidify. Store in cabined until used.

Teflon Cleaning

1) Use isopropanol alcohol to wipe clean beakers

2) Add a small amount of reagent grade 16M HNO3 to the beakers, cap and leave to reflux for at least 24 hrs on a hot plate at 130°C. Rinse each beaker 3x with MQ water

3) Acid wash in 8M reagent grade HNO3 for 24 hrs (at least overnight) on a hotplate at 130°C, shake periodically. Rinse the beakers 3x with MQ water (inside the container), then carefully remove the beakers and leave in the fume hood until the next step.

4) Add a small amount of 10M HCl to the beakers, cap and leave to reflux for at least 24 hrs on a hot plate at 130°C.

5) Remove beakers from hot plate, cool, then discard the HCl. Rinse 3x with MQ.

Figure 5: Cleaning procedures for column chemistry

ALT 30/10/06 from an LFR protocol based on Edwards et al 1986 EPSL 81, 175-192; AM mod. 14/4/16

U-Th Chemistry
(U-Th-Ca separation)

A second column pass may be required to separate U from Th cut if samples have > 5 ug U, or Th from Pa cut for sediment samples.

Date: _____ Title: _____ Initials: _____

Samples:

1.	2.	3.	4.	5.	6.
7	8	9	10	11	12

Samples converted to nitrate form	[ ]	
Samples dissolved in 4 ml 7.5 N HNO_3	[ ]	
Clean 2ml columns in 7N HNO_3 and rinse with Milli-Q		
Column protocol:		
2 ml Biorad columns filled with 2 ml new resin slurry (washed 1x8 anion-exchange resin 100-200 mesh)	[ ]	
Wash with 10 ml 7.5M HNO_3	[ ]	
Wash with 10 ml 2% HNO_3	[ ]	
Wash with 10 ml 7.5M HNO_3	[ ]	
Wash with 10 ml 2% HNO_3	[ ]	
Wash with 10 ml 6M HCl	[ ]	
Wash with 10 ml H_2O	[ ]	
Conditioned with 2x5 ml 7.5 M HNO_3	[ ] [ ]	
Load samples directly from sample beaker	[ ]	COLLECT
Wash columns with 2x2 ml 7.5 M HNO_3	[ ] [ ]	AS
Convert the column with 4x0.25ml, 1x0.5ml 6M HCl	[ ] [ ] [ ] [ ] [ ]	RAD WASTE
Elute Th cut with 2x1 ml, 2x2 ml 6 M. HCl	[ ] [ ] [ ] [ ]	COLLECT Th
Elute Pa cut with 2x1 ml, 2x2 ml 6 M. HCl + 0.05N HF	[ ] [ ] [ ] [ ]	COLLECT Pa
Elute U cut with 2x1 ml, 1x4 ml H_2O	[ ] [ ] [ ]	COLLECT U
		in original beakers
Dry down each cut (without boiling)	Th [ ] U [ ] Pa [ ]	
Add 0.2 ml of conc HNO_3 to each cut and dry down	Th [ ] U [ ] Pa [ ]	
Dissolve in 42 ul of 7.5N HNO_3 to store for mass spec	Th [ ] U [ ] Pa [ ]	
(add 958 ul Milli-Q to male 1 ml 2% HNO_3)		

Figure 6: Column chemistry procedures

Batch Data	Sample(s)	$^{232}Th/^{230}Th$ (atomic)	^{232}Th (moles)	^{230}Th (moles)	^{238}U (moles)
Aug-19	L1G1, L1G2, L1G3, L4G7b, L1G4b	2.9E+03	1.79E-15	5.97E-19	2.87E-13
Jan-20	KFT-1, KFT-2, KFT-3	-	3.73E-15	0	4.34E-13
Aug-20	KFT-1, KFT-2, KFT-3, ASD-1, TPB1, QC_L	7.12E+03	6.94E-15	9.75E-19	1.13E-13
Nov-20	BZ-F, BZ-1, QC-1, TPB1, TPB2, TPB3, QC-S, TPB4	1.54E+04	4.46E-15	2.89E-19	1.96E-13
Jan-21	BZ-1B, KFT-1, TPB1, TPB2, TPB3, L4G7b	-	6.54E-15	0	9.97E-14
Apr-21	BZ-1, BZ-1B, QC-1, TPB2	4E+04	1.28E-14	3.78E-19	1.34E-13
Oct-21	BZ-1, QC-1, QC-S	2.3E+03	1.64E-14	7.7E-19	1.34E-13

Table 1: U-Th Blank Data

Appendix III

Appendix figures and additional text associated with Chapter 4. These are the supplementary materials for "North-West Saharan Holocene rainfall driven by interhemispheric temperature differences" to Science Advances.

Cave sites and sample descriptions

Caves sites from this study are in the South of Atlas arid-desert climate zone (BW; Köppen climate classification). Asdif and Kef Thaleb caves lie ∼10 km apart in the Anti-Atlas Mountains (30°N, 8°W, 1880 meters above sea level (masl) and 1890 masl respectively), and Ksar cave is in the southernmost foothills of the High Atlas Mountains (32°N, 4°W, 1380 masl) (Figure S1). All stalagmites presented were collected as fossil deposits, with no observed active dripping. Stalagmites ASD-1 (aragonite), KFT-1 (aragonite) and MM (calcite) were collected from Asdif, Kef Thaleb and Ksar caves respectively. Ksar Cave (32°N, 4°W, ∼1380 masl) is in the southern foothills of the High Atlas Mountains, north of Errachidia. The cave is in a cliff face of horizontally bedded limestones and dolomites. The surface above the cave is flat and broad, with a gentle slope to the NE; the highest point of this surface lies at ∼1500 masl, ∼1 km south of the cave entrance. Stalagmite MM, with ∼12 cm of Holocene growth, was found ∼60 m in from the small entrance. Asdif Cave (30°N, 7°W, ∼1880 masl) consists of a single chamber located at the top of a large, exposed escarpment of horizontally bedded limestones. Soil development is thin above the cave with irregular coverage and sparse vegetation. Stalagmite ASD-1 is ∼14 cm in length, collected ∼15 m from the entrance where the overlying bedrock was ∼4 m thick. Kef Thaleb and Idgh-Igre-Noudardore

lie ∼7 km SW of Asdif Cave (30°N, 8°W, ∼1890 masl). Speleothem decoration is in isolated pockets. Vegetation is denser here than at the other sites. Samples KFT-1, Igre-S and Igre-F are aragonite stalagmites collected from Kef Thaleb and Igre caves respectively.

Definition of north-west and south-west Saharan study areas

To investigate the patterns of rainfall in the Sahara of north-west Africa, we define two areas: i) a north-west Saharan region (28-32°N, 'NW-Sahara'); and (ii) a south-west Saharan region (18-22°N, 'SW-Sahara') (c.f. white boxes, Figure 4.1). The boundaries were defined ∼300 km inland from the Atlantic coast to avoid coastal influences, and are west of 10°E, to avoid eastern or northern Mediterranean sources of moisture. The NW-Saharan region is south-east of the Atlas Mountains. The 18-22°N range of latitudes was selected for the south-west Saharan region because, whilst it has a hot-arid, desert climate in the modern, it is geographically close to the West African Monsoonal system (WAM), with strong agreement in the literature that insolation-driven, northerly-migrations of monsoonal rainfall have increased rainfall within this SW region in the past (Gasse 2000; Kuhlmann et al. 2004; Hély et al., 2014; Dallmeyer et al., 2020). This allows for the comparison of the timing of increased rainfall in the NW (determined from the chronology of stalagmite growth), with the timing of increased moisture in the SW, caused by the northerly expansion of WAM.

Modern climate characteristics

Detailed analysis of 20 years of modern meteorological analysis (Knippertz et al., 2003a) outlines three climate regions within the north western corner of Africa: i) the 'Atlantic' (ATL) climate along the western coast; ii) the inland 'South of Atlas' (SOA) climate; and iii) the 'Mediterranean' climate north east of the Atlas mountains (Figure S1). Only two of these climate classifications, SOA and ATL, apply to this study south of the Atlas topography. Ksar cave is located at the heart of the SOA climate zone,

whilst our Anti-Atlas caves (Asdif, Kef Thaleb, Igre) are located midway between the coastal ATL and the inland SOA climate zones. Features distinguishing the coastal ATL climate from the inland SOA climate are: i) dominance of winter rainfall for ATL; ii) reduced rainfall levels, and a bimodal distribution of transition season rainfall for SOA; iii) Tropical-Plume rainfall contributes up to 40% of annual rainfall in SOA, but only a small percentage of rainfall in ATL (12). For both of these climate zones, south of the Atlas, there is minimal rainfall during the summer months ($\leq$ 10 mm/month). These trends are visible in average monthly rainfall data (Figure S2) from Global Historical Climatology Network-Monthly weather stations (GHCN-M) at Taroudant, Ouarzazate and Errachidia (map Figure S1). To account for the sparsity of weather stations in the Anti-Atlas, rainfall patterns from ERA5 reanalysis data (Hersbach et al., 2020) were also examined for a 4-grid box around our Anti-Atlas cave sites (Figure S1), with agreement between the reanalysis data from our Anti-Atlas sites and the closest weather station at Ouarzazate (Figure S2). The amount of winter rainfall (December, January, February) is highest close to the coast at Taroudant ($\sim$125 mm, 53% annual rainfall), lowest inland at Ksar cave ($\sim$28 mm, 22% annual rainfall), and intermediate at our Anti-Atlas cave sites ($\sim$49 mm, 31% annual rainfall). In the south-west Sahara (box 'SW-Sahara', Figure 4.1), the maximum observed rainfall amount in the modern day is 130 mm/year, based on data from 7 climate stations within this region.

Modern day oxygen isotopes of coastal winter rainfall, and of tropical plume rainfall

Average modern day oxygen isotope values of coastal $\delta^{18}O_{rain}$ and of Tropical-Plume $\delta^{18}O_{rain}$ were obtained from the literature, for illustration alongside stalagmite records. The oxygen isotopic composition of coastal rainfall at Wintimdouine cave (winter dominated) has a non-weighted average $\delta^{18}O_{rain}$ = -5.8 $\pm$ 2.4‰ (n=29, 1σ), relative to VSMOW, from Ait Brahim et al. (2019). The oxygen isotopic composition of Tropical-Plume rainfall events in the Anti-Atlas have a much lower mean weighted average

$\delta^{18}O_{rain}$ = -12.4 ± 4.3‰, relative to VSMOW, from Cappy (2007). To plot these $\delta^{18}O_{rain}$ values alongside stalagmite oxygen isotope records (Figure 4.3A), we convert $\delta^{18}O_{rain}$ to $\delta^{18}O_{calcite}$ using the fractionation factors of Kim and O'Neil (1997), with a temperature of 19°C applied to the Wintimdouine cave site (Ait Brahim et al., 2019), and an average temperature of 17°C applied to our higher altitude Anti-Atlas and Ksar cave sites. This suggests calcite oxygen isotope values (expressed relative to VPDB) of ∼-7‰ (for coastal stalagmites, such as those from Wintimdouine cave) and of ∼-13‰ for stalagmites supplied exclusively by Tropical-Plume rainfall. Anti-Atlas cave sites are fed by a mixture of coastal (winter season) rainfall and of Tropical-Plume rainfall, so an increase in the proportion of Tropical-Plume rainfall leads to lower stalagmite oxygen isotopes, and vice versa. A continentality effect on oxygen isotopes is not seen at these caves sites, as evidenced by periods of overlapping oxygen isotopes between Wintimdouine & Anti-Atlas caves, and between Anti-Atlas & Ksar caves (Figure 4.3A), despite hundreds of kilometres separating these three sites (Figure S1).

Oxygen isotope analyses and corrections

For samples ASD-1 and MM, 30-60 μg of carbonate powder was analysed for oxygen and carbon stable isotopes using a Thermo Scientific Delta V isotope ratio mass spectrometer (IRMS) coupled to a Kiel IV carbonate device at the University of Oxford, Department of Earth Sciences. All sample measurements were calibrated with NBS-18 and NBS-19 bracketing standards. All samples were reacted with 100% H3PO4 at 71 °C. For sample KFT-1, 120-160 μg of carbonate powder was analysed for oxygen and carbon stable isotopes using the same Thermo Scientific Delta V IRMS fitted with a GasBench II peripheral. The powdered samples, in 12 mL He-flushed exetainers (Labco), were reacted with 100% H_3PO_4 at 71 °C. In all cases the relative $^{13}C/^{12}C$ values are reported in the conventional $\delta^{13}C$ (‰) notation, relative to the Vienna Pee Dee Belemnite (V-PDB), by assigning a value of +1.95‰ exactly to NBS-19. The relative $^{18}O/^{16}O$ values are reported in the conventional $\delta^{18}O$ (‰) notation, relative to V-PDB, on a normalised

scale such that the $\delta^{18}O$ of NBS-19 is -2.2‰. Accuracy and precision were checked using a secondary standard's long-term average, included in all runs, with standard deviations of $\delta^{18}O = 0.07‰$ and $\delta^{13}C = 0.05‰$ (1σ). For measurements of aragonite $\delta^{18}O$, IUPAC guidelines were followed to account for the difference in acid fractionation factor applicable to the calcite bracketing standards (NBS-18 and NBS-19) and the aragonite samples. We used aragonite acid fractionation factors from Kim et al. (2007), calcite acid fractionation factors from Kim et al. (2015), and the method/software of Kim et al. (2015) for normalising the stable isotope data of these two different carbonate mineralogies. To directly compare the oxygen isotopes of aragonite and calcite stalagmite samples, a correction of -0.81‰ was applied to all $\delta^{18}O_{aragonite}$ values, to account for the difference in fractionation factor between aragonite and calcite mineralogies when precipitating from rain sourced water (Fohlmeister et al., 2018).

Anti-Atlas composite record

The composite Anti-Atlas $\delta^{18}O$ record, from the overlapping records of samples KFT-1 and ASD-1, was generated using ISCAM (Fohlmeister, 2012), a Monte Carlo statistical method using absolute ages to produce a single climate record from adjacent archives. KFT-1 and ASD-1 $\delta^{18}O$ records replicate each other within temporal uncertainties during periods of coeval growth (Figure S3). These replications are confirmed by statistically significant correlation between KFT-1 and ASD-1 ($r^2 = 0.77$ at 95% CI), calculated using ISCAM (Figure S3). This composite record is referred to as the Anti-Atlas (AA) record in the main text.

Calculation of interhemispheric temperature anomalies

The temperature difference between the extratropics (poleward of 30°) of the Northern and Southern Hemisphere relative to a modern reference period (Figure 4.2A, Figure 4.3B) is calculated using the regularised expectation-maximisation reconstructions (RegEM) algorithm (Schneider, 2001) with 73 globally distributed temperature records

(Marcott et al., 2013), as is shown in Figure 3a of (Schneider et al., 2014). Recently, Kaufman et al. (2020a) applied five different statistical methods to the Temperature 12k database (Kaufman et al., 2020b) to reconstruct global and latitudinal temperatures. For each method, a 500-member ensemble of plausible reconstructions was generated to produce a probabilistic analysis of uncertainties. Ensemble members from all methods were combined to generate a multi-method median global mean surface temperature (GMST) reconstruction. For comparison, Figure S4 plots the extratropics interhemispheric temperature contrast reconstruction used in Figure 4.2A and Figure 4.3B, alongside a calculated extratropics interhemispheric temperature contrast reconstruction using the statistical method ensembles of plausible latitudinal temperature reconstructions of Kaufman et al. (2020a). Note that the temperature dataset of (Marcott et al., 2013) uses 1960-1990 CE as the reference period to calculate Holocene temperature anomalies, while the ensembles of Kaufman et al. (2020a) use 1800-1900 CE as the reference period to calculate Holocene temperature anomalies. Thus, the interhemispheric temperature contract anomalies (y-axis) are offset between the two figures, but the relative differences through the Holocene are comparable. We note the interhemispheric temperature difference is increasing prior to ∼7-8 kyr BP and decreasing post ∼7-8 kyr BP regardless of the latitudinal temperature reconstruction used to calculate the interhemispheric temperature difference. Thus, our conclusions on the timing of NW-Sahara stalagmite growth relative to the peak interhemispheric temperature difference of the Holocene are not dependent on the chosen temperature reconstruction from the current collection available in the literature.

U-Th Dating Methods

Samples for U-Th chronology were hand-drilled for KFT-1 and MM. Samples were milled on a New Wave MicroMill for ASD-1. The powdered carbonate samples were dissolved in nitric acid and spiked with a ^{229}Th–^{236}U solution. The U and Th fractions were separated following chemical procedures from Edwards et al. (1987). At least 1

blank was included for every 9 samples processed through chemistry. U and Th isotopes were measured separately using a Nu Plasma multi-collector inductively coupled plasma mass spectrometer (MC-ICP-MS) at the University of Oxford department of Earth Sciences, following the procedures described in Carolin et al. (2019). Individual ages and 95% confidence intervals were calculated using an in-house Monte Carlo script (DONKEY) that incorporates chemical blank measurements, analytical uncertainties, and an initial $^{230}Th/^{232}Th$ ratio of 9.2 ± 4.6ppm based on Kaufman and Broecker (1965). All ages were corrected to the year 1950 C.E (i.e., BP). OxCal Version 4.3 was used to develop the age models for each stalagmite (Bronk Ramsey, 2009). The age models with 95% confidence intervals were produced using the P-Sequence Poisson-process deposition model [k0 = 1 cm−1, log10(k/k0) = U(−2,2)], defined by parameter k, which constrains the number of potential growth-rate changes per unit length (51, 52). Ko was set to 1 for ASD-1, 1 for KFT-1, and 26 for MM.

XRD analysis

Aliquots of milled carbonate powders of ∼0.25 mg were analysed at the University of Oxford, Department of Earth Sciences, using a Panalytical Empyrean Series 2 powder diffractometer. HighScore software was subsequently used to detect peaks and calculate % of minerals based on user-selected best fit mineral candidates. MM was shown to be high-magnesium calcite, KFT-1 and ASD-1 are aragonite, in agreement with visible aragonite needles.

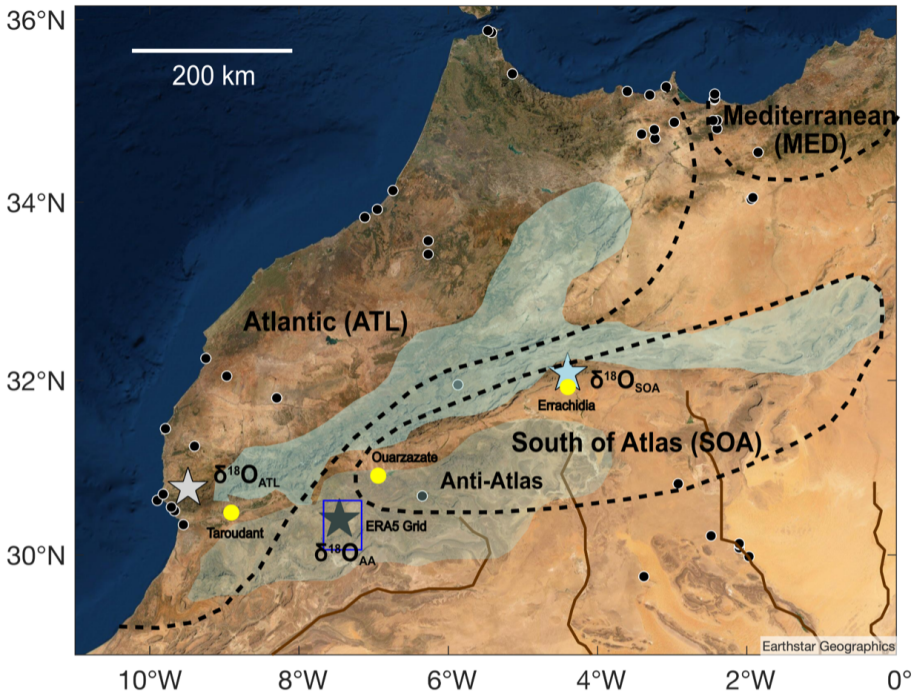


Figure 7: Figure S1: Map of this study's cave sites relative to modern-day climate zones and topography. The pale blue star is Ksar cave from this study. The black star is the location of three Anti-Atlas caves Asdif, Kef Thaleb and Igre from this study. The grey star is the coastal Wintimdouine cave (Sha et al., 2019). High topography is shaded green. Dashed black lines delineate the Atlantic, South of Atlas and Mediterranean climate zones defined by (Knippertz, 2003). Black dots are radiocarbon-dated Neolithic sites compiled by Manning and Timpson (2014). Brown lines are topographically-defined surface water flows modelled using NASA SRTM3 data and Topotoolbox2 (Schwanghart and Scherler, 2014).

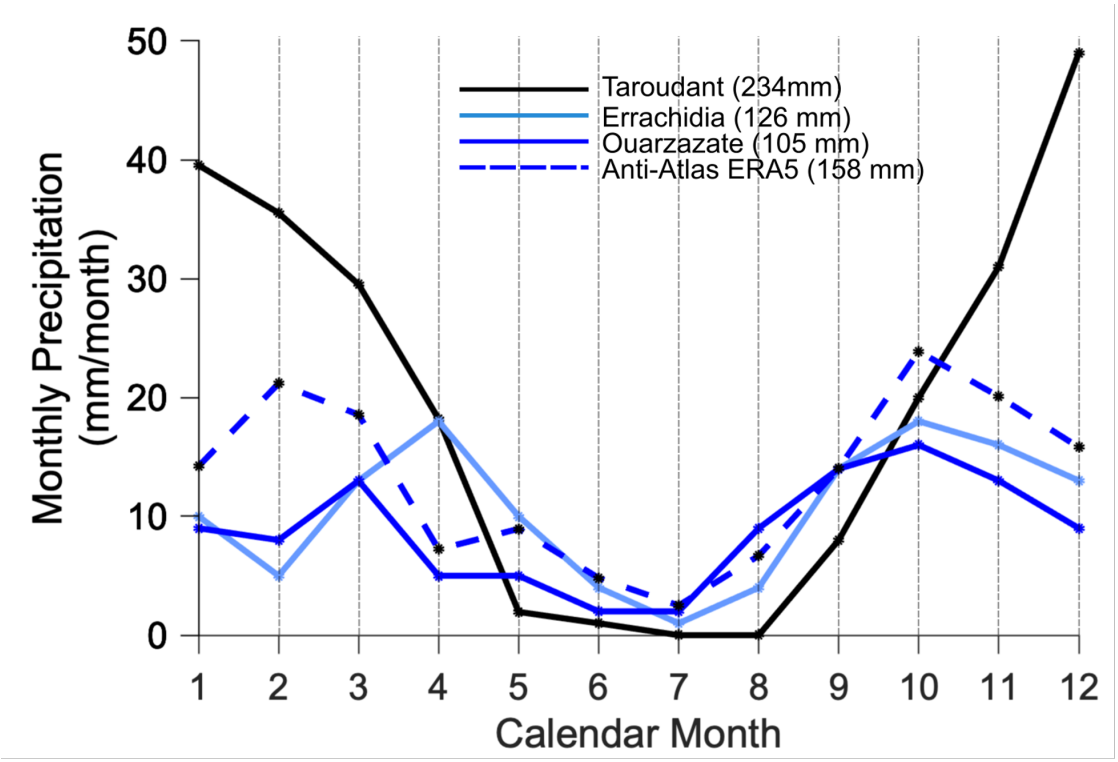


Figure 8: Figure S2: Modern day monthly rainfall amounts from weather station data (continuous lines) and from reanalysis data (dashed line) applicable to cave sites south of the Atlas Mountains. The annual average mm of rain for each site is given in brackets in the legend.

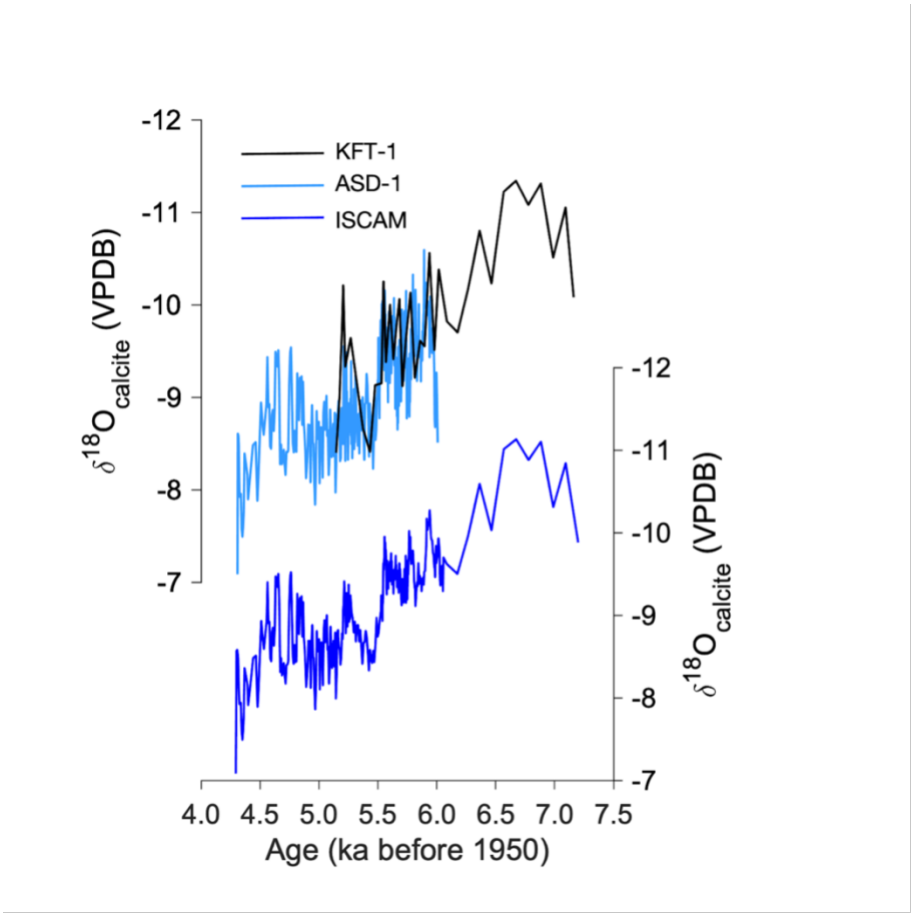


Figure 9: Figure S3: Composite record (dark blue) of $\delta^{18}O_{calcite}$, from Anti-Atlas stalagmites ASD-1 (light blue) and KFT-1 (black) using the statistical software tool ISCAM (Fohlmeister, 2012). A fifty-year smoothing of $\delta^{18}O_{calcite}$ was performed prior to processing with ISCAM. ISCAM input parameters were nrAR1 = 2000, nrAR1_MC = 1000, nrMC = 100,000 as per (Fohlmeister, 2012). This composite record is subsequently referred to as the Anti-Atlas (AA) record.

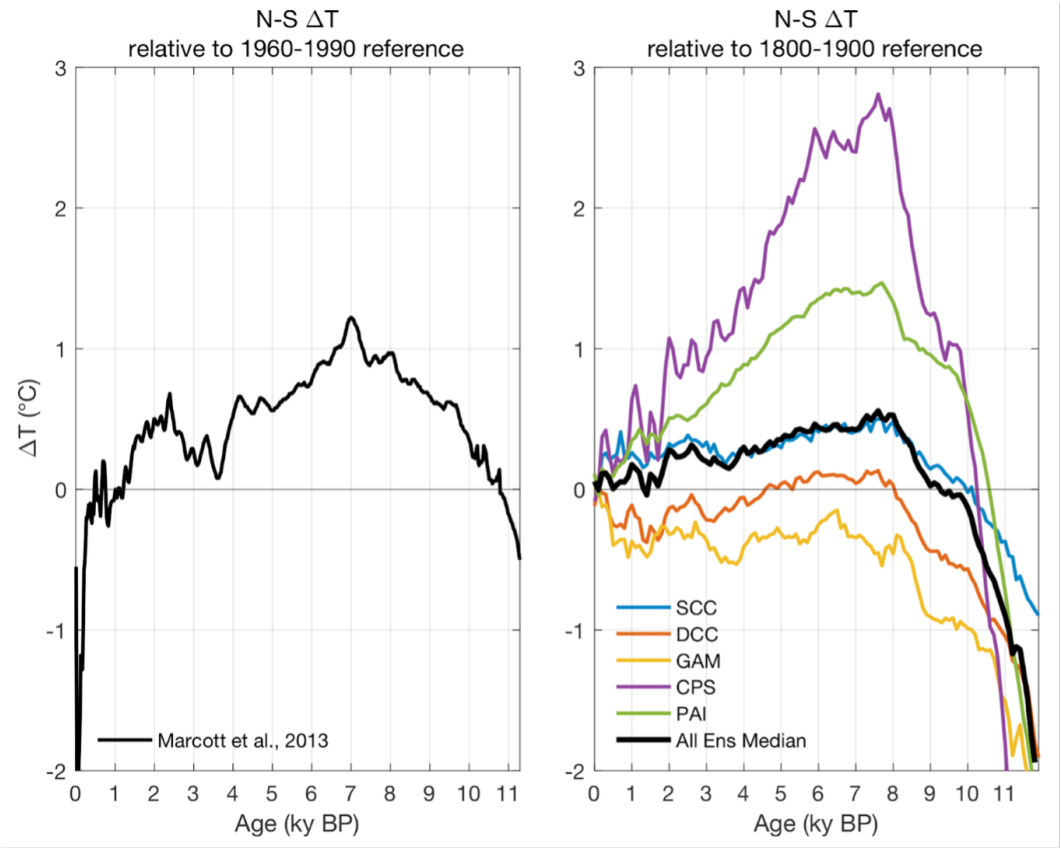


Figure 10: Figure S4: Comparison of extratropical interhemispheric temperature difference using the temperature reconstruction of Marcott et al. (2013) (left) and the statistical method temperature reconstruction ensembles of Kaufman et al. (2020a) (right). Different coloured lines in the right-hand plot represent the five different temperature reconstruction methods used in Kaufman et al. (2020a). Reconstructions in both figures define the interhemispheric temperature difference as the difference between the 30-90°N mean and the 30-90°S mean. Note the difference in reference periods to calculate the Holocene temperature difference anomaly listed at the top of each subplot.

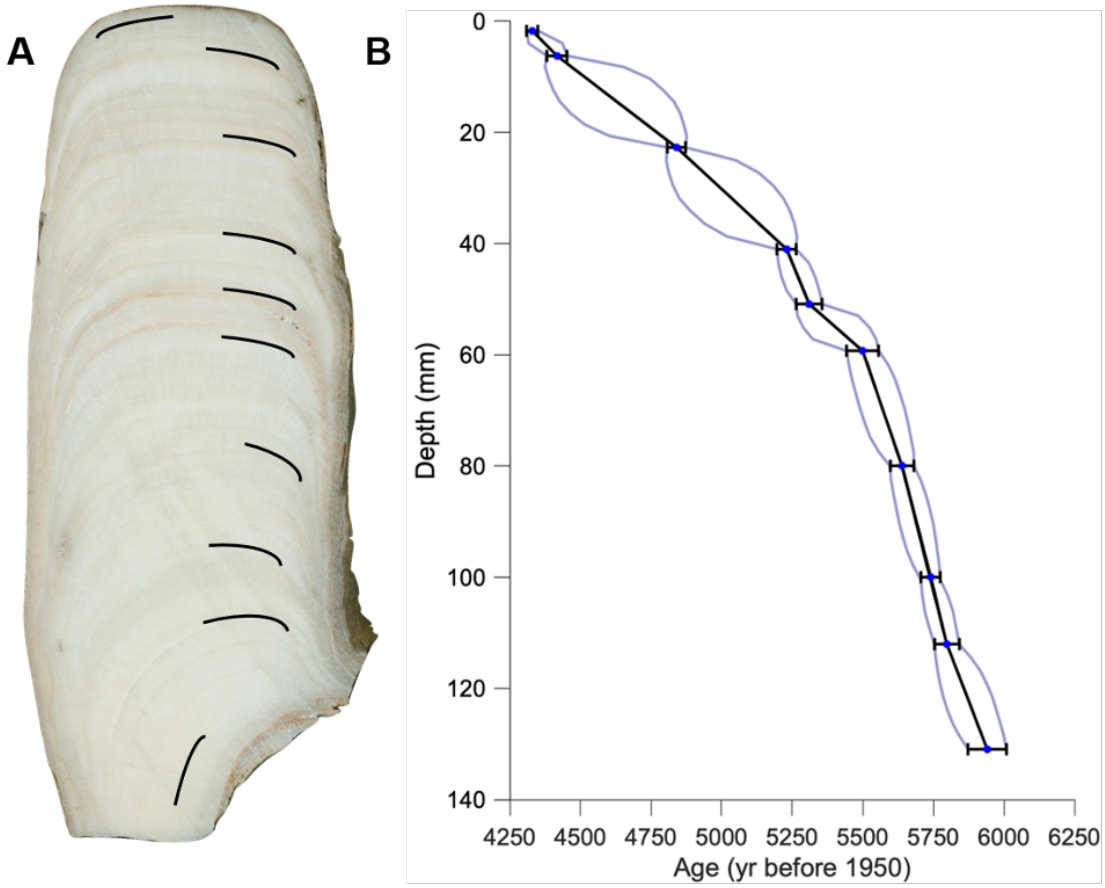


Figure 11: Figure S5: Scanned image of sample ASD-1 (A) with the corresponding age versus depth plot (B).

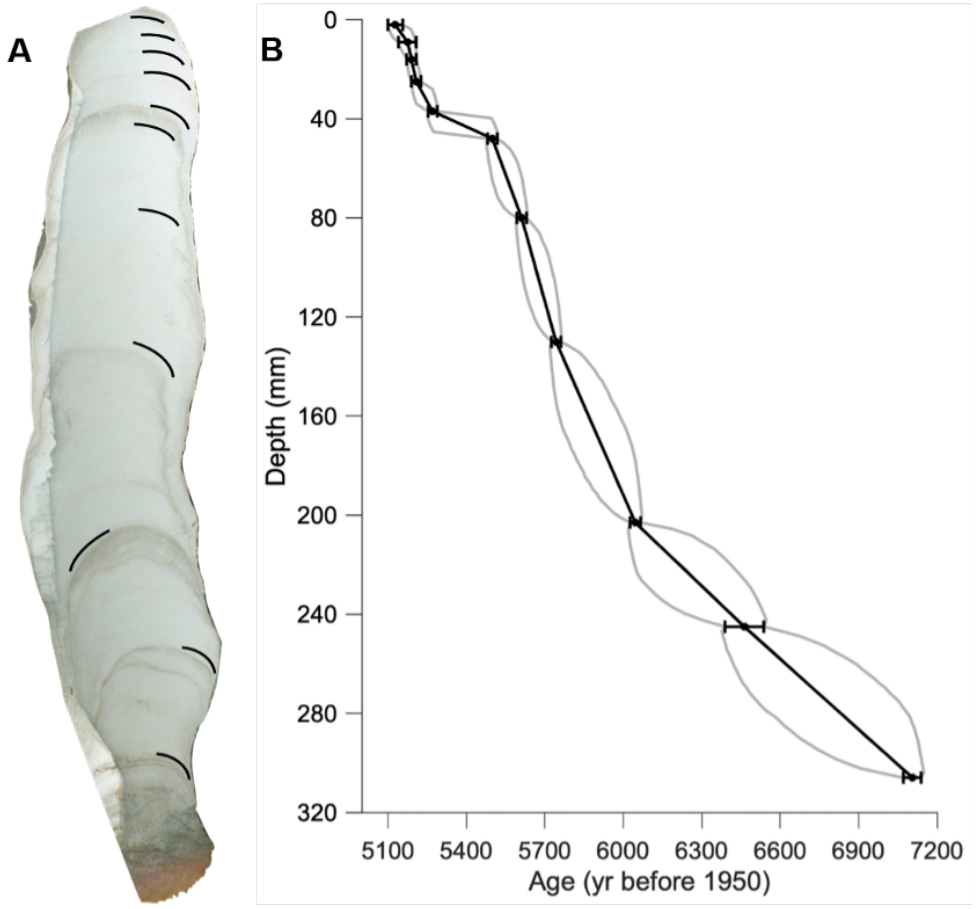


Figure 12: Figure S6: Scanned image of sample KFT-1 (A) with the corresponding age versus depth plot (B).

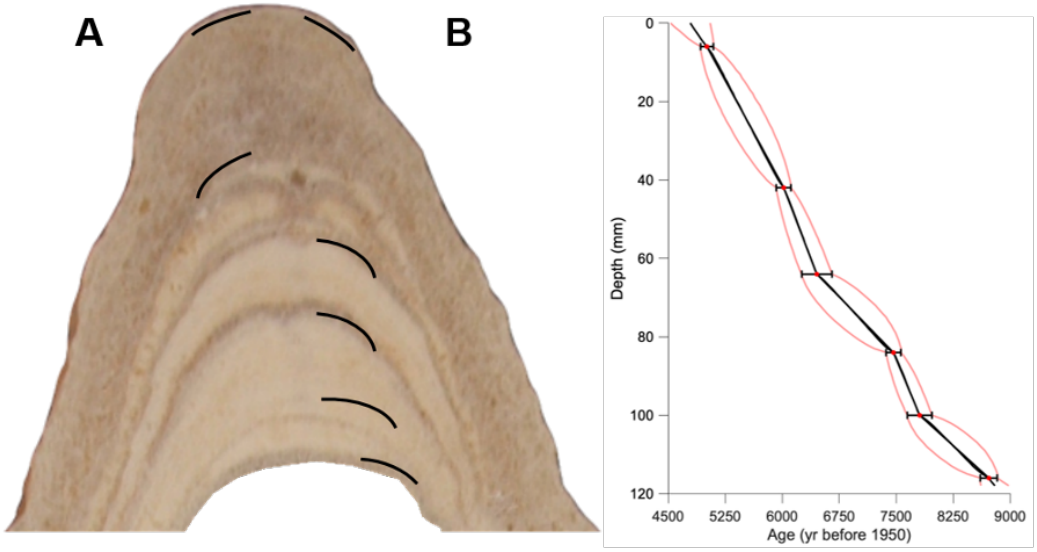


Figure 13: Figure S7: Scanned image of sample MM (A) with the corresponding age versus depth plot (B).

Stal ID	Distance (mm)	^{238}U conc ppm	(230/232)	(234/238)	(234/238) error (2s)	(230/238)	(230/238) error (2s)	(232/238)	(232/238) error (2s)	Uncorr. Age (yr b1950)	Corr. Age (yr b1950)	Corr. Age error (2s)
ASD-1	2	4.63	2079	3.093	0.010	0.1228	0.000	5.90E-05	1.46E-06	4330	4326	19
ASD-1	6	4.70	770	3.096	0.003	0.1245	0.001	1.58E-04	9.20E-07	4429	4419	36
ASD-1	23	5.50	45975	3.019	0.007	0.1334	0.001	2.90E-06	1.36E-06	4840	4840	32
ASD-1	41	6.40	2922	3.110	0.008	0.1482	0.001	5.07E-05	1.06E-06	5234	5231	34
ASD-1	51	3.50	16748	3.286	0.008	0.1588	0.001	9.48E-06	2.56E-06	5308	5307	48
ASD-1	59	2.80	32952	3.303	0.008	0.1656	0.002	5.02E-06	2.73E-06	5513	5513	58
ASD-1	80	2.40	17596	3.615	0.009	0.1853	0.001	1.05E-05	3.78E-06	5643	5642	47
ASD-1	100	3.40	61584	3.780	0.009	0.1970	0.001	3.20E-06	2.53E-06	5739	5738	37
ASD-1	112	3.50	69829	3.928	0.010	0.2068	0.002	2.96E-06	2.07E-06	5796	5796	48
ASD-1	131	2.45	8104	4.469	0.003	0.2387	0.003	2.42E-05	1.70E-06	5939	5938	70
KFT-1	2	2.36	1732	3.618	0.009	0.1693	0.001	9.78E-05	1.67E-06	5128	5123	27
KFT-1	9	1.67	1428	3.757	0.003	0.2180	0.002	1.50E-04	8.75E-07	5193	5192	51
KFT-1	16	2.88	39430	3.667	0.010	0.1735	0.001	4.40E-06	6.96E-07	5188	5188	20
KFT-1	25	2.65	4700	3.661	0.010	0.1740	0.000	3.70E-05	8.70E-07	5210	5208	18
KFT-1	37	3.47	34476	3.677	0.010	0.1767	0.000	5.13E-06	6.06E-07	5271	5270	18
KFT-1	48	2.68	6770	3.704	0.010	0.1855	0.001	2.74E-05	7.70E-07	5501	5500	19
KFT-1	80	2.56	60146	3.774	0.010	0.1927	0.001	3.20E-06	7.78E-07	5612	5612	20
KFT-1	130	3.33	25006	3.735	0.010	0.1950	0.001	7.80E-06	6.25E-07	5743	5743	18
KFT-1	203	3.14	10287	3.739	0.010	0.2052	0.001	1.99E-05	6.05E-07	6046	6045	19
KFT-1	245	2.46	4827	3.650	0.003	0.1719	0.002	3.28E-05	9.16E-07	6472	6464	77
KFT-1	306	3.98	2680	3.706	0.012	0.2378	0.001	8.87E-05	2.08E-06	7109	7105	32
Igre-S	2	0.09	963	6.013	0.003	0.4302	0.008	2.92E-04	1.11E-05	7988	7978	116
Igre-F	5	1.74	1021	4.405	0.003	0.1871	0.001	1.82E-04	1.06E-06	4691	4683	32
MM	6	0.12	145	2.493	0.022	0.1139	0.001	7.87E-04	2.23E-05	5017	4958	84
MM	42	0.11	73	2.438	0.011	0.1351	0.001	1.86E-03	4.84E-05	6122	5981	100
MM	64	0.10	26	2.483	0.008	0.1492	0.002	5.81E-03	3.22E-05	6661	6229	246
MM	84	0.16	126	2.552	0.007	0.1729	0.002	1.37E-03	1.13E-05	7539	7440	103
MM	100	0.10	38	2.410	0.007	0.1732	0.001	4.56E-03	2.04E-05	8012	7663	188
MM	116	0.15	219	2.582	0.007	0.2024	0.003	9.23E-04	1.30E-05	8760	8694	111

Figure 14: Table S1: U-Th chronology of stalagmite samples ASD-1 (Figure S5), KFT-1 (Figure S6), Igre, and MM (Figure S7). 'Distance' is distance from the stalagmite top of the sample, in mm, with smaller distance corresponding with younger age. Measured isotope ratios are given in activity format, where i.e. (234/238) = (N234*λ234)/(N238*λ238). Ages were calculated using half-lives found in Cheng et al. (2013). Uncorrected ages were calculated ignoring any initial ^{230}Th or ^{234}U from detrital contaminants. Corrected ages were calculated using an initial ^{230}Th/^{232}Th atomic ratio of 6 ± 4 ppm (uniform distribution) Kaufman and Broecker (1965).

Additional Interpretations

ASD-1 as a recorder of ITCZ variations

The strong correlation between the oxygen isotopes of our Anti-Atlas stalagmites with a calculated N-S temperature anomaly demonstrates the sensitivity of stalagmite growth and δ^{18}O variation in these samples to the more northerly mean position of the Atlantic northern hemisphere ITCZ. This relationship can be examined further by comparing the high-resolution datasets of ASD-1 δ^{18}O and Cariaco basin %Ti (Haug et al., 2001), which is a distal (central America) tropical recorder of mean latitude northern hemispheric ITCZ position. Within error, ASD-1 δ^{18}O and Cariaco basin %Ti

records are remarkably well correlated, further demonstrating the sensitivity of Anti-Atlas speleothems in recording changes in the mean northerly ITCZ position, and supporting interpretations that this positioning is important for increased rainfall in the Anti-Atlas, as opposed to the strength of the WAM system, which would not be recorded in Cariaco basin %Ti.

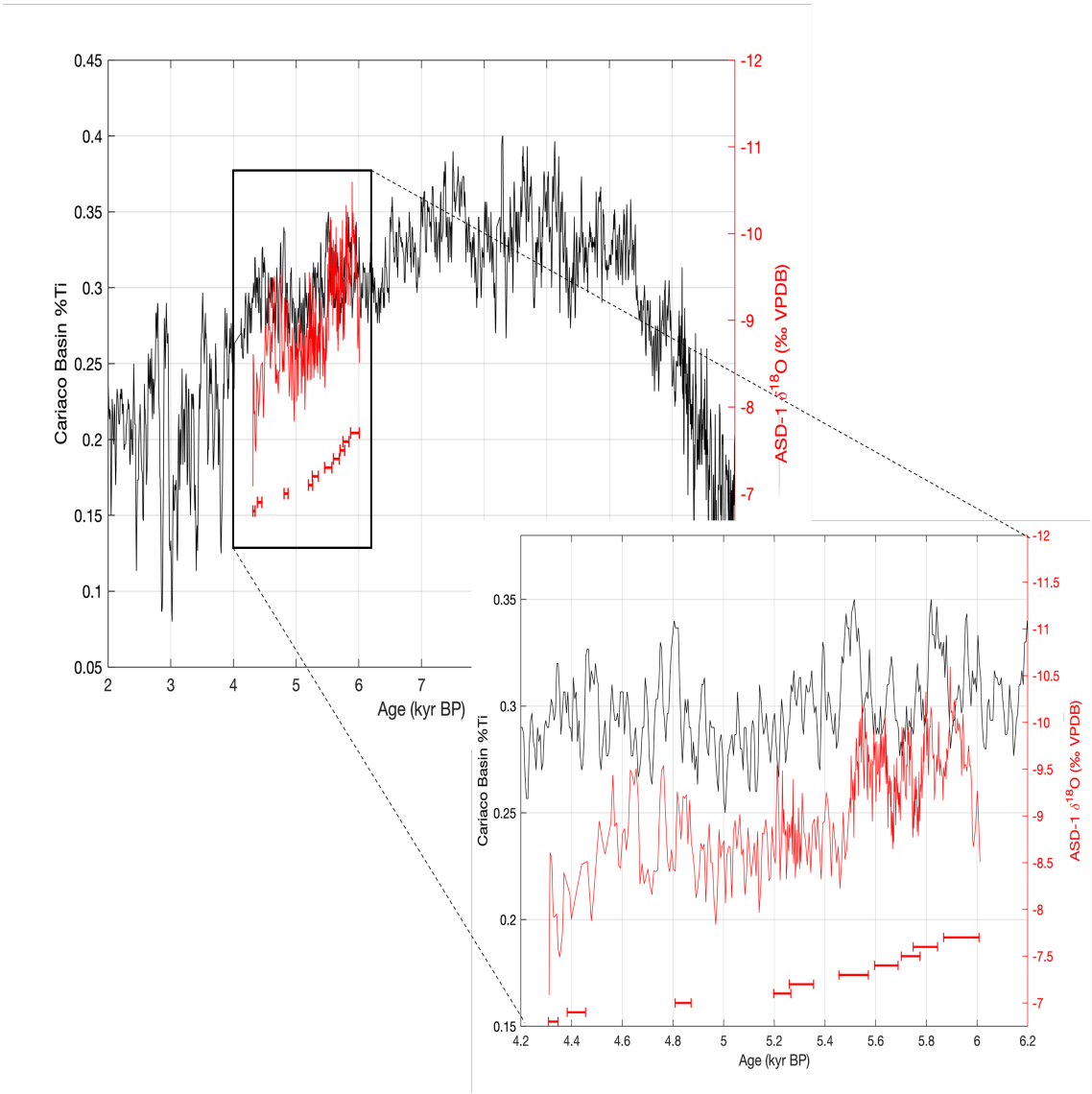


Figure 15: ASD-1 δ^{18}O vs Cariaco Basin %Ti

Appendix IV

Appendix figures associated with Chapter 5.

Pattern List

Sample	Ref.Code	Mineral Name	SemiQuant[%]	Score	Compound Name	Scale Fac.	Chem. Formula
BZ-1	01-085-1108	Calcite	100	81	Calcium Carbonate	0.680	Ca (C O3)
Sample	**Ref.Code**	**Mineral Name**	**SemiQuant[%]**	**Score**	**Compound Name**	**Scale Fac.**	**Chem. Formula**
KFT-1	04-007-0048	Aragonite, syn	100	58	Calcium Carbonate	0.677	Ca (C O3)
Sample	**Ref.Code**	**Mineral Name**	**SemiQuant[%]**	**Score**	**Compound Name**	**Scale Fac.**	**Chem. Formula**
TPB4	04-013-2116	Calcite, Mg-bearing	100	57	Calcium Magnesium Carbonate	0.915	Ca0.936 Mg0.064 (C O3)
Sample	**Ref.Code**	**Mineral Name**	**SemiQuant[%]**	**Score**	**Compound Name**	**Scale Fac.**	**Chem. Formula**
QC-1	04-012-0489	Calcite	100	76	Calcium Carbonate	0.926	Ca (C O3)
Sample	**Ref.Code**	**Mineral Name**	**SemiQuant[%]**	**Score**	**Compound Name**	**Scale Fac.**	**Chem. Formula**
TPB1	04-006-6528	Calcite, syn	100	45	Calcium Carbonate	0.773	Ca (C O3)

Figure 16: A range of XRD results from samples included in each data chapter within this thesis. Most samples are pure calcite in mineralogy, except for sample KFT-1 which is aragonite and TPB4 which has high levels of magnesium.

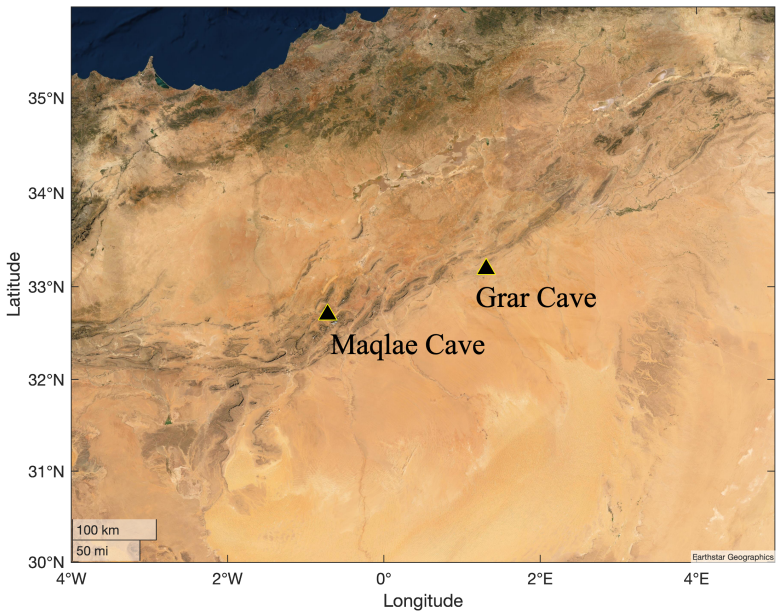


Figure 17: Zoomed in figure of Ksour Mountain field sites. There is less topography between the Mediterranean and Maqlae cave than between the Mediterranean and Grar cave, which may contribute to some speleothem growth at Maqlae cave during a northern hemisphere glacial, between 145-155 kyr BP.

Appendix V

Appendix figures associated with Chapter 6.

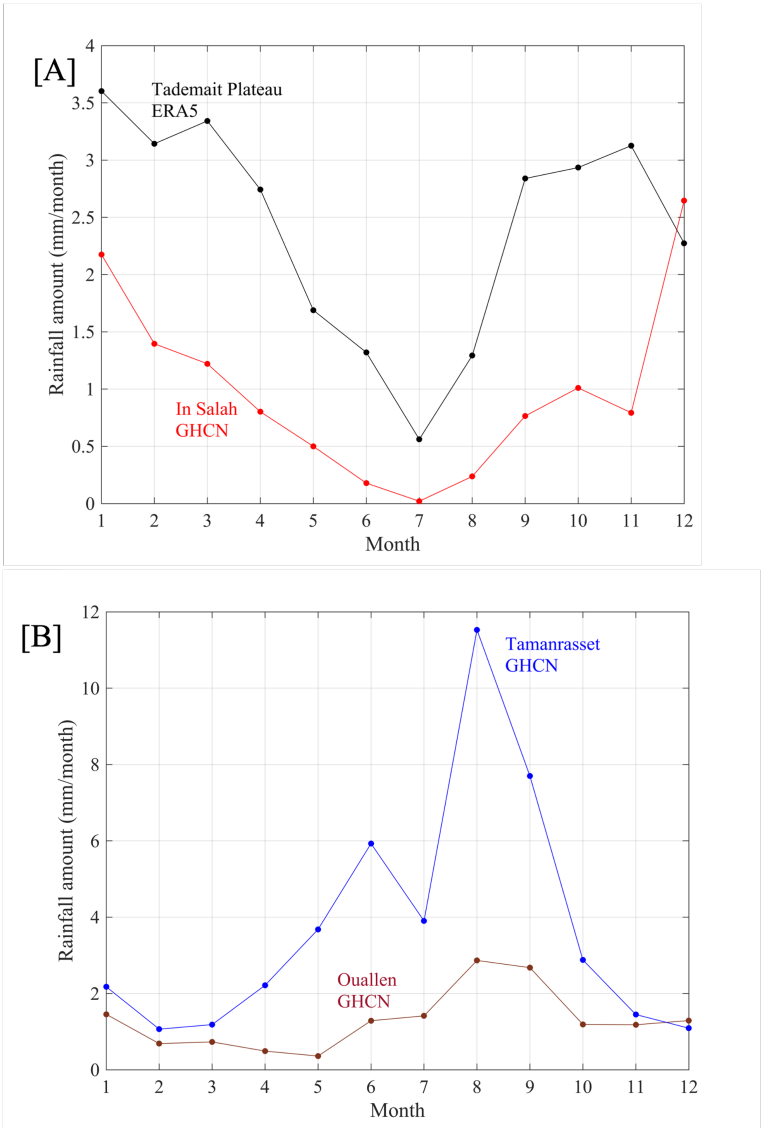


Figure 18: [A] GHCN-M monthly rainfall at In Salah (red) and ERA5 monthly reanalysis rainfall at the Tademaït Plateau (black), which peaks during boreal winter [B] GHCN monthly rainfall at Tamanrasset (blue) and Ouallen (maroon), which peaks during boreal summer Data sourced from http://climexp.knmi.nl (Trouet and Oldenborgh, 2013).

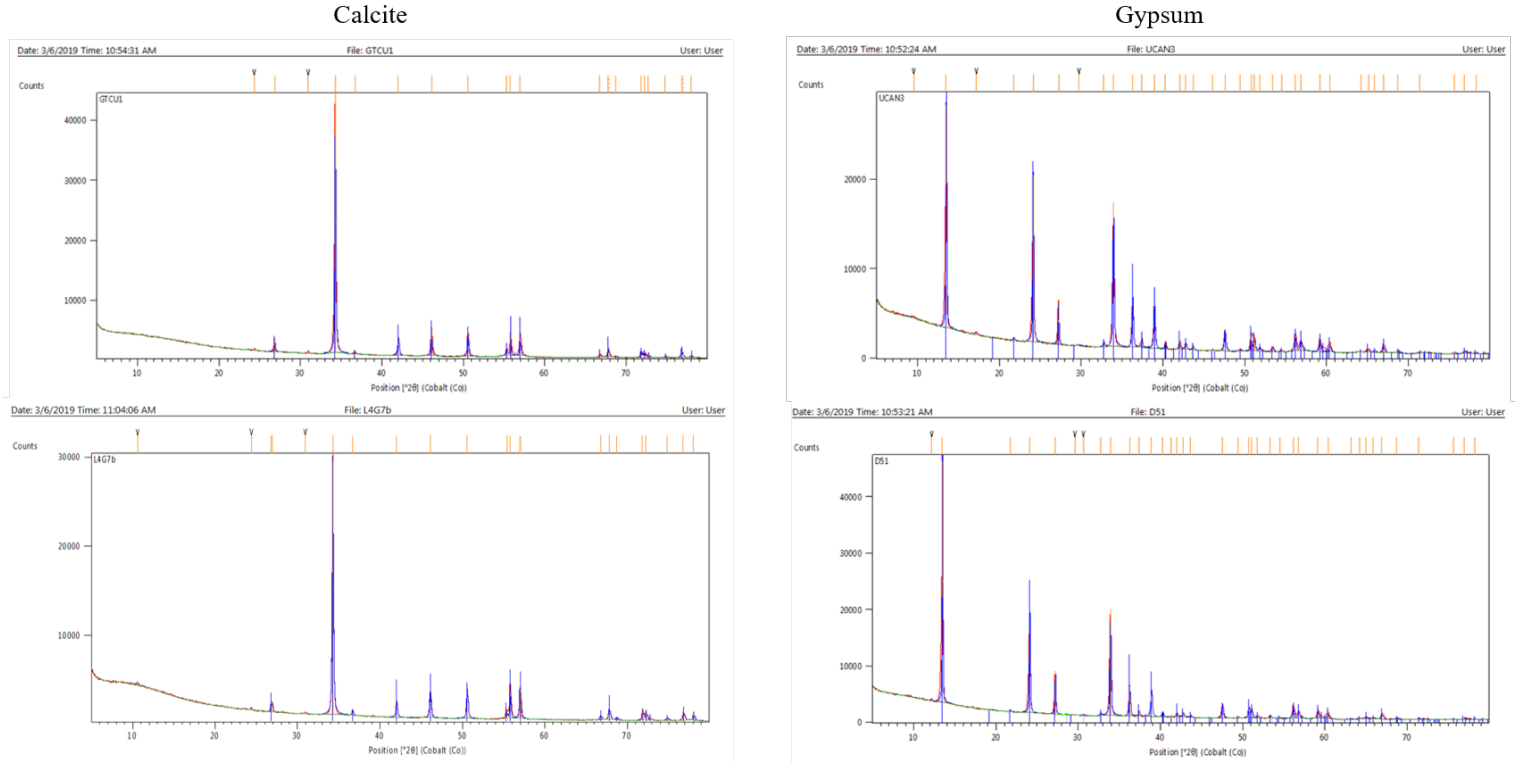


Figure 19: Examples of peak data from Tademaït Plateau samples XRD analyses. Left column are calcite and right column are gypsum. Peak matching was completed using HighScore software.

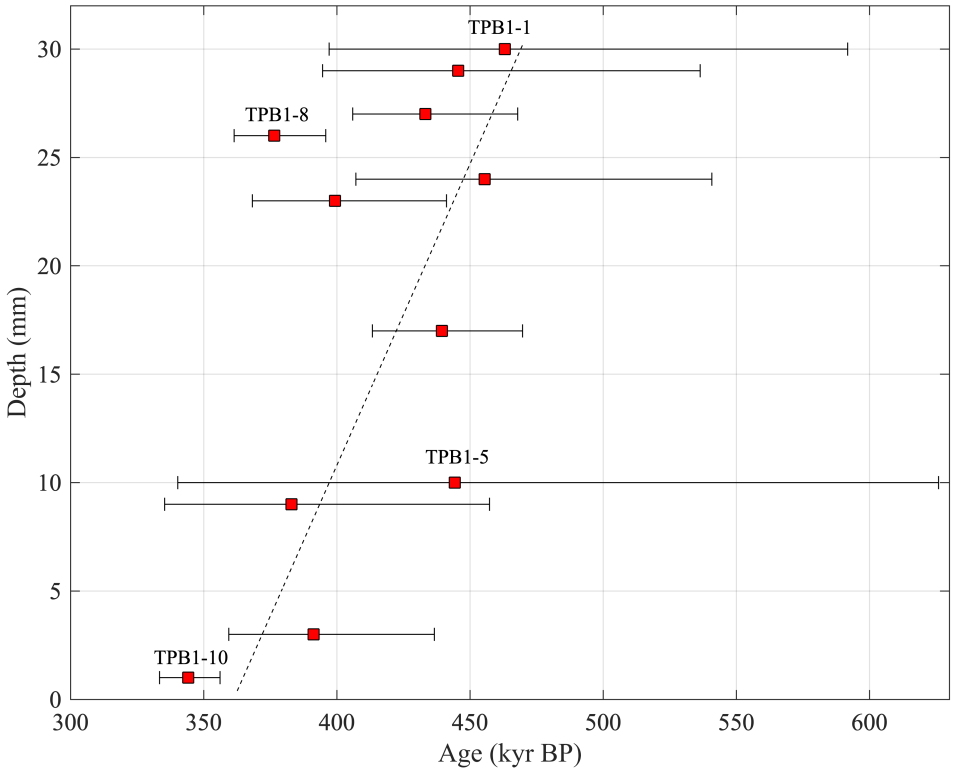


Figure 20: All TPB1 Ages vs depth from the top of the sample (top = 0mm depth)

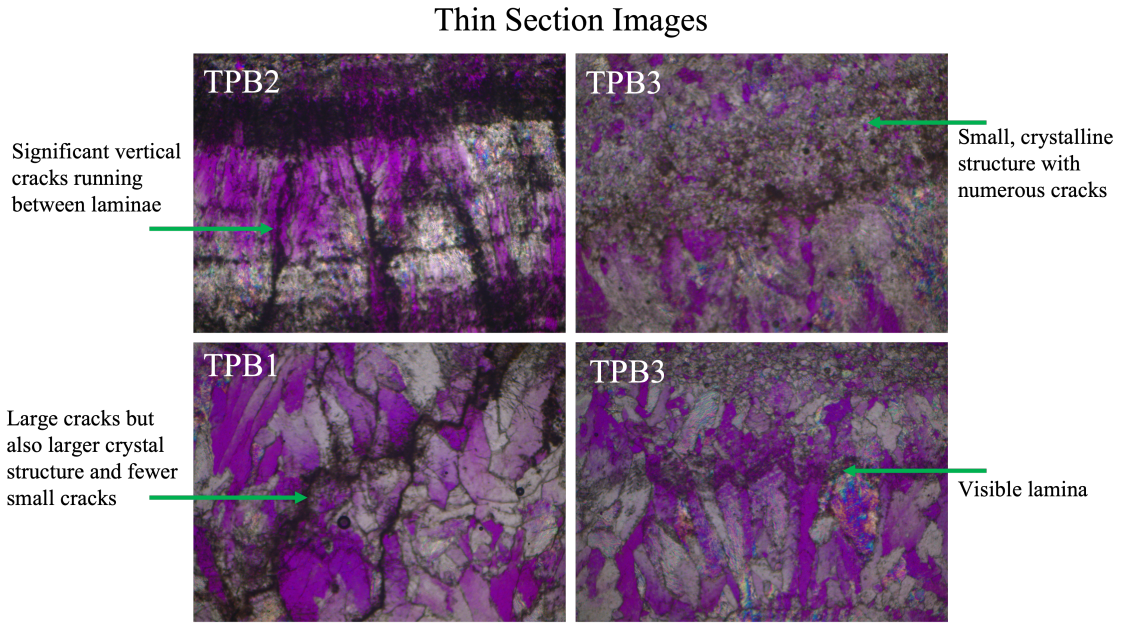


Figure 21: Tademaït Plateau thin section images in cross-polarized light. Notable features are annotated including cracks within the crystal lattices, as referenced in the text.

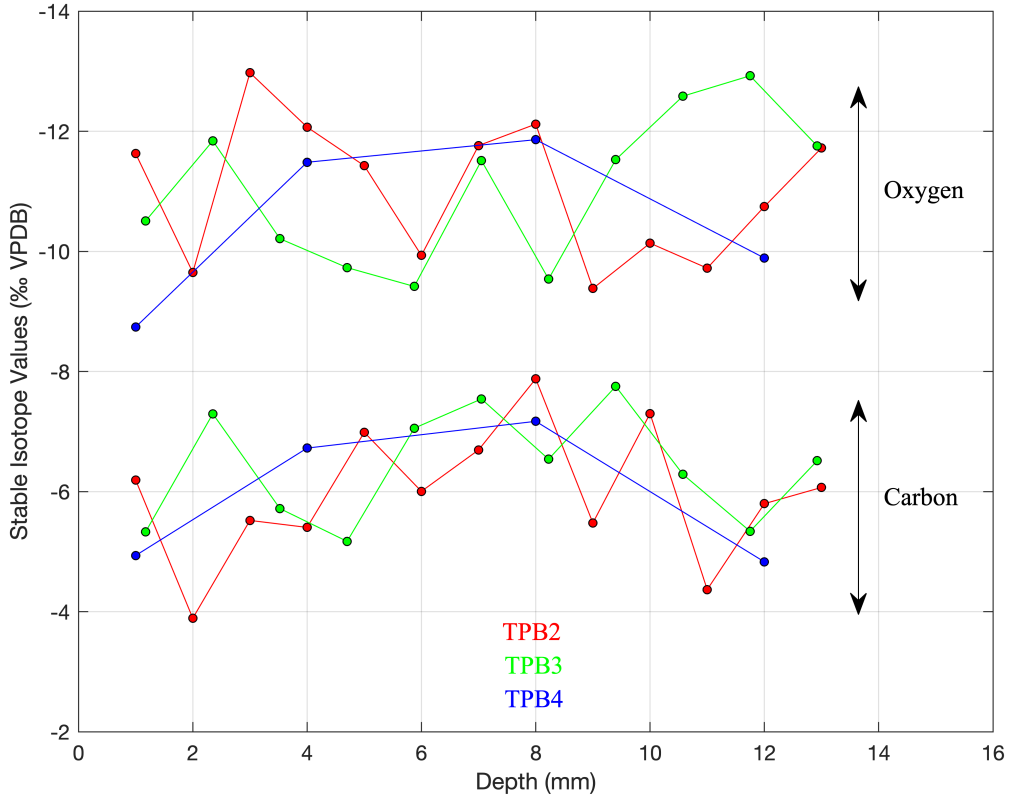


Figure 22: Low resolution stable isotope records from Tademaït Plateau calcite block samples TPB2 (red), TPB3 (green) and TPB4 (blue). Absolute values of each proxy in each sample are similar to that in TPB1, albeit with reduced variation, suggesting a homogenous moisture source and environmental conditions on the Tademaït Plateau during periods of increased rainfall throughout the middle-late Pleistocene.

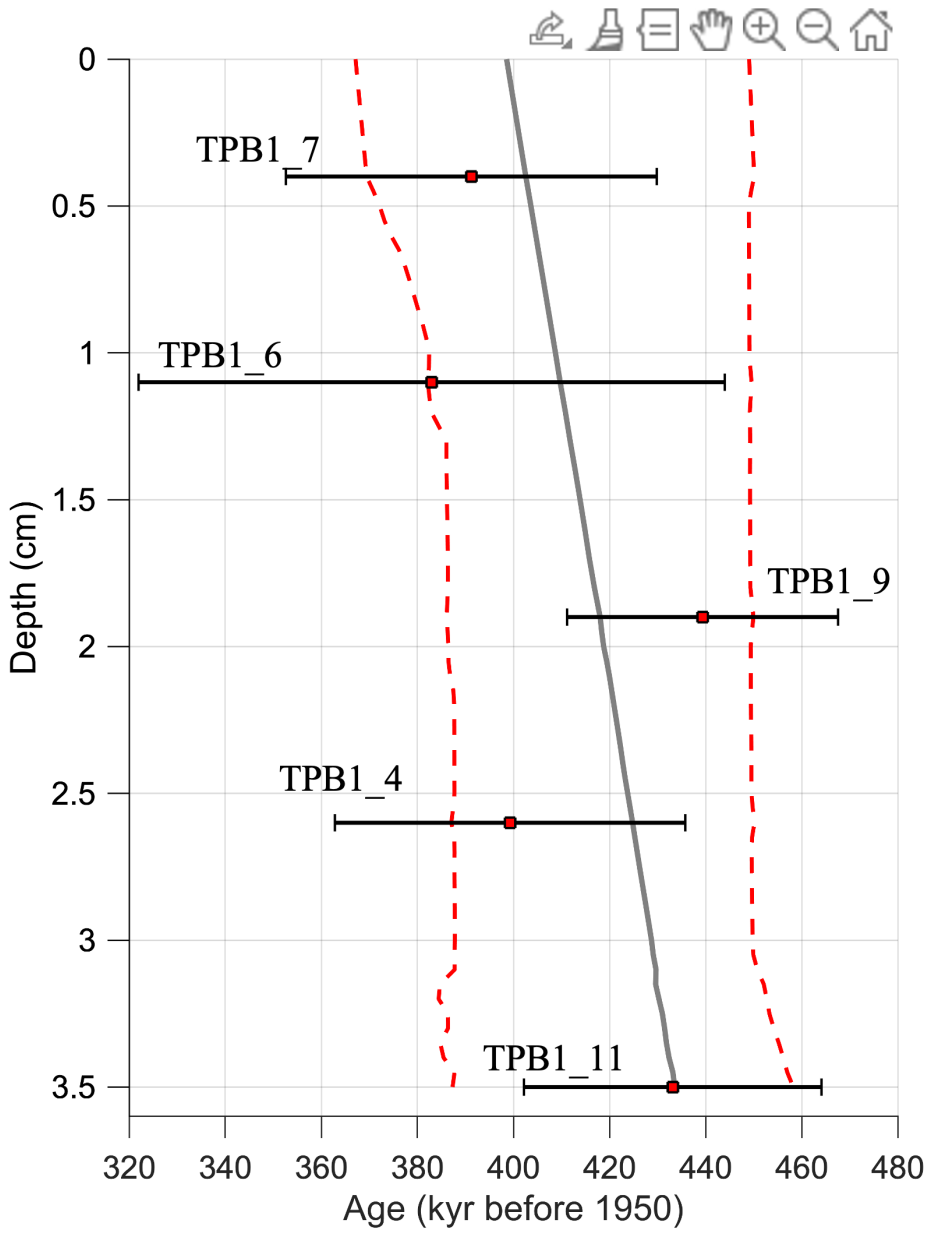


Figure 23: OxCal Age Model for TPB1. Unmodelled ages are plotted as red squares with black error bars. The mean age model, which is largely a line of best fit through sub-sample ages TPB1_4, _6, _7, _9 and _11, is plotted as a solid grey line, suggesting growth between 434 and 398 kyr BP. 95% Confidence intervals are plotted as red dashed lines.